Starspot properties and photometric parameters of transiting planets and their host stars

Jeremy Tregloan-Reed
Mphys (Hons) Lancaster University

Doctor of Philosophy

Department of Astrophysics, University of Keele.

October 2014

Abstract

To begin understanding how the architecture of hot Jupiter planetary systems can be so radically different from that of our own solar system, requires the dynamical evolution of planets to be known. By measuring the sky-projected obliquity λ of a system it is possible to determine the dominant process in the dynamical evolution.

If a transiting exoplanet that crosses the disc of its host star passes over a starspot, then the amount of received intensity from the star will change. By modelling the position of the anomaly in the lightcurve it is possible to precisely determine the position of the starspot on the stellar disc. If the position of the starspot can be found at two distinct times using two closely spaced transits, then it is possible to measure λ. Before now there was no definitive model capable of accurately modelling both a planetary transit and a starspot.

This research focuses on the development of PRISM which is capable of accurately modelling a transit containing a starspot anomaly. Due to the nature of the parameter space a new optimisation algorithm was developed, GEMC, which is a hybrid between a genetic algorithm and MCMC.

PRISM and GEMC were then used to model transit data of WASP-19, WASP-6 and WASP-50. From this it was then possible to determine $\lambda = 1.0^\circ \pm 1.2^\circ$ for WASP-19 b and $\lambda = 6.4^\circ \pm 2.3^\circ$ for WASP-6 b. These values imply that both WASP-19 b and WASP-6 b formed beyond the snowline and migrated in towards their host stars though tidal interactions with the protoplanetary discs.

No starspot anomalies were detected in the WASP-50 lightcurves but, due to the record-breaking photometric precision of the data, it was possible to reduce the uncertainties in the properties of WASP-50 b from 6% (mass), 4% (radius), 9% (density) and 6% (surface gravity) to 5%, 2%, 4% and 2%, respectively.

Acknowledgements

"*In this galaxy there's a mathematical probability of three million Earth-type planets. And in the universe, three million million galaxies like this. And in all that, and perhaps more...only one of each of us.*"

– Dr Leonard H. McCoy

I begin first by thanking my wife Lyndsay, for all her support during my Ph.D. research. I would like to thank John Taylor for being an exceptional and patient supervisor. I thank Pierre Maxted for his helpful discussions and his role as my shadow supervisor. I also thank Nigel Cassidy for all his help and support. I would also like to thank Luigi Mancini for his helpful and insightful email correspondences.

Jeremy Tregloan-Reed

October 2014

Contents

List of Figures

List of Tables

1 Introduction

The research of this thesis explores starspot anomalies in the lightcurves of transiting exoplanets and how accurately modelling the starspots can help probe the dynamical evolution of transiting exoplanetary systems. Chapter 1 begins with an introduction to exoplanets including the various observational techniques available to study them, then describes the dynamical evolution of hot-Jupiters and how measuring the spin-orbit alignment of the planetary system can lead to better understanding of the dynamical evolution of the system. Chapter 2 explains the methodology used in the research for this thesis. This includes the data reduction pipeline used and the creation of PRISM and GEMC, the codes used to model and optimise transit lightcurves containing a starspot anomaly. Chapters 3 and 4 give the results and analysis from using PRISM and GEMC on transits and starspots of WASP-19 and WASP-6, respectively. Chapter 5 presents two transits of WASP-50 taken using the ESO NTT and is an excellent example of how using defocused photometry can drive down photometric uncertainties. Chapter 6 then gives the final conclusions and discussion of the work carried out in this thesis and potential further work.

This chapter begins with Section 1.1, which gives a brief historical overview on the field of exoplanet research. Section 1.2 describes the four main observational techniques used to study exoplanets, including radial velocity (RV) and photometric observational techniques. Section 1.3 reviews the measured physical properties of the population of known transiting planets with emphasis on hot-Jupiters and correlations between their physical properties. Section 1.4 discusses the dynamical evolution of exoplanets and the artifacts that these processes leave on the planetary system's architecture. It then describes the Rossiter-McLaughlin effect and how it can be used to measure the sky-projected stellar obliquity, which can lead to understanding the dynamical evolution of the planetary system. Section 1.5 explains the effect of starspots on transit lightcurves and the current available techniques to model them. It also explains how starspots in transit lightcurves can be used to measure the sky-projected stellar obliquity.

1.1 Historical Overview

Since the dawn of mankind one of the fundamental philosophical questions has been 'Are we alone?'. To begin answering this question astronomers have looked to the solar system and our planetary neighbours. In recent times planetary scientists and astrobiologists have begun to speculate over the possibilities of finding microbial communities below the surface of Mars, protected from the harmful effects of the solar wind and cosmic rays (Boston et al., 1992; Dartnell et al., 2007). Mankind has also begun to look at one of the Galilean moons of Jupiter, Europa. Measurements of Europa's magnetic field suggest that a subsurface liquid water ocean may exist (Kivelson et al., 2000). This ocean can remain as a liquid by receiving thermal energy from tidal flexing of the moon from the eccentric orbit around Jupiter (Ross & Schubert, 1987). Another theory for the generation of thermal energy to form Europa's subsurface ocean is from the obliquity of Europa (the axial tilt of the moon with respect to its orbital plane) which has the right form and frequency to resonantly excite large-amplitude Rossby waves in Europa's subsurface ocean (Tyler, 2008). After exhausting the possibilities of finding intelligent life in our own solar system, astronomers started to look further out into the universe, but before they could even attempt to find intelligent life they had to find planets outside of our own solar system.

Wolszczan & Frail (1992) discovered the first planets outside of our solar system. They found two Earth mass planets orbiting the pulsar PSR1257 + 12 through pulsar timing variations. Pulsar planets are second generation planets formed after a supernova (Wolszczan & Frail, 1992). This tells us that planet formation may be physically possible in a range of environments. Then, Mayor & Queloz (1995) discovered the first planet around a sun-like star, 51 Peg, using radial velocity (RV) measurements (see Section 1.2.1 for details). This discovery was vitally important due to the fact that our own Sun is a main-sequence star and so 51 Peg can be viewed as an analogue to our own solar system. 51 Peg b was found to be a Jupiter-class planet (i.e comparable mass to Jupiter) orbiting the host star with a semimajor axis of approximately 8×10^6 km

or 0.05 astronomical units[1] (AU) (Mayor & Queloz, 1995). This contradicted our understanding of the evolution of our own solar system due to a distinct difference in the system architecture. The biggest gas giant in our solar system is Jupiter lying at a distance of 5 AU from the Sun. All the other gas giants lie outside of Jupiter's orbit while all the rocky terrestrial planets lie within Jupiter's orbit. Two competing planetary evolution models were put forward to explain how Jupiter-class planets come to orbit so close to their host stars: disc-migration in a protoplanetary disc which also explained low obliquities and eccentricities (Goldreich & Tremaine, 1980; Papaloizou & Larwood, 2000), and planet–planet interactions combined with tidal dissipation (Matsumura et al., 2010). An example of planetary migration is that the gas giant formed beyond the snow line and through tidal interactions with the protoplanetary disc migrated in towards the host star (see Section 1.4 for more details). The snow line represents a distance in a solar/stellar nebula from the protostar where hydrogen compounds such as water, methane and ammonia can condense to form ice grains. The typical temperature at the snow line is around 150–170 K. There are two possible types of disc-migration which can occur. Type I migration is due to a differential torque exerted on the planet from the interior and exterior portions of the protoplanetary disc (Ward, 1997a). Type II migration is caused when the planet clears its orbit of the disc material, creating a density discontinuity which locks the planet into the disc viscous evolution (Ward, 1997a). For the planet–planet interactions model the gas giant's orbit is altered gravitationally due to another planet/planetoid in the system. The gas giant's orbit then aligns and circularises due to tidal dissipation (Matsumura et al., 2010).

Henry et al. (2000) and Charbonneau et al. (2000) found the first transit from photometric observations (Section 1.2.2) of an exoplanet, HD 209458 b. The HD 209458 system was already known to contain an exoplanet from RV measurements (Henry et al., 2000). The first planet discovered using followup of a photometric detection of

[1] An AU is the mean distance from the Earth and the Sun, where one AU = $1.495978707 \times 10^{11}$ m. (IAU resolution B2 at the 2012 General Assembly.)
(`http://www.iau.org/static/resolutions/IAU2012_English.pdf`)

a transit was OGLE-TR-56 (Udalski et al., 2002; Konacki et al., 2003). An offshoot from transit photometry that was theorised by Holman & Murray (2005) is transit timing variations (TTVs see Section 1.2.4). The first discovery of an exoplanet from TTVs was Kepler 9 d (Holman et al., 2010). Furthermore in recent years it has become possible to directly image planets. Chauvin et al. (2004) performed the first direct imaging of a 5 ± 2 M_{Jup} planet at a distance of 55 AU from its brown dwarf host star (2MASSWJ 1207334-393254). Then Marois et al. (2008) directly imaged two planets around the star HR 8799 and in a later observation discovered a third planet orbiting HR 8799 (Marois et al., 2008). The projected separations of these new planets were found to be 24, 38 and 68 AU with a mass range of between 5–13 M_{Jup}.

So far to date[2] a total of 1810 planets (Schneider et al., 2011) outside of our own solar system have been discovered using the methods discussed above. These planets have been found using RV surveys (Butler et al., 1996, 1999; Queloz et al., 2000) coupled with both ground-based (e.g SuperWasp and HAT) (Pollacco et al., 2006; Bakos et al., 2004) and space-based (CoRoT and *Kepler*) (Baglin et al., 2006; Borucki et al., 2010) transit detection surveys. The NASA *Kepler* space satellite has detected Earth-size planets in the Habitable Zone (HZ) of their parent star, potentially indicating new habitable worlds similar to our own Earth (Borucki et al., 2012; Borucki et al., 2013). Once sufficiently sized ground-based telescopes such as the European Extremely Large Telescope (E-ELT) are built, it will be possible to perform high-dispersion spectroscopy and RV measurements on these planets in the effort of answering the question 'Are we alone?' (Snellen et al., 2013). High-dispersion spectroscopy is a technique which takes advantage of the relative velocity of an exoplanet with respect to the Earth, the lines in the exoplanet spectrum will be slightly Doppler shifted and the Doppler shift varies continuously based on the orbital positions of the Earth and the planet. Because of this it may be possible to separate the molecular oxygen in the planet's atmosphere from the molecular oxygen found in the Earth's atmosphere (Snellen et al., 2013).

With such an ensemble of planets known, the field of exoplanetary research has

[2] `(http://exoplanet.eu)` accessed on 2014/07/18

become an independent field of its own. It is also becoming important to ascertain the physical properties of exoplanets to a high-precision. This will allow the statistical characterisation of exoplanets and their formation, coupled with evolution channels, to be studied in great depth furthering our knowledge of these planets.

The present trend of exoplanets discovered so far tends toward Jupiter-sized planets in orbits of only a few stellar radii from their parent star. This trend is skewed away from the observational limits of ground-based detection surveys. While space detection surveys are finding Earth sized planets it is nearly impossible to perform detailed ground-based follow up observations of these 'Super-Earths'. Because of this the majority of research in the field is towards hot-Jupiters. The term hot-Jupiter refers to Jupiter mass planets with orbital periods of less than 10 days. Many unanswered questions remain, for example, how did these planets form and how did they come to orbit so close to their host star? Also, do they contain a rocky or liquid core or even no core at all? To help answer these questions we need high-precision measurements of the planet's radius and mass. While the mass of a planet can be found from RV measurements its radius can be found from transit photometry. Many lightcurves for known exoplanets are of medium to poor quality, with uncertainties in the radii of the planet around 10-15 %. To answer the questions listed above requires uncertainties in the measurements of the planetary radius of 1-3 %, for example a hot-Jupiter with a rocky core will have a slightly smaller radius compared to an equal mass hot-Jupiter without a core (Fortney et al., 2007). Using 51 Peg b as an example and by comparing it to Figure 1.1 we can see that if 51 Peg b was coreless its radius would be 1.12 R_{Jup} while by having a 25 $M_{\oplus}$ core its radius would be at 1.05 R_{Jup}, a decrease of 7%. Fortney et al. (2007) explains that the difference in radii due to having a core is from the stronger gravitational force exerted by the core on the outer layers of the gas giant. Two different models, core accretion (Pollack et al., 1996) and gravitational instability (Boss, 1997) both predict different core masses. As such, a precise measurement of a Transiting Extrasolar Planet's (TEP) radius is important in determining the dominant formation process.

Another reason why high-precision measurement of planetary radii are important

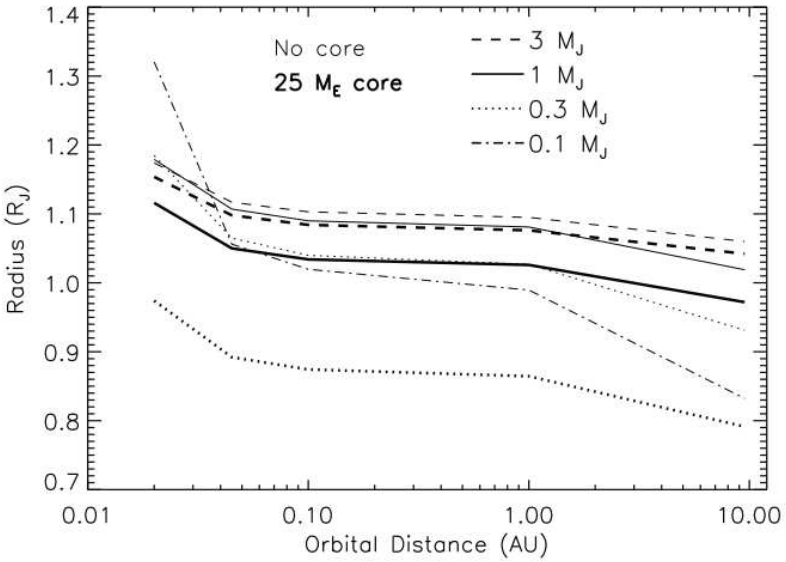

Figure 1.1: Planetary radii at 4.5 Gyr as a function of orbital distance from a Sun-like star (Fortney et al., 2007). The radii of four planets are calculated both with and without a core. The masses are 0.1, 0.3, 1.0 and 3.0 M_{Jup}. The fine lines represent a coreless planet while the thick lines represent planets with a 25 $M_\oplus$ core comprised of heavy elements. It should be noted that the 0.1 M_{Jup} planet with a core is off the plot at $\sim 0.5\,R_{Jup}$.

is that they can help us to determine the chemical composition of the outer layers of a hot-Jupiter. Fortney et al. (2008) defines two different types of hot-Jupiters using the chemicals TiO and VO. The pM class planet is thermally hot enough to allow both TiO and VO to be gases and hence allow the outer atmosphere to become slightly opaque. For cooler planets, on the other-hand, TiO and VO are predominantly in solid condensates and such planets are called pL class planets. Because of this the observed radii of hot-Jupiters will be dependent on which class they are (see Figure 1.2). This variation of the planet's radii is also wavelength dependent and observing a transit in multiple wavelengths would help reduce the uncertainties in the determination of the planet's class.

Therefore it is important to measure the radii of hot-Jupiters to high-precision

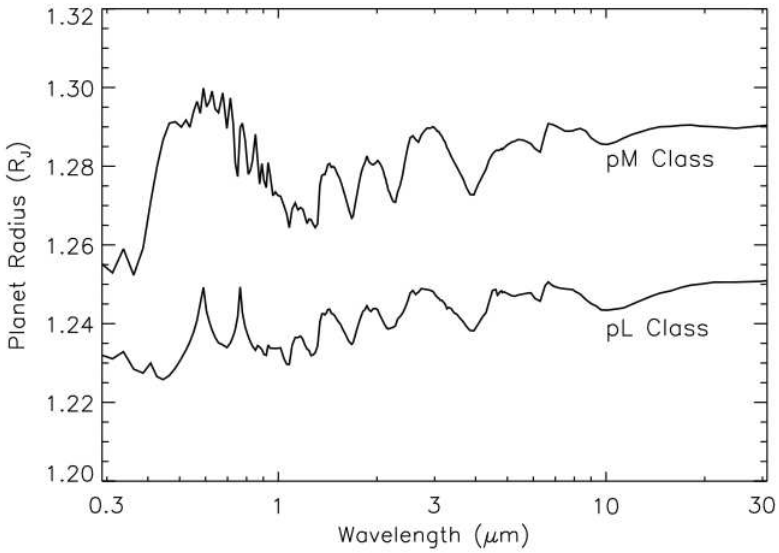

Figure 1.2: Radius as a function of wavelength for both a pM and pL class planet (Fortney et al., 2008). They have a 1 bar radius of 1.2 R_{Jup} and a surface gravity of $g = 15\,\mathrm{m\,s^{-2}}$.

to allow us to help constrain their structure and formation channels. To this end it is necessary to obtain precise transit photometry for the TEPs in question and through careful analysis determine their properties.

1.2 Observational Methods for Discovering Exoplanets

There are two main observational techniques used to both discover and measure the properties of exoplanets. The first uses radial velocity observations to measure the Doppler shift in the emitted light of the host star due to the rotational dynamics of the system. The second uses photometry to measure changes in the received intensity from a star as a function of time, from either a planet crossing the stellar disc or from gravitational bending of light from a lens star and planet.

1.2.1 Radial Velocity

In a planetary system both the planet and the star orbit around a point called the centre-of-mass. If m_1 and m_2 are the masses of the star and planet, respectively, a is the semimajor axis (average distance between the star and planet) and r is the distance from the centre of the star and the centre-of-mass, then the following equation (Hilditch, 2001) shows that when $m_1 \gg m_2$ then $r \approx 0$.

$$r = \frac{a}{1 + m_1/m_2} \tag{1.1}$$

So if m_2 is small enough then the centre-of-mass will lie within the star and the star's rotational axis will orbit around the centre-of-mass. This rotation can be observed by measuring the Doppler shift of the light emitted from the star. Figure 1.3 shows an example of radial velocity (RV) measurements for WASP-1 and WASP-2 taken with the SOPHIE spectrograph (Collier Cameron et al., 2007b).

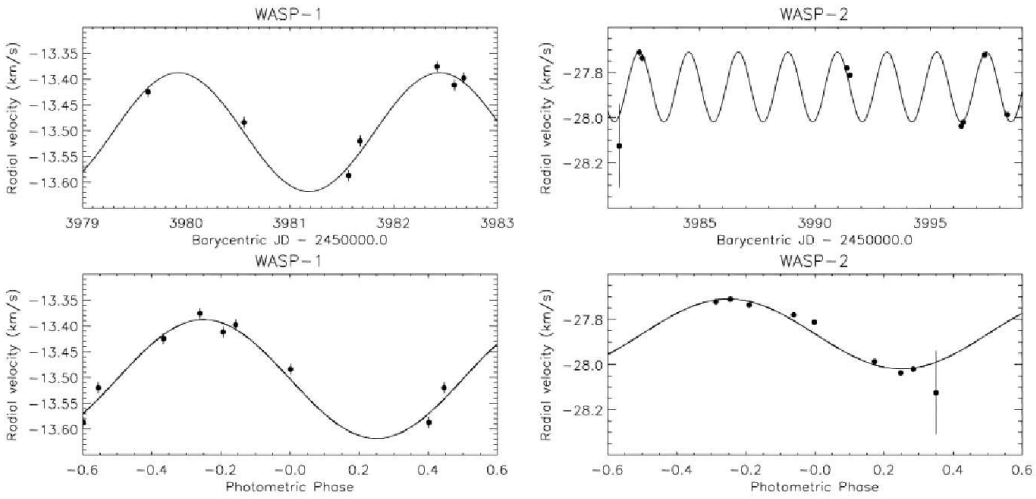

Figure 1.3: Radial velocity curves for WASP-1 and WASP-2 using the SOPHIE spectrograph (Collier Cameron et al., 2007b).

The first step in determining the minimum mass of the planet requires finding the RV of the star orbiting around the centre-of-mass. This is done by using a spectrograph

to observe the spectrum of a star. Then the wavelengths of the emission/absorption spectral features are found and compared to a stationary source. This comparison is done to measure the fractional shift in wavelength for a moving source. If an object is moving towards us then the emitted light is blue-shifted as the wavelength is shortened. Conversely if the object is moving away from us the light is red-shifted due to the wavelength being stretched. Assuming λ_{obs} is the observed wavelength and λ_0 is the wavelength from a stationary source (using the same spectral line) then the RV of the star, v, coupled with the speed of light, c, can be calculated:

$$\frac{v}{c} = \frac{\lambda_{obs}}{\lambda_0} - 1 \tag{1.2}$$

Once the RV of the star has been found for the individual data points a RV plot similar to Figure 1.3 can be created. This then allows the RV semi-amplitude of the star K, the orbital period P (the time difference between two peaks) and the orbital eccentricity e to be calculated. Eccentricity is a mathematical term used to describe the deviation from a circle into an ellipse, where $e = 0$ denotes a pure circle while $e = 1$ denotes an ellipse in which the longest axis is stretched out into infinity. The eccentricity can be found by the shape of the RV plot. If $e = 0$ then the shape would be purely a sine wave while as e increases the sine curve would become deformed. The following equation relates the above properties and allows us to determine the projected semimajor axis between the star and the centre-of-mass a_1 (e.g. Hilditch, 2001):

$$K = \frac{2\pi a_1 \sin i}{P\sqrt{1-e^2}} \tag{1.3}$$

The above equation also introduces a new variable i, the inclination of the planetary system. As can be seen $\sin i$ is a scalar and as such only affects the magnitude of the velocity amplitude and not the shape. If $i = 0$ then it would not be possible to perform a RV measurement of the system due to the plane of the orbit being aligned with the plane of the sky and as such the wavelength of the spectra observed along our line-of-sight would not be affected. The inclination of a planetary system can be found from photometric means (see Section 1.2.2). It is because of this unknown quantity

that we can only determine the lower mass limit of a planet using solely spectroscopic means (see Equation 1.11). The argument of periastron ω and the true anomaly θ (the angle between the periastron and the position of the planet) can also be found from the RV (Hilditch, 2001), where:

$$v = \frac{2\pi a_1 \sin i}{P\sqrt{1-e^2}} \left[\cos\left(\theta + \omega\right) + e\cos\omega\right] \tag{1.4}$$

By combining equations 1.3 and 1.4 we can obtain ω and θ in terms of v and K and hence can directly measure them from a RV plot.

$$v = K\left[\cos\left(\theta + \omega\right) + e\cos\omega\right] \tag{1.5}$$

To maintain convention if we re-write our variables from Equation 1.1 to be $r = a_1$ and $a = a_1 + a_2$ (where a_2 is the semimajor axis between the planet and the centre-of-mass) we can then express Equation 1.1 as follows:

$$m_1 a_1 = m_2 a_2 \tag{1.6}$$

This then allows us to write the projected semimajor axis between the star and the centre-of-mass, a_1, as a function of mass:

$$a_1 = \frac{m_2}{m_1} a_2 \tag{1.7}$$

Then, by combining Equations 1.3 and 1.7 we can write K in terms of the planet/star mass-ratio and the projected planet semimajor axis a_2:

$$K = \frac{2\pi a_2 \sin i}{P\sqrt{1-e^2}} \left(\frac{m_2}{m_1}\right) \tag{1.8}$$

The next stage in detailing the system makes use of Kepler's 3^{rd} law,

$$P^2 = \frac{4\pi^2 a_2^3}{GM} \tag{1.9}$$

By using the total mass $M = m_1 + m_2$, the orbital period of the planet P, the semimajor axis of the planet a_2 and the gravitational constant G. Then, by rearranging for the

planet's semimajor axis a_2, we arrive at:

$$a_2 = \left(\frac{GMP^2}{4\pi^2}\right)^{1/3} \tag{1.10}$$

Using this we can then combine Equations 1.8 and 1.10 to derive the mass function which allows the lower bound of the planetary mass to be found once the stellar mass is known:

$$K = \left(\frac{2\pi G}{P}\right)^{\frac{1}{3}} \frac{m_2 \sin\, i}{m_1^{2/3}} \frac{1}{\sqrt{1-e^2}} \tag{1.11}$$

In this case i is the inclination of the planetary orbit and hence only allows us to determine the lower bound of the planetary mass as discussed before. But when coupled with photometry it is possible to find a value for i, enabling a precise value for the planetary mass to be obtained.

The final stage in determining the lower bound of the planetary mass is to examine the line spectra from the star itself. This is accomplished using models of main-sequence stellar atmospheres (see Gray, 2008) to ascertain the effective temperature T_{eff}, surface gravity $\log(g)$ and metal abundance of the star $[Fe/H]$. The effective temperature of a star is that of a black body emitting an equal amount of electromagnetic radiation and the surface gravity is the net gravitational acceleration at the surface of the star. While the metal abundance of the star is the logarithmic ratio of metal to hydrogen of the star compared to that of the Sun. Different stellar atmospheric models (e.g. ATLAS9 (Kurucz, 1979; Castelli & Kurucz, 2003) and MARCS (Gustafsson et al., 1975, 2008)) predict different spectral line equivalent widths based on input parameters such as T_{eff}, $\log(g)$ and $[Fe/H]$. The equivalent width of a spectral line is the measure of the area within the spectral line on a plot of wavelength vs. intensity. Researchers can then use one of two different types of fitting algorithms. The first method used fits the observed spectra with synthetic spectra generated from the input parameters and stellar atmospheric models such as SME (Spectroscopy Made Easy)-(Valenti & Piskunov, 1996). The second method compares the spectral line equivalent widths between synthetic and observed spectra (e.g. GALA (Mucciarelli et al., 2013)). Both

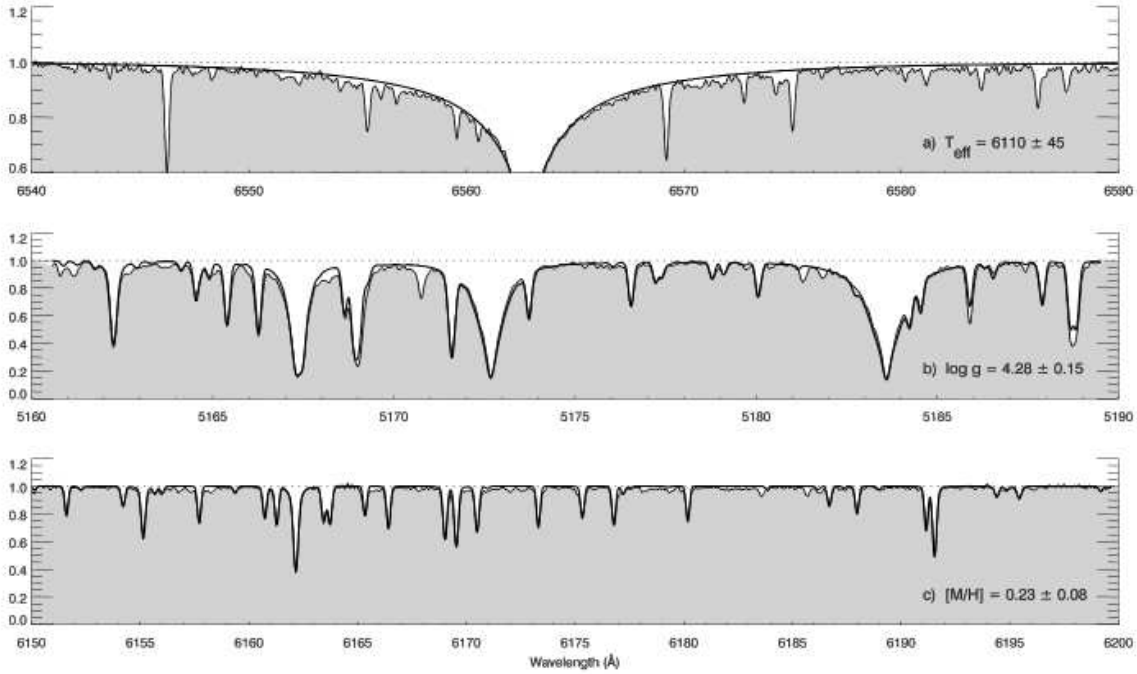

Figure 1.4: Panels comparing a synthetic spectrum (solid, thick line) to the observed spectrum (grey) of WASP-1 taken from Stempels et al. (2007). The top panel shows the temperature sensitive Hα 6563 Å line. The middle panel shows the $\log(g)$ sensitive Mg b 5175 Å triplet (the wavelengths are at 5167 Å, 5172 Å and 5183 Å (Aldenius et al., 2007)) spectral line. The bottom panel shows a section containing many lines which are sensitive to $[M/H]$.

methods work by varying the input parameters and inserting them into the different atmospheric models to produce synthetic spectra, which are then compared to the observed spectra either by using the spectral line equivalent widths or sections of the spectrum containing spectral lines sensitive to certain parameters (see Figure 1.4).

To find the values of T_{eff}, $\log(g)$ and $[Fe/H]$ for the observed star, spectral lines that are sensitive to these parameters are studied. For example, Stempels et al. (2007) used the Hα 6563 Å line to measure T_{eff} and the Mg b 5175 Å triplet lines (the wavelengths are at 5167 Å, 5172 Å and 5183 Å (Aldenius et al., 2007)) to measure $\log(g)$. It is also possible to measure $\log(g)$ from the Ca I 6122 Å and Ca I 6162 Å

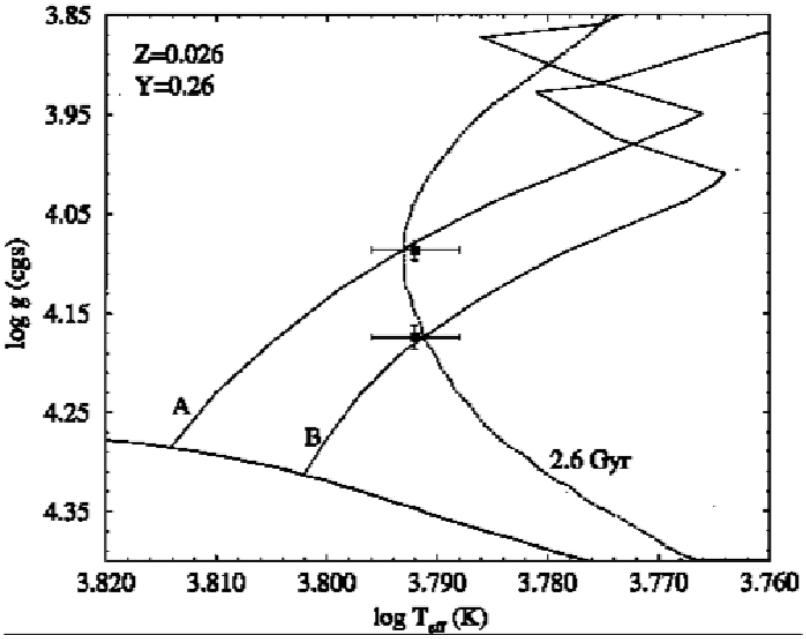

Figure 1.5: H-R diagram of effective temperature versus $\log(g)$ from Ribas et al. (1999). Here we see the zero-age main-sequence (ZAMS) line and the 2.6 Gyr isochrone indicating changing mass with respect to changing surface gravity and effective temperature. The isochrones marked A and B represent constant mass with changing age. The two points with error bars represent the two components of the detached eclipsing binary CD Tau A and B. This plot indicates that both stars are 2.6 Gyr old within the uncertainties.

spectral lines (Stempels et al., 2007).

Once this has been achieved the parameters are plotted on a H-R diagram of $\log(g)$ versus T_{eff} and are compared to theoretical stellar evolution models to ascertain the age and mass of the star (see Figure 1.5). It is worth pointing out that most researchers in the field of exoplanets plot a H-R diagram of effective temperature versus stellar density to ascertain the stellar age and mass (see Figure 1.6). To accomplish this would require the density of the star to be known and this can be found to high-precision from transit photometry (see Section 1.2.2 for more details).

There are different stellar evolution models available to find the age and mass of a star, these include Claret (Claret, 2004b, 2005, 2006, 2007), Yonsei-Yale (Y^2)

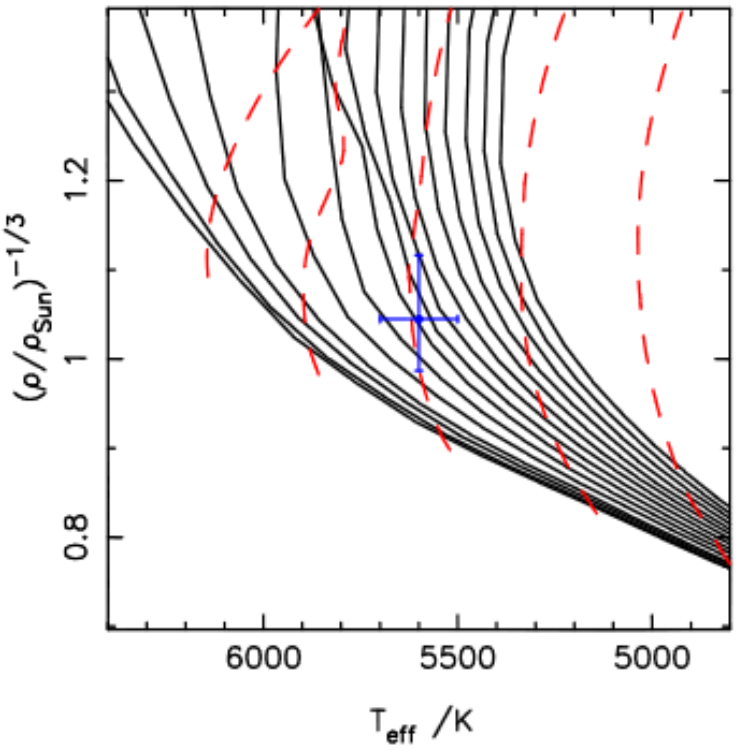

Figure 1.6: H-R diagram of effective temperature versus $(\rho/\rho_{\odot})^{-1/3}$ for WASP-56 from Faedi et al. (2013). Here we see isochrone tracks from the Yonsei-Yale (Y^2) model (Demarque et al., 2004) for WASP-56 using a metallicity of $[Fe/H] = 0.12$ dex and stellar density of $\rho_* = 0.88\rho_{\odot}$. From left to right the solid lines are for isochrones ranging from 1.8-14.0 Gyr. From left to right the red dashed lines are for mass tracks ranging from 1.2-0.8 $M_{\odot}$. This gives a stellar mass of $1.01^{+0.03}_{-0.04}$ $M_{\odot}$ and a stellar age of $6.2^{+3.0}_{-2.1}$ Gyr.

(Demarque et al., 2004) and Padova (Girardi et al., 2000). The final results for the age and mass of a star are either taken from a single model (e.g. Bakos et al. (2010, 2012); Hellier et al. (2012); Faedi et al. (2013)) or statistically derived from the individual results from multiple models (e.g. Southworth et al. (2009a,b, 2010); Southworth (2008, 2009, 2010, 2011)). The models are started from the zero-age of the main-sequence (ZAMS) for various starting masses and chemical compositions and are evolved through to the asymptotic giant branch or carbon burning stage. This generates isochrones that

can be directly compared to the T_{eff} and either $\log(g)$ or the stellar density $\log(\rho_*)$ of the star. Through this method it is possible to ascertain both the age and mass of the host star.

In summary, by using spectroscopy to observe exoplanets it is possible to not only deduce the lower bound of the planetary mass but ascertain key features of the host star and system. It is also possible to determine the effective temperature of the star coupled with the surface gravity and metal abundance. These in turn can allow us to determine the mass and age of the star within the model-dependent theoretical uncertainties. The orbital properties of the planet can also be deduced from spectroscopic methods. We can see from Kepler's 3^{rd} law that the orbital period in conjunction with the stellar mass can be used to find the orbital separation between the planet and host star (the sum of a_1 and a_2 found from Equations 1.3 and 1.10, respectively), while the eccentricity of the orbit can be found from direct analysis of the RV curve.

1.2.2 Photometry

As a planet transits the disc of its parent/host star the amount of received flux from the star decreases. This is in fact the same process seen when Venus transits the solar disc. For a planet to transit the disc of the parent/host star its orbital inclination i must be close to 90°. Photometry is in essence measuring the change in flux received from the target star with respect to time and creating a lightcurve. A lightcurve is a plot of flux as a function of time. The angular diameter θ of a celestial object in the sky is given by Equation 1.12, where R is the radius of the object and d is the distance between the observer and the object.

$$\theta = 2\arctan\left(\frac{R}{d}\right) \tag{1.12}$$

For a transiting planet the distance between the Earth and the planet is approximately the same as the distance between the Earth and the parent/host star. Because of this any change in flux ΔF due to the planet crossing the disc of the star is a direct indicator

of the square of the ratio between the radii of the planet R_p and star R_* as seen in Equation 1.13 for a uniformly illuminated disc (see Section 1.2.2.1).

$$\Delta F = \left(\frac{R_p}{R_*}\right)^2 \tag{1.13}$$

The ratio between the radii of the planet and star is usually denoted with the symbol k such that $R_p/R_* = k$. Hence Equation 1.13 can be written as:-

$$\Delta F = k^2 \tag{1.14}$$

By examining the shape of a lightcurve (see Figure 1.7) we can find an abundance of information about the planetary system not ascertainable from RV measurements (Section 1.2.1). The orbital period of the planet can be found from either RV measurements or from phase-folding multiple transits to ascertain the orbital period (Pollacco et al., 2008; Pepper et al., 2013). The inclination of the planetary orbit i can be written as the impact parameter b, which is the sky-projected distance from the stellar equator at mid-transit in units of the stellar radius. By using the semimajor axis of the system a, the eccentricity e and the argument of periastron ω found from RV measurements, Equations 1.15 and 1.16 give b for the transit and occultation, respectively (the transit is when the planet crosses in front of the star and the occultation is when the planet passes behind the star) (Winn, 2011).

$$b_{tra} = \frac{a\cos i}{R_*}\left(\frac{1-e^2}{1+e\sin\omega}\right) \tag{1.15}$$

$$b_{occ} = \frac{a\cos i}{R_*}\left(\frac{1-e^2}{1-e\sin\omega}\right) \tag{1.16}$$

For a circular orbit where $e = 0$ equations 1.15 and 1.16 can be simplified to the following:

$$b = \frac{a\cos i}{R_*} \tag{1.17}$$

In the case of a circular orbit b is the same for both the transit and occultation. It is shown in the literature that in general transiting exoplanets tend to have small

eccentricities (see Section 1.3.4) as a consequence in the event when e is not known, Equation 1.17 can be used to give a good approximation for the impact parameter. In the case of WASP-26 neglecting the eccentricity would increase the impact parameter of the transit by 0.1% (Mahtani et al., 2013).

The total transit length T_{tot} is used to describe the time from when the planet disc starts to touch the stellar disc to when the planet disc no longer is in contact with

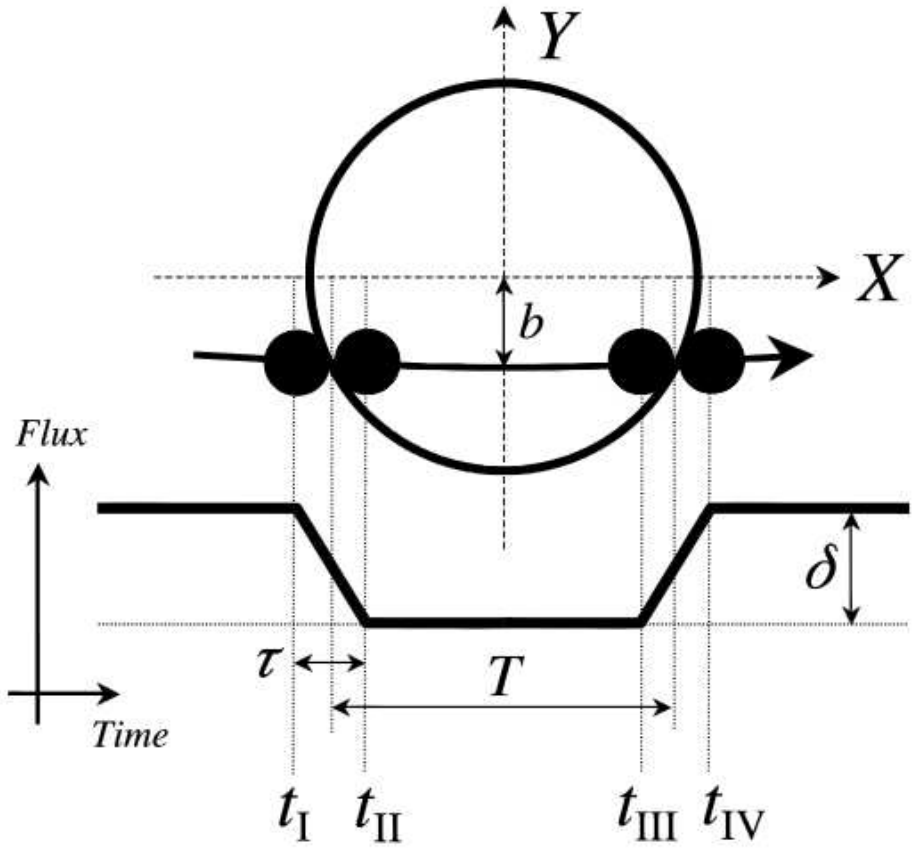

Figure 1.7: Illustration of a transit and corresponding lightcurve taken from Winn (2011). In this particular case the limb-darkening effect is being ignored. limb-darkening adds a curvature or rounding to the transit. b is the impact parameter, δ is the transit depth, τ is the duration of egress/ingress and t_I, t_{II}, t_{III} and t_{IV} are the four contact points.

the stellar disc (points t_I and t_{IV} from Figure 1.7) and is given by Equation 1.18 (Winn, 2011). The full transit length T_{full} is used to describe the time from when the planet disc is fully within the stellar disc to the point where it begins to leave the stellar disc (points t_{II} and t_{III} in Figure 1.7) and is given by Equation 1.19 (Winn, 2011).

$$T_{tot} \equiv t_{IV} - t_I = \frac{P}{\pi} \sin^{-1} \left[\frac{R_*}{a} \frac{\sqrt{(1+k)^2 - b^2}}{\sin i} \right] \tag{1.18}$$

$$T_{full} \equiv t_{III} - t_{II} = \frac{P}{\pi} \sin^{-1} \left[\frac{R_*}{a} \frac{\sqrt{(1-k)^2 - b^2}}{\sin i} \right] \tag{1.19}$$

One of the drawbacks from transit photometry is that it is not possible to discern the semimajor axis a, unless coupled with RV measurements. To deal with this during the modelling the radii of both the planet and star are scaled to units of a, where $r_p = R_p/a$ and $r_* = R_*/a$ are the fractional radii. This removes the dependence on a in Equations (1.15 to 1.19).

In summary, by measuring the length of totality, length of full transit, duration and depth of a planetary transit from transit photometry we can ascertain the orbital inclination and scaled radii of the planet and star. If the inclination is then combined with RV data and used in Equation 1.11 coupled with the stellar mass from stellar models, we can determine a precise measurement of the planetary mass. Using Equations 1.3 and 1.8 we can also ascertain the true semimajor axis by using the inclination. This in turn will then allow the radii of the planet and star to be calculated. With the radii and masses of the planet and star known it would then be possible to find their respective mean densities, which is important for structure and formation models.

As pointed out in Section 1.2.1 it is possible to directly determine the stellar density from transit photometry. If we combine the identity $R_* = a\, r_*$ with Kepler's 3^{rd} law (Equation 1.9) we get:

$$R_*^3 = \frac{GMP^2}{4\pi^2} r_*^3 \tag{1.20}$$

As the total mass M is equal to $m_* + m_p$ and density ρ for a sphere equals mass over volume:

$$\rho = \frac{M}{V} = \frac{3M}{4\pi R^3} \tag{1.21}$$

We can then combine Equations 1.20 and 1.21 into:

$$\rho_* + k^3\rho_p = \frac{3\pi}{GP^2} r_*^{-3} \tag{1.22}$$

Since k^3 is usually small (for example, the k value for WASP-19 is $k = 0.1428$ (see Chapter 3) which equates to a value of $k^3 = 0.002911955$, which renders the contribution from the planetary density insignificant) the planet's density term can be dropped to allow the stellar density to be directly calculated.

Independently both the RV and transit photometry methods can help us understand the planetary system in great detail but only to a certain extent. When combined to study a system, however, they both complement each other by filling in the gaps that the other method cannot address.

1.2.2.1 limb-darkening

In reality, lightcurves do not look like the one in Figure 1.7, but in fact the transit shape is more rounded (see Figure 1.8). This is caused by limb-darkening (LD). When stars are observed they do not appear as a uniform disc. The limb (the edge of the disc) appears to be fainter. Viewing the central region of a star allows us to see to deeper layers as compared to the limb of the star, which can be understood by the fact that our line-of-sight is along the surface normal $\hat{n}$ at the stellar centre but is perpendicular to $\hat{n}$ at the edge of the stellar disc. These deeper layers are hotter and hence produce more light than the cooler outer layers.

There are many different functions used to model LD, based on theoretical model atmospheres. Each LD law uses a set of coefficients that have been tabulated based on theoretical model atmospheres (e.g. Claret, 2004a). All the LD laws take into account

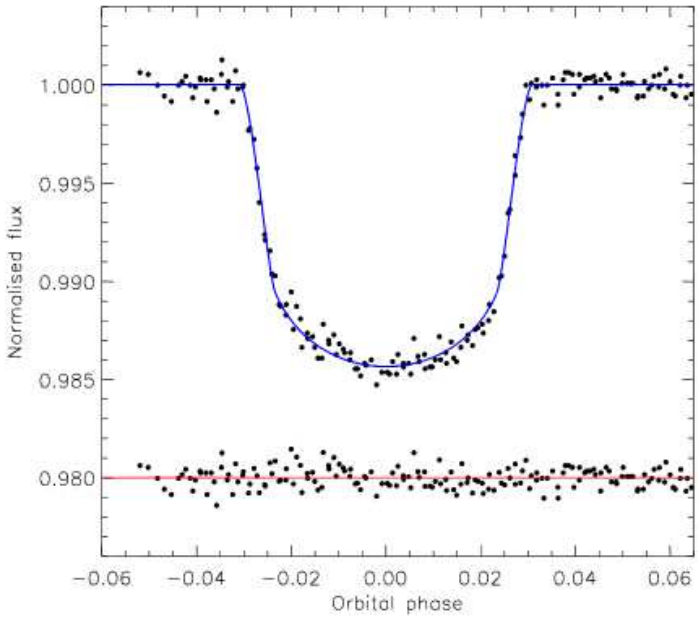

Figure 1.8: Phased light curve of two transits of WASP-5 (Southworth et al., 2009a). The data are compared to the best-fitting model (Blue solid line). The transit is rounded due to limb-darkening, which in this case is modelled using the quadratic law. The residuals of the fit are seen at the bottom of the figure.

the angle, μ, between the line-of-sight and $\hat{n}$ where $\mu = \cos\theta$. They also give the received intensity $I(\mu)$ at an angle θ in units of received intensity from the centre of the star I_0. The linear LD law (Equation 1.23) uses a single coefficient u, which if the lightcurve is of sufficient quality can be fitted for or fixed during the modelling process.

$$\frac{I(\mu)}{I_0} = 1 - u(1-\mu) \tag{1.23}$$

The quadratic LD law (Equation 1.24) uses two coefficients a and b.

$$\frac{I(\mu)}{I_0} = 1 - a(1-\mu) - b(1-\mu)^2 \tag{1.24}$$

The cubic LD law (Equation 1.25) uses three coefficients p, q and r (Barban et al., 2003).

$$\frac{I(\mu)}{I_0} = 1 - p(1-\mu) - q(1-\mu)^2 - r(1-\mu)^3 \tag{1.25}$$

A second cubic LD law (Equation 1.26) uses only two coefficients p and r (Van't Veer, 1960).

$$\frac{I(\mu)}{I_0} = 1 - p(1-\mu) - r(1-\mu)^3 \tag{1.26}$$

The square-root LD law (Equation 1.27) uses two coefficients e and f (Diaz-Cordoves & Gimenez, 1992).

$$\frac{I(\mu)}{I_0} = 1 - e(1-\mu) - f(1-\sqrt{\mu}) \tag{1.27}$$

The Logarithmic LD law (Equation 1.28) uses the two coefficients c and d (Klinglesmith & Sobieski, 1970).

$$\frac{I(\mu)}{I_0} = 1 - c(1-\mu) - d\mu\ln\mu \tag{1.28}$$

The fourth order LD law (Equation 1.29) uses the coefficient a subscripted between 1 to 4 (Claret, 2000, 2003).

$$\frac{I(\mu)}{I_0} = 1 - \sum_{k=1}^{4} a_k\left(1-\mu^{k/2}\right) \tag{1.29}$$

The exponential LD law (Equation 1.30) uses the coefficients g and h (Claret & Hauschildt, 2003).

$$\frac{I(\mu)}{I_0} = 1 - g(1-\mu) - \frac{h}{(1-e^{\mu})} \tag{1.30}$$

Southworth (2008) showed that to model a TEP accurately a non-linear LD law should be used while a LD law using three or more coefficients is unnecessary when data is of the accuracy of ground-based observations. It is obvious in the literature (e.g. Mandel & Agol, 2002; Bakos et al., 2009; Krejčová et al., 2010; Boisse et al., 2013; Hartman et al., 2012; Howard et al., 2012; Pepper et al., 2013; Bean et al., 2013; Mancini et al.,

2013a) that many TEP researchers use the quadratic LD law (Equation 1.24) when modelling ground-based transits of TEPs around main-sequence stars. To determine the effectiveness of a LD law for a particular star, the fitted coefficients are compared to the theoretical values. If the data are of insufficient quality the uncertainty interval for the LD coefficients will be large and as such the theoretical coefficients should be used. Howarth (2011) showed that the LD coefficients derived from transit photometry do not always agree with their tabulated counterparts and, in fact, the LD coefficients from transit photometry are biased away from the true values. This is due to trying to compare two different methods. The tabulated coefficients are calculated using theoretical stellar atmosphere models while the coefficients derived from transits have a degeneracy with the impact parameter. To derive the theoretical LD values requires the effective temperature T_{eff}, surface gravity $\log(g)$, metal abundance of the star $[Fe/H]$ and microturbulence to be known. Microturbulence is a form of turbulence which varies over small scales. Inside stars it is the micro-scale non-thermal gas velocity in the region of where the spectral line is formed and therefore, effects the width and strength of the absorption lines. The size of the cell is less than the mean-free path of a photon (Doyle et al., 2013). As discussed in Section 1.2.1 these values can be calculated from comparing spectral lines and synthetic spectra generated from model atmospheres.

There are various theoretical LD models to cover the range of LD laws and wavelengths. Claret (2004a) calculated theoretical LD coefficients for the linear, log, quadratic, square-root and fourth order laws in the Sloan u', g', r', i' and z' passbands. Klinglesmith & Sobieski (1970) produced coefficients for the linear and logarithmic laws for stars with a $T_{eff} \geq 10000\,\mathrm{K}$. Diaz-Cordoves et al. (1995) calculated LD coefficients for the Strömgren u, v, b and y bands and the Johnson U, B and V. Both Sing (2010) and Claret & Bloemen (2011) calculated the coefficients for the CoRoT and *Kepler* space satellite passbands. Claret & Bloemen (2011) also produced coefficients for the Spitzer satellite and the Sloan filters.

1.2.3 Gravitational Microlensing

Gravitational microlensing uses a lens star with a mass approximately 0.1 to 1.0 $M_{\odot}$ (Steves et al., 2011) to bend the light of a distant star. This causes the source star to brighten, in some cases by a couple of magnitudes, in the case of OGLE-2005-BLG-390 (see Figure 1.9) the source star's intensity was magnified by a factor of three (Beaulieu et al., 2006). A planet orbiting the lens star creates an anomaly in the light curve which can last a matter of hours or weeks depending on the planets size and the angular size of the source star (Steves et al., 2011). The use of gravitational microlensing to detect planets was put forward by Mao & Paczynski (1991) and Gould & Loeb (1992). They theorised about detecting planets around galactic disc stars through microlensing from stars in the galactic bulge. This technique can detect planets with a range of masses,

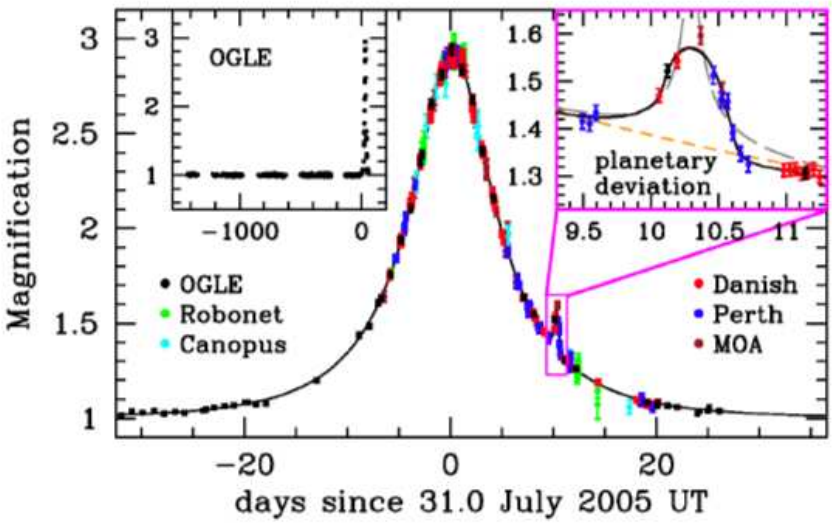

Figure 1.9: The observed lightcurve of the OGLE-2005-BLG-390 microlensing event and best fit model plotted as a function of time (Beaulieu et al., 2006). The top left inset shows the OGLE light curve extending over the previous 4 years, whereas the top right one shows a zoom of the planetary deviation, covering a time interval of 1.5 days. The solid curve is the best star-planet lens model. The dashed grey curve is the best binary source model that is rejected by the data, while the dashed orange line is the best single lens model.

from Jupiter to Earth mass (Bennett & Rhie, 1996).

To detect a planet in a microlensing event the planet must be within the lensing zone which can lie between 1 and 4 AU (Bennett & Rhie, 1996). In 2003 the first planet detected from gravitational microlensing was discovered, OGLE 2003BLG235/MOA 2003BLG53 (Bond et al., 2004). The planet of 1.5 Jupiter masses orbiting at a distance of 3 AU was detected by two separate gravitational microlensing surveys: the Optical Gravitational Lensing Experiment (OGLE) (Udalski, 2003) and Microlensing Observations in Astrophysics (MOA) (Bond et al., 2001). Both surveys were originally designed to observe gravitational microlensing events of the galactic bulge to find dark matter. It was later found, however, that the same technique could be used to find planets. During a microlensing event for a single point mass the lightcurve is symmetrical around a peak. The peak in the received intensity happens at the minimal angular impact parameter between lens and source star. But when the lensing object is a binary system a short deviation can be seen in the lightcurve (see Figure 1.9). The amplitude of the deviation indicates the mass ratio and orbital separation of the two objects.

1.2.4 Transit Timing Variations

By performing precise photometry of a transiting exoplanet for multiple transits it is possible to precisely measure variations in the transit timing. These variations, called Transit Timing Variations (TTVs), can be used to detect other planets in the system (Miralda-Escudé, 2002; Agol et al., 2005; Holman & Murray, 2005). In a planetary system with a single planet the measured transit time of the planet is non-variant (when ignoring stellar activity such as starspots, see Section 1.5.1). If a second planet is present it gravitationally interacts with both the star and the first planet. Through this interaction the first planet's angular momentum is varied and this variation can be measured through changes in the orbital period of the primary planet. TTV's have the potential to discover Earth-mass planets (Agol et al., 2005), for example a Earth-mass planet in a 2:1 orbital resonance with a transiting hot-Jupiter with an orbital period

of three days would cause an eight minute variation over a period of a year.

Holman et al. (2010) announced the first discovery of planets from the TTV method, Kepler-9 d and Kepler-9 e. From data collected from the *Kepler* satellite they discovered two Saturn sized planets (Kepler-9 b and Kepler-9 c) transiting the host star. They then detected variations in the orbital periods of the planets caused by two further planets in a 2:1 orbital resonance. Ballard et al. (2011) detected a TTV signature for another *Kepler* target, Kepler 19 b. While there are many different dynamical mechanisms which match the period, amplitude and shape of the transit timing signal (see Figure 1.10), they were able to confirm the existence of a second planet, Kepler 19 c. They deduced that the planet has a mass of $\leq 6\,\mathrm{M_{Jup}}$ coupled with an orbital period of ≤ 160 days. Kepler 88 b was also found to harbour a TTV (Nesvorný et al., 2013). This TTV signal was the largest ever discovered and Kepler 88 c was nicknamed the king of TTVs. They were able to detect a second non-transiting planet in the system with a mass of 0.626 ± 0.03 $\mathrm{M_{Jup}}$ and an orbital period of $22.3397^{+0.0021}_{-0.0018}$ days. Barros et al. (2014) later confirmed Kepler 88 c using RV measurements and determined the

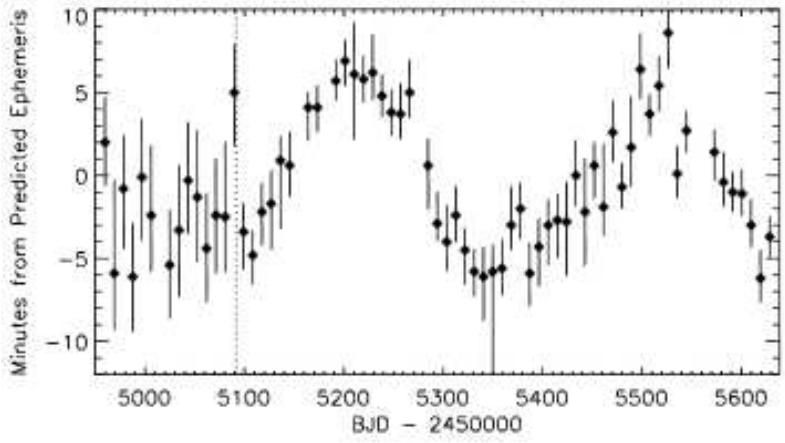

Figure 1.10: *Kepler* transit times for Kepler 19 b, as compared to a best fit linear ephemeris (Ballard et al., 2011). The sinusoidal pattern indicates that Kepler 19 b is undergoing a form of TTV. The dotted line denotes the change between long and short cadence from the *Kepler* satellite.

minimum mass to be $0.76^{+0.32}_{-0.16}$ M_{Jup} and found an orbital period of 22.10 ± 0.25 days.

Lissauer et al. (2011) also used TTVs in the Kepler-11 system. They discovered six planets transiting the host star and used TTV's to validate the planetary nature of the transits by determining the masses for five of the planets (Kepler-11 b, c, d, e and f). The masses of the five inner planets range from $2\,M_{\oplus}$ to $13\,M_{\oplus}$. Lissauer et al. (2011) was only able to determine the upper limit on the mass of the outer planet Kepler-11 g to be $< 300\,M_{\oplus}$.

1.3 Properties of Known Transiting Exoplanets

TEPs are the only planets outside of our own solar system for which we can directly measure the mass and radius. Through understanding these core attributes we can uncover further properties (e.g. density and surface gravity) which allow us to understand the formation and evolution of these systems and begin to answer how the architecture of these systems are so radically different from that of our own solar system. At present there are 372 published TEPs[3]. Due to such a large sample it is possible to statistically compare the physical properties of these systems. We can then look for trends to help improve existing theoretical models.

1.3.1 Mass-Radius Relations

Figures 1.11 and 1.12 show that there is a large concentration of TEPs centred around the 1.00 M_{Jup} and 1.25 R_{Jup} area. The reason for this large concentration is due to observational constraints. The detection of a transit is dependent on the amount of intensity lost, therefore Jovian planets around small stars will give deeper transits than

[3]All measured physical properties of the known TEPs were obtained from the 29/11/2013 version of the TEPCat catalogue (Southworth, 2011).
(`http://www.astro.keele.ac.uk/~jkt/tepcat/`)

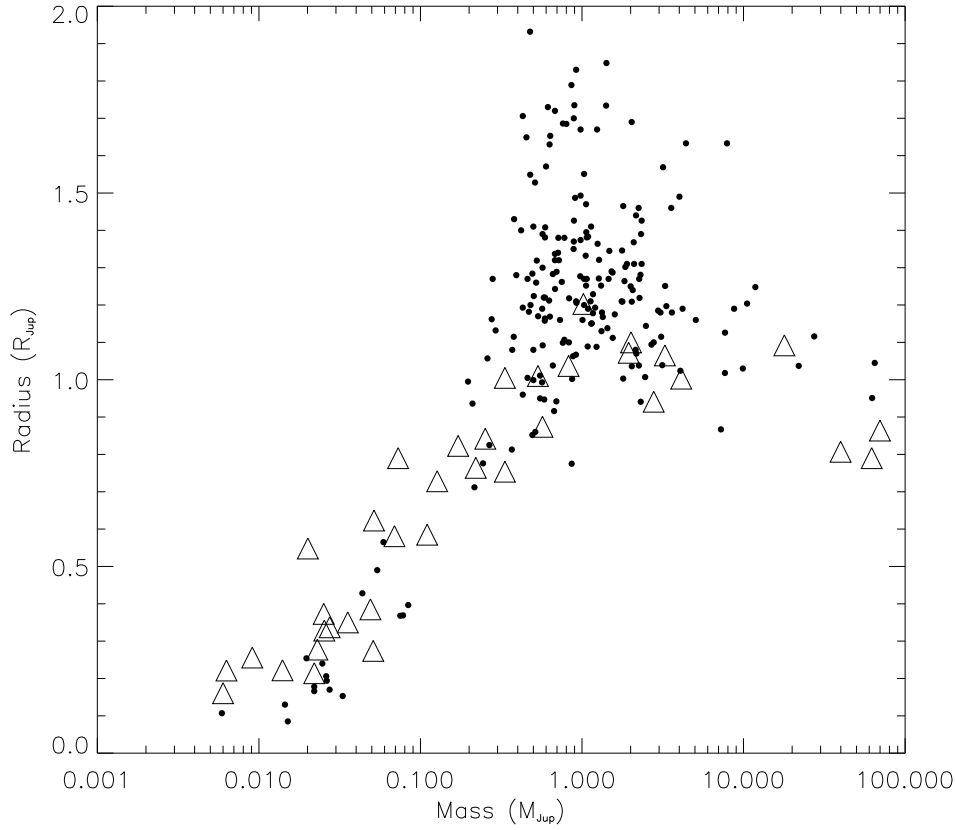

Figure 1.11: Plot of mass against radius for 372 TEPs from TEPcat. The circles represent TEPs with periods less than 10 days while the triangles represent TEPs with periods greater than 10 days.

Earth-like planets around giant stars. As many TEPs have been discovered by ground-based transit surveys that are not sensitive to Earth-size planets, this will place limits on the types of planets discovered. The planets that are in the bottom left corner of Figure 1.11 are super Earths. A super Earth is an exoplanet whose mass lies between 1.9–10.0 $M_{\oplus}$ (Charbonneau et al., 2009). Further to the right in the figure are the super-Neptune planets and then the Jupiter-class planets. The Brown dwarf zone is to the right of the 13 M_{Jup} mark (Spiegel et al., 2011). The collection of hot-Jupiters around 1 M_{Jup} and above 1.5 R_{Jup} are the inflated hot-Jupiters (e.g. WASP-17 b (Anderson et al., 2010b; Southworth et al., 2012b)).

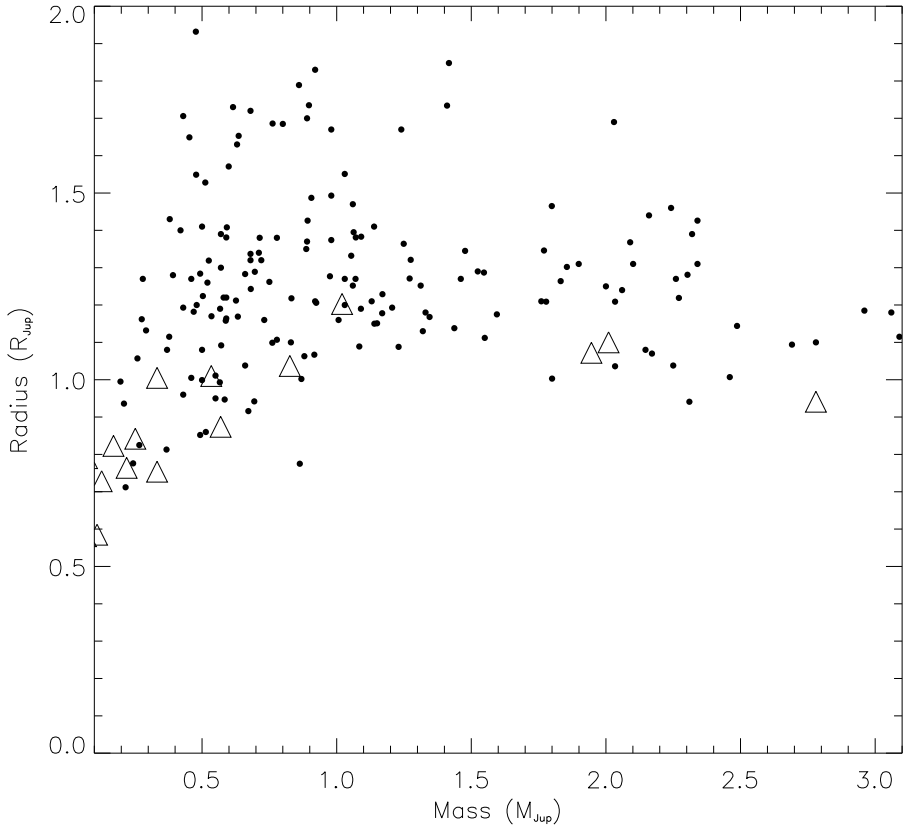

Figure 1.12: Plot of mass against radius between 0.1 M_{Jup} and 3.1 M_{Jup} for 372 TEPs from TEPcat. The circles represent TEPs with periods less than 10 days while the triangles represent TEPs with periods greater than 10 days.

Figure 1.12 allows us to see with better clarity that almost all of the TEPs with a mass of 1.0 M_{Jup} have radii larger than 1.0 R_{Jup}. This is because these TEPs are hot-Jupiters and due to being in close proximity to their host stars their outer layers are blasted by stellar radiation which causes the outer layers to inflate. There are other possible mechanisms for planetary inflation. After the formation of a gas giant the core begins to cool and the planet contracts. But there are certain atmospheric processes which can block the energy dissipation of the core and hence reduce the contraction of the planet (e.g. Burrows et al., 2007). Likewise the planetary atmosphere can also dump energy onto the planetary core and therefore reduce the rate of cooling and

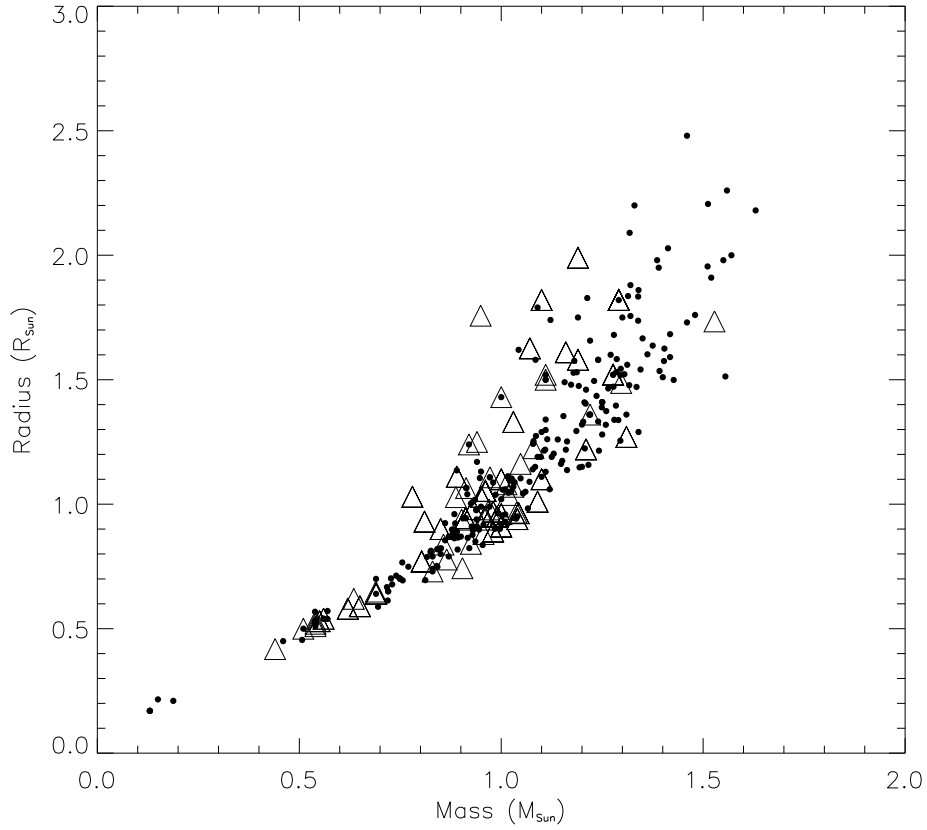

Figure 1.13: Plot of stellar mass against stellar radius for 372 TEPs host stars from TEPcat. The circles represent TEPs with periods less than 10 days while the triangles represent TEPs with periods greater than 10 days.

thus contraction (e.g. Showman & Guillot, 2002; Arras & Socrates, 2010; Batygin & Stevenson, 2010; Youdin & Mitchell, 2010). It is also possible to inflate a gas giant from the tidal dissipation onto the interior of the gas giant though eccentricity damping (Ibgui & Burrows, 2009; Miller et al., 2009).

Figure 1.13 shows the relationship between the stellar mass and the stellar radius for the 372 TEP systems. The stars on the left hand side (less than $0.7\,M_{\odot}$) are all unevolved and are on the main-sequence. The stars in the centre (between $0.7\,M_{\odot}$ and $1.7\,M_{\odot}$) are a mixture of both evolved and unevolved stars. The cut off above $1.7\,M_{\odot}$ is due to the stars being too hot to have many spectral lines, making RV confirmation

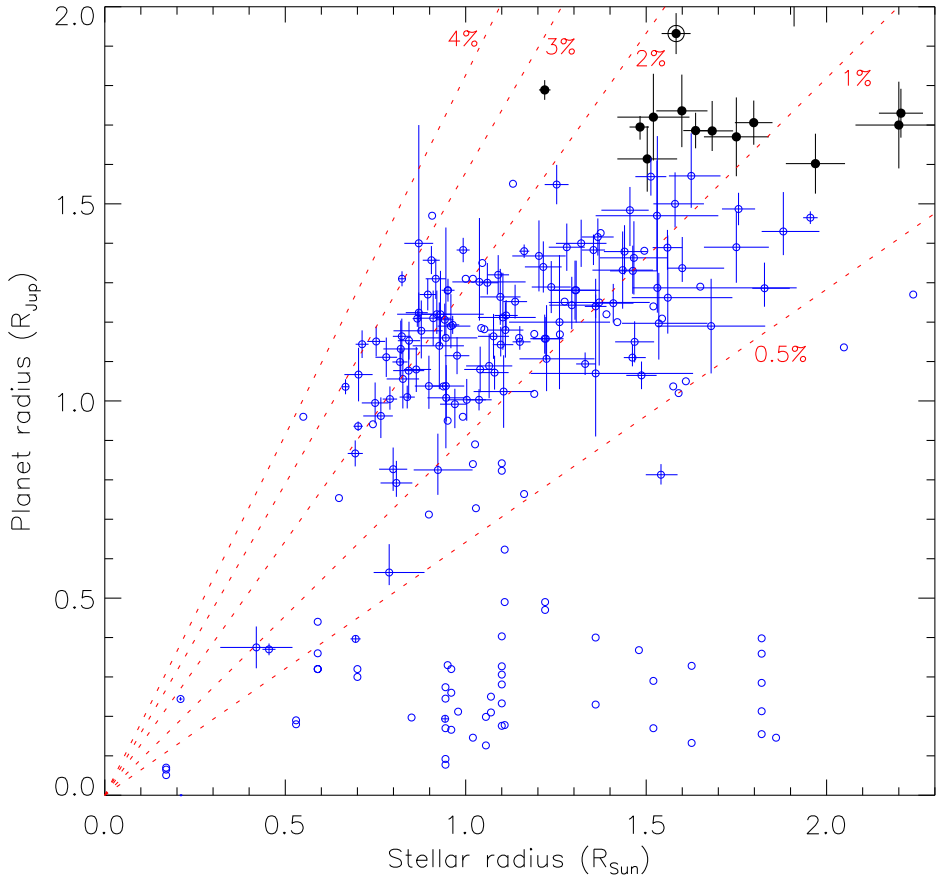

Figure 1.14: Plot of planetary radius against stellar radius for 372 TEPs from TEPcat courtesy of Dr John Taylor. The open circles represent the *Kepler* TEPs while the crossed circles represent ground-based detection of TEPs. The black circles represent systems where the sub-stellar companion is a brown dwarf. The dashed red lines represent fixed transit depths.

of planets difficult.

Figure 1.14 shows the relationship between the stellar and planetary radii (courtesy of Dr John Taylor). Two concentrations are clearly seen around the 0.25 R_{Jup} (lower section) and 1.25 R_{Jup} (upper section) marks. Planetary radii are measured from transit photometry where the transit depth is dependent on the ratio between the planetary and stellar radii. As a consequence the size in planetary radii discovered is dependent on both the observational efficiency of the telescope used and on

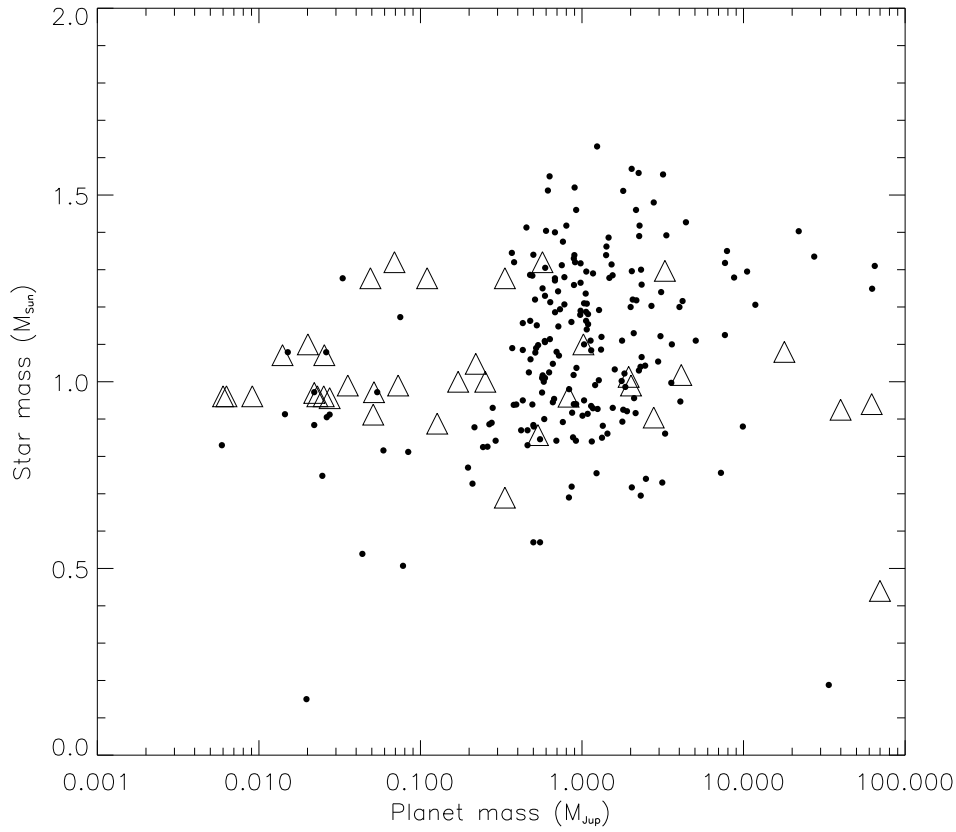

Figure 1.15: Plot of planetary mass against stellar radius for 372 TEPs from TEPcat. The circles represent TEPs with periods less than 10 days while the triangles represent TEPs with periods greater than 10 days.

the size of the star (the smaller the star the smaller the planet that can be detected). The first group around the 0.25 R_{Jup} mark are planets detected by the *Kepler* space satellite while the second group around the 1.25 R_{Jup} mark are planets detected by ground-based transit surveys.

Figure 1.15 shows the relationship between the planetary and stellar masses. It shows a similar pattern seen in Figure 1.14 with the exception that there is only one concentration around the 1 M_{Jup} mark. To discover the mass of a planet requires RV data (see Section 1.2.1) and planets discovered from ground-based transit surveys are ideal candidates for RV follow up observations. This is not always the case for planets

discovered from the *Kepler* satellite. This is because the target stars are too faint to be able to perform the precise ground-based RV measurements needed to measure the planets mass, though TTVs have allowed some *Kepler* planets to be validated by measuring the upper limit on their mass (Xie, 2013a,b).

1.3.2 Period-Planetary Surface Gravity Relationship

Southworth et al. (2007b) shows a correlation between the orbital period and the surface gravity of TEPs. The idea is that surface gravity has an influence on the evaporation rates of the outer atmospheres of hot-Jupiters. Figure 1.16 shows the same correlation within the hot-Jupiter zone. As the period increases the surface gravity reduces. To

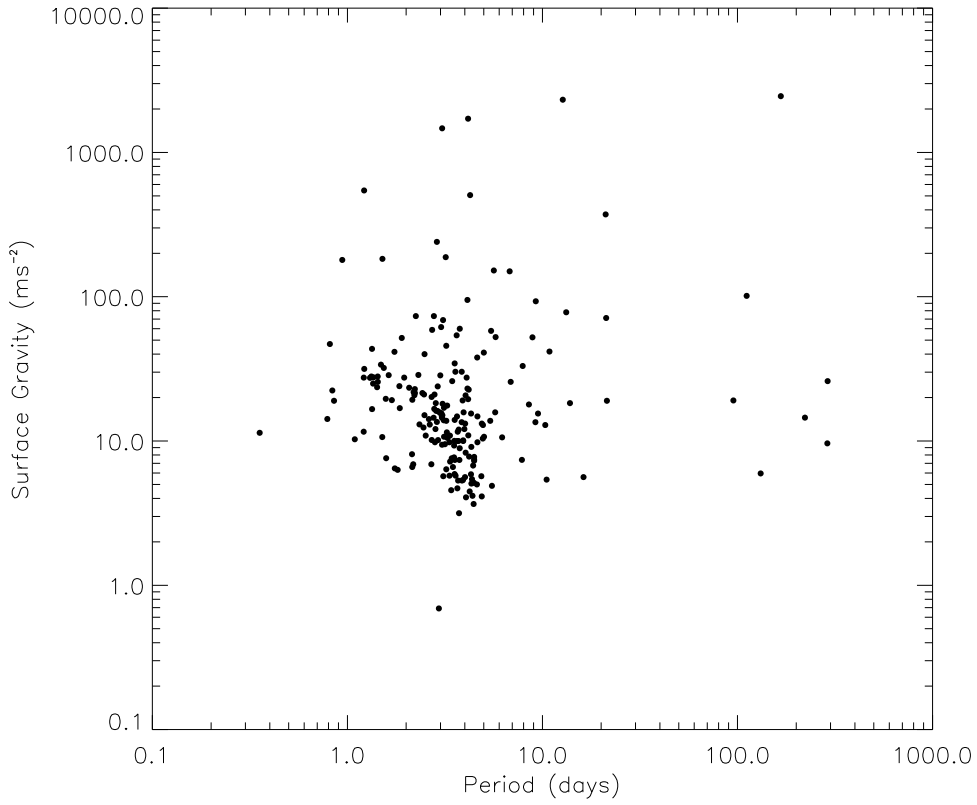

Figure 1.16: Plot of orbital period against surface gravity for 372 TEPs from TEPcat.

determine the confidence in the correlation the rank correlation test of Spearman (1904) was used. The test was used on the population of gaseous TEPs (i.e. having a mass between $10\,M_{\oplus}$ and $13\,M_{Jup}$). The test returned a probability of 99.836% ($3.1\,\sigma$) for the gaseous population. This shows that the correlation between the orbital period and surface gravity of hot-Jupiters is real and that it is supported by current data.

It is possible to calculate the surface gravity of a TEP using only observable quantities (Southworth et al., 2007b).

$$g_p = \frac{2\pi}{P} \frac{(1-e^2)^{\frac{1}{2}}\, K^*}{r_p^2 \sin i} \tag{1.31}$$

Equation 1.31 (Southworth et al., 2007b) shows all that is required to calculate the planets surface gravity g_p, is P, r_p, i, e and K_*. P can be found from either transit photometry of multiple transits or from RV observations. r_p and i are both found from transit photometry, while e and K_* are found from RV observations.

1.3.3 Planet Mass-Orbital Period Relationship

Figure 1.17 shows the relationship between the mass of a TEP and its orbital period. By studying Figure 1.17 we can see a correlation in the hot-Jupiter zone. As the planet's mass increases the orbital period decreases. Kepler's 3^{rd} law (Equation 1.9) shows that the orbital period increases as the orbital separation increases. Because a planet's surface gravity is directly related to the mass of the planet then we expect Figure 1.17 to show the same correlation for hot-Jupiters that is seen in Figure 1.16. Mazeh et al. (2005) also mentioned the same relationship between a planets mass and its semimajor axis. They explained that the underlying process for this correlation is due to thermal evaporation from extreme UV flux from the parent star. Thermal evaporation (Lammer et al., 2003) will affect planets with masses below a critical mass. Here the evaporation time scale is shorter than the planets thermal time scale. As such, below this critical mass the planets survival time is relatively short. At greater distances from the host star the amount of extreme UV flux reduces hence increasing the critical mass limit.

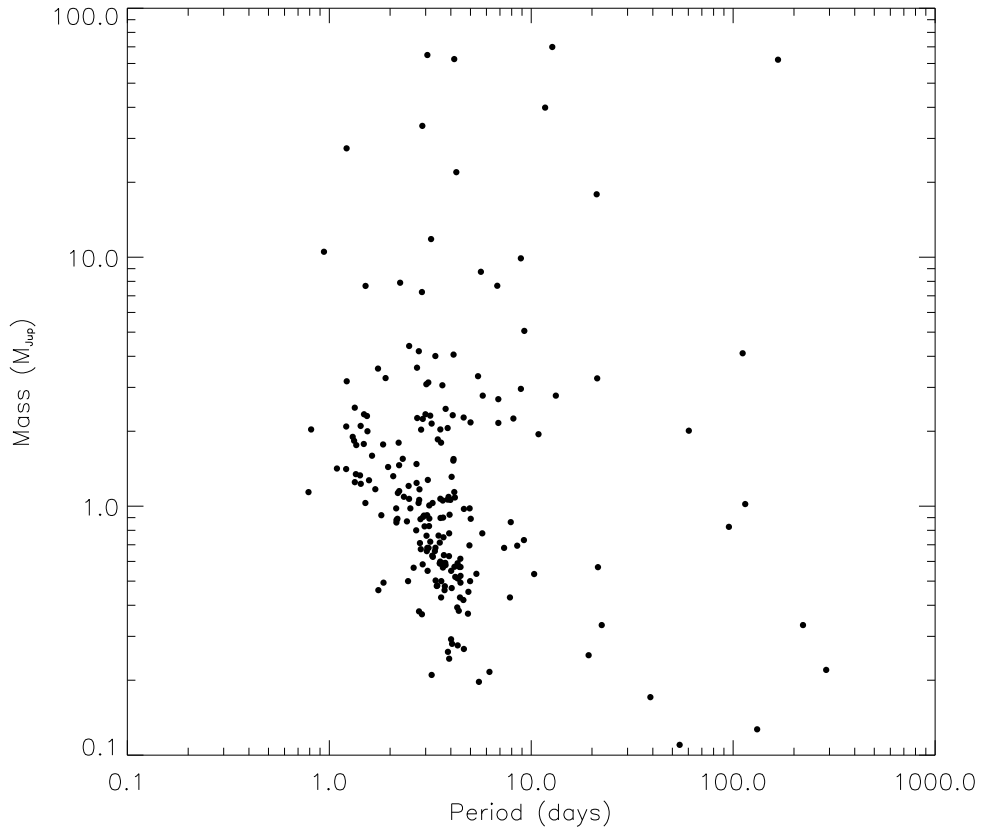

Figure 1.17: Plot of orbital period against planet mass for 372 TEPs from TEPcat.

To determine the confidence in the correlation the rank correlation test of Spearman (1904) was used. The test was used on the population of gaseous TEPs (i.e. having a mass between $10\,M_{\oplus}$ and $13\,M_{Jup}$). The test returned a probability of 99.999% ($5.4\,\sigma$) for the gaseous population. This shows that the correlation between the orbital period and planetary mass of hot-Jupiters is real and that it is supported by current data. The relationship between the orbital period and planetary mass is more correlated than the relationship between the orbital period and the surface gravity (see previous Section). This is expected because the surface gravity is dependent on both the mass and radius of the planet. By including the radius, extra scatter is included into the correlation between the orbital period and surface gravity. However, both of these correlations

explain why stars with a high UV flux have dense planets. To survive the high UV flux the planet requires a high mass but also requires a high surface gravity. To obtain a high surface gravity requires the planetary radius to be smaller which causes the planet to increase in density.

1.3.4 Orbital Eccentricity-Semimajor Axis Relationship

Figure 1.18 shows the relationship between the orbital eccentricity and the semimajor axis of 372 currently known TEPs. 272 TEPs in the catalogue have either a value of $e = 0$ or an unmeasured value. Most TEP systems have an assumed eccentricity of

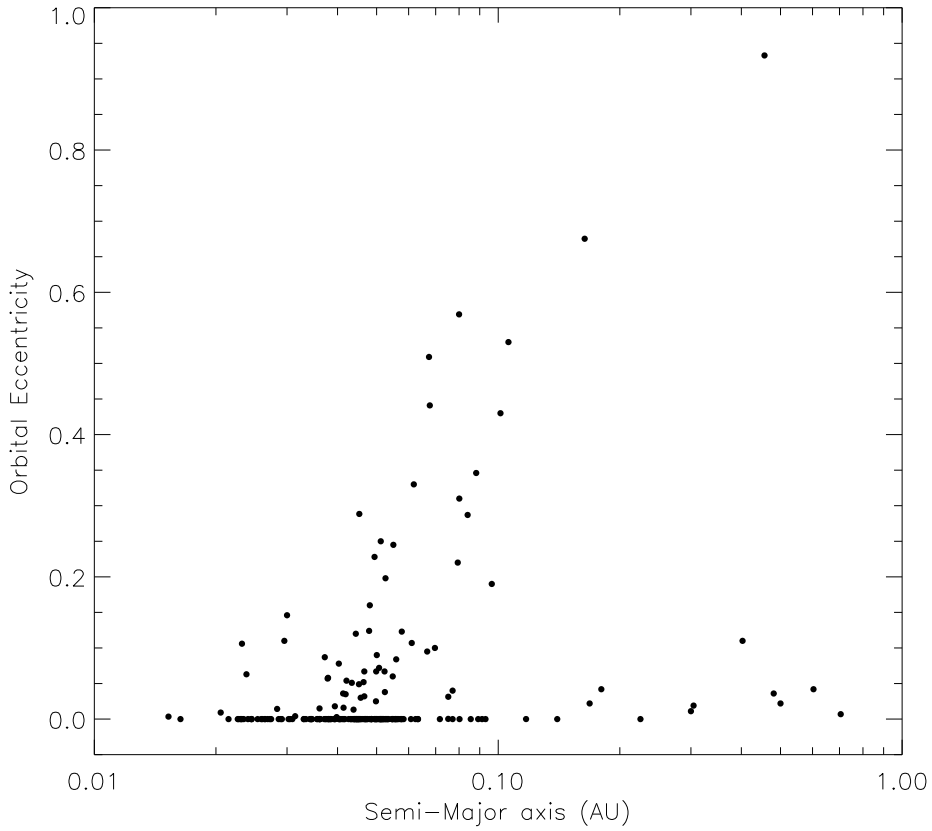

Figure 1.18: Plot of semimajor axis against orbital eccentricity for 372 TEPs from TEPcat.

zero (Anderson et al., 2012). It also suggests that the magnitude of the eccentricity is weakly dependent on the size of the semimajor axis. The closer the planet is to the host star the greater the probability that the orbit is circular. This is due to the interaction between the planet and the convective envelope of the host star, which circularises the planetary orbit (e.g. Jackson et al., 2009).

To determine the confidence in the correlation the rank correlation test of Spearman (1904) was used. The test was used on the population of gaseous TEPs (i.e. having a mass between $10\,M_{\oplus}$ and $13\,M_{Jup}$) of which had orbital eccentricities greater than zero. The test returned a probability of 97.409% ($2.2\,\sigma$) for this population. This shows that the correlation between the orbital eccentricity and the semimajor axis of hot-Jupiters is real and that it is supported by current data. Compared to previous Sections this correlation has the greatest scatter. This is due to the fact that the circularisation of the planetary orbit is dependant on the interaction between the planet with the convective envelope of the star. Hot stars (i.e. $T_{eff} > 6250\,K$) have a thinner convective envelope compared to cooler stars and therefore the time frame required to circularise an eccentric orbit will be longer. From this it is possible to see that the relationship between the orbital eccentricity and the semimajor axis is dependent on both the stellar T_{eff} and the age of the system.

1.4 Dynamical Evolution of Hot Jupiters

Prior to the discovery of 51 Peg b (Mayor & Queloz, 1995) the general belief was that gas giant planets formed beyond the snow line and evolved into stable orbits close to their formation orbit. For our own solar system this is thought to be at 5 AU (Mumma et al., 2003). The discovery of 51 Peg b and consequent further discoveries of hot Jupiters, meant that new dynamical evolution models had to be created.

Goldreich & Tremaine (1980) showed that the evolution of a planet's orbital eccentricity depended on the ratio between the torque exerted by the planet interacting with the disc on both the corotation and Lindblad resonance sites. If the orbit was

circular then the only torque exerted would be close to the Lindblad resonance site and the transport of angular momentum would be outward. On the other-hand if the planetary orbit was eccentric then the torque exerted on the corotation resonance site would create a damping effect to the eccentricity and circularise the orbit, while the torque generated at the Lindblad resonance site increases the eccentricity of the planets orbit. It was also shown that, for a Keplerian disc, and for when the resonances sites are not saturated, the net result is that the eccentricity of the planet is damped, therefore allowing the planet's orbit to circularise while the protoplanetary disc remains. As the planetary orbit becomes circular, the torque exerted on the corotation resonance site decreases, therefore reducing the damping effect and the transport of angular momentum would become more outward. Using these models, Goldreich & Tremaine (1980) calculated that Jupiter's semimajor axis evolved over an extremely small time scale of a few thousand years.

Ward (1997a) put forward the idea of Type I and Type II migration. These two distinct processes have the same end result in that the planet suffers from orbital decay through interactions with the protoplanetary disc and spirals in towards the host star. Type I migration occurs when the planet is not yet large enough to clear its orbit of disc material. The planet therefore interacts with the surrounding protoplanetary disc through interactions at the Lindblad resonance sites. Since the net torque from the disc is not zero (Goldreich & Tremaine, 1980) there will be intrinsic asymmetries in the planets interaction with the protoplanetary disc. The outer resonances will become systematically stronger and the resulting differential torque will push the planet in towards the star. The rate for this type I migration dr/dt_1 can be calculated using the mass of the planet M_p, the mass of the star M_*, the orbital frequency of the disc Ω, at a distance r, the gas sound speed c and the surface density of the disc σ (Ward, 1997b).

$$\frac{dr}{dt_1} \sim c_1 \left(\frac{M_p}{M_*}\right) \left(\frac{\sigma r^2}{M_*}\right) \left(\frac{r\Omega}{c}\right)^3 r\Omega \tag{1.32}$$

The leading coefficient c_1 is of order unity and since the outer resonances are normally

dominant the coefficient is negative and the orbit decays. If the disc lifetime is longer than the orbital decay time the planet will collide with the host star. If it is shorter then once the disc dissipates the planet will stop migrating towards the star (Ward, 1997b).

Type II migration occurs when the planet is large enough to clear its surrounding orbit of material, creating a gap in the protoplanetary disc. The planet then becomes tidally locked with the disc and migrates with the disc. The conservation of angular momentum shows that the bulk of the disc mass will migrate inward while a small fraction containing the majority of the angular momentum will migrate outward (Lynden-Bell & Pringle, 1974). The rate of Type II migration dr/dt_2 is therefore dependent only on the disc's viscosity ν and not the mass of the planet (Ward, 1997b) described by:

$$\frac{dr}{dt_2} \sim \frac{\nu}{r} \sim c_2 \alpha \left(\frac{c}{r\Omega}\right)^2 r\Omega \tag{1.33}$$

where α is a free parameter between the values of zero and one, where zero denotes zero accretion. The viscosity used in Equation 1.33 is based on the Sakura-Sunyaev viscosity law ($\nu \sim \alpha c^2/\Omega$). The coefficient c_2 is of order unity and the sign denotes the directional flow of the surrounding disc material. By inspecting Equations 1.32 and 1.33 we can clearly see that the rate of Type I migration is faster than Type II migration. By combining Equations 1.32 and 1.33 we can see that this is the case:-

$$\frac{dr}{dt_1} \sim \frac{c_1}{c_2 \alpha} \left(\frac{M_p}{M_*}\right) \left(\frac{\sigma r^2}{M_*}\right) \left(\frac{r\Omega}{c}\right)^5 \frac{dr}{dt_2} \tag{1.34}$$

Through both Type I and II migration the planet's orbit decays and the inclination and orbital eccentricity is damped (Goldreich & Tremaine, 1980; Papaloizou & Larwood, 2000; Matsumura et al., 2010). However, it has been shown that some exoplanets have high eccentricities (e.g. CoRoT-10, CoRoT-16, HAT-P-17, HAT-P-21 and HAT-P-34) and retrograde orbits (e.g. WASP-17 and HAT-P-7). Gravitational scattering, ejection and Kozai cycles (Kozai, 1962; Lidov, 1962; Fabrycky & Tremaine, 2007) can increase the orbital eccentricity and modify the alignment between the planetary orbit and the host star's rotation axis (Matsumura et al., 2010). In a three-body model it was

shown that it is possible for a planet to achieve a retrograde orbit via gravitational planet–planet scattering (Chatterjee et al., 2008). Kozai migration occurs when the Kozai cycles increase the orbital eccentricity of a planet (Wu & Murray, 2003). While these processes can increase the orbital eccentricity of a planet they alone do not explain how these planets come to orbit so close to their host stars. The answer to this is tidal dissipation (Matsumura et al., 2010). After the protoplanetary disc has dissipated the planet can undergo strong planet-planet scattering to achieve a highly eccentric orbit. Due to the high eccentricity the distance between the planet and the host star at periastron can become slightly larger than twice the Roche limit and tidal circularization can occur (Rasio & Ford, 1996; Chatterjee et al., 2008). Over the course of the stellar lifetime an alignment between the planet's orbit and the stellar rotation axis will take place (Matsumura et al., 2010).

While both disc-migration and gravitational scattering coupled with tidal dissipation can form close-in hot-Jupiter planets, the two different models produce differences in both the eccentricity and alignment of the planetary orbit. Therefore, it is possible to determine the type of dynamical evolution which took place in a particular planetary system, by measuring the alignment between the stellar rotation axis and the orbital axis of the planet which is more commonly known as the stellar obliquity.

1.4.1 Stellar Obliquity

The stellar obliquity ψ of a planetary system is a fundamental geometric property. It is the angle of alignment between the stellar rotation axis and the orbital plane of a planet. Coupled with the semimajor axis, the eccentricity of the orbit and the orbital inclination it allows us to build a complete geometric model of the planetary system. While in general it is not possible to measure ψ it is possible to measure the sky-projected obliquity λ, for transiting exoplanets, which can then be used to derive statistical constraints on ψ.

We choose a coordinate system where the $\hat{Z}$ axis points towards the observer and the $\hat{X}$-$\hat{Y}$ plane is the plane of the sky (see Figure 1.19). Then $\mathbf{n_o}$ lies in the $\hat{Y}$-$\hat{Z}$

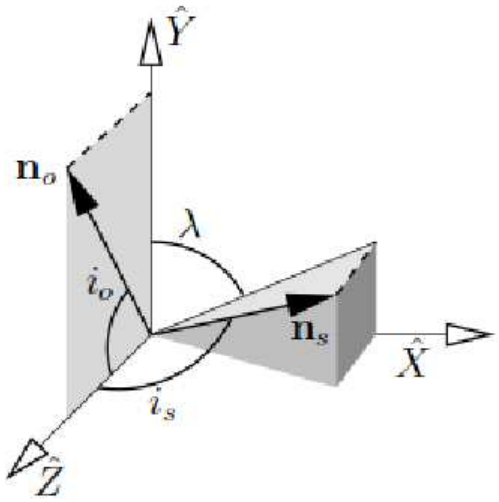

Figure 1.19: Coordinate system defining the sky projected obliquity angle (Fabrycky & Winn, 2009). The $\hat{Z}$ axis points towards the observer, while the $\hat{X}$-$\hat{Y}$ plane is the plane of the sky, i_o is the orbital inclination, i_s is the stellar inclination and λ is the sky projected obliquity.

plane and denotes the normal vector of the orbital plane and is found by the orbital inclination angle $i_o = \arccos\left(\mathbf{n_o} \cdot \hat{Z}\right)$. The normal vector of the stellar inclination $\mathbf{n_s}$ is generated by two components: the stellar inclination angle[4] $I = \arccos\left(\mathbf{n_s} \cdot \hat{Z}\right)$ and the azimuthal angle, which in this case is the sky-projected obliquity λ. From this we can then generate equations for the normal vectors of the system.

$$\mathbf{n_o} = \hat{Y} \sin i_o + \hat{Z} \cos i_o \tag{1.35}$$

$$\mathbf{n_s} = \hat{X} \sin I \sin \lambda + \hat{Y} \sin I \cos \lambda + \hat{Z} \cos I \tag{1.36}$$

By using the following identity:-

$$\cos \psi = \frac{\mathbf{n_o} \cdot \mathbf{n_s}}{|\mathbf{n_o}| \cdot |\mathbf{n_s}|} \tag{1.37}$$

[4]It should be noted that $i_s \equiv I$ in Figure 1.19

we can then calculate ψ from the angle between the two vectors $\mathbf{n_o}$ and $\mathbf{n_s}$ where

$$\cos\psi = \sin I \cos\lambda \sin i_o + \cos I \cos i_o \tag{1.38}$$

In reality i_o can be measured from transit photometry and λ can be measured using the Rossiter-McLaughlin effect and/or starspot occultations (see Sections 1.4.2 & 1.5.2, respectively). Unfortunately, I is not directly measurable but it is possible to place constraints on the value from asteroseismology (Gizon & Solanki, 2003). Alternatively Winn et al. (2007b); Schlaufman (2010) showed that it is possible to infer the value of I from estimates of the stellar rotation period, stellar radius and the projected rotational velocity $v \sin I$. For a transiting planetary system i_o is close to 90 degrees and as such the second term in Equation 1.38 can be approximated to zero and the $\sin i_o$ in the first term can be approximated to one. As I is unknown then $\sin I$ can range from -1 to 1 this then gives

$$\cos\psi \geq \cos\lambda \tag{1.39}$$

By inspecting Equation 1.39 we can see that for a small value of λ the range of ψ is large, while as λ approaches 90 degrees the range for ψ reduces. This adds an interesting situation, where if a large value of λ is found then the system is misaligned but if a small value of λ is discovered then it is unknown whether the system is truly aligned or not, unless information on I is available from other sources. Fabrycky & Winn (2009) came to the same conclusion via a different set of calculations.

It is in fact possible to directly determine ψ from transit photometry coupled with starspots (see Section 1.5.2). Apart from the benefit of identifying the dominant dynamical evolution process in the system it also allows I to be modelled for the host star. Since I is not directly observable this would be an important step in better understanding the stellar properties.

1.4.2 The Rossiter-McLaughlin Effect

As a star rotates, half of the hemisphere is rotating towards us while the other half is rotating away from us. During Doppler spectroscopy the spectral lines from the hemisphere that is rotating towards us are blue-shifted while the same spectral lines from the hemisphere rotating away from us are red-shifted. While the effect of rotation does broaden the spectral line widths, it does not have an effect on the net Doppler shift of the integrated starlight (Winn, 2011). When a transiting planet crosses in front of the stellar disc, however, it blocks out a portion of a hemisphere. This then destabilises the balance between the integrated starlight from the two hemispheres and allows a net blue-shift (when the planet is crossing the hemisphere rotating away from us) or a net red-shift (when the planet is crossing the hemisphere rotating towards us) to be observed in the spectra. This effect is known as the Rossiter-Mclaughlin (RM) effect (Holt, 1893; Schlesinger, 1910, 1916; Rossiter, 1924; McLaughlin, 1924). The RM effect appears as a RV anomaly for which the maximum amplitude can be calculated. Using b for the impact parameter, the ratio of the planetary and stellar radii k and $v_* \sin I_*$ as the line-of-sight component of the stellar equatorial rotational velocity, Winn (2011) gives an approximation to find the maximum amplitude.

$$\Delta V_{RM} \approx k\sqrt{1-b^2}\,(v_* \sin I_*) \tag{1.40}$$

Gaudi & Winn (2007) gives an equivalence relation for the change in the RV semi-amplitude K due to the RM effect and using $k = r_p/r_*$.

$$K_R \equiv v_* \sin I_* \frac{k}{1-k} \tag{1.41}$$

The shape of the RV anomaly can be seen in Figure 1.20. The shape of the RM anomaly is dependent on the sky-projected obliquity of the system. In the case of $\lambda = 0°$ the anomaly is equal in magnitude both above and below the normal RV line. This is due to the planet spending equal amounts of time crossing both hemispheres of the star. In the second case $\lambda = 30°$ and we can see that the upper magnitude of the anomaly has reduced while the lower magnitude of the anomaly has increased. By inspecting the

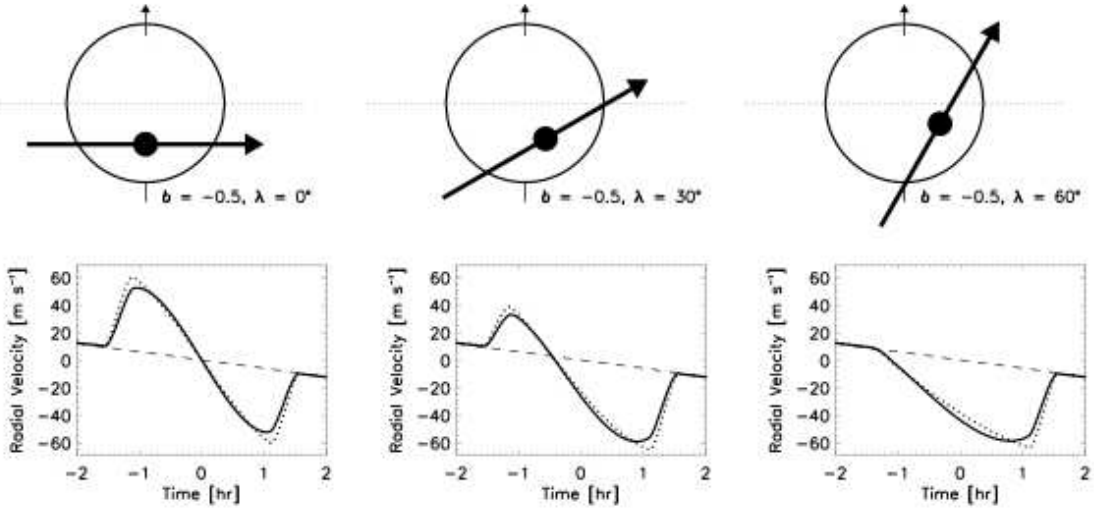

Figure 1.20: The dependence of the RM anomaly shape on λ (Gaudi & Winn, 2007). The top panels show three different trajectories of a transiting exoplanet and the bottom panels show the corresponding RM anomaly shape. All three trajectories have the same impact parameter but have different values for λ. The effect on the shape of the RM anomaly can be seen in the bottom panels. In the bottom panels the dotted line represents a stellar disc with no limb-darkening while the solid line represents linear limb-darkening.

second trajectory in the upper panel in Figure 1.20 we can see that the planet spends the majority of the transit crossing the hemisphere that is rotating away from us. In the final case where $\lambda = 60°$ the planet only crosses one hemisphere and as such the magnitude of the RM anomaly is only below the RV line. If the impact parameter of the transiting planet is zero (i.e. it passes across the centre of the star) and $\lambda \approx 90°$ then the amplitude of the RV anomaly will be negligible and the shape will have hardly any asymmetry (Gaudi & Winn, 2007; Albrecht et al., 2011).

At present, obtaining precise measurements for λ from the RM effect is not always possible. For example, Albrecht et al. (2012) found for WASP-18 that $\lambda = 13 \pm 7°$ (see Figure 1.21) and for WASP-19 Albrecht et al. (2012) found $\lambda = 15 \pm 11°$ (see Figure 1.22).

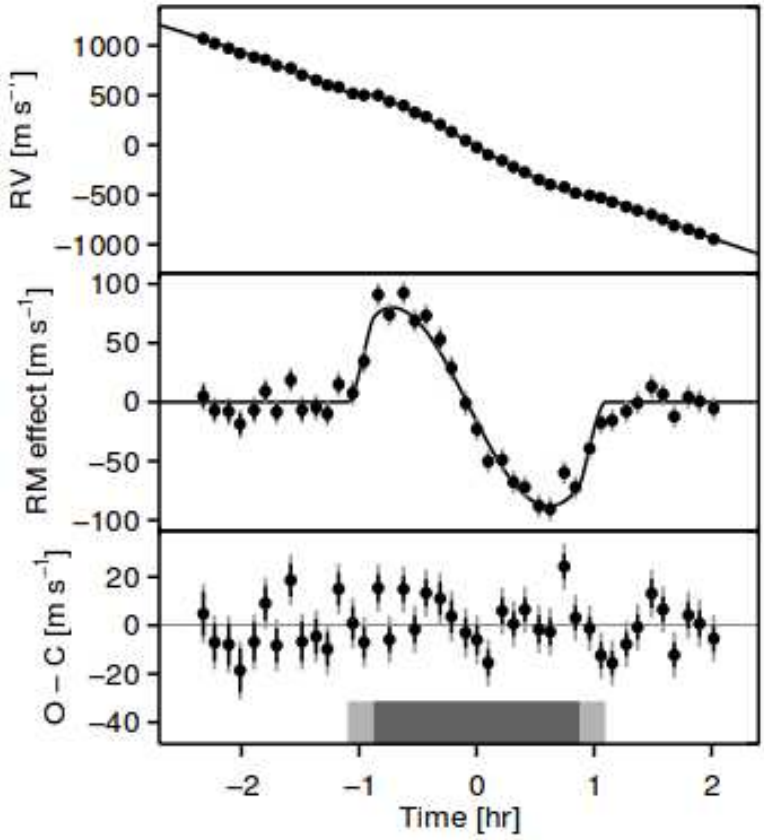

Figure 1.21: Spectroscopy of a WASP-18 transit (Albrecht et al., 2012). The top panel shows the RV measurements taken for WASP-18 plotted as a function of time from inferior conjunction with the best-fitting model. The middle panel shows the RM component of the RV after the orbital component had been removed. The bottom panel shows the residuals.

One of the causes of the large uncertainties is from performing RM measurements of partially eclipsing planets (Gaudi & Winn, 2007). Another cause is from RV jitter. If the signal-to-noise ratio (SNR) is low then this can cause large uncertainties in the measurement of λ (Gaudi & Winn, 2007; Albrecht et al., 2011, 2012). The cause of stellar jitter is due to stellar activity. If the star is magnetically active its surface will show evidence of starspot activity. If a starspot lies on the transit cord (a path traced out by the orbit of the planet over the surface of the stellar disc) then, due to the

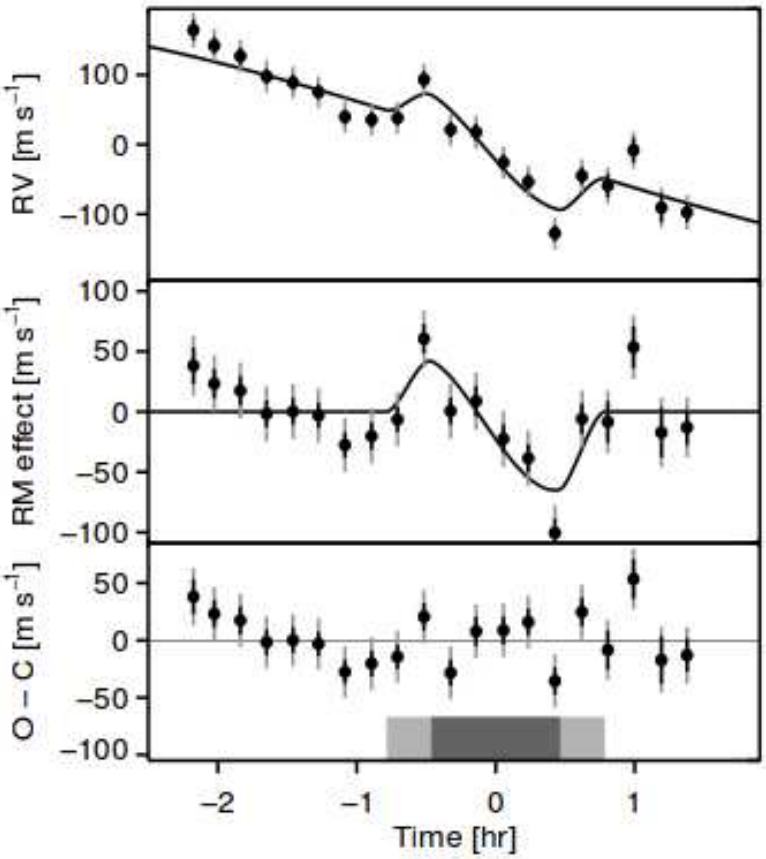

Figure 1.22: Spectroscopy of a WASP-19 transit (Albrecht et al., 2012). The top panel shows the RV measurements taken for WASP-19 plotted as a function of time from inferior conjunction with the best-fitting model. The middle panel shows the RM component of the RV after the orbital component had been removed. The bottom panel shows the residuals.

difference in temperature and thus surface brightness, a spectral distortion is caused in the resulting RV measurement (Hatzes, 1999). These variations are modulated with the rotation of the star. Upon reviewing Figure 1.23 the shape of the RV distortion is identical to that of the RM effect for a planet with a value of $\lambda = 0°$ but the distortion will last much longer, due to the time taken for the spot to rotate round 180 degrees.

The reason why the shape of RV distortion for the RM effect and starspots is similar, is that they are due to the same underlying process. In the case of a

single starspot being on a particular hemisphere the overall integrated starlight will show either a blue or red shift in the Doppler measurements. Because the starspot is at a different temperature compared to the surrounding photosphere it will radiate a different amount of flux. This will therefore make the hemisphere with the spot brighter or darker when compared to the spot free hemisphere and hence create a shift in the spectral lines (due to making either the blue or red shifted component of the spectral line brighter or darker) of the observed integrated starlight.

The RM effect can also be used to find the sky projected equatorial rotation velocity (Gaudi & Winn, 2007; Winn, 2011). Equations 1.40 and 1.41 show how $v_* \sin I_*$ can be calculated from the amplitude of the RV anomaly. Because of this the RM effect can be used to discover two important properties for the transiting system. If the true rotational velocity of the host star is known then it is possible to infer the true obliquity

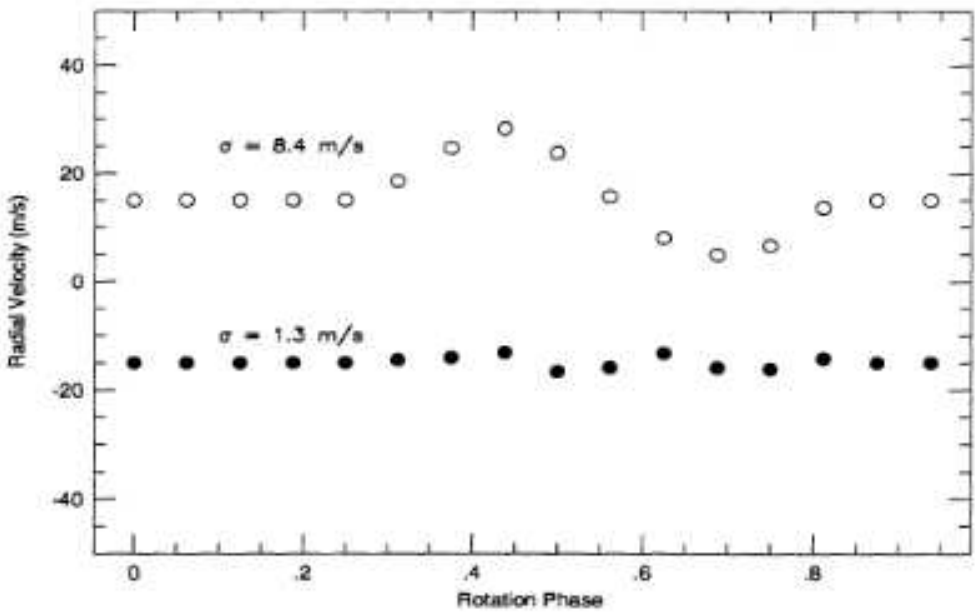

Figure 1.23: RV variations due to starspots (Hatzes, 1999). The open circles represent the RV measurements using a random distribution of six starspots. The filled circles represent the corrected RV measurements. This data was generated using the Fe I 6430 Å spectral line.

of the system from $v_* \sin I_*$ and λ (Winn et al., 2007b; Anderson et al., 2011; Hellier et al., 2011).

Winn et al. (2010a) also showed that for hot stars ψ will be large and for cool stars ψ will be small. This is due to cooler stars having larger convective envelopes. Through this the tidal dissipation effects from cooler stars have a greater effect on aligning the planetary orbit. However, since cool stars exhibit greater stellar activity (Berdyugina, 2005) then the precise measurements required to observe a low λ are hindered by increased uncertainties in the RV measurements due to increased starspot activity on the stellar disc.

1.5 Starspot Anomalies in Exoplanet Lightcurves

Stellar rotation coupled with convective motions in the stellar interior, create strong magnetic fields which can lead to starspots in the photosphere of the star (Berdyugina, 2005). In the convection zone of a star, heat is transported by the motion of heated ionised plasma rising and then cooling. Once cooled the ionised plasma then sinks which forms a convective loop. By creating a loop of charged plasma a magnetic field is created. When this field covers a large enough area the differential rotation of the star will cause different sections of the magnetic loop (sometimes called magnetic flux tube) to rotate around the star at different velocities. This then has the effect of warping the magnetic loop and when the stress of the loop reaches a critical point the loop breaks and punctures the stellar surface creating a starspot.

At the surface of a star where a starspot lies the magnetic flux tube which has punctured the surface inhibits convective motions under the spot and therefore decreases the energy flux from the star's interior. Because of this the temperature of the starspot is reduced compared to the surrounding photosphere and appears dark.

As is the case for the Sun, the number of spots on the photosphere are indicative of the level of magnetic activity. For a main-sequence star, the amount of stellar activity is related to the age of the star where an older star will rotate slower than a younger

star due to the loss of angular momentum (i.e.magnetic braking) during its lifetime (Skumanich, 1972; Noyes et al., 1984; Baliunas et al., 1995; Güedel et al., 1997).

During a planetary transit, the planet follows a path (called the transit cord) across the surface of the stellar disc and can be used to probe changes in surface brightness on the stellar surface (Silva, 2003). Starspots have different temperatures compared to the surrounding photosphere and as a consequence emit a different amount of flux. As photometry measures the change in intensity as a function of time, then if the planet crosses a starspot during a transit an anomaly can be seen in the resulting lightcurve (Silva, 2003). The anomaly is either an increase or decrease in the amount of received intensity from the star (see Figure 1.24). If the starspot is a cool spot then the amount of received intensity from the star will increase when the planet crosses the starspot (Rabus et al., 2009; Pont et al., 2007; Winn et al., 2010b). Conversely if the starspot is a hot spot then the amount of intensity measured will reduce when the planet crosses over the spot.

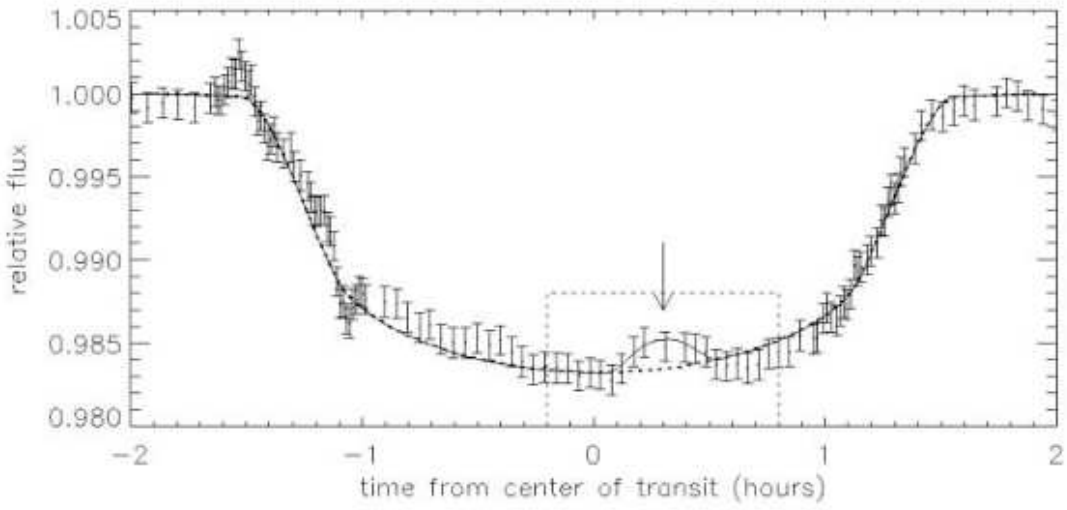

Figure 1.24: Lightcurve of HD 209458 containing a starspot anomaly (Silva, 2003). The original data (Deeg et al., 2001) show a clear flux increase just after mid-transit. The solid line shows the best fit model from Silva (2003) and the dotted line shows the spot-free model.

1.5.1 Current Methods of Modelling Starspot Anomalies

At present when a lightcurve of a transiting exoplanet is observed to have a starspot anomaly, the transit and the spot are generally modelled separately (e.g Désert et al., 2011; Maciejewski et al., 2011; Nutzman et al., 2011; Sanchis-Ojeda et al., 2011). First the data points affected by the starspot anomaly are removed from the data and the rest of the data are modelled using a transit model (see Figures 1.25 and 1.26). After this the residuals are compared to the best-fitting model to allow the spot anomaly to be modelled using a Gaussian function (e.g. Sanchis-Ojeda et al., 2011; Sanchis-Ojeda & Winn, 2011). There is a problem with this method in respect that the starspot affects the entire transit shape and not just the section where the planet crosses the spot (Ballerini et al., 2012). Carter et al. (2011) use the idea that a starspot on the stellar disc will affect the transit depth to explain the change in transit depth for each observed transit of GJ-1214. This is due to the change in intensity received from the star when starspots rotate on and off the stellar disc.

Let say there are two identical stars, one of which is spotted while the other is un-spotted. The spotted star will therefore have a lower intensity compared to the un-spotted star. Now if both stars are transited by the same planet with identical system parameters and in the case of the spotted star the transit cord does not occult any of the spots, then in the absence of limb-darkening the scale of the transit depth for the two lightcurves would be the same (but for the spotted star all the data points will be equally shifted down in intensity). The problem arises due to the data reduction technique used. During data reduction the out-of-transit data is normalised to zero differential magnitude (see Section 2.5.1). This normalisation therefore scales all the data points so that the out-of-transit data points have a value of zero differential magnitude for both stars. In the case of the spotted star this scaling will be larger due to all the data points being shifted down in intensity compared to the un-spotted star. This therefore causes the scale of the transit depth for the spotted star to be larger than the scale of the transit depth of the un-spotted star. Because of this the transit depth of the spotted star will appear deeper than that of the un-spotted star.

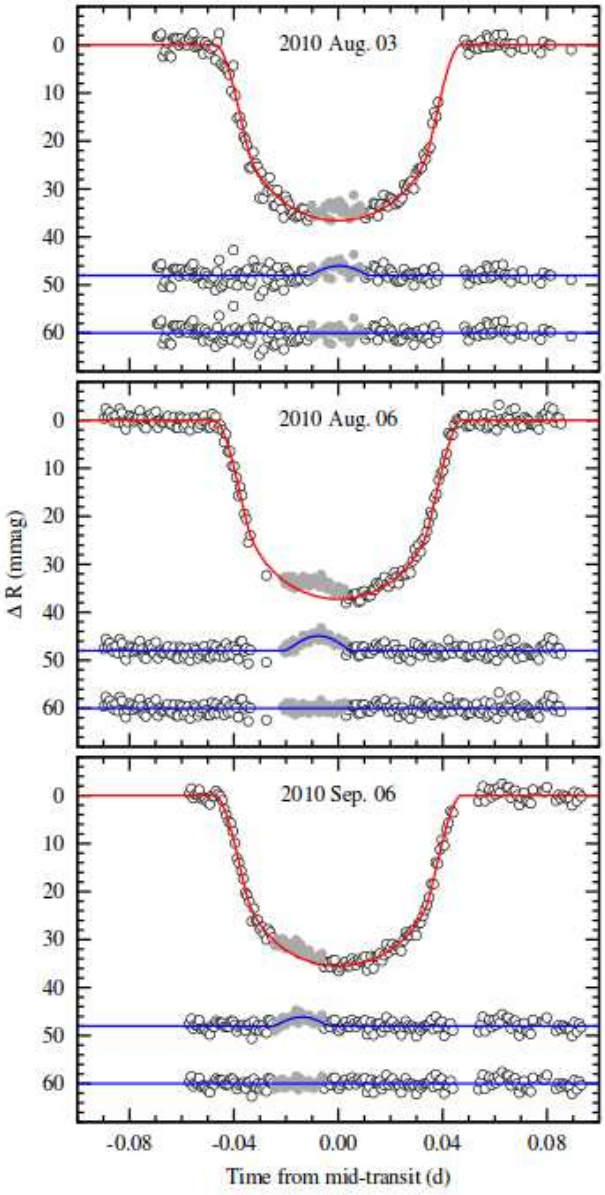

Figure 1.25: Three lightcurves of WASP-10 containing starspot anomalies (Maciejewski et al., 2011). The grey data points represent the data affected by starspots. Below each transit are two sets of residuals. The upper residuals show the data versus the best transit model and the spot anomaly is clearly seen. The bottom residuals show the data versus the best-fitting transit model coupled with the spot model.

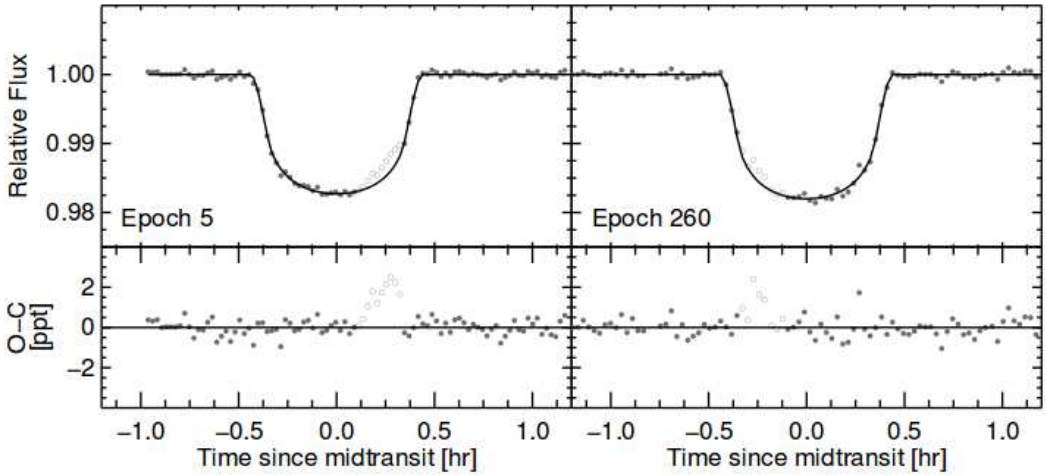

Figure 1.26: Two lightcurves of GJ-1214 each containing a starspot anomaly (Carter et al., 2011). The solid line represents the best-fitting transit model. The open circles represent the data points affected by a starspot, they were assigned a zero weight in the fitting process.

The transit depth is not the only property of a transit lightcurve that the starspot affects, it also affects the determination of the stellar radii, inclination and LD coefficients (Ballerini et al., 2012). The LD coefficients are wavelength dependent (see Section 1.2.2.1) and because a starspot has a different temperature compared to the surrounding photosphere, spots will radiate a different amount of flux. Due to this, the flux emitted by the starspot will be at a different wavelength compared to the surrounding photosphere. Therefore by applying a LD law with a set of coefficients to the entire stellar surface uncertainties will be created in the modelling process (Ballerini et al., 2012). The difference in LD coefficients in the UV-band between the spot and the photosphere can be as much as 30%. The effects on the stellar radii and the inclination of the system are artifacts from errors in the planetary radii. When examining Equation 1.16 we can see that the planetary radii is directly used to calculate the impact parameter and thus the inclination, while Equations 1.18 and 1.19 both use k the ratio between the planetary and stellar radii. The transit durations have to be considered

constant for a single transit but if k increases due to a deeper transit then either the stellar radius reduces or the semimajor axis must increase to compensate. Starspots can also affect the measured transit midpoint (Sanchis-Ojeda et al., 2011; Barros et al., 2013) and create false positives in transit timing measurements. Sanchis-Ojeda et al. (2011) calculated that a starspot anomaly in a transit of WASP-4 with an amplitude of 0.3 to 0.5 mmag could produce a timing noise of five to ten seconds.

Therefore, to accurately and correctly model a starspot in a transit lightcurve both the transit and spot must be modelled with a physically realistic model. Silva (2003) produced a model that allowed the physical properties of a starspot inside a transit to be found. These properties are the spot's position, size and temperature (contrast). The model worked by producing a two dimensional image of the star with either a linear or a quadratic LD law. An opaque disk representing a planet then transits across the star in an orbit which crosses over a starspot. While the model shows some degree of success it lacks the ability to fit data (Silva-Valio, 2008). Instead the model requires the user to input pre-determined values of the transit parameters (i.e. ratio of the radii, inclination and LD coefficients). Once this is done the model produces a spot free transit for the user to subtract from the data. This is in essence the same as examining the residuals but with the ability to see the overall change in the shape of the lightcurve due to the starspot. The model then moves the position of the spot along the transit cord in steps and produces comparison lightcurves with a standard deviation for the difference between the data points and the model. While this model allows the physical properties of the spot to be determined it does not allow the extraction of the transit parameters from the data.

Another code developed to model starspot anomalies is the Spot Oscillation And Planet (SOAP) algorithm (Boisse et al., 2012) as well as the improved version SOAP-T (Oshagh et al., 2013). SOAP models RV data while SOAP-T models photometric and RV data using analytical equations. The strength of SOAP-T is the fact that it models both the transit and starspot simultaneously. The down side is that SOAP and SOAP-T are

web based applications[5] and the authors did not make the source code available. As a result of this, users first upload an input file to the site and then the code creates a model based on the pre-selected input parameters. This creates a problem for researchers as it is not possible to check or alter any parts of the code which may not be running correctly. At present the codes can only fit RV data and users must know beforehand the photometric parameters of the transiting system. This is due to the full model using 18 parameters, and by using Markov Chain Monte Carlo (MCMC) simulations to fit the data results in poor convergence due to the chains getting trapped in local solutions (Oshagh et al., 2013). Therefore both SOAP and SOAP-T are not applicable to fitting transit photometry data containing a starspot anomaly.

Moulds et al. (2013) produced a model Clearing Activity Signals In Line-profiles (ClearASIL) to model the effects of starspots on stellar line profiles for moderately rotating active stars. The idea is to remove the spot signature from RV data to allow the planetary RV signal to be seen. This has the potential to allow detailed RV studies of young active stars in the bid to detect new hot-Jupiter planets. Due to ClearASIL only modelling stellar line profiles and not transit photometry it is not viable to use this code for starspots in transit photometry.

1.5.2 Starspots and Stellar Obliquity

When a starspot anomaly is found in transit photometry it can allow a wealth of information to be discovered. When modelled it is possible to precisely determine the spot's longitude and latitude position on the stellar photosphere (Silva, 2003; Silva-Valio, 2008; Sanchis-Ojeda et al., 2011; Sanchis-Ojeda & Winn, 2011; Maciejewski et al., 2011). Silva-Valio (2008) shows that it is also possible to measure the rotation period of the star using starspot anomalies in transit lightcurves. If two or more planetary transits in close succession[6] are observed and both contain a starspot anomaly due to

[5] SOAP and SOAP-T can be used at `http://www.astro.up.pt/soap/`

[6] Over time starspots evolve and as such their size and intensity can dramatically change. Therefore the greater amount of time between the anomalies will increase the uncertainty in whether the second

the same spot it is possible to calculate the stellar rotation period. Each transit allows the precise position of the starspot to be known at a certain time. Therefore, with just two transits each containing a starspot anomaly, it is possible to ascertain a change in position as a function of time. This then allows the stellar rotation period at a given latitude of the star to be calculated. It is important to stress that the rotation period discovered using this method is in fact a rotation period at the latitude of the spot and not the whole star due to differential rotation (i.e. different latitudes of the star have different rotation periods). If the system is not aligned then it may be hard to detect the same spot in different transits and therefore two transits will not be enough to calculate the latitudinal rotation period. For a non-aligned system the planet will transit across different latitudes and as such a number of transits will be required to calculate the latitudinal rotation period. It would also be possible to measure the rotation period for these different latitudes.

Measuring the position of a starspot at a given time allows the sky projected λ and the stellar ψ obliquities to be calculated (Désert et al., 2011; Nutzman et al., 2011; Sanchis-Ojeda et al., 2011; Sanchis-Ojeda & Winn, 2011; Sanchis-Ojeda et al., 2012). In a sky projected image of a stellar disc the rotation vector appears linear when the inclination of the stellar rotation axis I is 0° (see Figure 1.27 a). If $I > 0^\circ$ then the rotation vector becomes circularised (see Figure 1.27 b, c, d). Therefore measuring the rotation path taken by a starspot it is possible to measure λ and ψ. Sanchis-Ojeda et al. (2011) concluded that for WASP-4 $\lambda = -1^{+14}_{-12}$ degrees. They determined this value by a concatenation of the four best-fitting solutions (see Figure 1.27).

Given a set of consecutive transits a starspot anomaly would be seen moving from ingress to egress over the course of the transits and would indicate an aligned system. Conversely if the system was mis-aligned so that the transit cord was not confined to a single latitude on the stellar disc, the appearance of starspot anomalies would appear random in the consecutive transits (see Figure 1.28).

Sanchis-Ojeda & Winn (2011) looked at 26 consecutive transits of HAT-P-11

anomaly is in fact the same or a different spot.

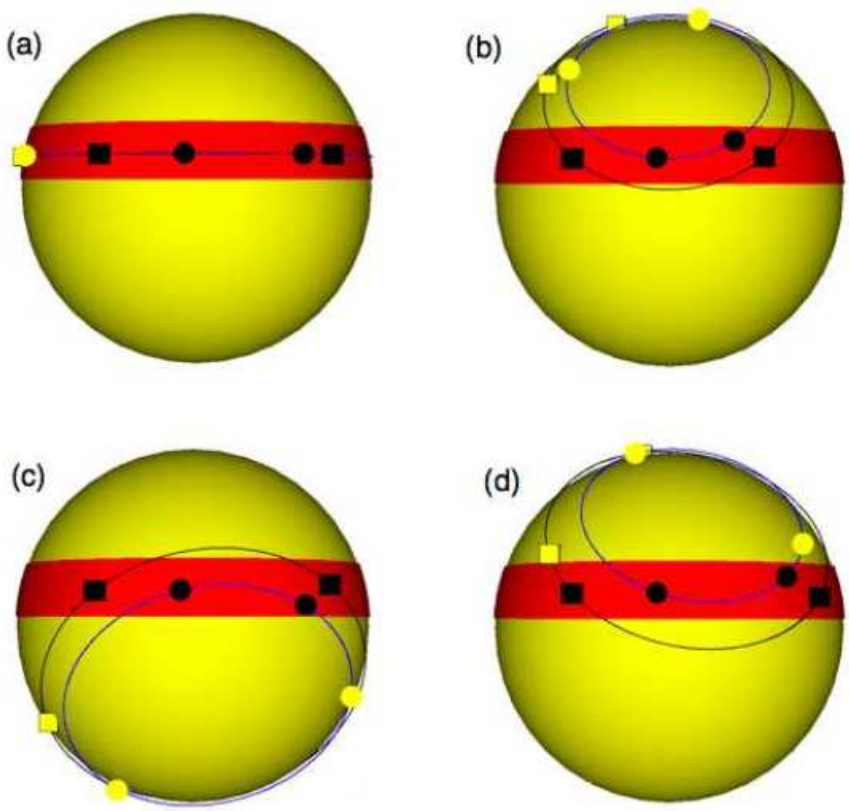

Figure 1.27: Stellar rotation angles of WASP-4 using starspots (Sanchis-Ojeda et al., 2011). The circles represent the positions of the starspot in the Sanchis-Ojeda et al. (2011) transits, while the squares represent positions of a starspot in the Southworth et al. (2009b) transits. The dark symbols represent spot detections and the light symbols represent non-detections. The red band represents the transit cord. All four orientations can explain the transits with or without spot anomalies. The stellar rotation axis lies at the centre of the grey rings. Sanchis-Ojeda et al. (2011) gives the angle of the stellar rotation axis in terms of λ and I. For (a) $\lambda = -0.3^\circ \pm 4.3^\circ$ and $I = 88^\circ \pm 19^\circ$, (b) $\lambda = -11.5^\circ \pm 3.9^\circ$ and $I = 43^\circ \pm 5^\circ$, (c) $\lambda = 13^\circ \pm 7^\circ$ and $I = 144^\circ \pm 5^\circ$ and (d) $\lambda = -13^\circ \pm 5^\circ$ and $I = 38^\circ \pm 5^\circ$.

observed by the *Kepler* satellite. Starspot anomalies were seen in the transits but did not appear in consecutive transits (see Figure 1.28). The spot anomalies appeared at two distinct points in the transits indicating that the planet was misaligned and crossing two distinctive active latitudes. Their analysis confirmed a previous RM measurement

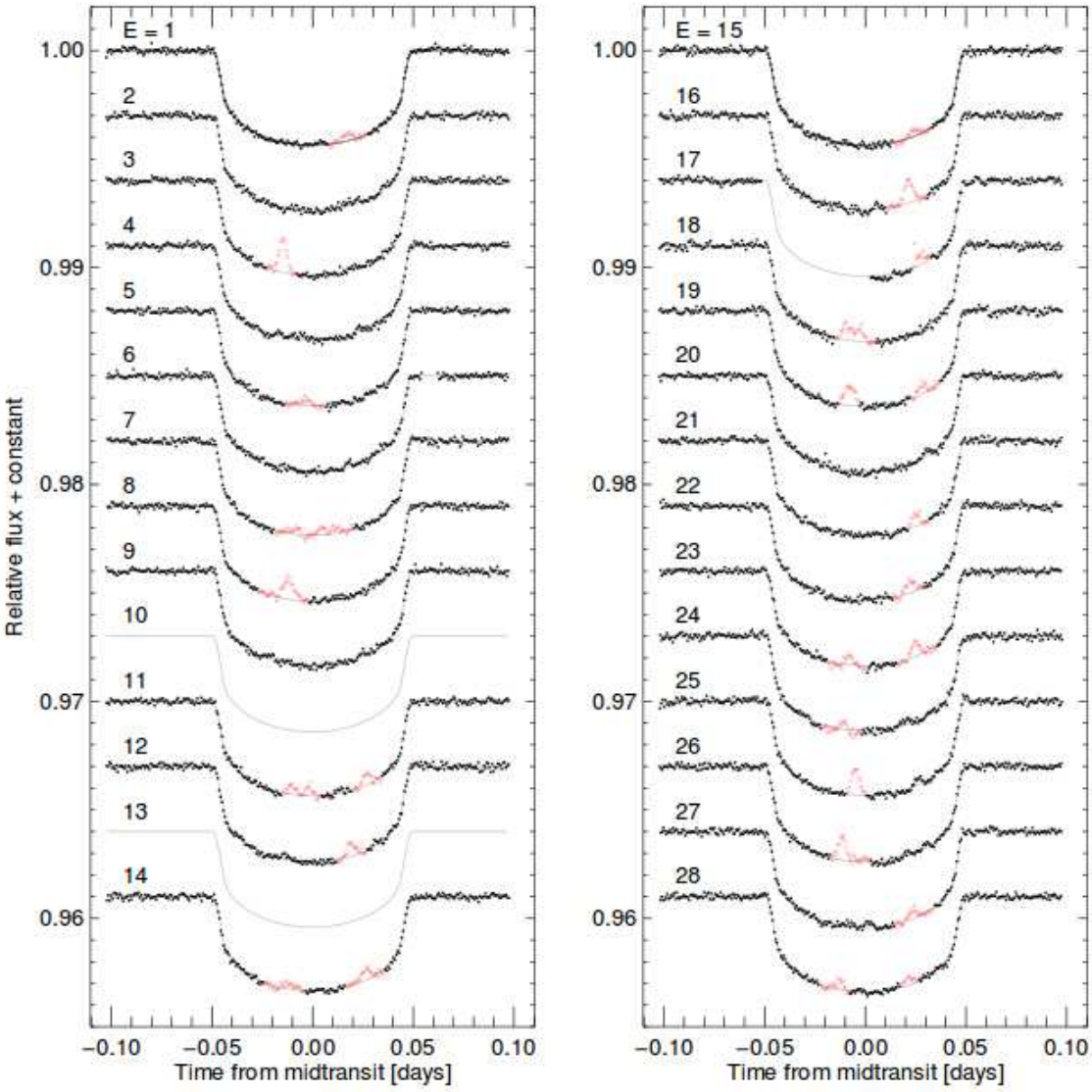

Figure 1.28: Consecutive *Kepler* observations of transits of HAT-P-11 (Sanchis-Ojeda & Winn, 2011). The thin grey lines represent the best-fitting model. The red data points are believed to be starspot anomalies and were assigned a zero weight in the fitting process. Due to the starspot anomalies not appearing to reproduce from transit to transit it is believed that HAT-P-11 is a misaligned system.

of λ taken of HAT-P-11 (Winn et al., 2010b; Hirano et al., 2011) with two potential solutions, equator edge on and pole on. Both solutions agreed on both λ and ψ but

they differed on the spot latitudes. For HAT-P-11 Sanchis-Ojeda & Winn (2011) found $\lambda \approx 90^\circ$ and $\psi \approx 90^\circ$ indicating that HAT-P-11 was not aligned.

This showed that it is possible to measure both the sky projected and the true stellar obliquity using the starspot method as opposed to the RM effect in which only λ could be measured. In the simple case in which the system is aligned, potentially only two lightcurves separated by a small amount of time could be used to determine the dynamical evolution of the system. Misaligned systems, however, will require a larger number of lightcurves. A further obvious consideration is that for this method to be effective transit observations of active stars are required, and the transit cord must occult active regions on the stellar disc.

Finally another interesting case is Kepler-30 (Fabrycky et al., 2012). Kepler-30 is a multi-planetary system with three confirmed planets with radii ranging from $4R_\oplus$ to $13R_\oplus$. By using starspots Sanchis-Ojeda et al. (2012) were able to measure the sky projected obliquity of the system. They found that $\lambda = -1 \pm 10$ degrees and that the planets are coplanar.

1.6 Summary

One of the primary research focus in exoplanets at present is in hot-Jupiters. They allow us to study planetary formation, evolution and to understand the processes of the dynamical evolution of planetary systems. While dedicated planet hunter space telescopes such as the *Kepler* satellite (Borucki et al., 2010) have the ability to detect rocky planets in the habitable zone[7] in star systems, ground-based spectroscopic follow up is not always possible. The two major methods of observing exoplanets are spectroscopic measurements and transit photometry. Each method has its strengths and weaknesses, spectroscopic measurements combined with theoretical stellar models

[7]The habitable zone is loosely defined as where a planet can sustain liquid water on its surface and depends on its distance from the host star as well as the host star's luminosity (Kasting et al., 1993; Kopparapu et al., 2013)

allows the minimum mass of the planet, the stellar radius, the orbital period, eccentricity, semimajor axis, the stellar age and mass to be known. Transit photometry can allow the precise radius of the planet to be determined in units of the stellar radii, as well as the orbital inclination, the stellar density and the orbital period. By combining these two observational methods we can deduce the full set of fundamental physical properties of the planetary system. For example, Equation 1.11 gives the minimum mass of the planet but transit photometry gives the orbital inclination which allows Equation 1.11 to be solved for the exact planetary mass.

The dominant form of dynamical evolution for a TEP can leave traces in the geometry of the system. Disc-migration (Ward, 1997a) leaves a planet in a circular orbit aligned with the rotation axis of the host star. Gravitational scattering coupled with tidal dissipation (Matsumura et al., 2010) can leave planets with eccentric orbits which are misaligned with the stellar rotation axis. Though the eccentricity of the orbit will reduce if the planet comes close enough to the host star during periastron when the planet will interact with the convective envelope of the star via tidal effects. Therefore, by measuring the alignment between the planetary orbit and the stellar rotation axis (stellar obliquity, ψ) it is possible to decipher the dominant process in the dynamical evolution of the system.

There are two possible methods to measure the sky-projected stellar obliquity λ of a system. One method relies on spectroscopic measurements while the other is a photometric method. Each method has its own strengths and weaknesses but the two methods complement each other in terms of the type of targets they can be applied to. The Rossiter Mclaughlin (RM) effect (Rossiter, 1924; McLaughlin, 1924) is a measure of RV changes in the spectral lines when a planet transits across a star. From this it is possible to measure the sky-projected equatorial rotation velocity and λ. The downside is that this method is affected by stellar activity, namely starspots lying on the transit cord (Hatzes, 1999). The second method relies on starspots being on the transit cord. During transit photometry if a planet occults a starspot on the stellar surface there will be a change in the received intensity from the star (Rabus et al., 2009; Pont et al., 2007; Winn et al., 2010b). If multiple transits in close proximity contain a

starspot anomaly that can be deduced as being generated by the same starspot then it is possible to measure the latitudinal rotation period of the star (Silva-Valio, 2008). It is also possible to measure λ and in some cases ψ (Sanchis-Ojeda et al., 2011; Sanchis-Ojeda & Winn, 2011; Désert et al., 2011; Nutzman et al., 2011). This is possible due to being able to measure the position of a starspot at different points in time. From this it is then possible to determine the starspot's trajectory across the stellar surface. The downside to this method is the fact that it relies on starspots being on the transit cord. As a consequence, the RM effect and transit photometry containing starspot anomalies compliment each other in the respect that the RM effect is ideal to be used on magnetically quiet stars and starspot anomalies are best used on magnetically active stars.

Currently there is another downside to using starspot anomalies in transit photometry to measure both λ and ψ. At present there is a lack of an ability to correctly model starspot anomalies in transit photometry. Apart from the fact that starspots on the stellar disc affect the transit shape (Carter et al., 2011; Ballerini et al., 2012), there is also no complete model or optimisation package with the capability to determine the properties of both the transit and the starspot. As a consequence, researchers remove the affected data points from the transit and then model the transit. After this they then model the affected data points from the residuals using a simple function (Sanchis-Ojeda et al., 2011). Because of this systematic uncertainties are introduced to the final physical properties of the planetary system. There are currently models able to fit the properties of a starspot but this requires the properties of the transiting system to be known beforehand (e.g. Silva, 2003; Oshagh et al., 2013). The logic of this method is also flawed because if a starspot anomaly is seen in a lightcurve of a particular planetary system then the chance that a previous lightcurve has been affected by a starspot (either on of off the transit cord) is relatively high. As such any previous measurements of the properties of the contaminated system will potentially contain systematic uncertainties and therefore cannot reliably be used in the process to model the starspot. For these reasons it is imperative to model both the transit and the starspot with a physically realistic model using the same data set.

2 Methodology

This chapter explains the methodology used in my research. It begins with Sections 2.1 and 2.2 by explaining how raw photometric data is collected and reduced. Sections 2.3 and 2.4 explain the principles behind aperture photometry and how defocused photometry can be used to drive down the uncertainties in transit photometry. Section 2.5 explains how a transit lightcurve is produced and the details of the data reduction pipeline used in this research coupled with the different variations of the Julian date that can be used. Then, in Section 2.6, there is a short discussion on the three different methods used to model transit lightcurves. Section 2.7 then explains my model PRISM, which can be used to model a planetary transit containing a starspot anomaly. Finally Section 2.8 discusses two different optimisation algorithms used for PRISM and the difficulties in using them for a large and rugged parameter space. It then introduces my new hybrid optimisation algorithm GEMC, created to reduce the computation time required for optimising PRISM. Part of Sections 2.7 and 2.8 were published as first author in Monthly Notices of the Royal Astronomical Society (see Appendix A.1 for publication details).

2.1 CCD Cameras

The Charged Coupled Devise (CCD), invented by Boyle & Smith (1970), is a semiconductor device that uses potential wells (known as pixels) on its surface to store charge. The charge is then moved across the surface by moving the potential wells. This allows information to be transmitted across the CCD (Boyle & Smith, 1970). When a photon interacts with a pixel the pixel generates an electron through the photoelectric effect. The charge is then stored until the CCD is read-out whereby the electrons are digitised by being converted to a voltage and the voltage is read as an Analogue Digital Units (ADU). Different CCD cameras have different gains, where a gain of three equates to one electron per three ADUs. During the readout of a CCD, uncorrelated noise can be

introduced as the image is read from the CCD chip (see Section 2.4.1). At low counts a CCD camera behaves linearly, but as the charge builds up in each pixel/potential well a repulsive electric field is generated reducing the efficiency of the photoelectric effect. The efficiency of the photoelectric effect is therefore proportional to the strength of the electric field. At this point the CCD camera deviates away from linearity. Each pixel/potential well can only contain a maximum amount of electrons, beyond this point the pixel is said to be saturated and all further electrons generated spill over into the surrounding pixels. Also, another factor which can reduce the maximum ADU count is from the digitisation limit. For example, a 16-bit controller will only allow a maximum count of $2^{16} - 1 = 65535$ ADU per pixel.

2.2 Data Acquisition

Once an image has been read from a CCD a Flexible Image Transport System (FITS) file is created to store the image (Wells et al., 1981). The FITS file also contains a header containing extra information including, but not limited to, exposure length, the mean Julian date of the image, number of pixels, and both the telescope's and instrument's name and status. Because of this a FITS file not only contains the total intensity of each star in the image but it also contains a time stamp of when the image was taken. Therefore a series of FITS files can allow any changes in intensity to be seen as a function of time.

2.2.1 Bias Frames

A bias voltage is applied to a CCD chip to move the charge generated from the photoelectric effect across the surface of the CCD. A way to remove this voltage is to 'clean' the science images with a master bias image. If an image is created with the shutter of the CCD camera closed with an exposure time of zero seconds then only the bias voltage is collected. In general, 5 to 100 bias images are taken at the start of each ob-

serving night. Then the master bias image is created by median combining the images. A master bias image is created to reduce the read-out noise from the bias images by a factor of $\sqrt{N}$, where N is the number of bias images. Once the master bias image has been created it is applied to the science images. This is done by subtracting the master bias image from both the science images and flat-field frames, therefore removing the bias voltage. If the master bias frame is not applied to the science images then the bias voltage from the CCD camera would contaminate the sky-background of the science images.

2.2.2 Flat Field Frames

A CCD camera is used to collect photons from a target and is made from an array of pixels. In general the pixels have slightly different efficiencies and as such the CCD does not produce a uniform image. To remove this effect from the science images the CCD camera is used to create images of a uniformly light background (either the sky during twilight or a white screen illuminated by a lamp). Usually a large number of sky flat images are taken at the start of each observing night for each filter being used. The flat field images are then de-biased by subtracting the master bias image before the master flat image is created by scaled median combining the images. Once the master flat image has been created it is applied to the science images by dividing the science images by the master flat frame. This process removes the difference in pixel efficiencies from the science images but it does not fully remove the effects of dead pixels and pixels which are severely under efficient.

2.3 Aperture Photometry

To measure the change in intensity from the target star, aperture photometry is performed to the set of FITS files. Three aperture rings are set around the target and comparison stars. The inner ring is used to set the star boundary the second ring

indicates the start of the sky background boundary, while the third ring represents the outer limit of the sky background boundary. This creates a gap between the pixels being used for the star and the sky background that helps ensure that none of the star's intensity contaminates the sky background count. This is done for each star being analysed in order to create a local sky background count for each star's position. This is done under the assumption that the sky background count near the star is the same as that at the position of the star. The mean pixel value is then calculated from the sky background and is subtracted from each of the pixel values inside the star boundary. This is to remove the intensity from the sky background from the pixels on which the star is centred. After this the sum of the pixel values within the star is calculated and the instrumental magnitude of the target star and each of the comparison stars is then calculated. The calculated instrumental magnitude, M_{inst}, is the counts c of the star corrected for the exposure time t (see Equation 2.1). This ensures that the magnitude of the stars are always the same irrespective of the exposure times. This is done for each FITS file to build a profile of instrumental magnitudes as a function of time.

$$M_{inst} = -2.5 \log \left(\frac{c}{t} \right) \tag{2.1}$$

The comparison stars are used to help determine that any variation in the intensity from the target star is due to the star and not an environmental effect such as clouds or changing airmass. If a thin cloud passes over the field of view then the intensity received from the target star and the comparison stars will be reduced.

2.4 Defocused Photometry

To better understand the formation and evolution of transiting exoplanets (TEPs) requires precise measurements of their mass and radii (see Chapter 1 for full details). In particular a radius measurement with a precision of 1-3% can allow the distinction between whether or not a hot-Jupiter will have a rocky core. This is because hot-Jupiter planets with cores will have a slightly smaller radius when compared to an equal-mass

coreless planet (Bodenheimer et al., 2003; Fortney et al., 2007). Two different models, core accretion (Pollack et al., 1996) and gravitational instability (Boss, 1997) both predict different core masses. As such a precise measurement of a TEPs radius is important in determining the dominant formation process. As discussed in Section 1.2.2 transit photometry is an observational technique which can be used to measure the radius of a TEP. For a uniformly illuminated stellar disc the transit depth (the change in received flux ΔF) is equal to the squared ratio between the planetary and stellar radii $(R_p/R_*)^2$. Transits can also allow the stellar density to be found (see Equation 1.22), this is vital because when it is combined with the stellar effective temperature it allows

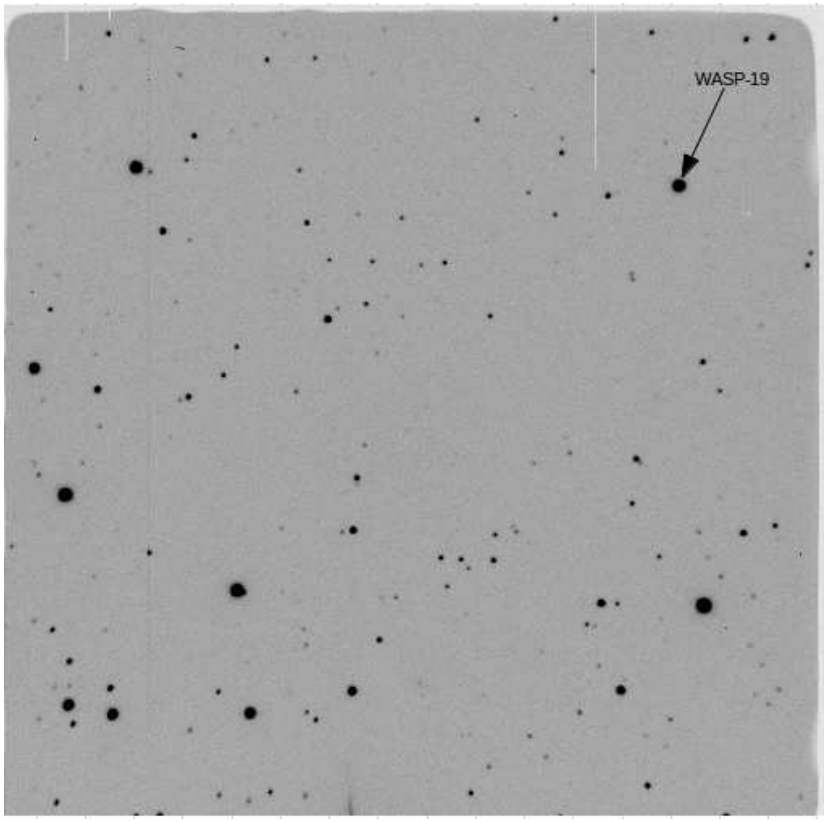

Figure 2.1: Focused image of WASP-19 (top right corner) and surrounding field of view. Observed using the ESO NTT. Due to being a focused image the stars appear point-like and each cover only a few pixels.

the stellar mass and age to be calculated from theoretical stellar evolution models (see Section 1.2.1). Therefore obtaining a precise measurement of the transit depth and duration is important.

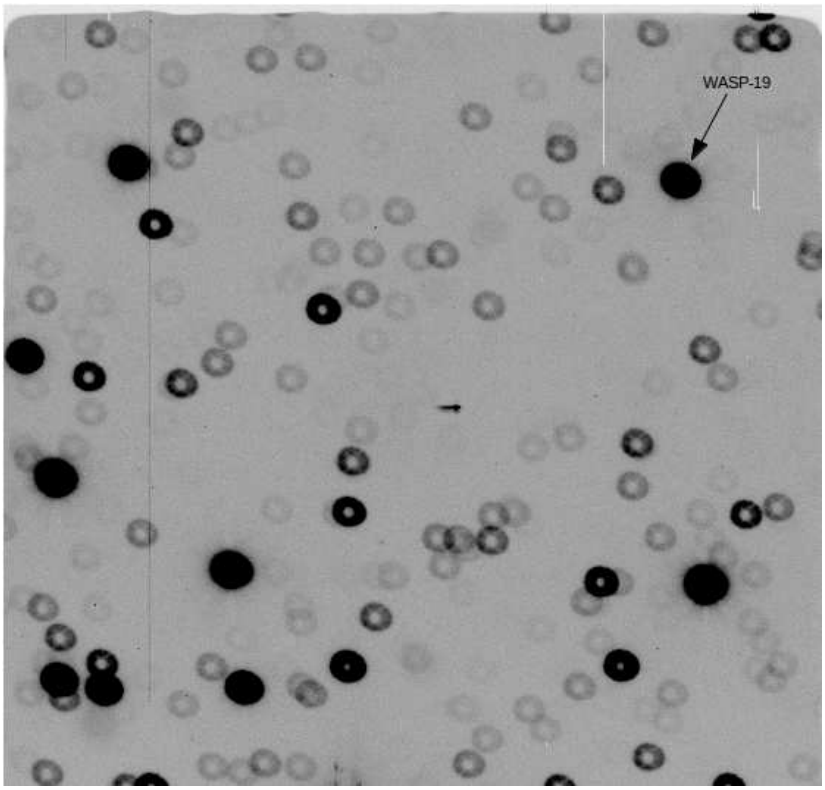

Figure 2.2: Defocused image of WASP-19 (top right corner) and surrounding field of view. Observed using the ESO NTT. Due to being a defocused image the stars appear as ringed doughnuts and cover thousands of pixels.

To obtain a precise measurement of a transit requires either a strong signal strength or low observational noise. Both of these will give a high SNR. To increase the signal strength requires either the use of a large ground-based telescope such as the ESO VLT or a space-based telescope such as NASA's HST. Another way to increase the SNR is to use the defocused photometry technique (Southworth et al., 2009a,b, 2010). Whilst defocused photometry does increase the amount of observational noise it also increases the signal by a greater factor and therefore the SNR increases (see

Section 2.4.1). When viewing a star though a defocused telescope the star no longer appears as a circular point source (see Figure 2.1) covering only a few pixels but instead appears as a round doughnut shape (see Figure 2.2) covering many hundreds if not thousands of pixels. The doughnut shape is roughly the image of the primary mirror as illuminated by each star.

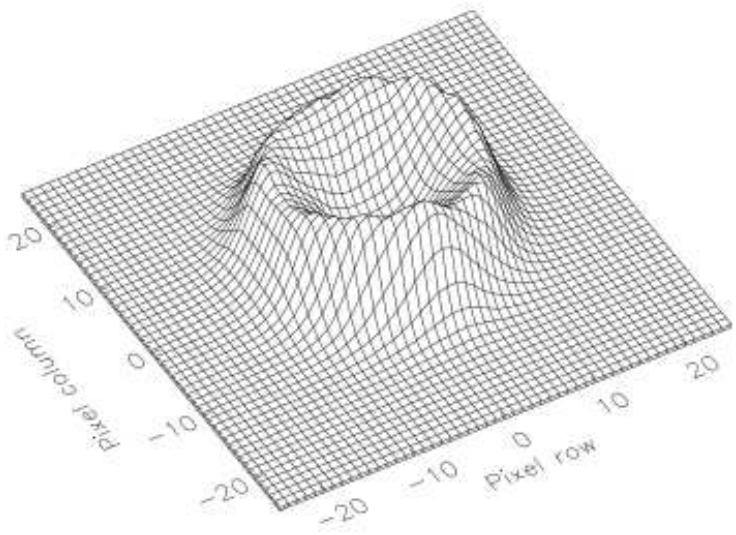

Figure 2.3: Surface plot of the defocused PSF of WASP-4 (Southworth et al., 2009b). The x and y axes are in pixels and the z axis is in ADUs and is linear. The minimum and maximum ADUs are 587 and 25823, respectively. Due to being a defocused image we can see that the PSF is a circular ring with a base with an approximate radius of 15 pixels.

When a surface plot of the Point Spread Function (PSF) of a defocused star is viewed, it shows a circular ring of pixels containing a high level of ADUs (see Figure 2.3), compared to a focused image where the PSF is a single peak (see Figure 2.4). As can be seen from examining Figures 2.1 and 2.2 by using defocused photometry a star's PSF is increased in size and hence increases the total number of pixels collecting the star's intensity. As each pixel can only hold a set number of electrons before becoming saturated, increasing the total number of pixels covered by the target will allow for

longer exposure times without saturation, which therefore increases the observation efficiency due to the lower percentage of time spent during readouts (which may take ~ 1 minute). In the case of Figures 2.3 and 2.4 we can see that the radius of the circular base has more than doubled, which has increased the number of pixels within the PSF by a factor of five to six. This in turn will allow the exposure time of one image to increase by roughly a factor of five to six depending on the situation of the observations.

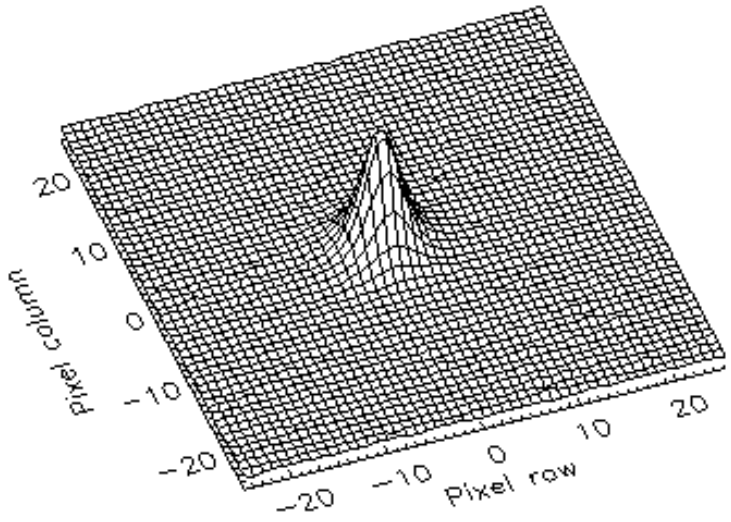

Figure 2.4: Surface plot of the focused PSF of WASP-4 courtesy of Dr J. Taylor. The x and y axis are in pixels and the z axis is in ADUs and is linear. Due to being a focused image we can see that the PSF is a single peak with a circular base with an approximate radius of seven pixels.

As shown in Section 2.4.1 by increasing both the number of pixels and the exposure time of photometric observations it is possible to increase the SNR to allow precise measurements of the photometric properties of TEPs. As such using defocused photometry on a small telescope can achieve high levels of precision compared to conventional photometry on large telescopes. An example of the precision achievable from defocused photometry can be seen in Chapter 5 where it was possible to achieve a rms scatter of 211 parts per million (ppm) for a transit of WASP-50 using the 3.58 m NTT,

compared to a rms scatter of 479 ppm for CoRoT-1 using the 8.2 m VLT (Pont et al., 2010).

2.4.1 Photometric Uncertainties

There are different causes of uncertainties in photometry. These uncertainties are generated by observational noise and therefore if the noise is high then the uncertainties will increase.

Scintillation is caused by changing atmospheric effects. As starlight passes through the atmosphere it passes through small-scale fluctuations in the air density, caused by temperature gradients in the atmosphere. This causes the starlight to be refracted. As such, the intensity received from a star will vary over very short timescales. Dravins et al. (1998) gives an equation to calculate the amount of scintillation noise σ_{scint} in magnitude units for a telescope with an aperture D (m), at an altitude h (m),

$$\sigma_{scint} = 0.004 D^{-2/3} X^{7/4} e^{-h/H} \left(2t_{exp}\right)^{-1/2} \tag{2.2}$$

where X is the airmass, $H = 8000$ m and is the scale height of the atmosphere and t_{exp} is the exposure time. From this we can see that by increasing either D, h or t_{exp} we can decrease σ_{scint}. It also shows that the noise from scintillation reduces the closer the target is to the zenith (i.e. $X = 1$). It should be noted that the exponent of X changes from 1.5 to 2 dependent on wind direction (Dravins et al., 1998).

Flat-fielding also introduces noise N_{flat} into photometry (Southworth et al., 2009a). If the intensity of a star is centred on ten pixels and two of the pixels are operating far below the efficiency of the remaining eight pixels then at least 20% of the collected intensity is being severely affected. A way to counter this is to produce flat-field images (see Section 2.2.2). These images highlight the affected pixels. A master flat-field image is created and is applied to the science images (see Section 2.2.2 for more details) to reduce the flat-field noise. The following equation approximates the noise from flat fielding (corrected from Southworth et al., 2009a).

$$N_{flat} = \sqrt{\left[f_{flat}\left(\frac{S_{target} + S_{sky}}{n_{pix}}\right)\right]^2 n_{flat}} \tag{2.3}$$

where f_{flat} is the approximate flat field noise per pixel, expressed as a fraction of the electrons in a pixel. S_{target} is the total number of electrons from the target. n_{pix} is the number of pixels that the target lies on. S_{sky} is the total number of electrons from the sky in the PSF and n_{flat} is the number of flat field pixels where $n_{flat} \leq n_{pix}$. Equation 2.3 shows that increasing n_{pix} will reduce the flat field noise. Using the previous example, if the star is now centred over 100 pixels then the two pixels which are operating far below the efficiency of the remaining 98 pixels will only at least affect 2% of the total intensity.

Southworth et al. (2009a) also gives equations describing the noise from the intensity of the star, N_{target}, (Equation 2.4) and the sky background, N_{sky}, (Equation 2.5). Both of these are Poisson noise and as such are the roots of the signal.

$$N_{target} = \sqrt{t_{exp} C_{target}} \tag{2.4}$$

where C_{target} is the total number of electrons per second from the target.

$$N_{sky} = \sqrt{t_{exp} n_{pix} C_{sky}} \tag{2.5}$$

where C_{sky} is the number of electrons per second per pixel due to the sky background. Since both Equations 2.4 and 2.5 represent Poisson noise then increasing t_{exp} will increase the SNR for the target due to t_{exp} being proportional to the signal. Increasing t_{exp} will also improve the SNR for the sky background plus increasing n_{pix} will also improve the SNR. Therefore, to improve the SNR requires either an increase in the signal strength from using a larger telescope or an increase of the exposure times and/or the number of pixels that the target lies on the CCD camera.

(Southworth et al., 2009a) also quantified the total amount of readout noise N_{ron} using the readout noise per pixel n_{ron}

$$N_{ron} = n_{ron}\sqrt{n_{pix}} \tag{2.6}$$

As a consequence by increasing the number of pixels in the PSF, the readout noise will increase and will act to deteriorate the SNR.

The dominant source of error in photometry is from systematics caused by flat-fielding noise, such as tracking errors. These enter because tracking issues (or changes in seeing) mean the PSF moves on to different pixels with different efficiencies. Defocused photometry can greatly reduce these systematics. With defocussing, changes in telescope pointing will in general affect more pixels, but these will be a smaller fraction of the overall number of pixels in the PSF. The real gain is that flat-fielding noise goes down with the square root of the number of pixels ($N_{flat} \propto (n_{pix})^{-0.5}$), so the more pixels that are used the more the noise averages down.

2.5 Lightcurve Photometry

A lightcurve is in essence the change in intensity of the target star relative to the intensity of the comparison star(s) as a function of time. As mentioned in Section 2.3, by performing aperture photometry the instrumental magnitudes of the target and the comparison stars is measured from the FITS files. In order to produce a lightcurve we need to know how the instrumental magnitude of the target star compares to the comparison stars. This is, in essence, the differential magnitude. First, the mean instrumental magnitude of the comparison stars are calculated. This mean value is then subtracted from the instrumental magnitude of the target star, giving a differential magnitude for the target star against the different comparison stars at a specific time period. Therefore, it is important to use a large number of comparison stars to reduce the uncertainties in the comparison star's instrumental magnitude.

The differential magnitudes between the target and comparison stars are then plotted as a function of time. In the case of a TEP the plot contains two parts, the transit and the out-of-transit data. The out-of-transit data sometimes contain either a positive or negative trend. This trend is often caused by the increasing or decreasing airmass during the observation night. The trend could also be caused by changes in

the sky transparency, variability in either or both the target and comparison stars or telescope pointing shifts. As the Earth rotates the positions of the stars slowly drift across the sky. When a target is at 30° above the horizon the airmass is twice the amount of when the target is at 90° (zenith). As such, during the course of the observing night the target passes across different values of airmass and the received intensity changes accordingly. This can be removed by fitting a polynomial to the out-of-transit data then subtracting it from the data. This then leaves a normalised transit lightcurve ready for fitting. When normalising a transit, the lowest order polynomial that gives a good fit to the out-of-transit data should be used. Lendl et al. (2013) explains that higher order polynomials provide better quality lightcurves due to taking into account the time, FWHM, coordinate shifts, and background variations. In general it is best to use multiple types of polynomials and to select the one which provides the highest quality lightcurve.

2.5.1 Data Reduction Pipeline

The data reduction pipeline used in this thesis (DEFOT) to reduce the data in Chapters 3, 4 and 5 was written in IDL[1] by Dr John Taylor and uses the DAOPHOT package (Stetson, 1987). This package comes as part of the ASTROLIB[2] library. From this, aperture photometry (see Section 2.3) was performed on the defocused images (see Section 2.4). During this process the aperture ring sizes can be manually altered to achieve the lowest out-of-transit scatter. After this the ASTROLIB/APER routine is run to perform the aperture photometry on the target star and all the selected comparison stars. It was mentioned in Section 2.3 that the instrumental magnitude is calculated using the exposure time of the images (Equation 2.1). However the APER routine does

[1] IDL stands for Interactive Data Language. It is a trademark of ITT Visual Information Systems. For more details see `http://www.exelisvis.com/ProductsServices/IDL.aspx`

[2] The ASTROLIB library is distributed though NASA.
For more information see `http://idlastro.gsfc.nasa.gov/`

not use the exposure time as an input parameter, as such DEFOT calculates the instrumental magnitudes using Equation 2.7 instead of Equation 2.1,

$$M_{inst} = -2.5 \log (c) \tag{2.7}$$

This results in the generation of a differential magnitude lightcurve for the target star. As such, if five comparison stars are used then this process will create a mean instrumental magnitude from the five comparison stars and use this mean value with the target star's instrumental magnitude to create the differential magnitude lightcurve. The data reduction pipeline written by Dr John Taylor also allows the differential magnitude of each comparison star to be calculated, this allows the comparison stars to be checked for variability which would contaminate the transit lightcurve and to be removed from the final analysis. Non variable comparison stars will still show signs of slow variability due to atmospheric effects (Southworth et al., 2009a). Before the data can be modelled this trend needs to be removed. This is done by fitting a polynomial to the out-of-transit data by using the IDL/AMOEBA routine. This minimises the sum of the squares of the magnitudes in the out-of-transit data, and then normalises the transit lightcurve to zero differential magnitude. Each comparison star is then weighted against the first comparison star. The comparison stars which are considered good are combined using a weighted intensity summation, to create a differential magnitude lightcurve.

Apart from using defocused photometry to increase the SNR, sky flats and bias images are also taken to help reduce the associated noise. In general 20 sky flats and 20 bias images are taken at the start of each observing night. Then the master flat and bias images are created by median combining the images, this is done using DEFOT. Once the master flat and master bias images are created they are applied to the science images. The master bias is subtracted from each of the science and flat-field images while the science images are divided by the master flat image. Under normal focused aperture photometry applying the master flat and bias images to the science images is important to help reduce both the electronic and flat fielding noise. When they are

applied to defocused images, however, the master bias correction has a negligible effect, while the master flat correction does have a small but noticeable effect (Southworth et al., 2009a).

2.5.2 Julian Date

The header of a FITS file contains the Julian date (see Section 2.2) of when the image was taken. The Julian date is the number of continuous days with the starting Julian date (0 JD) being set at mean noon (GMT) on the 1^{st} January 4713 BC, Julian proleptic calendar -4712[3]. This reference system would be fine if the Earth was a static object in space but it both rotates on its axis and orbits around the Sun. This then creates problems when trying to precisely time certain astronomical events (such as the transit midpoint of TEPs and pulsar timings). Because the speed of light is finite it will have a different travel time to different points along the Earth's orbit. This is called the Rømer delay (Eastman et al., 2010). Because of this astronomers started using the Heliocentric Julian date (HJD) which is centred on the Sun and could produce precise timing measurements to ~ 8 s (Eastman et al., 2010). Using HJD still can not produce the necessary precision needed in TTV measurements because the Sun is not the centre of the solar system. The Sun wobbles around its rotation axis due to gravitational forces from Jupiter and the other planets in the solar system. Therefore it is best practice to use the barycentre of the solar system as the reference point when precise time measurements are needed. Barycentric Julian date (BJD) is therefore set to the centre of the solar system and not the centre of the Sun (Eastman et al., 2010).

It is also important to take into account different time standards. The JD read at different time standards can introduce uncertainties of over a minute (Eastman et al., 2010). Therefore, it is advisable to convert all time standards to an absolute time frame. FITS file headers contain the time of the exposure in Coordinate Universal

[3]IAU resolution B1 at the 1997 General Assembly)
(`http://www.iau.org/static/resolutions/IAU1997_French.pdf`)

Time (UTC). UTC runs at the same rate as the International Atomic Time[4] (TAI) but is modified by adding or subtracting a leap second on both the 31^{st} December and the 30^{th} June. This causes UTC to drift relative to TAI with the slowing of the Earth's rotation due to the Moon (Eastman et al., 2010). As mentioned UTC should be converted to an absolute time reference, this is usually the Barycentric Dynamical Time (TDB). TDB takes into account the delay due to the gravitational redshift and the time dilation effect due to the motions of the Sun and other bodies in the Solar system. This delay is referred to as the Einstein Delay and is taken to the geocenter of the Earth (Eastman et al., 2010).

2.6 Transit Modelling

In the case of a TEP the type of variation in a lightcurve is a transit dip where the planet crosses the disc of the star and blocks out a portion of the stellar intensity (see Figure 2.5). When a planet transits the star the observed brightness of the star is reduced. For example, in Figure 2.5 this drop is approximately 2.25%. As such to see the transit signal the background noise must be less than this.

The transit properties of a TEP can be derived from modelling its lightcurve. This is done in essence by using a model with a set of input parameters resulting in an output lightcurve. The model lightcurve is then compared to the data lightcurve and a goodness of fit is calculated. The input parameters are then varied using an optimisation algorithm (e.g. Markov Chain Monte Carlo) to find a model lightcurve with the best fit to the data lightcurve. There are three main ways to model a TEP system. The first is an analytical approach using a set of equations to describe the observed/received intensity of a star during the planetary orbit at specific times during the transit (e.g. Mandel & Agol, 2002; Giménez, 2006). The second approach is to model the TEP using a geometrical model (e.g. JKTEBOP (Southworth et al., 2004a)).

[4]based on the decay rate of the caesium 133 atom (Eastman et al., 2010)

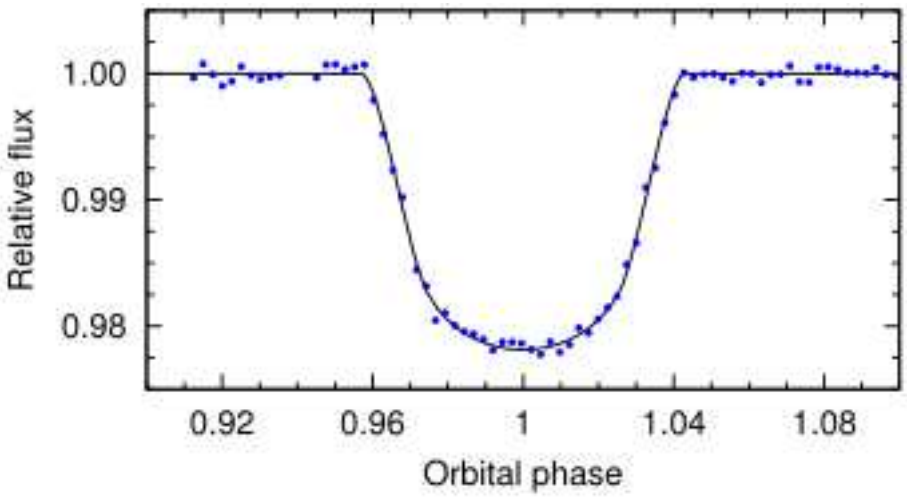

Figure 2.5: Transit and best-fitting model of WASP-19 b (Hellier et al., 2011).

A third approach uses a pixellation method to describe the surface of the host star (e.g. Silva, 2003). Each approach has both its advantages and disadvantages, which are now discussed in more detail.

2.6.1 Analytical Approach

The analytical approach provides a fast computational option which can find the best-fitting parameters and the associated uncertainties of the TEP. It can also model different types of LD laws (see Section 1.2.2.1) by applying these laws to the received intensity from the star. For the case of the analytical approach the transit is split up into sections where each section is governed by a different equation to calculate the received intensity from the star. In the case of a limb-darkened transit, the transit is split up into three sections (Mandel & Agol, 2002). The disadvantage to this approach lies in the difficulty in modelling structures on the stellar disc (i.e. starspots). As a consequence, to add a starspot would make the model very complex by requiring a new set of equations to describe a planet occulting a starspot on a curved stellar disc. This would also require the transit to be split up into further different sections.

2.6.2 Geometrical Approach

A geometrical model provides a fast and efficient method to find the best-fitting parameters from transit photometry. An example of a geometrical model is JKTEBOP, written by Southworth et al. (2004a) and based on the model EBOP (Nelson & Davis, 1972; Popper & Etzel, 1981; Etzel, 1981). JKTEBOP is a geometrical model using biaxial ellipsoids to model eclipsing binary stars and planetary transits. To minimise the amount of degeneracy between the transit parameters requires the selection and parametrisation of the transit parameters. Here the major parameters that JKTEBOP uses are both the sum and the ratio of the fractional planetary and stellar radii (see Section 1.2.2), the orbital inclination, LD coefficients, transit midpoint and the orbital period. JKTEBOP works by reading in an input file and the transit data. The input file contains the initial guesses of the parameter values and which parameters to vary during the optimisation. The input file also contains which LD law to use ranging from the linear law to the cubic law (Equations 1.23 and 1.26 respectively). Once the input file has been read JKTEBOP then uses the Levenberg-Marquardt (Levenberg, 1944; Marquardt, 1963) optimisation algorithm to converge on the best-fitting solution by using the MRQMIN subroutine from Press et al. (1993). The Levenberg-Marquardt algorithm uses a form of gradient descent to solve non-linear least squares problems (i.e. it looks to minimises the sum of the squares between the model and the data). This makes the algorithm very fast at converging on a solution, but because of this the Levenberg-Marquardt algorithm will find the closest solution to the starting location of the parameters. Hence, if the parameter space contains multiple local solutions, then the algorithm will only find the global solution if the initial guess of the parameters is close to this solution.

JKTEBOP then outputs the best-fitting model and best-fitting parameters together with the parameter uncertainties derived from the covariance matrix in the MRQMIN subroutine. Since these are not the overall uncertainties it is required to rerun JKTEBOP using Monte Carlo simulations to estimate the parameter uncertainties (see Press et al., 1993, chapter 15). By performing these two steps JKTEBOP can be

used to find the best fit and the associated uncertainties to a lightcurve of both a TEP and an eclipsing binary in a fast and efficient manner.

2.6.3 Pixellation Approach

In the pixellation approach the stellar disc is modelled in a two-dimensional array by subdividing the star into many individual elements. These elements can then be described by a two-dimensional vector in either polar or Cartesian coordinates. Each element is then assigned a intensity value using a LD law and the planet is then set to transit the star (e.g. Silva, 2003). At certain points in the transit the total received intensity is calculated based on which elements of the star are visible. The pixellation method is an ideal type of model to introduce stellar features to the disc of the star due to the fact that the model re-creates the stellar disc and allows individual intensities to be assigned at specific coordinates. The disadvantage to this approach is the amount of computations required to calculate the intensity of each element and to determine which elements are visible at each point in the transit.

2.7 PRISM

Before designing a model capable of modelling both a planetary transit and starspots on the stellar surface it was important to decide on both an approach and computer modelling language. As discussed in Section 2.6, while an analytical approach would produce a fast and efficient model, the difficulty in introducing starspots into a planetary transit would be quite difficult and time consuming. Using the pixellation approach would be the ideal option as it allows starspots to be placed directly on the stellar disc, with minimal coding time required. Because this approach would produce a slower model, a further investigation into potential optimisation algorithms beyond MCMC was required (see Section 2.8).

Due to the nature of the pixellation approach the model will be making extensive

use of arrays. In particular an array will be required to hold the individual intensity values of the star. This primary array will also be used at each iteration of the planetary orbit. Therefore a computing language which is optimised for use with vectors and arrays would be best suited to this type of problem. It was therefore decided to use IDL[5] due to the fact that IDL is a dynamical computing language and is optimised for use with arrays and vectors. IDL also comes with built in multi-threading with certain array commands allowing automatic parallel programming when running large calculations using arrays.

2.7.1 Modelling the Stellar Disc and Transit

Before modelling a planetary transit, a set of transit parameters need to be selected to help reduce any degeneracy between the parameters. It was decided to use the same transit parameters that are used in JKTEBOP, to not only reduce the degeneracy between the parameters (Southworth, 2008) but to also allow a direct comparison between the output lightcurves when performing tests and validating the model. Because of this, PRISM (Planetary Retrospective Integrated Starspot Model) uses six parameters to model the transit. Both the planetary (R_p) and stellar radii (R_*) are reduced to the fractional radii by the semimajor axis a where $r_p = R_p/a$ and $r_* = R_*/a$. PRISM then uses the sum $r_p + r_*$ (Equation 2.8) and the ratio k (Equation 2.9) of r_p and r_*.

$$r_p + r_* = \frac{R_p + R_*}{a} \tag{2.8}$$

$$k = \frac{r_p}{r_*} = \frac{R_p}{R_*} \tag{2.9}$$

The three major measurable qualities of a transit lightcurve are the transit depth, the overall duration of the transit and the duration of totality. Coupled with k and $r_p + r_*$, a third parameter is needed to help describe the three measurable properties

[5]See `http://www.exelisvis.com/ProductsServices/IDL.aspx`

of a transit. This third parameter used is the orbital inclination i. In reality because of LD both k and i affect the transit depth[6], while by looking at both Equations 1.18 and 1.19 we can see that the overall transit duration and the duration of totality are governed by k, i and $r_p + r_*$. The impact parameter b in Equations 1.18 and 1.19 can also be rewritten in terms of r_* by substituting $r_* = R_*/a$ into Equation 1.17 and by assuming zero eccentricity,

$$b = \frac{\cos i}{r_*} \tag{2.10}$$

r_* can be calculated from both k and $r_p + r_*$ using equation 2.12. The only other unknown variable in the Equations 1.18 and 1.19 is the orbital period P but as mentioned by Southworth (2008) P is usually known to a high-precision from either the detection or confirmation of the planetary system though phase-folding of a large number of transits (see Figure 3.1 for an example of a phase-folded lightcurve).

The next two parameters that PRISM uses are the LD coefficients. As mentioned in Section 1.2.2.1 the quadratic LD law (Equation 1.24) is most suited for ground-based transit photometry and as such PRISM is programmed to use the quadratic law requiring only two coefficients u_1 and u_2.

The final parameter for modelling a planetary transit in PRISM is the reference transit midpoint T_0. This parameter refers to the inferior conjunction[7]. This parameter is used when fitting PRISM to data and this is done by fitting t_0 to the point where the orbital phase equals zero (i.e. when the planet is at minimum light).

To aid in the reduction of the time required to develop PRISM it was decided to not include the orbital eccentricity but to add it at a later date (see Section 6.2.1). This was considered acceptable as the majority of TEPs have circular orbits (see Section 1.3.4). Because PRISM models transit photometry then unless the transit and an occultation are both observed it is not possible to derive the orbital eccentricity alone (Kipping

[6]At $i = 90°$ the planet crosses the centre of the star and therefore the brightest part, while at higher latitudes the planet crosses fainter sections of the star and therefore blocks out a lower amount of intensity.

[7]This is sometimes referred to as the point of minimum light.

et al., 2012). Therefore any addition of eccentricity to PRISM will have to be treated as a fixed value rather than as a fitted parameter.

PRISM also does not take into account the reflex motion of the star. The reflex motion of the star is when the star's rotational axis orbits around the centre-of-mass and is detected in RV measurements. Because the length of the transit is a fraction of the full orbital period then the effect of the stellar reflex motion will be small. Coupled with the added difficulties of modelling a moving star on a pixel grid it was decided to not add the reflex motion of the star to PRISM.

Once the input transit parameters have been selected PRISM then creates the main 2D array which contains the stellar disc. There were two options available, to either have a fixed grid size for all possible planetary radii or to have a variable grid size based on a fixed planetary radii. It was decided to have a variable grid size by using a fixed planetary radius of 50 pixels. This was done to make sure that PRISM maintained a certain level of numerical accuracy. For example, if a fixed stellar grid of 100 by 100 pixels was used and the planetary radius was one tenth of the stellar radius it would mean that the planet would only have a radius of five pixels. The stellar grid that contains the stellar disc is set to have each side n equal to two stellar radii with the centre of the star being set at the centre of the grid. Because the planet's diameter in pixels is preset to be 100 pixels then n is simply:

$$n = 100\,\frac{r_*}{r_p} = \frac{100}{k} \tag{2.11}$$

This expresses n as the diameter of the star in units of planetary diameter. Next PRISM needs to calculate the value for r_*, this is done using Equation 2.12 while to calculate the value of r_p is a simple matter of subtracting r_* from the sum of the radii.

$$r_* = \frac{r_p + r_*}{k + 1} \tag{2.12}$$

With the stellar grid created PRISM then runs though each element of the grid to check to see if the element is within the star's disc. If the element is within the disc it assigns a intensity value between zero and one based on the pixel's angular distance from the

centre of the star using the quadratic LD law. If the pixel falls outside of the stellar boundary then it is assigned a intensity value of zero.

Once the stellar grid has been created PRISM then creates the planet's grid. The planet grid has the same dimensions as the stellar grid and all the pixels are assigned a value of one. The pixels that are covered by the planet are then re-assigned a value of zero and the two grids are multiplied by each other to create the final intensity grid. The y-coordinate of the planet's centre is simply b (Equation 2.10), while the x-coordinate of the planet's centre is based on the planet's orbital phase. PRISM uses Equation 2.13 to calculate the x-coordinate of the planet, where $\theta = 0°$ is when the planet is at inferior conjunction.

$$x = a \sin \theta \tag{2.13}$$

To calculate x we do not need to know the absolute value of a. We can instead adopt the idea that if R_* is set to one (i.e. the planetary system is converted into units of stellar radii) then by using the fact that $r_* = R_*/a$ then we can say that $a = 1/r_*$ which allows us to rewrite Equation 2.13 into,

$$x = \frac{\sin \theta}{r_*} \tag{2.14}$$

This then gives us a value for x without a dependence on a. The next step in determining the x-coordinate of the planet's centre is to determine θ. Because PRISM models a circular orbit then θ can be directly calculated from the orbital period. For example, if the time step between two points is one tenth of the orbital period then the change in angle is only 36°.

When fitting PRISM to transit data the planet's position is calculated only at the orbital points which match the data. Therefore, if there are 67 data points within the transit then PRISM will only calculate the position of the planet 67 times. This is done to help improve the computational efficiency. PRISM then creates a new final intensity grid at each point.

With each final intensity grid PRISM then calculates the total intensity value for

the grid and takes the ratio between the value calculated and the original total intensity value from the stellar grid. PRISM then outputs a vector containing the total intensity values at each point in the transit.

2.7.1.1 Model Testing and Validation

PRISM's ability to model the stellar disc and transit was tested by using JKTEBOP as a benchmark transit modelling program. For this a series of lightcurves were generated by both PRISM and JKTEBOP using the same transit parameter values. The lightcurves were then directly compared first by eye and then numerically. Figure 2.6 shows an

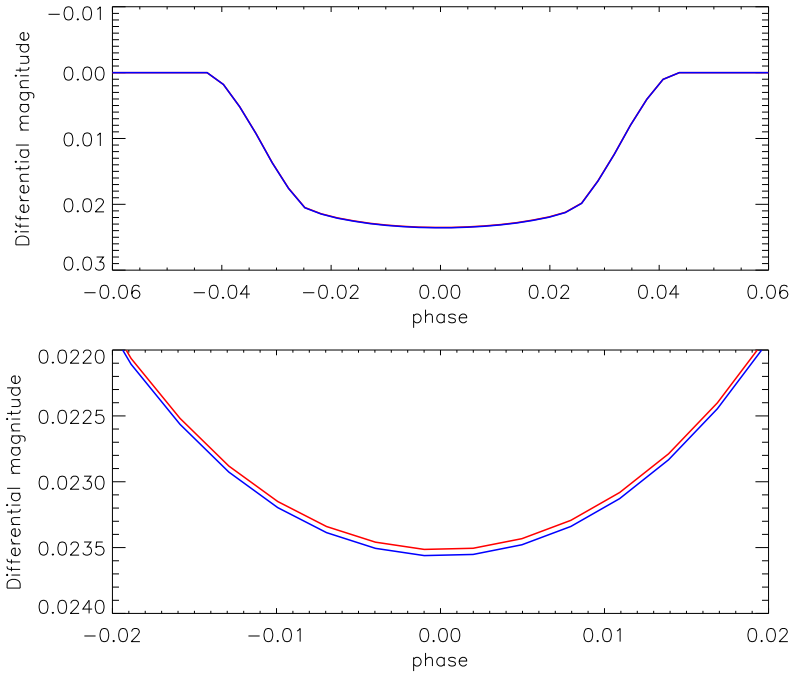

Figure 2.6: Comparison between models from PRISM and JKTEBOP. The parameter values used were $k = 0.14$, $r_p + r_* = 0.3$, $u_1 = 0.3$, $u_2 = 0.1$ and $i = 79°$. The red line represents the output model from PRISM and the blue line represents the output model from JKTEBOP. The top panel show the full transit while the bottom panel shows a close up of the inferior conjunction and the difference between the two models can be seen. The mean difference between the two models equates to only 16 ppm.

example of one of the tests. Here we can see by eye that the two different model outputs are almost identical (in the top panel) with the exception that the JKTEBOP transit is slightly (a line width) deeper (bottom panel) and numerically there is a difference of only 16 ppm. Each test produced a fitness number which was calculated by taking the root mean squared (rms) difference between each point in the two lightcurves. It was expected that there would be some slight differences between the two models due to the two different approaches used. The average difference between the two models for all the tests was ~ 10 ppm. In contrast, a typical transit depth of a hot-Jupiter is 15000 ppm and the precision obtained from defocused photometry is approximately 500 ppm. As such the differences between the two models is within the noise of the highest ground-based precision. If the two models were used on the same set of data any differences in the best-fitting parameters would be within the 1-σ confidence level. By performing these tests it was possible to ascertain the validity of PRISM in accurately modelling a planet transiting across a limb-darkened stellar disc.

2.7.2 Modelling Starspots

To enable PRISM to model starspots in lightcurves first required deciding on the spot parameters. Four parameters were chosen, the longitude and co-latitude coordinates of the spot centre on the stellar disc θ and ϕ, the spot's angular size in degrees r_{spot} and the spot's contrast as compared to the immaculate photosphere ρ_{spot}. It was decided to set the spot's coordinate system so that the left hand limb of the star was at $-90°$ and the right hand limb was at $90°$. This meant that a longitude position of $0°$ would place the spot at the point of maximum light for the stellar disc. The co-latitude coordinate system is set so that the north pole of the star was at $0°$ and the stellar equator is at $90°$.

Due to the nature of PRISM, modelling starspots would just require modifying individual pixels on the main stellar grid within the spot's boundary. The difficulty lay in determining which pixels were within the spot. Silva (2003) placed a small circular spot on the stellar disc (see Figure 2.7), but this method did not take into account that

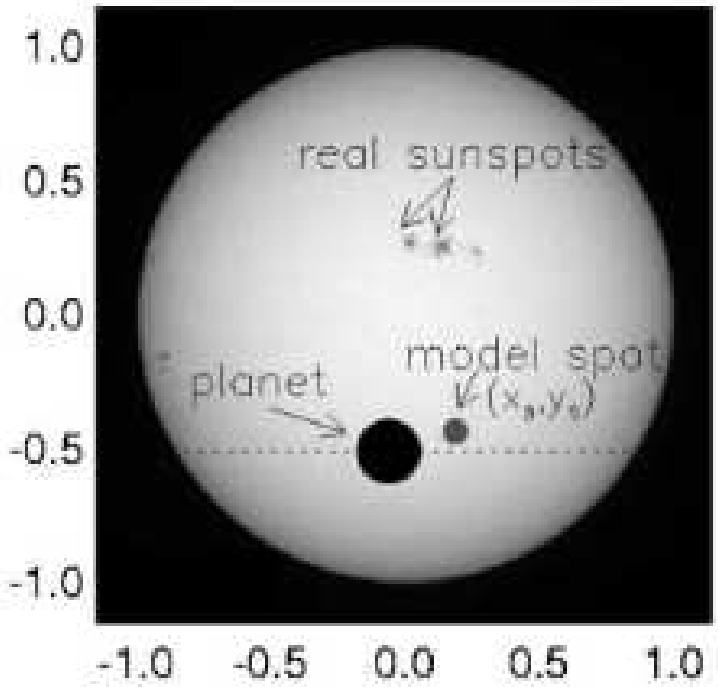

Figure 2.7: Model showing the solar disc, a model planet, sunspots and a model spot (Silva, 2003). Here Silva (2003) places a circular model starspot directly on the stellar disc.

the stellar disc is a curved surface and when the spot moves closer to the limb of the star its circular shape distorts into an elliptical shape.

To project a circular spot on a curved stellar surface PRISM first calculates the plane which intercepts the stellar surface at the spot's boundary. The centre of this plane lies directly below the central point of the spot at a distance of $r_* \sin r_{spot}$ from the stellar core (see Figure 2.8). PRISM then scans an area slightly larger than the expected spot and calculates all the vectors $\mathbf{V}$ between the centre of the spot plane and each pixel. PRISM then calculates the angle θ between $\mathbf{V}$ and the vertical line passing though the centre of the star, spot and plane. If $\theta = 90°$ then the pixel must lie on the spot boundary, while if $\theta < 90°$ then the pixel lies within the starspot. All

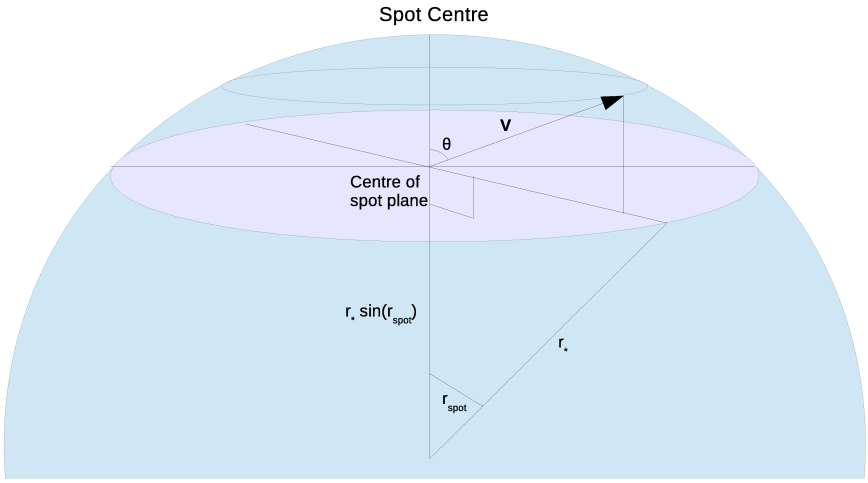

Figure 2.8: Diagram showing how PRISM calculates the pixel vectors for spots. PRISM calculates the vector **V** of each pixel element and then determines the angle between **V** and the centre of the spot plane θ.

pixels that lie outside the starspot will have $\theta > 90°$. By testing θ, PRISM can find which pixels are affected by the starspot and multiply their intensity value by ρ_{spot}.

Using this method for modelling starspots and combining it with the approach to model the stellar disc and transit as shown in Section 2.7.1, it is possible to build an array containing hundreds of thousands of pixels to map out the stellar disc, limb-darkening, starspots and the position of the planet at specific intervals (see Figure 2.9). By calculating the total intensity from each array PRISM is then able to model a transit lightcurve containing a starspot both physically and realistically without introducing any of the transit shape uncertainties that were mentioned in Section 1.5.1.

It was decided to only let PRISM model circular spots. The reason behind this idea was that a starspot anomaly appearing in a transit lightcurve is in fact a measurement of the change in intensity from the star. The only things that the anomaly can give us is the position of the spot and a difference in intensity (i.e. size and contrast). At present using current technology and techniques it is not possible to achieve the required precision to map out in detail the exact shape of the starspot. Therefore it

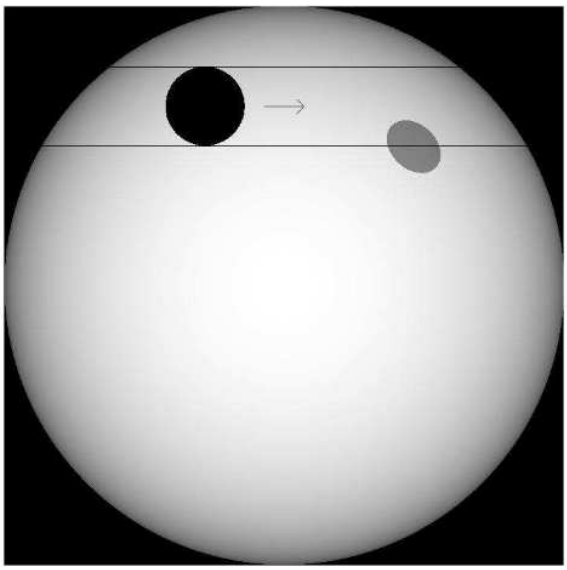

Figure 2.9: An output model of a transit and a starspot using PRISM. The transit cord are the two black horizontal lines and the black disc in the top left represents the planet. A starspot is also shown to the top right. This shows how PRISM projects an elliptical shape for a circular spot on a curved surface.

was decided to use a circle as an approximation to the shape of the starspot, just like how Sunspots appear circular in low resolution images of the solar disc.

2.7.2.1 Model Testing and Validation

Unlike when testing the transit modelling component of PRISM with another transit model (JKTEBOP) the starspot modelling component of PRISM has no other model to be compared to. Therefore, to test PRISM's ability to accurately model a starspot on the stellar disc required viewing the stellar grid. PRISM was set to create starspots at the centre of the star and at each pole. This was to check that PRISM was properly modelling the spots. Another test (see Figure 2.10) was to to place a spot on the limb of the star at a high altitude and to then shift its longitudinal position by 20°. The position of the spot was shifted in eight steps to allow the spot to rotate around the

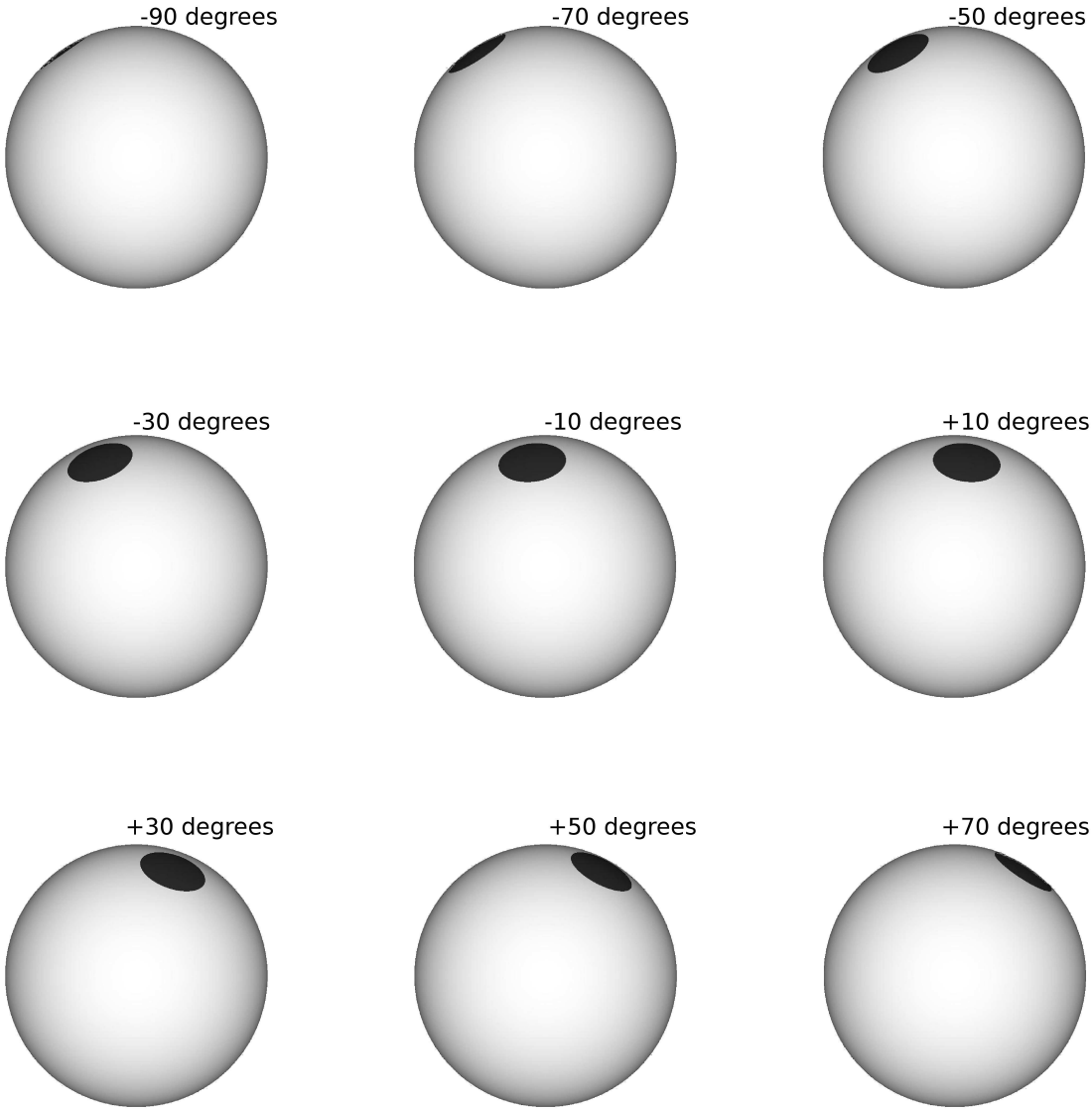

Figure 2.10: Output models from PRISM showing a starspot rotating around a star. The stellar rotation axis lies in the plane of the page and points upwards. The images move from left to right. The starting longitude of the spot's centre is at $-90°$ and with each image rotates around the star by $20°$. The longitude angle of the spot's centre is displayed for each image. These images shows how PRISM can accurately model an elliptical projection of a circular spot.

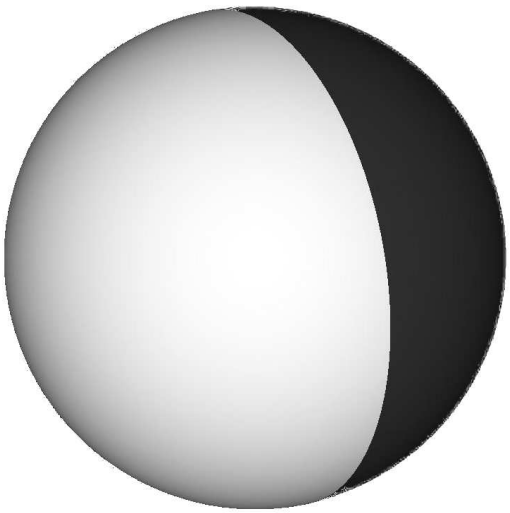

Figure 2.11: Output model from PRISM showing a 90° starspot. The centre of the spot is behind the star. The physical properties of the simulated spot are $\theta = 120°$, $\phi = 80°$, $r_{spot} = 90°$ and $\rho = 0.2$.

surface of the star by 160°. Each of the images was then checked and used to create a two second animation. The purpose of this was to check that the projected elliptical shape of the spot was maintained while viewing the spot at different angles. As can be seen in Figure 2.10 PRISM successfully passed this test. Another test was to use a spot with an angular diameter of 90°. This size of spot equates to an area of a single hemisphere (50% surface coverage). The spot's centre was then placed just behind the stellar disc. In reality we would still be able to observe a section of the starspot that covers a section of the stellar disc in our field of view. Figure 2.11 shows the output from PRISM and as can be seen PRISM correctly models the position and shape of the elliptical projection of the starspot.

2.7.3 Sample Lightcurves

When a spot anomaly is viewed during a transit the total intensity received increases for a dark spot. The total change in intensity is based on the surface area and contrast

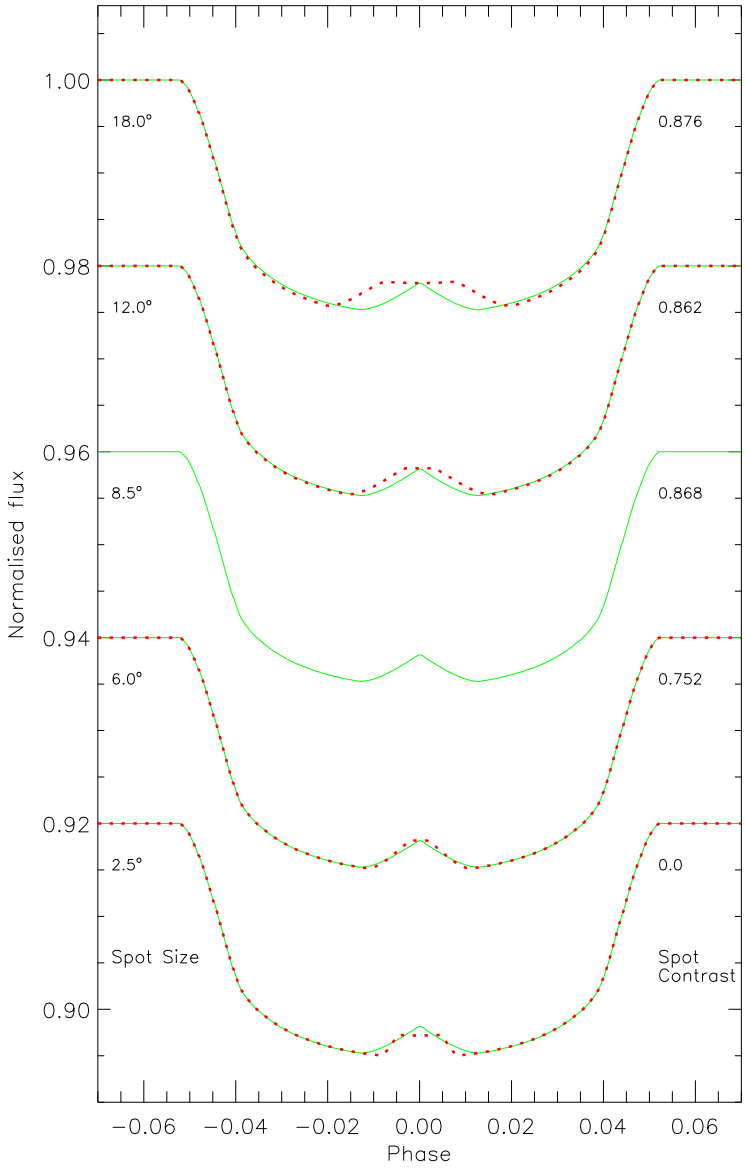

Figure 2.12: Five light curves showing how the shape of the spot anomaly changes with the size of the spot relative to that of the planet. The spot contrast was also modified for each light curve to maintain an approximately constant spot anomaly amplitude. This amplitude gives a lower limit for the size of the spot. The spot sizes are labelled on the left of the plot and the spot contrasts on the right. The 8.5° spot (green solid line) is the representation of when the spot is of equal size to the transiting planet. There is a degeneracy between the spot radius and contrast, which can be broken when modelling data of sufficiently high-precision and cadence.

of the spot (Silva, 2003). Therefore there is a degeneracy between these two parameters. Figure 2.12 shows example light curves for anomalies of approximately the same amplitude and due to a range of spot sizes and contrast. It is possible to discern three regimes from this diagram. First, when the spot is of a similar size to the planet the shape of the spot-occultation is an inverted 'V'. This is due to the fact that the amount of time the planet spends fully eclipsing the spot is very small compared to the duration of the partial eclipse phases. Second, for a larger spot, both the peak and base of the spot-transit increase, because the planet reaches the spot earlier and spends more time fully eclipsing the spot. Third, for a smaller spot, the peak broadens due to the planet fully eclipsing the spot for longer, while the base shortens due to the fact that the total duration is shorter. These three distinct shapes allow the degeneracy between the spot radius and contrast to be broken for data of sufficient precision and time sampling.

It is also apparent that the amplitude of the spot-transit gives a lower limit on the size of the spot, below which the spot is too small to give such an amplitude even if its contrast is zero. In Figure 2.12 the 2.5° spot has a contrast of zero and is still unable to achieve the same change in intensity as the other spots.

2.8 Optimisation Algorithms

We now have a model (PRISM) capable of modelling both a planetary transit and starspots on the stellar surface, using ten different parameters. The next step is to develop an optimisation algorithm to allow PRISM to fit transit data. The first optimisation algorithm used was a Markov Chain Monte Carlo (MCMC). MCMC (Section 2.8.1) is similar to the Levenberg-Marquardt algorithm in the respect that they are both local optimisers. As such, when using MCMC to determine the best-fitting values of the ten parameters, the chains regularly became stuck in local solutions. This forced a large number of chains to run for over 10^6 iterations to find the global best-fitting solution. The next algorithm used was a Genetic Algorithm (GA). The GA (Section 2.8.2) is considered as a global optimiser but due to its nature it is unable to perform Bayesian

statistics to ascertain the uncertainties in the parameter values. The final optimisation algorithm used to fit the transit data is a hybrid between a GA and MCMC. GEMC (Section 2.8.3) is based on Differential Evolution Markov Chain (DE-MC) developed by Ter Braak (2006). DE-MC runs by allowing multiple MC chains to run parallel and to learn from each other, resulting in the chains evolving (converging) to the optimal solution.

2.8.1 Markov Chain Monte Carlo Simulations

The MCMC algorithm is a type of random walk around a given parameter space. Each MCMC chain begins at a randomly generated set of parameter values and is evaluated and assigned a goodness of fit value. At each next step the parameters are randomly perturbed and the chain is re-evaluated using the new parameter values and assigned a new goodness of fit. If the goodness of fit has improved then the new parameters are accepted, while if the fitness has deteriorated then the new parameters are either accepted or rejected based on a Gaussian probability function (see Equation 2.17). This form of MCMC is classified as the Metropolis-Hastings random walk (Metropolis et al., 1953; Hastings, 1970) and is also widely used in the exoplanet community (e.g. Collier Cameron et al., 2007a; Winn et al., 2007a; Pollacco et al., 2008; Anderson et al., 2011; Hellier et al., 2011; Sanchis-Ojeda et al., 2011; Pepper et al., 2013).

When fitting transit data the goodness of fit is evaluated as the Chi squared, χ^2,

$$\chi^2 = \sum_{i=1}^{n} \left(\frac{x_i - y_i}{\sigma_i} \right)^2 \tag{2.15}$$

where n is the number of data points, x_i is the value of the ith data point, y_i is the value of the model at the ith data point and σ_i is the uncertainty in the ith data point. Another way to measure the fitness of a set of parameters is to use the reduced Chi squared, χ^2_ν,

$$\chi^2_\nu = \frac{\chi^2}{n_{data} - n_{para}} \tag{2.16}$$

Here n_{data} is the number of data points and n_{para} is the number of free parameters. $n_{data} - n_{para}$ is also called the number of degrees of freedom. When χ^2 is being used by an optimisation algorithm as a measure for the fitness of a set of parameters the algorithm tries to find the set of parameters which produce the lowest value for χ^2. Using Equation 2.15 we can see that having a low χ^2 value would imply that the model produced from a set of parameter values is close to the actual data.

As discussed earlier when the parameters in the MCMC are perturbed their fitness is calculated using χ^2. There are two ways in which the parameters can be perturbed. The first uses a fixed maximum perturbation size and randomly selects the size of the perturbation between zero and some maximum size. The maximum size is selected to allow a 20% acceptance rate (Winn et al., 2007a). The second method uses a step size controller (Collier Cameron et al., 2007a) to ensure that the acceptance rate remains close to the desired value. In the case of Collier Cameron et al. (2007a) the acceptance rate was measured for the previous 100 accepted values and by using a linear equation the step size controller was adjusted to achieve an acceptance rate close to 25%. This new χ^2 value is then compared to the previous value and if it has been improved then the new set of parameters are accepted. On the other-hand, if the χ^2 has increased (i.e. degraded) then the probability p that the new parameters are accepted is,

$$p = \exp\left(\frac{\left(\chi^2_{(n-1)} - \chi^2_n\right)}{2}\right) \tag{2.17}$$

where $\chi^2_{(n-1)}$ is the χ^2 value from before the perturbation and χ^2_n is the current χ^2 being evaluated. Because χ^2_n is larger than $\chi^2_{(n-1)}$ this results in p ranging between zero and one (where one would mean a 100% probability). In the event that the new parameters are rejected then the parameters from the previous iteration are added into the chain. This is an integral part of MCMC.

Sometimes, depending on the data being fitted, a prior is attached in calculating p. For example, Collier Cameron et al. (2007a) uses a prior for the stellar mass and radius based on the mass-radius relation for main-sequence stars. They then replace χ^2 with the logarithm of the posterior probability distribution. Winn et al. (2007a)

also used a prior for the stellar limb-darkening based on the LD models from Claret (2000).

Once a MCMC chain has been completed it is split into two sections with the first being discarded. This is called the 'burn in' stage. This is because it takes a certain number of iterations before the chain reaches the global solution. To estimate the uncertainties in the parameters requires taking the standard deviation of the parameter values and if these values contain random values that have no reflection on the actual values, this will affect the measurement of the parameter uncertainties.

There have been a few diagnostic tools developed to help ascertain if the results from an MCMC analysis are for the global solution and not a local solution. Gelman & Rubin (1992) proposed a diagnostic to test the variance within an MCMC chain and the global variance of multiple chains. The idea is that if multiple chains are run then they should all reach the global solution after a certain number of iterations. The Gelman-Rubin statistic R is used to test the variance of the stationary distribution $\hat{\sigma}^2$. This statistic is comprised from measuring the variance of a single parameter both within a chain and the overall variance of the parameter for all the combined chains. If R is close to one then the chains are thought to have converged and are well mixed.

2.8.1.1 Application of MCMC to PRISM

The first attempt at fitting real data with PRISM utilised a MCMC algorithm. Both a constant and an adaptive step size was used. This was introduced in order to use Bayesian methods to find the best fit and associated uncertainties. The problem with this approach was that there were many local solutions in the parameter space, which tended to trap the MCMC chains, resulting in poor mixing and convergence according to testing with the Gelman-Rubin statistic. This could be solved by using a large number of iterations, but such an approach was ill-suited to PRISM due to the significant amount of processing time required per iteration. A single evaluation of a model appropriate for WASP-19, with 70 datapoints, takes PRISM typically 0.7 s using a 2.7 GHz dual-core desktop computer. We found that MCMC chains required up to

10^6 iterations to converge properly, depending on how often they got stuck in the local solutions, which equated to about a week of calculation time. Using individual step sizes for each of the parameters (instead of a global step size) only slightly helped in improving the ability of the MCMC to converge properly, which resulted in reducing the calculation time by a few hours.

2.8.2 Genetic Algorithms

A Genetic Algorithm (GA) mimics biological processes by spawning successive generations of solutions based on breeding and mutation operators from the previous generation. By performing these operations the new solutions are generated based on the fitness of the parent solutions, not a perturbation of their parameters. Because of this a GA can be considered as a global optimiser where solutions can jump large distances across the solution space.

Because the GA optimiser mimics the natural selection process, its foundation should also represent the foundation of natural selection and therefore it is ideal to base the solutions (members of the population) on a population of living individuals (phenotypes). The ability of the individuals to successfully breed and subsequently pass on their genetic material to the next generation depends on their genes (genotypes). Charbonneau (1995) explains the difference between the genotype and the phenotype from a biological stand point. The genotype contains the genetic material stored in chromosomes in the form of linear gene sequences, while the phenotype is the outward manifestation of the genotype (i.e. the individual) that feeds and breeds in real space. During breeding genetic material from both parents is used in constructing a new set of genes, which gives rise to a new individual. Therefore the phenotype is the decoded version of the genotype. To this end each solution will be considered a phenotype and will require a corresponding coded genotype. Charbonneau (1995) explains that in terms of optimisation problems the phenotype is the list of parameter values that make up a solution or population member and the genotype is the encoded parameter values, usually as a linear string of digits. It is this linear string of digits that is used by

all of the GA operators, which afterwards are decoded to give rise to new solutions. In essence the genotype contains a list of instructions on how to build the corresponding phenotype just like in the biological world. The GA operators are used on the genotype and are then decoded to create new solutions with each generation (see Figure 2.13). When a new generation is being created (bred) the parents are selected based on their fitness (just like in natural selection). This helps to increase the probability that the best-fitting members of a population go on to spawn a population with a higher proportion of high fitness members.

As seen in Figure 2.13 to evolve a population to the next generation requires the use of breeding and mutation operators (see Section 2.8.2.1). Before a population can be used to breed the next generation the genotypes need to be encoded from the phenotypes in the population. To begin with, an initial population is drawn from a random Gaussian distribution. From this point on each GA needs to be tailored for each model the GA is being used to optimise. In the example used by Charbonneau (1995) the two parameters ranged from zero to one and therefore the decimal point was known to come after the first digit. For transit lightcurves, however the decimal point comes after the first digit for k but comes after the second digit for i. Therefore the encoding of the genotypes needs to be designed based on the type of problem to be solved. Once this has been achieved then to encode the genotypes requires the digits of each parameter to be combined into a single string. In the example given by Charbonneau (1995) this equated to a 16-digit string due to using two 8 decimal point numbers (one for each parameter). It should be mentioned that the encoded genotypes are sometimes in binary form (Rajpaul, 2012b,a). However, as mentioned by Charbonneau (1995), encoding the genotypes in binary or base 10 has little impact on the efficiency of the GA in finding the global solution.

Once the genotypes have been encoded the next step is to assign a fitness to each population (solution) member. This is achieved in the same manner as in MCMC (see Section 2.8.1) by which a χ^2 value is determined for each population member using the parameter values contained in the phenotype (Charbonneau, 1995). When picking a pair of solutions (parents) to generate two new solutions (offspring) a bias random

selection is used. In an unbiased random selection the probability of selecting each individual is equal, while in a biased random selection the solutions with the lowest χ^2 values have a greater probability of being selected. For example, if one solution has $\chi^2 = 800$ while another has $\chi^2 = 400$, the latter solution is therefore twice as likely to be selected as the first. Two different selection methods can be used to select which two solutions go on to breed. The first method selects just two members of the population to become parents, while the second method draws n solutions (Tournament selection)

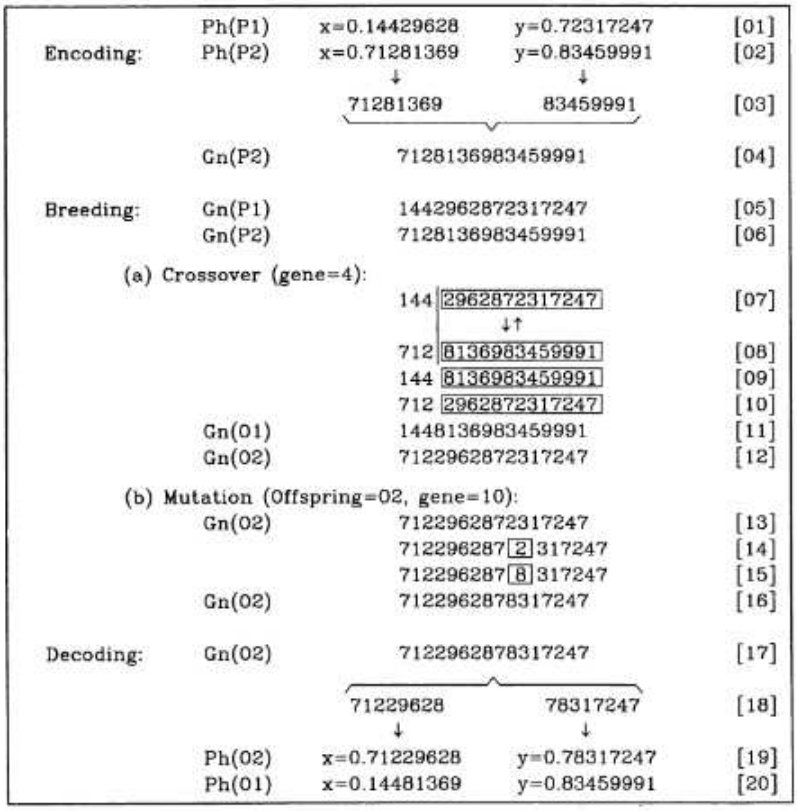

Figure 2.13: Encoding, breeding and decoding in genetic algorithms (Charbonneau, 1995). Phenotypes are defined as two real numbers and are encoded into a 16 digit number (8 from each real number). 'Ph' means phenotype, 'Gn' means genotype, 'P' means parent and 'O' means offspring. The encoding and decoding are only shown for the the second parent and offspring. The crossover and mutation operators are performed based on a probability test.

and selects the two best-fitting to become parents (Miller & Goldberg, 1995). The second method increases the probability that better fitting solutions are selected to become parents[8] and a mixture of the two methods can allow the sensitivity of the GA to alter from probing a global (large) parameter space to probing a local (smaller confined) parameter space. Once the parents of the population have been selected, breeding and mutation operations are performed to generate the next generation of solutions.

2.8.2.1 Breeding, Mutation and Extinction Operators

When two parents have been selected their genotypes undergo a breeding operation. Figure 2.13 shows an example when a single crossover point is used but multiple crossover points may be used. For example, if two crossover points are specified then the digits between the two points are swapped between the parents to form the two offspring. In the single crossover point method a position in the genotype string is randomly selected as the crossover point. This creates two sections in the parent genotype strings. The sections are then swapped to create two new offspring. This creates the initial offspring genotypes, ready to be tested for any mutations. Mutations in a GA mimic mutations in biological process. Depending on the position of the mutation in the genotype they can cause either a small or large alteration in the phenotype. For an eight digit parameter a mutation on the first digit can alter the parameter value by a 1^{st} order factor or if the last digit is altered the parameter is only affect by one part in 10^8. There are two main types of point (single-digit) mutations, creep and jump mutations. Charbonneau (1995) uses a jump mutation in which the digit selected to mutate is replaced with a new randomly generated digit. Creep mutation causes the selected digit to undergo a ± 1 perturbation (Metcalfe & Charbonneau, 2003). In either case a mutation rate is set in which there is a probability that a digit will undergo a mutation. If the digit selected for creep mutation is at the numerical boundary (i.e.

[8]This probability is refereed to as the selection pressure (Miller & Goldberg, 1995).

using a base 10 system the numerical boundary is either a 0 or a 9) then the one is carried over. Once each digit of the offspring genotypes have been tested for mutation and any mutation operators have been used the offspring genotypes are then decoded into the offspring's phenotype. The new phenotypes describe the new parameter values for the next generation of solutions, ready to be evaluated by the model being optimised and assigned a new fitness value.

A mutation operator is used in a GA to help maintain variance in the population and to help prevent the population getting stuck in a local solution (Charbonneau, 1995; Metcalfe & Charbonneau, 2003). Another method to use instead of a mutation operator is an extinction operator (Yao & Sethares, 1994). When the variance within a population falls below a threshold the population is deemed to have congregated around either a global or local solution. To check whether this is a global or local solution the population is killed off and replaced by an entirely new randomly generated population. Some GA's (e.g. Yao & Sethares, 1994) allow the highest fitting population member to survive the extinction. This process allows a GA to sample many different local solutions while still being able to determine the global solution.

Through breeding, mutation and extinction the population of a GA is able to sample a large parameter space and converge on the global solution rapidly. Due to the nature of how the population members are evolved into the next generation through modifying the genotypes, a GA is capable of traversing a parameter space cluttered with many local solutions without getting stuck, unlike MCMC.

2.8.2.2 Performance of the GA

Charbonneau (1995) describes the use of a GA called PIKAIA. To test the performance of PIKAIA the function

$$f(x,y) = [16x(1-x)y(1-y)\sin(n\pi x)\sin(n\pi y)]^2$$
$$x, y \in [0,1],\ n = 1, 2, ... \tag{2.18}$$

was used, where x and y range between zero and one. There is a central global solution to this function that lies at the centre ($f(0.5, 0.5) = 1$) and there are $n^2 - 1$ local solutions. This function was selected as it proves difficult to find the global solution with MCMC and other optimisers that use potential gradients in the parameter space to find the best-fitting solutions. When the AMOEBA subroutine (Press et al., 1993) was used, it found the global peak quite efficiently. Charbonneau (1995) states that this is due to the low dimensionality of the problem being tested and in higher dimensional problems linear optimisers are not truly effective.

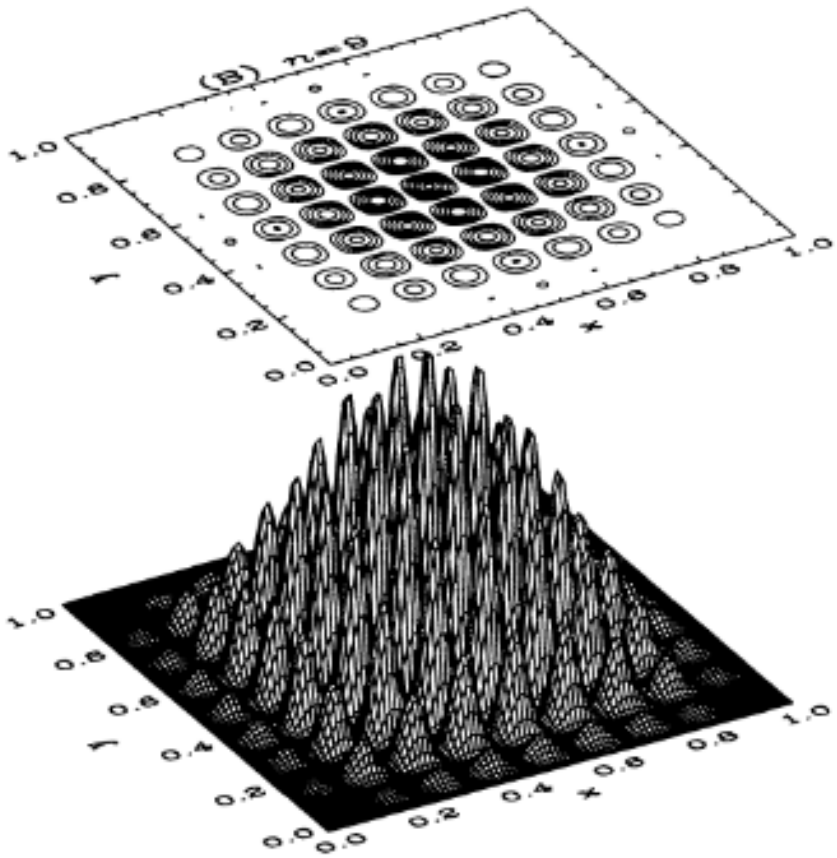

Figure 2.14: Surface and contour plots of the function used to test PIKAIA (Charbonneau, 1995). The function defined by Equation 2.18 is set with $n = 9$. There are 81 local solutions with the global solution at $f(0.5, 0.5) = 1$.

To test PIKAIA, Charbonneau (1995) used $n = 9$ to give 80 local solutions and one global solution (see Figure 2.14). The GA was setup with a population of 100 members and was designed to run for 100 generations. The crossover and mutation operators were set at 0.65 and 0.003, respectively. This meant that there was a 65% chance that the parents genotypes were crossed over and for those which did not the offspring were exact replicas of the parents. The mutation rate meant that on average 0.3% of the digits in the offspring were mutated using the jump mutation.

Figure 2.15 shows the population distribution in the parameter space for five generations. After 100 generations the maximum function value found was approximately 0.99 with both the parameters close to 0.5. By studying Figure 2.15 we can see how a GA can cluster around local solutions (panel b) and migrate towards the global solution (panels c and d). By the 20^{th} generation the GA has found the central peak where the global solution lies. This equates to 2000 function iterations. However, even by the 100^{th} generation (10000 function iterations) the GA had still not found the exact optimal solution, but 100 generations is a short evolutionary run.

Charbonneau (1995) states that the initial 20 generations are when the GA is probing the parameter space and then after this as the variance in the population declines due to more members of the population evolving onto the central peak the rate of evolution of the population becomes slower which leads to slow incremental improvements. Figure 2.15 is only representative of a single run and Charbonneau (1995) states that its performance is worse than typical runs using PIKAIA on this function but it was selected to show that a GA can jump from a local solution to the global solution.

Charbonneau (1995) also experimented with various values for the mutation, crossover, selection pressures and population sizes (see Figure 2.16). They chose three values for each property and ran PIKAIA 100 times and took the average fittest member. For the mutation they chose the values 1.4%, 0.3% and 0.1%. From examining Figure 2.16 it can seen that high mutation rates can increase the GA's efficiency at finding the global solution. This is due to the fact that random mutation can help a population explore the parameter space as it can shoot a member into a more favourable position.

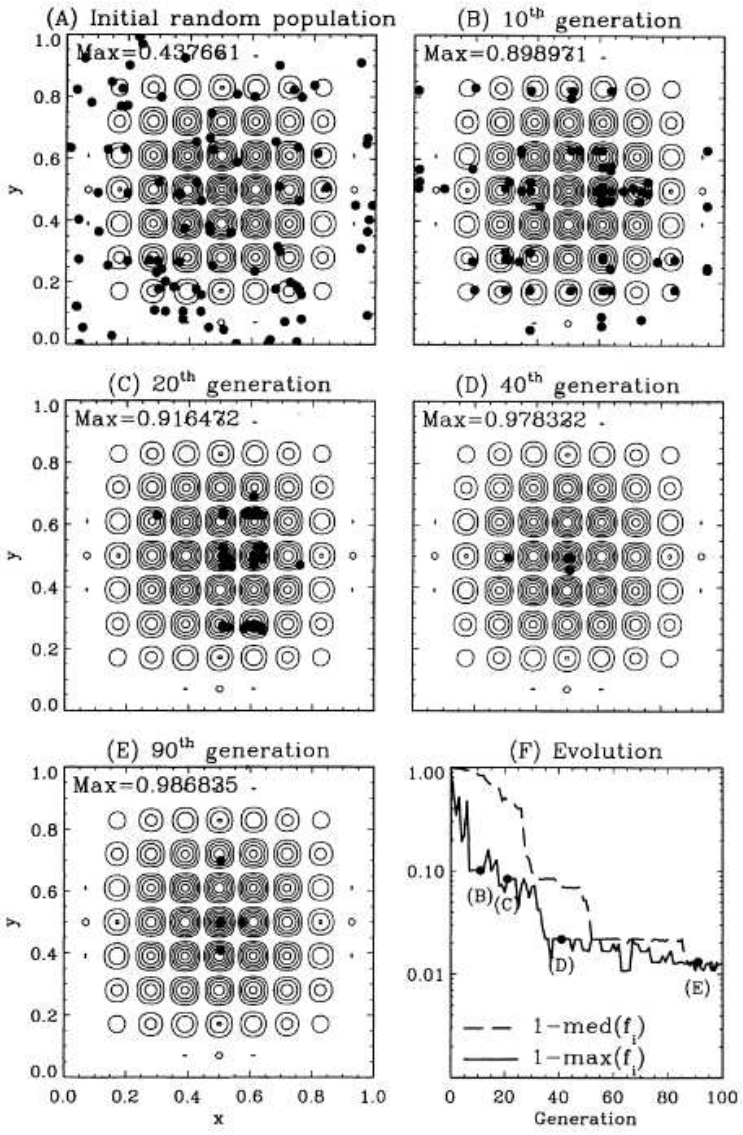

Figure 2.15: A genetic solution to the model optimisation problem (Charbonneau, 1995). The first five panels show the population distribution in space, with the function contours overlaid. Starting with the initial population in panel (a) and proceeding to the 90^{th} generation in panel (e). Panel (f) shows the evolution of the fittest population member (solid line) and the median fitness population member (dashed line) as measured by $1 - f(x, y)$.

The crossover values chosen were 100%, 65% and 6%. Figure 2.16 helps to show that high crossover rates are required to allow the GA to find the global solution. If crossover is low then each generation will be a direct copy of itself and there would be little to no evolution over the generations.

As mentioned by Miller & Goldberg (1995), selective pressure is a term used to describe the probability of the fittest members of the population being bred. Charbonneau (1995) states that a high, medium and low selective pressure are used. Where

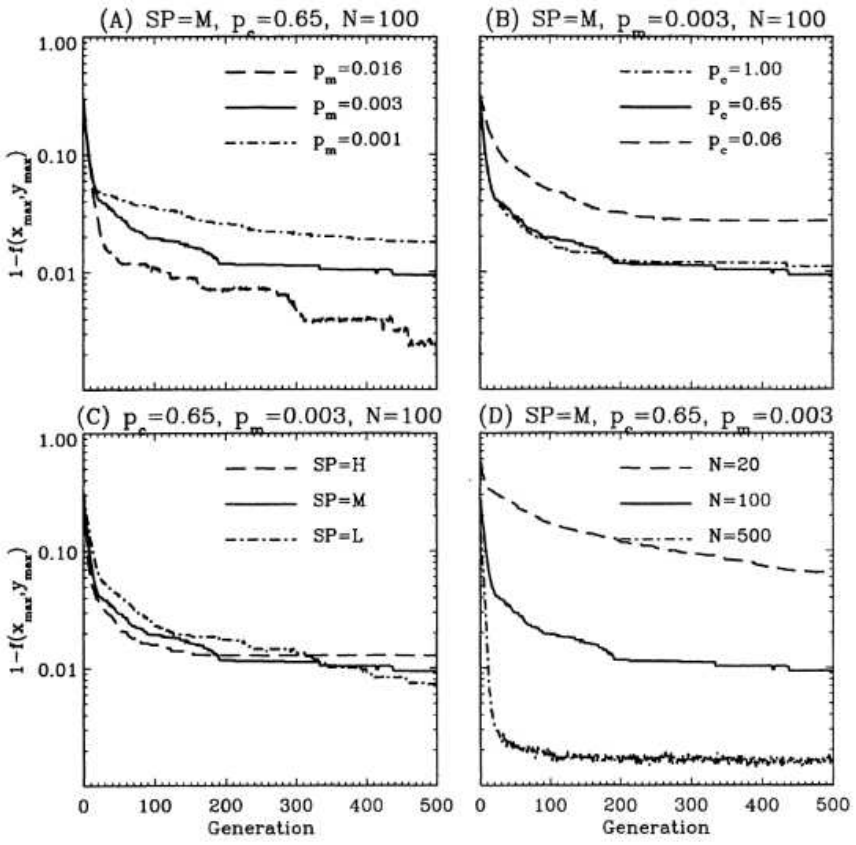

Figure 2.16: Fitness as measured by $1 - f(x, y)$ against generation count for PIKAIA (Charbonneau, 1995). Panel (a) is using various mutation rates. Panel (b) is for different crossover points. Panel (c) is for three different selection pressures and panel (d) is for various population sizes. The curves represent the fittest individual averaged over 100 runs of the GA.

the high selective pressure is used then the probability distribution is heavily biased for the fittest members of the population, while the low selective pressure gives the less fit members greater probability of being selected to breed. Figure 2.16 shows that, while a high selective pressure increases the convergence rate, a low selective pressure is more likely to find the global fit. This is because when a population cluster forms over a local solution and they contain the fittest members then the offspring of the next generation will be made solely from these parents, while with a low selection pressure the fittest members can breed with less fit members allowing for a larger variance in the next generation, but at the expense of a slower convergence rate.

For the population sizes Charbonneau (1995) chose 20, 100 and 500 population members. The outcome was that the population of 500 members was able to reach a fitness of 0.001, ten times smaller than the population of only 100 members. This seems to indicate that larger population sizes allows both faster and better convergence. Charbonneau (1995) states that the reason why having a larger population gives a better convergence is due to the initial population covering a larger area and thus increases the probability that an initial solution starts close to the optimal solution.

Each of the GA runs in Figure 2.16 was allowed to run for 500 generations. Using a population size of 100 meant that in total 50000 function iterations were undertaken in each run. By testing PIKAIA against this function, Charbonneau (1995) was able to show the global optimisation power of the GA in a parameter space filled with a large number of local solutions, but the tests also highlighted a weakness. While a GA can find where the global solution is, it is poor at locating its exact position (Charbonneau, 1995; Rajpaul, 2012b). Once the GA has finished, its result should be used as a starting point for a local optimisation algorithm (e.g. a Levenberg-Marquardt algorithm).

2.8.2.3 Estimating the Parameter Uncertainties from a GA

Due to the nature of the GA it is not possible to perform a Bayesian statistical analysis to determine the posterior distribution of the parameters. However, as mentioned in the previous section, the GA gives an area of where the best-fitting solution is.

Charbonneau (1995) also mentions the use of hybrid optimisation algorithms where a GA is used to find the global best fit and a rapid convergence algorithm then takes over to find the exact position. To estimate the parameter uncertainties once the GA has found the global best fit an MCMC algorithm can then take over to explore the local parameter space to find not just the exact position of the best fit but to also estimate the parameter uncertainties. The initial starting point of the MCMC chain would have the same parameter values as the best-fitting solution found from the GA. Because of this, convergence tests such as the Gelman and Rubin statistic are not needed as the chains are already starting at the global solution and hence begin converging on the global solution. A burn-in period may still be required while the parameter step size is being refined to give a 20% acceptance rate.

By combining the GA with MCMC it is possible to efficiently explore a large parameter space filled with many local solutions and find the exact position of the global best fit. Once found it is then possible to perform a Bayesian analysis of the posterior distribution to ascertain the parameter uncertainties.

2.8.2.4 Application of a GA to PRISM

A GA was used to find and constrain the global solution for PRISM with a data set, then a MCMC algorithm was used to perform the error analysis for this solution. The GA was set to use both mutation and extinction operators with a population size of 5000. The crossover rate was set at 100% but the GA also used eight crossover points. This was due to the fact that when PRISM is modelling a starspot there are 10 parameters that need to be optimised. During the encoding of the genotype each parameter would contribute eight digits thus creating an 80-digit string. Using a single crossover point would therefore not produce an efficient exploration of the parameter space. When a pair of parents had been selected eight random numbers were generated ranging from 0 to 79 representing which digits were the crossover points in the genotype string.

A tournament selection process was used and was proportional to the variance in the population. For a large variance, 5% of the population was randomly selected

and the two fittest individuals in the selection went on to become parents. When the variance was low only two members were randomly selected to become parents. This was done to allow the GA to rapidly converge on the global best fit and to increase the GA's ability to explore the local parameter space and increase the likelihood of finding the best fit. Two types of mutation were also used, creep and jump mutations. Jump mutations were set at 0.1%, while creep mutations were set at 0.5%.

Multiple runs of the GA were completed. Half of the runs used mutation while the other half used an extinction operator. When the variance in the population fell below 1% the population was killed off and a new randomly generated population was created. The parameter values of the extinct population were then recorded for comparison with both other extinct populations and the final population to help determine the global solution.

Once the global solution had been found an MCMC analysis was conducted with a starting location randomly selected within the parameter range of the population containing the best-fitting individual. The final best-fitting model and the parameter uncertainties was then taken from the MCMC results. In essence the GA was used to reduce a large parameter search space filled with local solutions, into a small manageable search space containing only the global solution.

Forward modelling tests of a simulated transit containing a starspot anomaly generated by PRISM were conducted. In each case the GA recovered the initial model parameters within the 1-σ confidence limit. The same tests were also conducted using GEMC and further details can be found in Section 2.8.3.4.

The GA was tested on fitting PRISM to three sets of transit data of WASP-19, two of which contained a starspot anomaly (see Chapter 3). The fitness of each solution was measured using χ^2_ν. A good fit should have a χ^2_ν value close to unity (Taylor, 1997; Southworth et al., 2007a), but the best-fitting solutions from both the GA and the MCMC had χ^2_ν values close to seven. The reason for such a large χ^2_ν was not due to bad fits of the model, but was due to underestimated observational error bars in the data (Taylor, 1997; Bruntt et al., 2006; Southworth et al., 2007a). This underestimation is caused by small systematic contributions to the photometric

errors from the observations. When the root mean squared (rms) scatters between the best-fitting model and the data using the GA and MCMC were compared to the rms residuals from JKTEBOP they were the same. Also, the χ^2_ν for the best fit from JKTEBOP was also close to seven. This indicated that it was indeed due to underestimated observational error bars in the data and not the model or the optimisation algorithms used. To solve this the errors in the data were multiplied by $\sqrt{\chi^2_\nu}$ to give a χ^2_ν value of one for the best fit.

This allowed a reduction in the computation time from seven to five days compared to solely using an MCMC algorithm. Dissatisfied with the fact that two different optimisation algorithms had to be used, one to locate the global solution and the other to obtain the parameter uncertainties, a new optimisation algorithm was developed, that combined the global optimisation power of the GA but was also able to perform Bayesian statistics on the solutions.

2.8.3 A New Hybrid: Genetic Evolutionary Markov Chains

In an attempt to produce an optimisation algorithm which combined the global optimisation power of a GA and the Bayesian statistical analysis of MCMC it was decided to create an algorithm called Genetic Evolutionary Markov Chains (GEMC). GEMC is based on DE-MC, an idea put forward by Ter Braak (2006). GEMC begins by randomly generating parameters for N chains, within the user-defined parameter space, and then simultaneously evolves the chains for X generations. At each generation the chains are evaluated for their fitness. During the 'burn in' phase the perturbation of each chain is determined by the best-fitting chain in the population. Once the 'burn in' has completed the chains cease communication and begin independent MCMC runs.

2.8.3.1 DE-MC

DE-MC (Ter Braak, 2006) combines the GA Differential Evolution (DE) (Price & Storn, 1997; Storn & Price, 1997) with MCMC. The combination of DE and MCMC is

used to solve a problem in MCMC by determining the orientation and the scale of the step sizes. Adaptive directional sampling in MCMC does solve the orientation problem, but not the scale (Ter Braak, 2006). DE-MC works by creating a population of MCMC chains whose starting points are initialised from overdispersed states and instead of letting the chains run independently and checking for convergence (Gelman & Rubin, 1992) they are instead run in parallel and learn from each other. The perturbation steps taken by each chain is given by Equation 2.19. Assuming a d dimensional parameter space and using N chains then the population $\mathbf{X}$ is a $N \times d$ matrix, with the chains labelled $\mathbf{x}_1, \mathbf{x}_2, ...\mathbf{x}_N$. Therefore the proposal vector $\mathbf{x}_p$ is generated by:

$$\mathbf{x}_p = \mathbf{x}_i + \gamma \left(\mathbf{x}_{R1} - \mathbf{x}_{R2}\right) + \mathbf{e} \tag{2.19}$$

where $\mathbf{x}_i$ is the current i^{th} chain, γ is the scale factor calculated from $\gamma = 2.4/\sqrt{2d}$, $\mathbf{x}_{R1}$ and $\mathbf{x}_{R2}$ are two randomly selected chains and $\mathbf{e}$ is drawn from a symmetric distribution with a small variance compared to that of the target. $\mathbf{x}_p$ is then tested for fitness and if accepted it is used as the next step in $\mathbf{x}_i$.

For example, in a two dimensional parameter space ($d = 2$) there are 40 chains ($N = 40$) (see Figure 2.17). At each step, for each chain, a proposal vector is generated. A difference vector between two randomly drawn chains is calculated ($\mathbf{x}_{R1} - \mathbf{x}_{R2}$) and multiplied by γ (in this case $\gamma = 1.2$). This new vector is then added to the current step in the chain and is evaluated for its fitness. In the example given $\mathbf{e}$ is equal to zero but Ter Braak (2006) gives $\mathbf{e} \sim N\left(0, b\right)^d$. Therefore the addition of $\mathbf{e}$ to the proposal vector adds a different random number to each element of the proposal vector. From this method the proposal vector contains information on both the orientation and on the scale.

After the 'burn in' stage of a MCMC chain, determining the required step size to allow a 20-25% acceptance rate can be difficult. For a transit lightcurve altering i by 0.05% should only cause a small increase in χ^2 but a 0.05% alteration in T_0 could cause a large increase in χ^2. Using DE-MC can solve this problem. Because the chains are clustered around the global solution after the 'burn in', then the difference

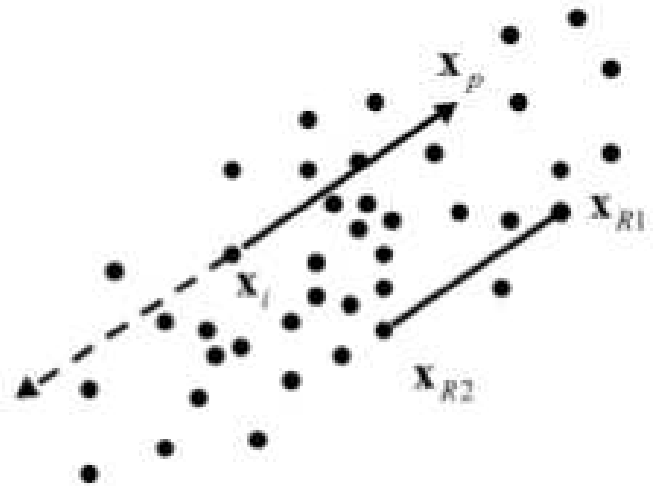

Figure 2.17: Differential evolution in two dimensions, with 40 population members (Ter Braak, 2006). The proposal vector $\mathbf{x}_p$ to update the i^{th} member is generated from $\mathbf{x}_i$ and the randomly drawn members $\mathbf{x}_{R1}$ and $\mathbf{x}_{R2}$. The dashed arrow represents the proposal vector if $\mathbf{x}_{R1}$ and $\mathbf{x}_{R2}$ had been selected in opposite order.

vector between two randomly selected chains will contain the individual scale for each parameter (i.e. 0.05% for i and 0.00001% for T_0). Ter Braak (2006) argues that DE-MC is a single N-chain that is simply a single random walk Markov Chain in a $N \times d$ dimensional space. The use of DE-MC in the exoplanet community is increasing. At present DE-MC is being used to fit models of transiting circumbinary planets which contain over 30 parameters (e.g. Doyle et al., 2011; Orosz et al., 2012; Welsh et al., 2012; Schwamb et al., 2013).

2.8.3.2 Conceptual Workings of GEMC

It was decided to try and improve upon DE-MC by increasing the efficiency in which the algorithm converged on the global solution. This new algorithm called GEMC uses multiple Markov Chains but the generation of the proposal vector was altered. Instead of randomly selecting two different chains, the chains used in generating the difference vector are the current best-fitting chain and the chain undergoing the perturbation.

This causes the direction of the proposal vector to be biased towards the current best fit. When the population is being evaluated the parameters of the fittest member undergo up to a $\pm 1\%$ perturbation and its fitness is then re-evaluated. If the fitness has improved it is accepted but if the fitness has deteriorated it is accepted based on a Gaussian probability distribution (see Equation 2.17). The next step is to then evolve the other chains. This is accomplished in a similar way as a GA, in that the chain parameters are modified by incorporating the parameters of another chain. However, unlike a GA where a member is picked by a weighted random number and then the digits of each parameter are crossed over with the digits from a different member, GEMC directly perturbs the parameters of each chain in a vector towards the best-fitting chain. The size of this perturbation is between zero and twice the distance to the best-fitting chain, allowing the chain to not only move towards but also to overshoot the position of the best-fitting chain. While DE-MC multiplies the difference vector by a pre-determined γ value and adds a random number, GEMC just multiplies the parameters in the difference vector by a random number.

An example would be a two-dimensional function $f(x, y)$ (see Figure 2.18). The difference vector between a given chain and the best-fitting chain in this case is $(\Delta x, \Delta y)$. This difference is then multiplied by a random scalar γ for each parameter, where γ is in the interval [0,2], and then added to the given chain's parameters (x_0, y_0) to form the new potential solution $f(x_1, y_1)$.

$$x_1 = x_0 + \gamma_x \Delta x \tag{2.20}$$

$$y_1 = y_0 + \gamma_y \Delta y \tag{2.21}$$

When $\gamma = 0$ the parameter is not perturbed, $\gamma = 1$ the parameter equals the current best-fitting value and when $\gamma = 2$ the parameter is perturbed to the opposite position of the current best-fitting value. This allows the potential solution to travel large distances across the parameter space unimpeded by local peaks. After the parameters have been perturbed the chain is then re-evaluated and is selected using the same method as the best-fitting chain. Figure 2.18 shows an example of two chains operating

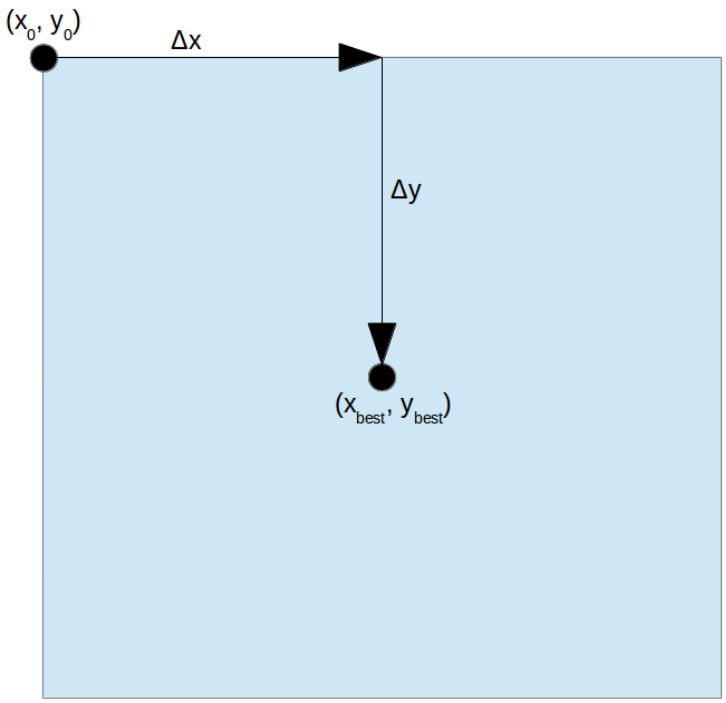

Figure 2.18: Potential perturbation space for a 2 D function using GEMC. Here just two chains are shown, the best-fitting chain (x_{best}, y_{best}) and the chain whose proposal vector is being generated (x_0, y_0). The best-fitting chain lies at the centre of the potential perturbation space (blue box). Depending on the size of γ_x and γ_y in the interval [0,2] the solution (x_0, y_0) can be perturbed to any position within the blue box.

in a two-dimensional space. The required number of chains needed depends on both the size and the number of dimensions of the parameter space (see Section 2.8.3.3), but potentially there can be hundreds if not thousands of chains operating and covering a huge area of the parameter space in a few generations.

GEMC runs in two stages. The first stage, called the 'burn in', is used to find the optimal solution to the data using the above method. After this the second stage starts in which each chain undertakes an independent MCMC run. The starting points for each MCMC chain lie close but not exactly at the optimal solution. In essence what we have is the same outcome from running a GA to find the best-fitting solution and to use this to tightly constrain the starting parameter range of an MCMC run.

2.8.3.3 Performance of GEMC

To test the performance of GEMC it was decided to use the same function (Equation 2.18) that Charbonneau (1995) used to test the GA PIKAIA. Charbonneau (1995) showed that it took PIKAIA with a population of 100 solutions up to 20 generations to find the global maximum peak but even after 100 generations it still had not found the global maximum point, confirming the GA inability to find best solutions with precision.

Figure 2.19 is an output from a run using GEMC on the function (Equation 2.18) with $n = 9$ creating 80 local solutions. We can clearly see that GEMC, using a population of only 40 chains, has found the global maximum peak within 10 generations and then went on to find the global maximum point within 20 generations. We can also see from Fig. 2.20 the power of GEMC. The global maximum peak was actually found at the fifth generation and all solutions were very close to the global maximum point by the twentieth generation. This performance indicates that the required burn-in for GEMC is extremely short and as such greatly reduces the computing time required to find the global solution.

Using the results generated from the GEMC run in Figures 2.19 and 2.20 we can see that it only took 200 function iterations for GEMC to find the global maximum peak, while PIKAIA took 2000 function iterations to do the same (see Section 2.8.2.2). This equates to a 10-fold increase in efficiency. It also only took GEMC less than 400 function iterations to find the optimal solution and less than 1200 function iterations for full convergence on the optimal solution.

Due to the nature of GEMC the choice of the number of chains to use is important, just like a GA, if the population size is too small then the probability of finding the global solution drops. Conversely if the population size is too large then the parameter space is saturated and results in wasted processing time. To demonstrate this, GEMC was used with the function (Equation 2.18) and success rates were calculated. A value for N was selected and an initial number of chains was selected. GEMC was then run 1000 times and the success at finding the central peak was measured. After this the

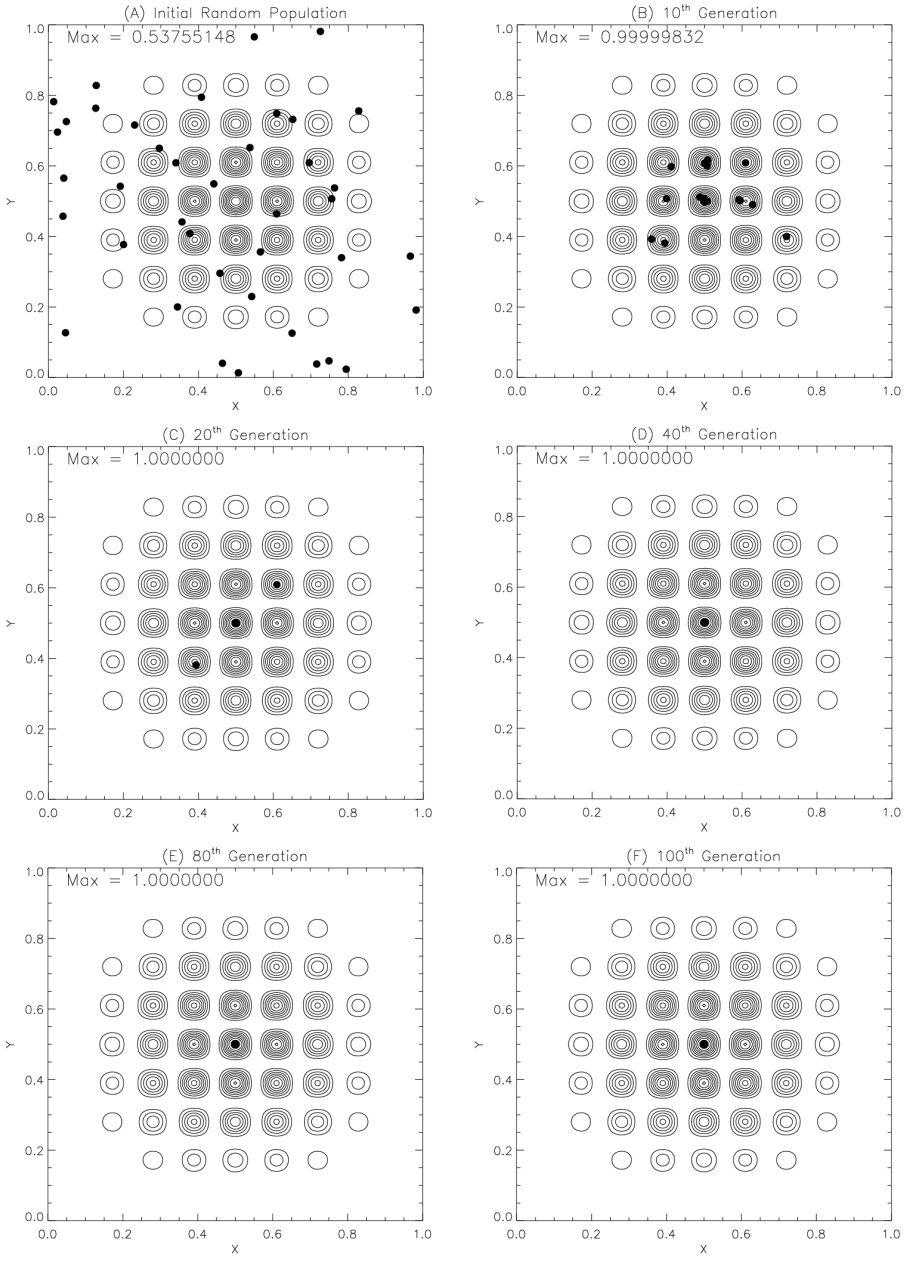

Figure 2.19: GEMC results for $N = 40$ chains and for $X = 100$ generations. The global maximum peak and global maximum point have been discovered by the 10th and 20th generations, respectively. By the 40th generation all 40 chains have found the global maximum point.

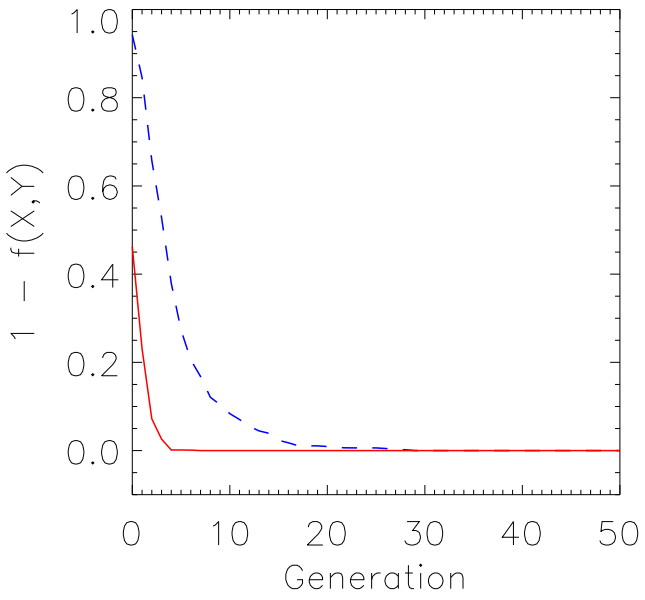

Figure 2.20: The evolution of the fittest chain (solid line) and the mean fitness chain (dashed line) from each generation. The maximum peak was found in five generations. The fitness is measured as $1 - f(x, y)$.

number of chains that were used was increased and the test was repeated. This was done for a range of different chain numbers each for three different values of N. The results can be found in Table 2.1

These results indicate that the number of chains required for a success rate of 100% at finding the optimal solution depends on the complexity of the parameter space in terms of the number of local solutions. For these tests GEMC was modified to only accept a new proposal solution if the fitness was improved. As a consequence, when the population begins to cluster around a local solution the chances that it will evolve to find the global solution is almost non-existent. Allowing a certain probability of accepting a degraded fitness would increase the success rate for GEMC in these tests by increasing the number of allowed generations. This behaviour is evident in optimising transit data (see Section 2.8.3.4) where if the population gets stuck at a local solution

Table 2.1: GEMC success rates for increasing number of chains and values of N.

Number of Chains	5	10	20	30	40	50	60	100	200	500
					$N = 5$					
Success Rate	2.9%	49.9%	84.8%	93.1%	97.7%	99.1%	99.6%	100.0%	100.0%	100.0%
					$N = 9$					
Success Rate	2.0%	32.3%	58.5%	77.0%	86.3%	93.1%	95.9%	99.2%	100.0%	100.0%
					$N = 15$					
Success Rate	0.4%	14.1%	41.5%	59.5%	71.8%	81.5%	86.4%	97.2%	99.9%	100.0%

it will eventually move away towards the global solution if enough generations are allowed to pass. From the results of these tests it was decided that when GEMC was used to optimise transit data a large number of chains would be used (over 1000). This was decided because PRISM uses 10 parameters and there would be an untold number of potential solutions within the parameter space. While this may seem like a large number of chains it is still five times smaller than the population sizes used in the GA discussed in Section 2.8.2.4.

By testing the performance of GEMC against the performance of PIKAIA it was possible to determine the effectiveness of GEMC as a global optimiser. The results are astonishing with a 10-fold increase in the efficiency at finding the central peak. Coupled with the fact that GEMC was also able to find the exact location of the central point which PIKAIA was not able to accomplish, this suggests that GEMC is capable of optimising PRISM with transit data at a more efficient rate. Also, because after the 'burn in' stage the chains become independent, GEMC solves the problem of needing two different optimisation algorithms by being able to perform Bayesian statistics.

2.8.3.4 Application of GEMC to PRISM

After testing GEMC on the function used by PIKAIA, the next step was to use GEMC with PRISM to model simulated transit data containing a starspot anomaly. For this test PRISM was used to create multiple simulated transits with a range of parameters. Once this was done noise was then added to the lightcurves so that the rms scatter between the original simulated lightcurves and the lightcurves with added noise was ≈ 500 ppm.

This was to approximate a realistic level of noise found in transit lightcurves observed using the defocused photometry technique. The error bars were then assigned to each data point to give the original noise-free models a $\chi^2_\nu = 1$.

Once a simulated transit lightcurve had been created, GEMC and PRISM was then used in an attempt to recover the initial input parameters. Table 2.2 shows the results for one of the tests, while Figure 2.21 shows the simulated transit lightcurve together with the original and recovered models for the same test.

Table 2.2: Original & recovered parameters from a simulated transit lightcurve, plus the interval within which the best fit was searched for using GEMC.

Parameter	Original value	Search interval	Recovered value
Radius ratio	0.15	0.05 to 0.30	0.1496 ± 0.0013
Sum of fractional radii	0.25	0.10 to 0.50	0.2486 ± 0.0024
Linear LD coefficient	0.3	0.0 to 1.0	0.291 ± 0.104
Quadratic LD coefficient	0.2	0.0 to 1.0	0.192 ± 0.042
Inclination (degrees)	85.0	70.0 to 90.0	85.16 ± 0.46
Longitude of spot (degrees)	30.0	-90 to +90	30.50 ± 1.17
Co-latitude of spot (degrees)	65.0	0.0 to 90.0	64.51 ± 5.83
Spot angular radius (degrees)	12.0	0.0 to 30.0	12.73 ± 2.00
Spot contrast	0.8	0.0 to 1.0	0.797 ± 0.057

From studying both Table 2.2 and Figure 2.21, it can seen that the recovered parameter values agree with the original values within their 1-σ uncertainties. For some of the parameters the difference is as small as 0.08-σ. Interestingly the rms scatter of the recovered model was found to be 499 ppm while the rms scatter of the original model is at 511 ppm. This showed that GEMC not only explored the large parameter search space but it also scanned the local area around the global solution to find the best possible fit[9] to the simulated data. This result is expected and a testament to an optimisation algorithm designed to find the lowest achievable χ^2_ν (the recovered solution in this case had a $\chi^2_\nu = 0.94$) in a given parameter space. Similar results were found on all the simulation tests and therefore help to conclude that both

[9]This best-fit is in fact a phantom solution generated by the addition of noise.

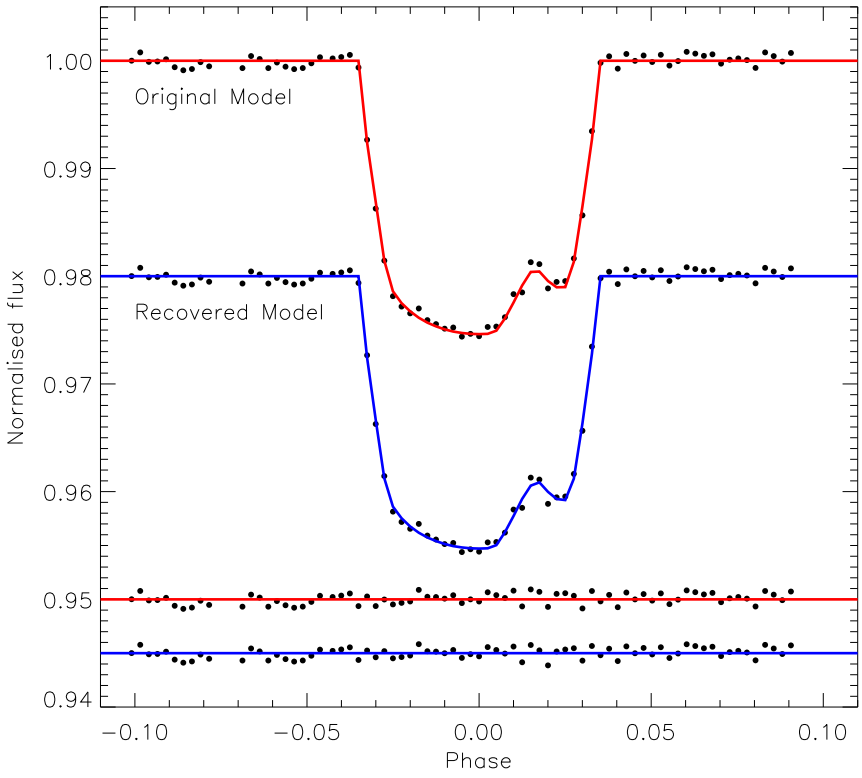

Figure 2.21: Recovered and original models to simulated transit data created by PRISM and recovered by GEMC and PRISM. The residuals are shown at the bottom.

GEMC and PRISM are capable of accurately and precisely determining the properties of transit lightcurves.

After testing GEMC on the simulated transits the next step was to use GEMC and PRISM to model real transit data. This was originally done on the spot-free WASP-19 transit data (Chapter 3) and then on the WASP-19 transit data containing starspot anomalies. Figure 2.22 shows an example of a best-fitting PRISM model to a set of WASP-19 data (see Section 3.4).

When GEMC was used in conjunction with PRISM to find the best-fitting solution to the WASP-19 data set, the computational time reduced dramatically, from five days to 14 hours using a large parameter range (see Section 3.3). When the parameter range

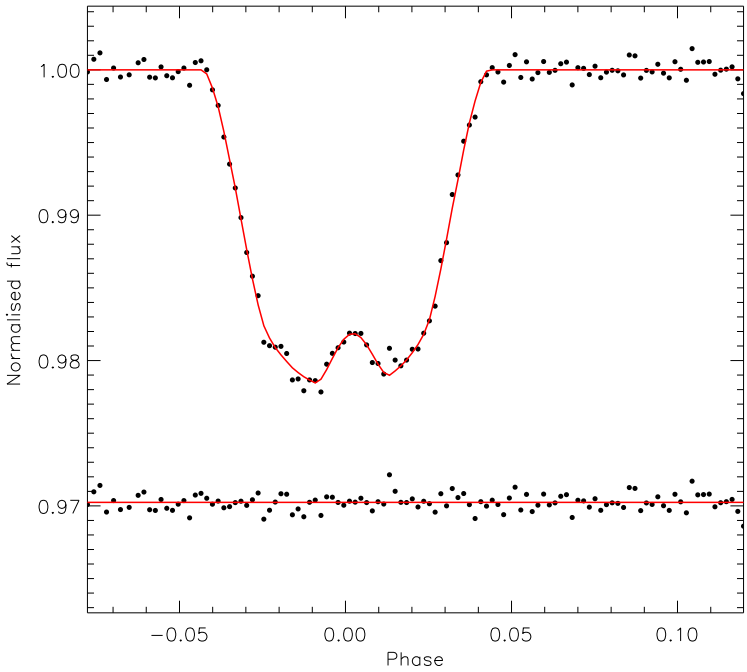

Figure 2.22: Best-fitting model and transit data for WASP-19. The residuals are shown at the bottom. The model (PRISM) was optimised by using GEMC. The data and model was later used by Mancini et al. (2013c).

was set to the same as used by the GA or the MCMC, GEMC was able to produce the best-fitting solution and similar uncertainties in the fitted parameters as the MCMC within 10 hours.

In Section 2.8.2.4 it was mentioned that the error bars in the WASP-19 data were scaled to allow the best fit to the data to have $\chi^2_\nu = 1$. This was done as it was assumed that both the MCMC and the GA algorithms had found the best fits to the three data sets. Upon running GEMC on the first WASP-19 data set, χ^2_ν was found to be 0.478 for the best-fitting model. This meant that GEMC was able to find a new solution for which both MCMC and the GA could not find. Similar χ^2_ν values were also found for the other WASP-19 data sets indicating the power of GEMC's ability to converge on the optimal solution.

It is possible to measure the success of GEMC from these tests and applications.

Apart from being able to find the global maximum peak in the PIKAIA test function 10 times quicker than PIKAIA, GEMC is also able to find the global solution to transit data 12 times faster than using a GA. Coupled with the fact that GEMC was able to find a new solution with twice the fitness of the best-fitting solution found by the GA or MCMC, this shows just how well suited GEMC is at finding the global solution in a large parameter space filled with many local solutions fast and efficiently.

3 The WASP-19 Planetary System

This Chapter describes the WASP-19 planetary system and the collection and analysis of three transit lightcurves. Section 3.1 begins with an overview of WASP-19 from the discovery of WASP-19 b to recent observations of the planet's transmission spectrum. Section 3.2 describes the data collection and reduction for three transits of WASP-19 using the ESO NTT. Then, in Section 3.3, the data analysis is presented along with both the photometric and the physical results. The photometric results of the starspots are also given together with the latitudinal rotation period of WASP-19 and the system's sky-projected spin orbit alignment (λ) value. Section 3.4 explains my work on a set of multiband photometry collected from the 2.2 m ESO-MPG telescope using the GROND instrument. These data contained a starspot anomaly and my analysis has since been published in Mancini et al. (2013c). Section 3.5 then ends the chapter with a brief discussion and conclusions. Sections 3.2 and 3.3 were published as first author in Monthly Notices of the Royal Astronomical Society and as a poster at the 2012 IAU general Assembly (see Appendix A.1 for publication details). While Section 3.4 was published as co-author in Monthly Notices of the Royal Astronomical Society (see Appendix A.2 for publication details).

3.1 Overview of the WASP-19 Planetary System

The WASP-19 b planet was discovered by Hebb et al. (2010) using photometry from the WASP-South telescope (see Figure 3.1). Subsequent photometric followup observations (Hebb et al., 2010) were done using the 2 m Faulkes Telescope South (FTS) and RV followup observations using the CORALIE spectrograph (Baranne et al., 1996; Queloz et al., 2000) on the 1.2 m Euler telescope. At the time of discovery WASP-19 b had the shortest orbital period known, 0.78883999 days or 19 hours (Hebb et al., 2010). Through the analysis of the data they determined the mass and radius of WASP-19 b to be $1.15 \pm 0.08\,\mathrm{M_{Jup}}$ and $1.31 \pm 0.06\,\mathrm{R_{Jup}}$, respectively. From the spectroscopic analysis

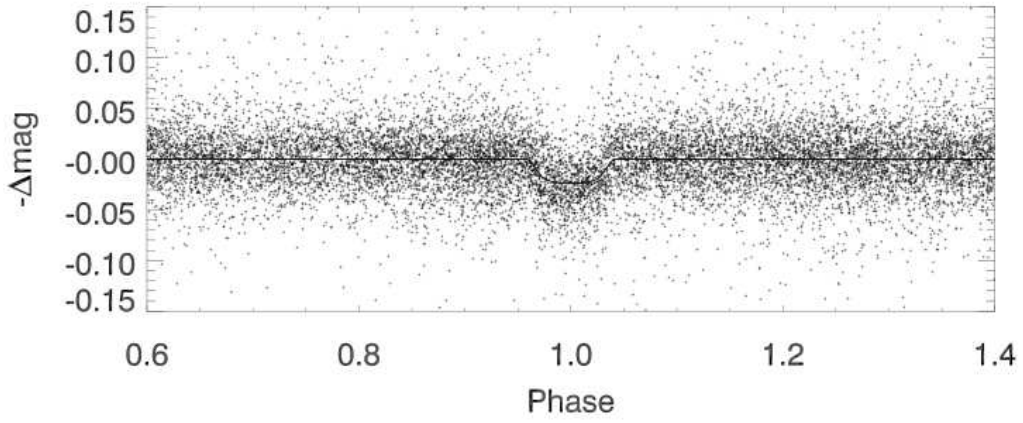

Figure 3.1: WASP-South discovery photometry of WASP-19 b (Hebb et al., 2010). The data are phase folded using $T_0 = 54775.3372$ and a period of $P = 0.78883999$ days.

they determined that the host star has a slightly super-solar metallicity of [M/H] = 0.1 ± 0.1 dex and is a G-type dwarf with an effective temperature of 5500 ± 100 K.

Hebb et al. (2010) also searched for variability in the WASP-South data due to starspots rotating on and off the stellar disc. This variability can allow a determination of the stellar rotation period. They found a sinusoidal signal in the data corresponding to a rotation period of $P_{rot} = 10.5 \pm 0.2$ days (see Figure 3.2). They removed the transit from the WASP-South lightcurve data and phase folded the data at multiple periods. Figure 3.3 shows the periodogram of normalised $\Delta\chi^2$ and indicates a strong signal at $P_{rot} = 10.5$ days with a False Alarm Probability (FAP) of 10^{-7}.

When a planet is occulted by its host star it is possible to measure the planet's brightness temperature (e.g. Charbonneau et al., 2005; Deming et al., 2005). Anderson et al. (2010a) measured a H-band occultation of WASP-19 b using the HAWK-I on the VLT (see Figure 3.4). They found WASP-19 b to have a H-band brightness temperature of $T_H = 2580 \pm 125$ K. The analysis also indicated that WASP-19 b followed a non-circular orbit at the 2.6-σ confidence level.

Gibson et al. (2010) also performed occultation photometry on WASP-19 using the HAWK-I instrument on the VLT. They measured a K-band brightness temperature

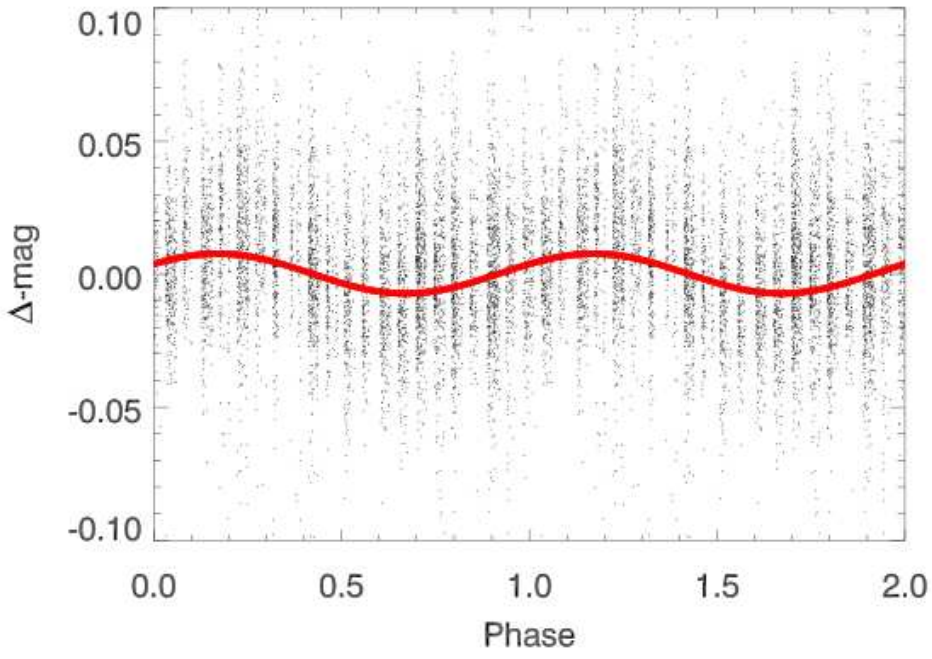

Figure 3.2: WASP-South lightcurve data from 2007 of WASP-19 (Hebb et al., 2010). The data are phase folded on the rotation period detected in the sine fitting (red sine wave) $P_{rot} = 10.5$ days.

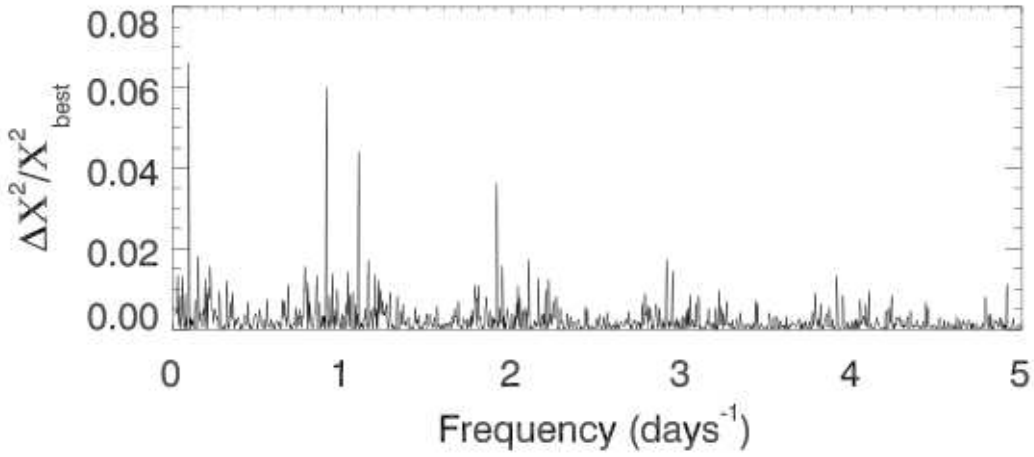

Figure 3.3: Periodogram of $\Delta\chi^2/\chi^2_{best}$ versus frequency, resulting from fitting a sine wave to the WASP-South lightcurve data from 2007 for WASP-19 (Hebb et al., 2010). The highest peak has a FAP of 10^{-7} and occurs at $P_{rot} = 10.5$ days. This indicates the stellar rotation period for WASP-19.

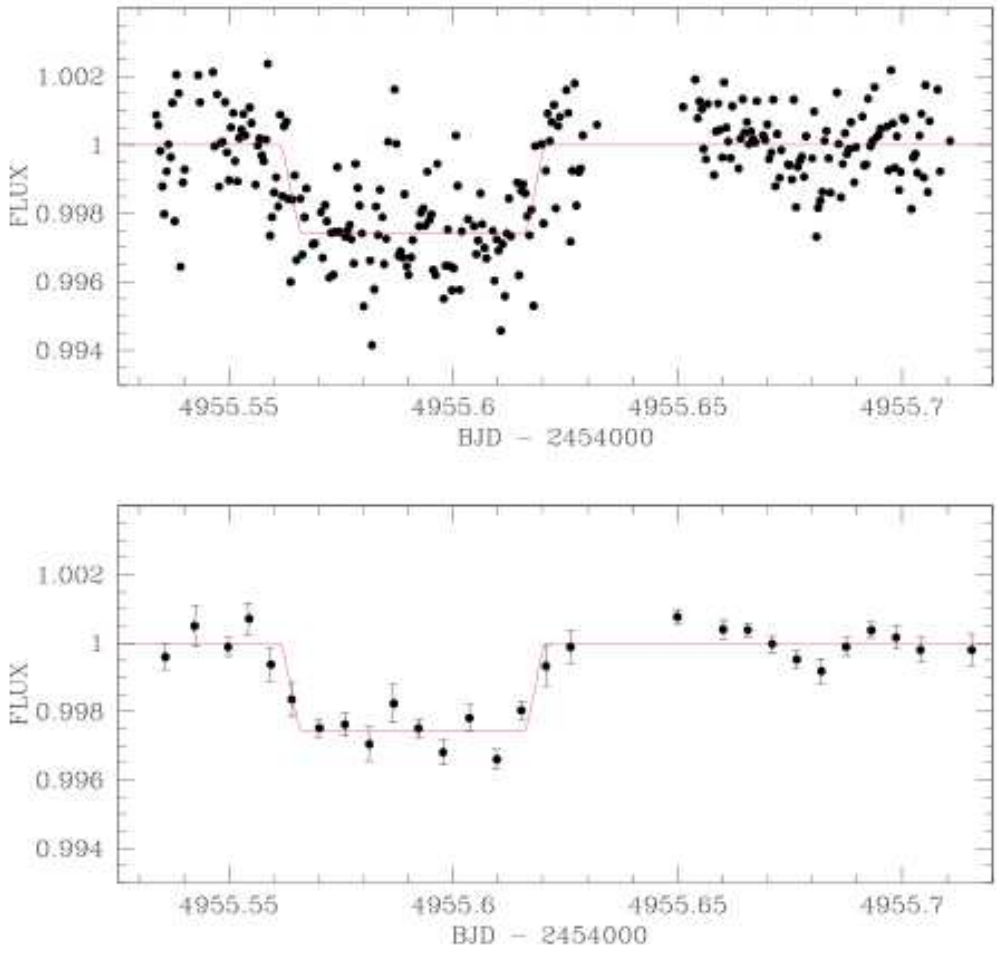

Figure 3.4: H-band occultation of WASP-19 b (Anderson et al., 2010a). This data was collected using HAWK-I on the VLT. The top panel shows the data and the best fit model, while the bottom panel shows the data binned every ten data points.

of $T_K = 2540 \pm 180$ K, and showed that this temperature is higher than the calculated equilibrium temperature that could indicate the planet's inability to redistribute heat to the night side, consistent with irradiated planet models. Gibson et al. (2010) measured the central transit time and, coupled with the ephemeris from Hebb et al. (2010), concluded that the planet's orbit is circular.

Hellier et al. (2011) performed Rossiter-McLaughlin measurements on spectro-

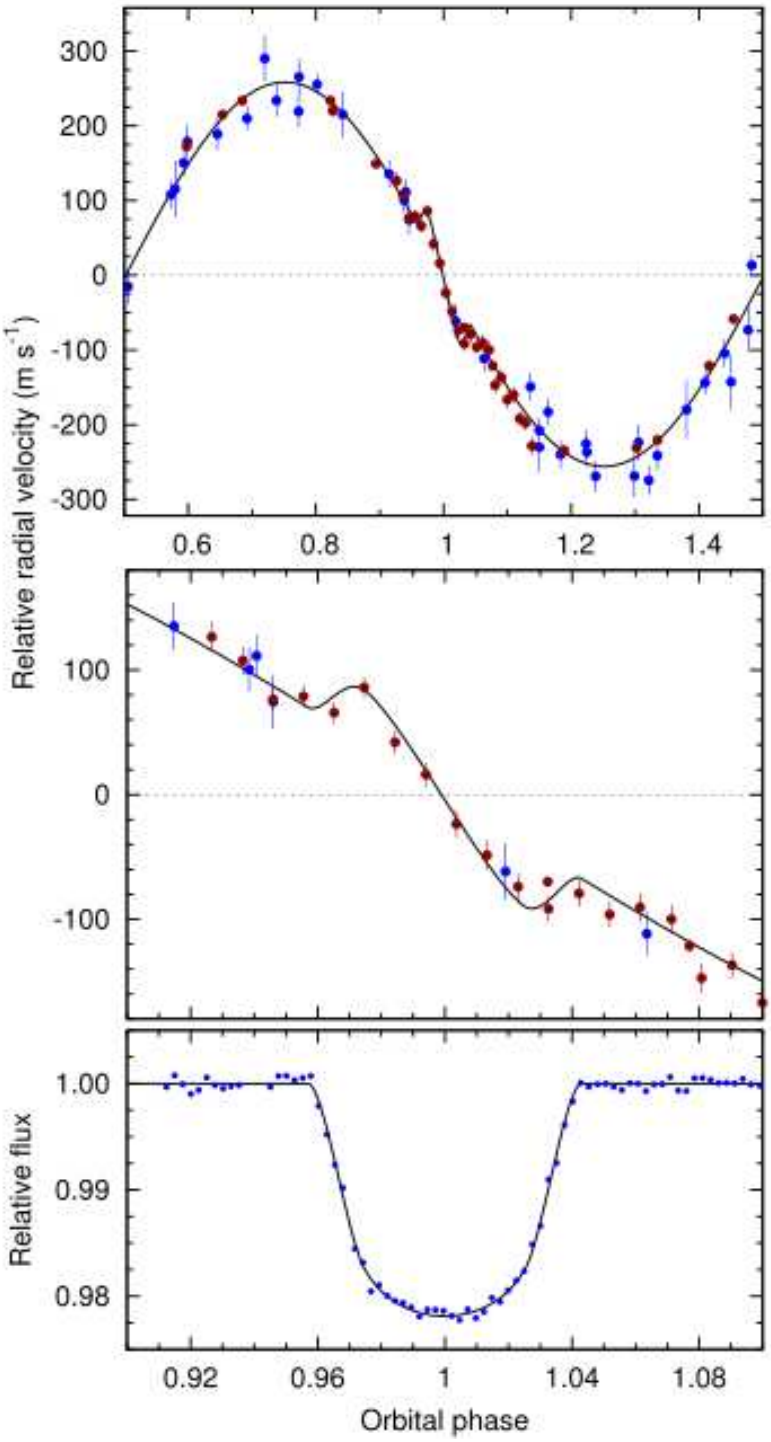

Figure 3.5: RV and RM measurements of WASP-19 b (Hellier et al., 2011). The top panel shows RV data and the best-fitting model. The middle panel shows the RV data and the best-fitting model for the transit region. The bottom panel shows transit data and the best-fitting model.

scopic data collected during a transit of WASP-19 b using the HARPS spectrograph on the ESO 3.6 m telescope and the CORALIE spectrograph on the 1.2 m Euler telescope (see Figure 3.5). They deduced that the orbit is aligned, with the sky-projected spin orbit alignment being $\lambda = 4.6 \pm 5.2°$. Coupled with a measurement of $v \sin I$ and the stellar rotation period from Hebb et al. (2010) they conclude that the true spin orbit alignment is $\psi < 20°$. To help improve the RM measurements they included a transit of WASP-19 in their analysis (see Figure 3.5). This transit was observed with the ESO NTT and the transit data are also used in the analysis of this Chapter (see Section 3.2). Albrecht et al. (2012) also performed RM measurements of WASP-19 and found $\lambda = 15 \pm 11°$ coupled with $v \sin I = 4.4 \pm 0.9\,\mathrm{km\,s^{-1}}$. They attributed the high uncertainty in λ to the low SNR in the data.

Anderson et al. (2013) used the Spitzer satellite to detect the thermal emission of WASP-19 b by observing two occultations of WASP-19 b by its host star. The emission was observed in the 3.6, 4.5, 5.8 and 8.0 μm passbands. They then constructed a spectral energy distribution of the planet's dayside atmosphere. They concluded that the atmosphere of WASP-19 b lacks a strong temperature inversion. They also measured the CaII H + K emissions lines and determined that the WASP-19 star is magnetically active. This would help explain the difficulty in obtaining a high SNR for the RM observation from Albrecht et al. (2012). This also improves the likelihood of detecting starspot anomalies in transit lightcurves of WASP-19.

An occultation of WASP-19 b by its host star has also been observed in the z-band (Burton et al., 2012). The ULTRACAM instrument on the ESO NTT was used to obtain the occultation data. They measured an occultation depth of $0.088 \pm 0.019\,\%$ and found the centre of the occultation occurred at $T_{occ} = 2455578.7676\,\mathrm{HJD}$. Burton et al. (2012) used the measurement of T_{occ} to determine that WASP-19 b follows a circular orbit.

Doyle et al. (2013) performed a detailed spectral analysis of 11 WASP planet host stars. They used high SNR spectra from the HARPS spectrograph. They determined the mass and radius of WASP-19 to be $1.01 \pm 0.08\,\mathrm{M_\odot}$ and $1.07 \pm 0.19\,\mathrm{R_\odot}$, respectively. They also found a sky-projected rotational velocity of $v \sin I = 5.1 \pm 0.3\,\mathrm{km\,s^{-1}}$ which

is in agreement with previous measurements (e.g. Hellier et al., 2011; Albrecht et al., 2012).

Since the completion of the analysis of the WASP-19 transit data (see Section 3.3) there have been further publications on the WASP-19 planetary system. This also includes transit data from multiband transit photometry containing a starspot anomaly (see Section 3.4).

Lendl et al. (2013) obtained 14 transit lightcurves of WASP-19 observed in the r'-Gunn, I-Cousins and z'-Gunn filters (Figure 3.6), coupled with 10 occultations in the z'-Gunn filter. They were able to refine the planet's mass and radius to $1.165 \pm 0.068\,\mathrm{M_{Jup}}$ and $1.376 \pm 0.046\,\mathrm{R_{Jup}}$, respectively. They also determined a value for the eccentricity of the orbit with $e = 0.0077^{+0.0068}_{-0.0032}$ which is compatible with a circular orbit.

Abe et al. (2013) used the ASTEP (Antarctica Search for Transiting ExoPlanets) 400 telescope in Antarctica to observe both transits and occultations of WASP-19 for 24 nights. They determined the stellar rotation period of the star from rotational modulation to be $P_{rot} = 10.7 \pm 0.5$ days, which agrees with the measurement from (Hebb et al., 2010). From the occultation data they found a K-band brightness temperature of $T_K = 2690^{+150}_{-220}\,\mathrm{K}$ agreeing with previous brightness temperature observations. They concluded that the brightness temperature is indicative of either that WASP-19 b has little thermal redistribution to the night side or that the planet is directly reflecting the starlight.

WASP-19 has also been observed using the Hubble Space Telescope (HST) (Huitson et al., 2013). They measured the transmission spectrum of WASP-19 b using low resolution spectroscopy with the Space Telescope Imaging Spectrograph (STIS). Huitson et al. (2013) combined their data with transits in the near-IR archival data from the HST Wide Field Camera 3 (WFC3). Due to WASP-19 being active they corrected the lightcurves for starspots by using ground-based activity monitoring. They compared their results to transmission spectrum models from Burrows et al. (2010), Howe & Burrows (2012) and Fortney et al. (2008, 2010). Their results showed a lack of TiO in the atmosphere of WASP-19 b but they found strong H_2O absorption features in the WFC3 transmission spectrum (see Figure 3.7).

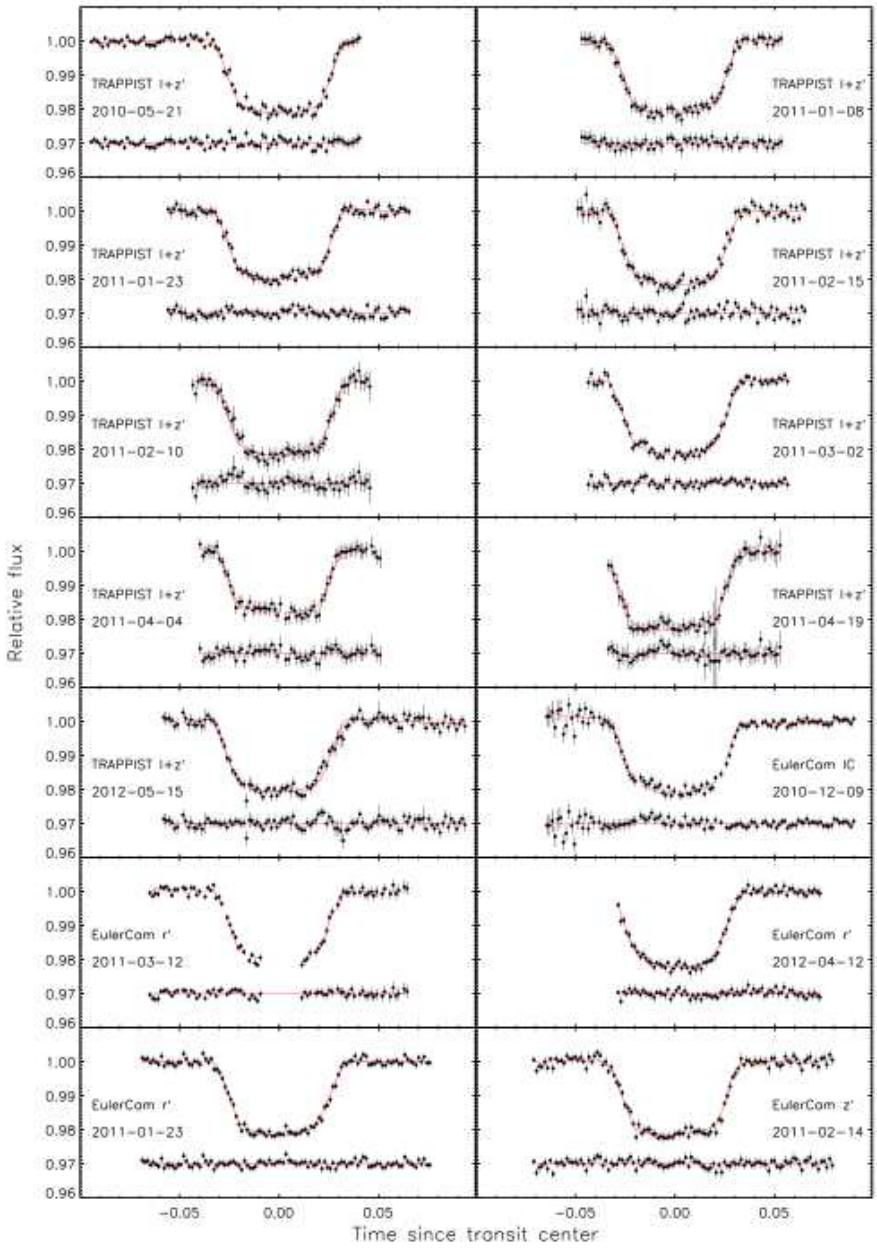

Figure 3.6: 14 transits of WASP-19 b together with their models and residuals (Lendl et al., 2013). The data are binned into two minute intervals and the instrument and filter used to observe the transit is displayed.

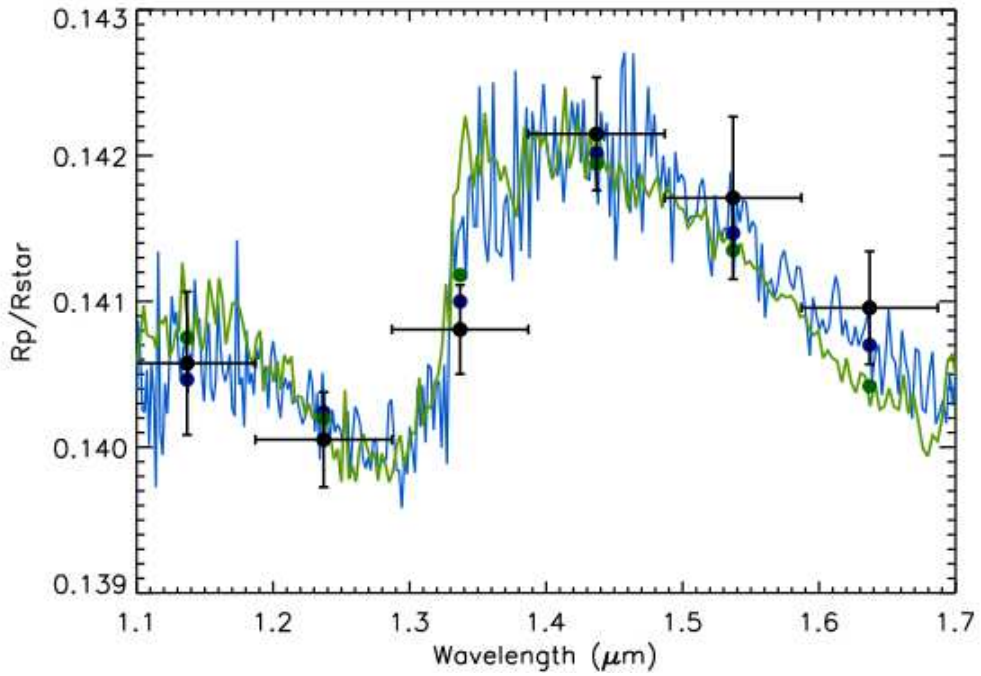

Figure 3.7: Transmission spectrum of WASP-19 b between 1.1 and 1.7μm (Huitson et al., 2013). WFC3 data (black data points) combined with two models (green Burrows et al., 2010; Howe & Burrows, 2012) and (blue Fortney et al., 2008, 2010) for water opacities but no TiO opacities.

3.1.1 WASP-19 and Starspots

After observing three light curves of WASP-19 with the aim of obtaining accurate physical properties, it was discovered that two of the datasets contained a starspot anomaly. With a precisely known position of the starspot at two close but distinct times it was possible to calculate the obliquity of the system and compare this to the values found from measurement of the Rossiter-McLaughlin effect (Hellier et al., 2011; Albrecht et al., 2012) and check if WASP-19 follows the theory put forward by Winn et al. (2010a) that 'cool' systems will have low obliquities (see also Triaud 2011a). This would also allow the rotation period of the star to be measured and compared to the value found by photometric modulation (Hebb et al., 2010).

3.2 Observations and Data Reduction

Three transits of WASP-19 were observed in February 2010 by Dr Claus Tappert using the 3.6 m New Technology Telescope (NTT) operated at ESO La Silla, Chile. The instrument used was EFOSC2, operated in imaging mode and with a Gunn r filter (ESO filter #786). In this setup the CCD covered a field of view of $(4.1')^2$ with a pixel scale of $0.12''\,\mathrm{pixel}^{-1}$. No binning or windowing was used, resulting in a dead time between consecutive images of 83 s. The exposure times were 60–90 s. The Moon was bright and relatively close to the target star. The amount of defocus applied caused the resulting PSFs to have a diameter of 78 pixels for the night of 2010/02/24, 88 pixels for the night of 2010/02/25 and 80 pixels for the night of 2010/02/28. The pointing of the telescope was adjusted to allow five good comparison stars to be observed simultaneously with WASP-19 itself (see Figure 2.1). The telescope autoguiding was maintained through all observations. An observing log is given in Table 3.1.

Table 3.1: Log of the observations presented for WASP-19. N_{obs} is the number of observations.

Date	2010/02/24	2010/02/25	2010/02/28
Start time (UT)	06:18	00:44	04:01
End time (UT)	09:34	04:26	07:41
N_{obs}	68	76	74
Exposure time (s)	90	60–90	90
Filter	Gunn r	Gunn r	Gunn r
Airmass	$1.14 \rightarrow 2.30$	$1.40 \rightarrow 1.04$	$1.04 \rightarrow 1.42$
Fractional Moon illumination	0.742	0.818	0.996
Moon distance (°)	85.5	78.1	53.0
Aperture sizes (pixel)	42, 60, 100	52, 70, 90	44, 64, 88
Scatter (mmag)	0.573	0.464	0.499

These observations were experimental for two reasons. First, the NTT is an alt-az telescope fitted with an image derotator. This means that the path of light from each star through the telescope is continually changing, raising the possibility of correlated

noise due to any optical imperfections. Second, the NTT is fitted with an actively controlled thin primary mirror designed to provide the best possible focus for normal observing strategies. Defocussing such a telescope might lead to a point spread function (PSF) which is variable in time, and thus correlated noise via flat-fielding errors.

In practise it was found that, whilst careful attention had to be paid to the amount of defocussing, the NTT is perfectly capable of producing high-quality light curves whilst a long way out of focus due to stable symmetric PSFs. The observations that used this approach are not plagued by correlated noise. This situation is similar to that of Winn et al. (2009), who successfully observed WASP-4 using the Magellan Baade telescope. By contrast, Gillon et al. (2009b) encountered serious problems in obtaining photometry of WASP-4 and WASP-5 with the ESO Very Large Telescope. This problem was attributed to the need to turn off the active optics system in order to achieve strong defocussing, and our results support the contention that this is not a general problem with alt-az telescopes or active-optics systems.

The data were reduced using the data reduction pipeline discussed in Section 2.5.1 and in an identical fashion to Southworth et al. (2009a,b,c, 2010). In short, aperture photometry using an IDL implementation of DAOPHOT (Stetson, 1987) was used and the aperture sizes were adjusted to obtain the best results (see Table 3.1). A first order polynomial was then fitted to the outside-transit data whilst simultaneously optimising the weights of the comparison stars. The resulting data have scatters ranging from 0.464 to 0.573 mmag per point versus a transit fit using PRISM. The timescale from the fits files was converted to HJD/UTC.

3.3 Data Analysis

The data were modelled using PRISM and GEMC. To do this a large parameter search space was selected to allow the global best fit solution to be found. As discussed in Section 2.8.3.4, the ability of GEMC to find the global minimum in a short amount of computing time meant that it was possible to search a large area of the parameter

space to avoid the possibility of missing the best solution. The parameter search range used in analysing the WASP-19 datasets are given in Tables 3.2, 3.3 and 3.4.

Table 3.2: Derived photometric parameters from the lightcurve taken on 2010/02/24, plus the interval within which the best fit was searched for using GEMC.

Parameter	Symbol	Search interval	2010/02/24
Radius ratio	r_p/r_s	0.05 to 0.30	0.1435 ± 0.0014
Sum of fractional radii	$r_s + r_p$	0.10 to 0.50	0.3298 ± 0.0041
Linear LD coefficient	u_1	0.0 to 1.0	0.314 ± 0.095
Quadratic LD coefficient	u_2	0.0 to 1.0	0.192 ± 0.023
Inclination (degrees)	i	70.0 to 90.0	78.97 ± 0.39
Transit epoch (HJD/UTC)	T_0	±0.5 in phase	2455251.79628 ± 0.00014
Longitude of spot (degrees)	θ	-90 to +90	-9.54 ± 0.15
Co-latitude of spot (degrees)	ϕ	0.0 to 90.0	64.93 ± 0.32
Spot angular radius (degrees)	$r_{\rm spot}$	0.0 to 30.0	15.01 ± 0.21
Spot contrast	$\rho_{\rm spot}$	0.0 to 1.0	0.777 ± 0.011

Table 3.3: Derived photometric parameters from the lightcurve taken on 2010/02/25, plus the interval within which the best fit was searched for using GEMC.

Parameter	Symbol	Search interval	2010/02/25
Radius ratio	r_p/r_s	0.05 to 0.30	0.1417 ± 0.0013
Sum of fractional radii	$r_s + r_p$	0.10 to 0.50	0.3300 ± 0.0025
Linear LD coefficient	u_1	0.0 to 1.0	0.501 ± 0.083
Quadratic LD coefficient	u_2	0.0 to 1.0	0.222 ± 0.019
Inclination (degrees)	i	70.0 to 90.0	78.92 ± 0.37
Transit epoch (HJD/UTC)	T_0	±0.5 in phase	2455252.58506 ± 0.00010
Longitude of spot (degrees)	θ	-90 to +90	14.98 ± 0.13
Co-latitude of spot (degrees)	ϕ	0.0 to 90.0	65.37 ± 0.21
Spot angular radius (degrees)	$r_{\rm spot}$	0.0 to 30.0	15.18 ± 0.15
Spot contrast	$\rho_{\rm spot}$	0.0 to 1.0	0.760 ± 0.017

First, the three datasets of WASP-19 were modelled separately using PRISM, finding that the modelled parameters were within 1-σ of each other (Table 3.2, 3.3 and 3.4). The three datasets were then modelled simultaneously. The ensuing parameters agreed with the individual results found previously, but it was not possible to get as good a fit to the data. The reason for this seems to be the LD coefficients, which are in comparatively poor agreement when the three light curves are fitted individually. The scatter

Table 3.4: Derived photometric parameters from the lightcurve taken on 2010/02/28, plus the interval within which the best fit was searched for using GEMC.

Parameter	Symbol	Search interval	2010/02/28
Radius ratio	r_p/r_s	0.05 to 0.30	0.1430 ± 0.0008
Sum of fractional radii	$r_s + r_p$	0.10 to 0.50	0.3311 ± 0.0044
Linear LD coefficient	u_1	0.0 to 1.0	0.438 ± 0.077
Quadratic LD coefficient	u_2	0.0 to 1.0	0.226 ± 0.009
Inclination (degrees)	i	70.0 to 90.0	78.91 ± 0.44
Transit epoch (HJD/UTC)	T_0	±0.5 in phase	2455255.74045 ± 0.00012

around the weighted mean is $\chi^2_\nu = 2.2$ for the linear coefficient and 1.9 for the quadratic coefficient. This situation could be caused by the influence of the starspot on the LD coefficients. Ballerini et al. (2012) found that starspots can affect LD coefficients by up to 30% in the ultraviolet, with a weaker effect expected at redder wavelengths. If we assume a 10% variation in the LD coefficients for the r-band data, the coefficients move into 1-σ agreement between the datasets.

3.3.1 Photometric Results

Since the combined fit to the three datasets had significantly larger residuals than the individual fits, the final results were based on the individual fits to the data. The final photometric parameters for the WASP-19 system are given in Table 3.5 and are weighted means plus 1-σ uncertainties of the results from the three individual fits. Figure 3.8 compares the light curves to the best-fitting models, including the residuals.

The results from modelling the spot anomalies on the nights of 2010/02/24 and 2010/02/25 confirm that they are due to the same spot rotating around the surface of the star, as the spot sizes and contrasts are in good agreement. Figure. 3.9 is a representation of the stellar disc, the spot and the transit chord for the two nights of observations.

From the positions of the starspot at the time of the transits on the nights of 2010/02/24 and 2010/02/25, it is possible to calculate the rotational period of the star and the sky-projected spin orbit alignment of the system using simple geometry. The

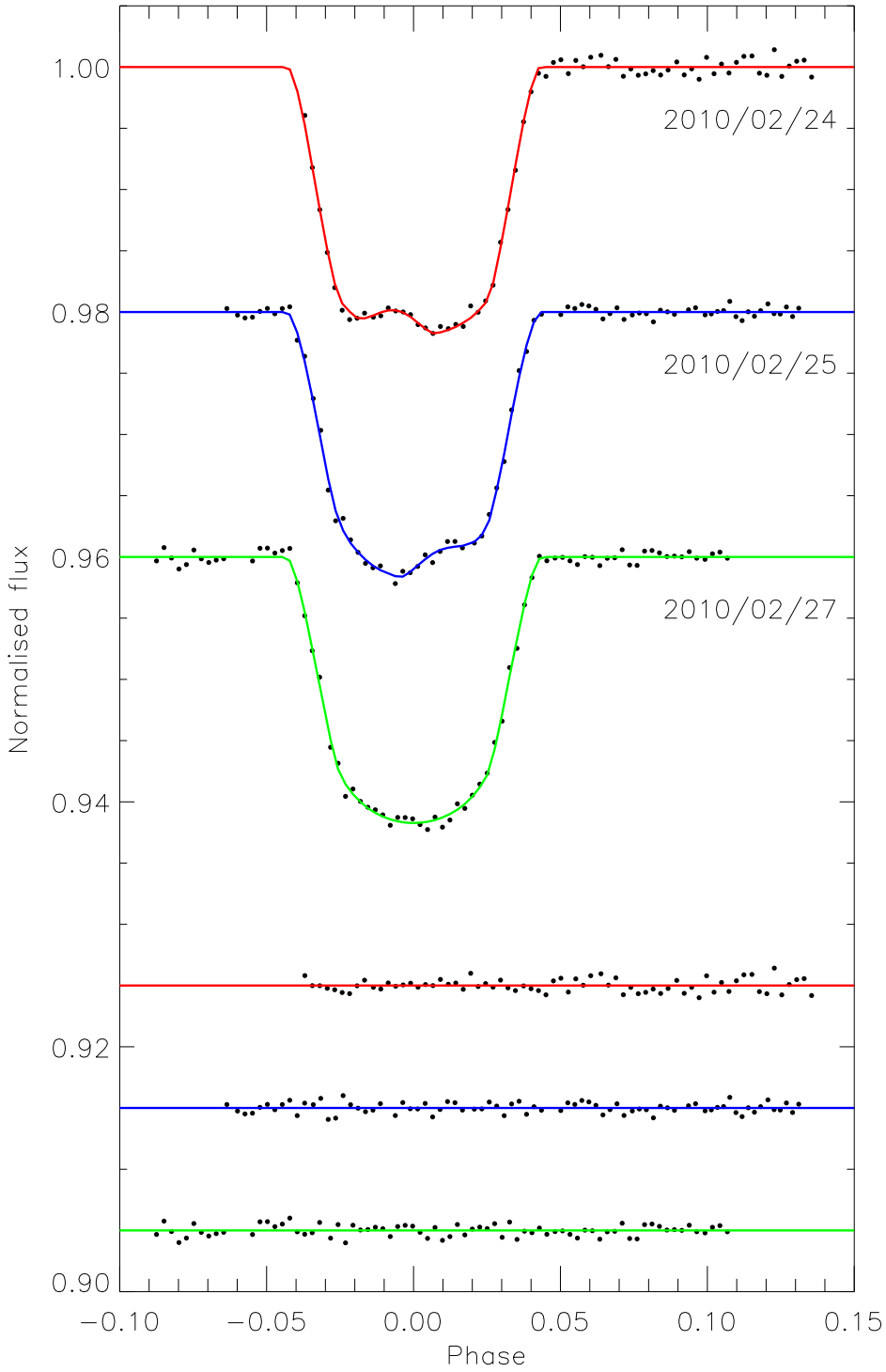

Figure 3.8: Transit light curves and the best-fitting models of WASP-19. The residuals are displayed at the base of the figure.

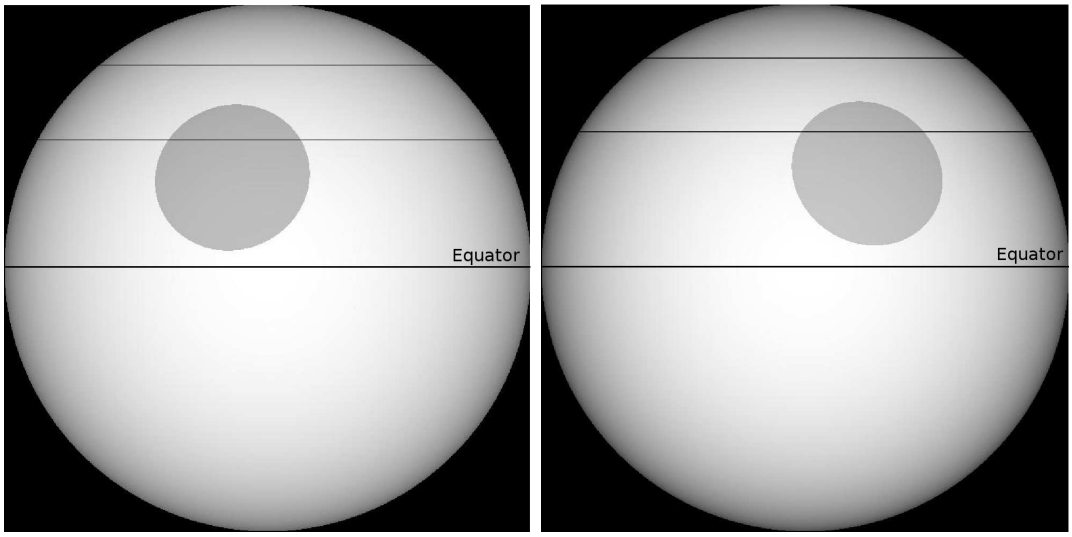

Figure 3.9: Representation of the stellar disc, starspot, transit chord and equator for the two datasets of WASP-19, containing spot anomalies. The axis of stellar rotation lies in the plane of the page and points upwards.

Table 3.5: Combined system and spot parameters for WASP-19. The system parameters are the weighted means from all three data sets. The spot angular size and contrast are the weighted mean from the two transits containing a starspot anomaly.

Parameter	Symbol	Value
Radius ratio	r_p/r_s	0.1428 ± 0.0006
Sum of fractional radii	$r_s + r_p$	0.3301 ± 0.0019
Linear LD coefficient	u_1	0.427 ± 0.049
Quadratic LD coefficient	u_2	0.222 ± 0.008
Inclination (degrees)	i	78.94 ± 0.23
Spot angular radius (degrees)	$r_{\rm spot}$	15.13 ± 0.12
Spot contrast	$\rho_{\rm spot}$	0.771 ± 0.010
Stellar rotation period (d)	$P_{\rm rot}$	11.76 ± 0.09
Projected spin orbit alignment (degrees)	λ	1.0 ± 1.2

Table 3.6: Times of minimum light of WASP-19 and their residuals versus the ephemeris derived in this work.

Time of minimum (HJD/TDB − 2400000)	Cycle no.	Residual (HJD)	Reference
54775.33757 ± 0.00020	0.0	0.00004	1
55168.96839 ± 0.00011	499.0	-0.00001	2
55183.16748 ± 0.00007	517.0	-0.00003	3
55251.79657 ± 0.00014	604.0	0.00003	4
55252.58544 ± 0.00010	605.0	0.00005	4
55255.74077 ± 0.00012	609.0	0.00003	4
55580.74238 ± 0.00058	1021.0	-0.00020	5

References: (1) Hebb et al. (2010); (2) Albrecht et al. (2012); (3) Anderson et al. (2013); (4) This work; (5) Dragomir et al. (2011).

spot has travelled $24.52° \pm 0.28°$ in 1.015 ± 0.001 orbital periods, giving a rotational period of $P_{\rm rot} = 11.76 \pm 0.09$ d at a co-latitude of 65°. Combining this with the stellar radius (see Table 3.7), the latitudinal rotational velocity of the star was calculated to be $v_{(65°)} = 3.88 \pm 0.15\,{\rm km\,s^{-1}}$. The positions of the spot finally yielded a sky-projected spin orbit alignment of $\lambda = 1.0° \pm 1.2°$ for WASP-19.

The available times of mid-transit for WASP-19 were collected from the literature (Hebb et al., 2010; Dragomir et al., 2011; Albrecht et al., 2012; Anderson et al., 2013). All timings were converted to the HJD/TDB timescale and used to obtain a new orbital ephemeris:

$$T_0 = {\rm HJD/TDB}\ 2\,454\,775.33754(18) + 0.78883942(33) \times E$$

where E represents the cycle count with respect to the reference epoch and the bracketed quantities represent the uncertainty in the final digit of the preceding number. Figure 3.10 and Table 3.6 show the residuals of these times against the ephemeris. Figure 3.10 shows no evidence for transit timing variations in the system.

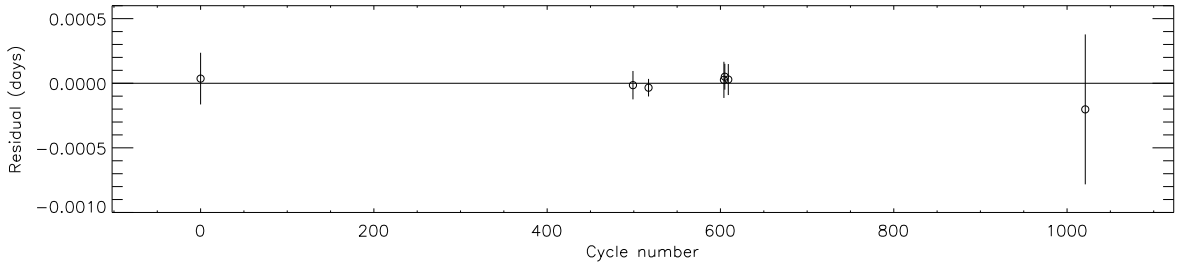

Figure 3.10: Residuals of the available times of mid-transit versus the orbital ephemeris found in this work. The three timings from this work are the cluster of three points around cycle number 600.

3.3.2 Physical Properties of the WASP-19 System

The work in this subsection was performed by Dr John Taylor and is included here because it is an integral part of the analysis of WASP-19.

With the photometric properties of WASP-19 measured the physical characteristics could be determined. The analysis followed the method of Southworth (2009), which uses the parameters measured from the light curves and spectra, plus tabulated predictions of theoretical models. The values of i, r_p/r_s and $r_s + r_p$ were adopted from Table 3.5 and coupled with the stellar properties of effective temperature $T_{\rm eff} = 5440 \pm 60\,{\rm K}$ (Maxted et al., 2011a), velocity amplitude $K_{\rm s} = 257 \pm 3\,{\rm m\,s^{-1}}$ (Hellier et al., 2011) and metal abundance [Fe/H] $= 0.02 \pm 0.09$ (Hellier et al., 2011).

An initial value of the velocity amplitude of the planet, $K_{\rm p}$, was used to calculate the physical properties of the system using standard formulae and the physical constants listed by Southworth (2011). The mass and [Fe/H] of the star were then used to obtain the expected $T_{\rm eff}$ and radius, by interpolation within a set of tabulated predictions from stellar theoretical models. $K_{\rm p}$ was iteratively refined until the best agreement was found between the observed and expected $T_{\rm eff}$, and the measured $r_{\rm s}$ and expected $\frac{R_{\rm s}}{a}$. This was performed for ages ranging from the zero-age to the terminal-age main-sequence, in steps of 0.01 Gyr. The overall best fit was found, yielding estimates of the system parameters and the evolutionary age of the star.

This procedure was performed separately using five different sets of stellar theoretical models (see Southworth, 2010), and the spread of values for each output parameter was used to assign a systematic error. Statistical errors were propagated using a perturbation algorithm.

Table 3.7: Physical properties of the WASP-19 system. Both statistical and systematic uncertainties are given. The first uncertainty is the statistical uncertainty and the second is the systematic uncertainty.

Parameter	Value
Stellar mass ($M_{\odot}$)	$0.904 \pm 0.040 \pm 0.021$
Stellar radius ($R_{\odot}$)	$1.004 \pm 0.016 \pm 0.008$
Stellar surface gravity (cgs)	$4.391 \pm 0.008 \pm 0.003$
Stellar density ($\rho_{\odot}$)	0.893 ± 0.015
Planet mass ($M_{\rm Jup}$)	$1.114 \pm 0.036 \pm 0.017$
Planet radius ($R_{\rm Jup}$)	$1.395 \pm 0.023 \pm 0.011$
Planet surface gravity ($\mathrm{m\,s^{-2}}$)	14.19 ± 0.26
Planet density ($\rho_{\rm Jup}$)	$0.384 \pm 0.011 \pm 0.003$
Equilibrium temperature	2067 ± 23
Safronov number	$0.02852 \pm 0.00057 \pm 0.00023$
Semimajor axis (AU)	$0.01616 \pm 0.00024 \pm 0.00013$
Age (Gyr)	$11.5\,^{+2.7\ +0.7}_{-2.3\ -1.5}$

The final results of this process are in reasonable agreement with themselves and with published results for WASP-19. The final physical properties are given in Table 3.7 and incorporate separate statistical and systematic errorbars for those parameters which depend on the theoretical models. The final statistical errorbar for each parameter is the largest of the individual ones from the solutions using each of the five different stellar models. The systematic errorbar is the largest difference between the mean and the individual values of the parameter from the five solutions. One point to note is that the inferred age of the star is rather large, particularly given its rotation period and activity level. The age is governed primarily by the input $T_{\rm eff}$ and [Fe/H], so a check of these spectroscopic parameters would be useful.

3.4 Multiband Defocused Photometry

WASP-19 was observed using the Gamma Ray burst Optical and Near-infrared Detector (GROND) instrument on the ESO-MPG 2.2 m telescope (Mancini et al., 2013c). From this a transit was observed simultaneously in four optical bands (similar to Sloan g', r', i' and z') and three near-infrared (J, H, K) passbands (Greiner et al., 2008). The optical transit data showed an anomaly typical in amplitude to that of a starspot (see Figure 3.11). The amplitude of the anomaly reduces with increasing wavelength, which would be expected for a dark spot with a cooler temperature compared to that of the surrounding photosphere. The spot anomaly was not visible in the NIR transits and as such the NIR transit data were modelled using JKTEBOP.

The optical transit data allows for a rare opportunity to view a starspot simultaneously in four different passbands. It was mentioned in Section 2.7.3 that there is a degeneracy between the size and contrast of a starspot in a transit lightcurve. Because a dark starspot will appear darker in the ultraviolet compared to the infrared, then

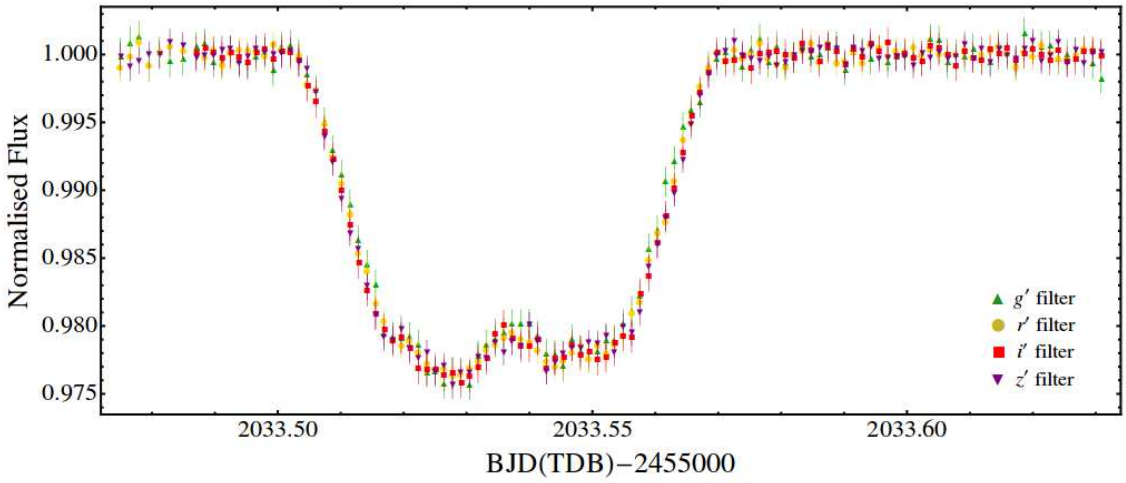

Figure 3.11: Superimposed optical light curves of WASP-19 obtained using GROND (Mancini et al., 2013c). The starspot anomaly can be seen approximately at the transit midpoint.

viewing a starspot in multiple wavelengths will allow the degeneracy to be broken by obtaining different contrast values at different wavelengths.

As a consequence it was tasked to PRISM and GEMC to model and fit the optical GROND data. PRISM was first modified to allow the optical data to be fitted simultaneously. This, though, did not produce good fits. Upon examining the individual lightcurves it was seen that the spot position in the different bands was not well constrained due to the noise in the data.

To model the starspot it was necessary to determine the common value for the spot position (θ and ϕ) from all four transits. The first step was to combine all four transits into a single transit. This was done by calculating the mean of each corresponding data point. The new lightcurve was then modelled and fitted and common values were determined: $\theta = 3.36° \pm 0.08°$ and $\phi = 59.98° \pm 0.80°$. The co-latitude coordinate of the spot is similar to that found from Section 3.3 which is expected due the transit cord being the same. Once this was completed the four lightcurves were then modelled individually but with the values of θ and ϕ fixed at the determined values. This then allowed the determination of the values r_{spot} and ρ_{spot} for each different passband.

3.4.1 Multiband Defocused Photometry Results

The four optical transits from GROND were modelled separately and the system parameters were then determined. The final results for each passband can be found in Table 3.8. The different transit depths from each of the four lightcurves were then used together with the NIR data to produce a broadband transmission spectrum (see Mancini et al., 2013c).

Once a common value for the position of the starspot had been found the individual GROND optical transits were then modelled and fitted using PRISM to find the size and contrast of the starspot (see Figure 3.12 and Table 3.9).

The final spot size is taken from the weighted mean of the results from each optical band, where $r_{spot} = 9.46° \pm 0.26°$. The size of the starspot in the GROND

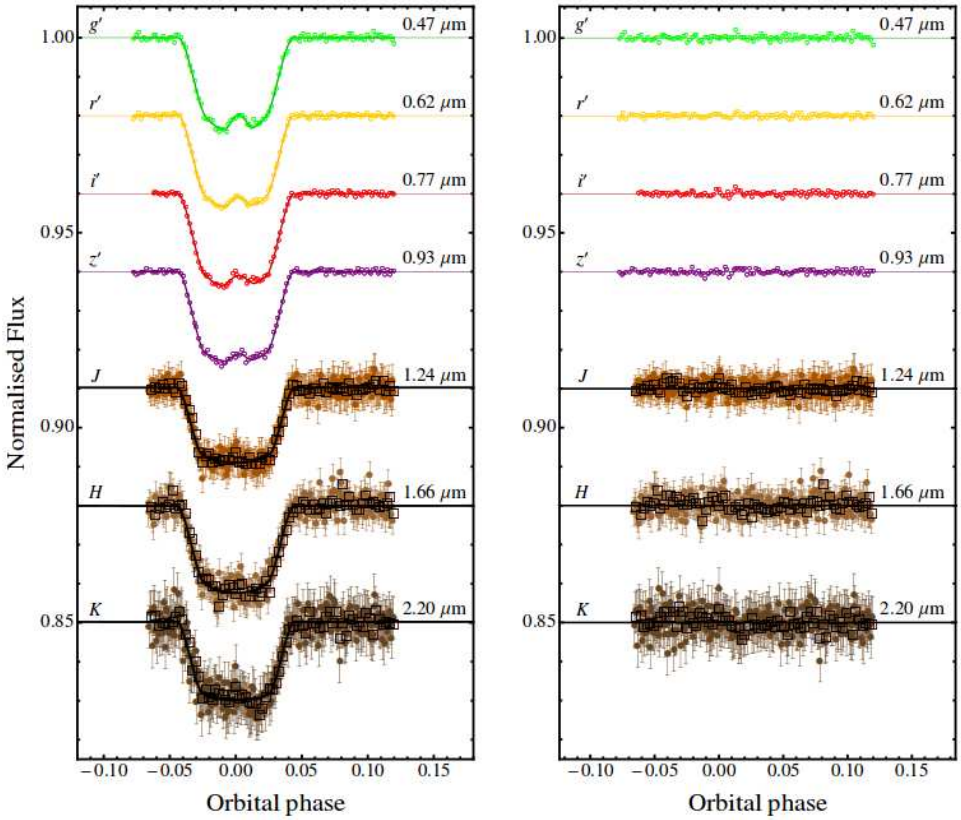

Figure 3.12: Simultaneous optical and NIR transits of WASP-19 observed using GROND (Mancini et al., 2013c). The left panel shows the transits and best-fitting models and the right panel shows the residuals. The four optical transits were modelled using PRISM and GEMC. The three NIR light curves were modelled using JKTEBOP. The passband and central wavelengths are given for each transit. The amplitude of the starspot anomaly can be seen to decrease when moving down through the transits.

Table 3.8: Parameters of the fits for WASP-19 from GROND using PRISM.

Filter	$r_s + r_p$	r_p/r_s	i
g'	0.33106 ± 0.00085	0.14206 ± 0.00038	78.39 ± 0.42
r'	0.33437 ± 0.00374	0.14372 ± 0.00056	78.37 ± 0.28
i'	0.32958 ± 0.00450	0.14386 ± 0.00080	78.98 ± 0.36
z'	0.32983 ± 0.00410	0.14207 ± 0.00058	78.95 ± 0.31

Table 3.9: Starspot parameters from the optical GROND lightcurves, fitted using PRISM. The common spot position is at $\theta = 3.36° \pm 0.08°$ and $\phi = 59.98° \pm 0.80°$.

Parameter	Symbol	g'	r'	i'	z'
Starspot angular radius (°)	r_{spot}	9.37 ± 0.45	9.65 ± 0.50	10.50 ± 0.67	8.60 ± 0.57
Starspot contrast	ρ_{spot}	0.347 ± 0.050	0.590 ± 0.037	0.638 ± 0.020	0.618 ± 0.040

data is approximately 60% of the size of the starspot in the NTT data. Because r_{spot} is the angular size of the starspot it is possible to combine R_* to find $R_{spot} = 116900 \pm 3220\,\mathrm{km}$, therefore the starspot covers only 2.7% of the stellar disc. This measurement is in agreement with other measurements of starspots from G-type stars and is also comparable to large Sunspots (Mancini et al., 2013c).

3.4.2 Starspot Temperature

With the contrast of the starspot known in four different wavelengths it is then possible to calculate the temperature of the starspot. This is done by modelling both the starspot and the photosphere as black bodies (Rabus et al., 2009; Sanchis-Ojeda & Winn, 2011). Silva (2003) gives an equation to find the temperature of a starspot T_{spot} using the starspots contrast ρ_{spot} and the effective temperature of the photosphere T_{eff},

$$\rho_{spot} = \frac{\exp\left(h\nu/K_B T_{eff}\right) - 1}{\exp\left(h\nu/K_B T_{spot}\right) - 1} \tag{3.1}$$

where h is Planck's constant, ν is the frequency of the observation and K_B is the Boltzmann constant. When calculating the temperature of the starspot a value of $T_{eff} = 5460 \pm 90\,\mathrm{K}$ was used (Doyle et al., 2013). It was found that the starspot's temperature in each of the passbands was: $T_{spot,g} = 4595 \pm 118\,\mathrm{K}$, $T_{spot,r} = 4864 \pm 96\,\mathrm{K}$, $T_{spot,i} = 4842 \pm 81\,\mathrm{K}$ and $T_{spot,z} = 4698 \pm 112\,\mathrm{K}$. The temperature of the starspot in the four different bands are in good agreement and were combined using a weighted mean to find the overall temperature, $T_{spot} = 4777 \pm 80\,\mathrm{K}$. This measurement of the temperature of the starspot seen in the GROND data of WASP-19 is consistent with measurements of starspot temperatures for other stars (see Figure 3.13). The temperature is also

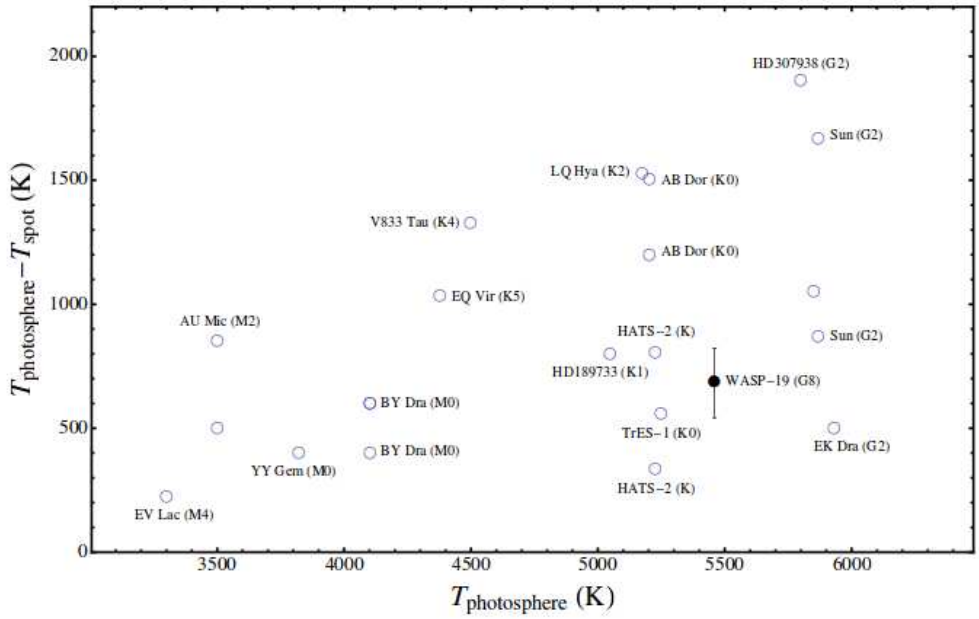

Figure 3.13: Starspot temperature contrast compared to effective temperature of the photosphere for several stars (Mancini et al., 2013c). The names and spectral class for the majority of the stars are given.

consistent with starspot temperature measurements taken for stars harbouring a TEP (e.g. TrES-1, Rabus et al. 2009; HD 189733, Sing et al. 2011; and HATS-2, Mohler-Fischer et al. 2013).

3.5 Discussion and Conclusions

The three transits of WASP-19 coupled with the GROND optical transits were the first real data tests of the modelling and optimisation codes PRISM and GEMC. The results show that both of these codes are capable of being used to model and fit real transit data containing a starspot anomaly.

PRISM and GEMC were applied to three transit light curves of the WASP-19 planetary system. Two of the light curves are of consecutive transits and show anomalies

due to the occultation of a starspot by the planet. The measured co-latitudes and longitudes of the spot during the two transits were used to calculate the rotation period of the star and the sky-projected obliquity of the system. The model assumes that the spot anomaly can be represented by a circular spot of uniform brightness. It is quite likely that the "spot" is in fact a group of smaller spots with higher contrasts (i.e. between the values found in the model and one), but investigation of this puts extreme demands on data quality and quantity which are practically impossible to satisfy for ground-based observations.

The rotation period of $P_{\rm rot} = 11.76 \pm 0.09\,{\rm d}$ at a co-latitude of 65° was found, whereas Hebb et al. (2010) found a $P_{\rm rot}$ of $10.5 \pm 0.2\,{\rm d}$ from rotational modulation of the star's brightness over several years. The latter value comes from the spot activity over the whole visible surface of the star, whereas the value from this work is for a specific co-latitude. The difference between these two numbers may therefore indicate differential rotation. Anderson et al. (2013) used the measured Ca H&K line activity index, $\log R'_{\rm HK}$, to infer $P_{\rm rot} = 12.3 \pm 1.5\,{\rm d}$ using the activity–rotation calibration by Mamajek & Hillenbrand (2008), which is in good agreement with the values measured in this Chapter and by Hebb et al. (2010).

A rotational velocity of $v_{(65^\circ)} = 3.88 \pm 0.15\,{\rm km\,s^{-1}}$ for WASP-19 was found, which in the absence of differential rotation would yield an equatorial rotation velocity of $v_{(90^\circ)} = 4.30 \pm 0.15\,{\rm km\,s^{-1}}$. Hellier et al. (2011) reported a spectroscopic measurement for $v \sin I$ of $5.0 \pm 0.3\,{\rm km\,s^{-1}}$ and assumed this value represented the equatorial velocity. They included it as a prior when modelling the Rossiter-McLaughlin effect, finding a final value of $v \sin I = 4.6 \pm 0.3\,{\rm km\,s^{-1}}$. This last measurement is appropriate for the co-latitude at which the planet transits, and may differ from this result due to the effect of starspots on radial velocity measurements taken during transit.

The results show a sky-projected obliquity of $\lambda = 1.0^\circ \pm 1.2^\circ$ for WASP-19, which is in agreement with, but more precise than, published values based on observations of the Rossiter-McLaughlin effect ($4.6^\circ \pm 5.2^\circ$, Hellier et al. 2011; $15^\circ \pm 11^\circ$, Albrecht et al. 2012). λ gives the lower boundary of the true spin-orbit angle, ψ. As stated in Section 1.4.1 and by Fabrycky & Winn (2009), finding a small value for λ can be

interpreted in different ways. The spot method could allow the determination of ψ, rather than just λ, given light curves of three or more transits all showing anomalies due to the same spot. unfortunately with only two light curves it is difficult to be sure that ψ lies close to λ. If the stellar rotation axis is pointed along the line-of-sight of the observer, then the path taken by the starspot would be circular. In this scenario the stellar rotation period would equate to only 5.5 days. This result greatly disagrees with previous measurements (Hebb et al., 2010; Anderson et al., 2013) and is an indication that ψ does in fact lie close to λ. Whilst it is not possible to determine the true value of ψ with the data in hand, there is no evidence for a spin-orbit misalignment in the WASP-19 system. With a low obliquity and a cool host star, WASP-19 follows the idea put forward by Winn et al. (2010a) that planetary systems with cool stars will have a low obliquity. It also lends weight to the idea that WASP-19 b formed at a much greater distance from host star and suffered orbital decay through tidal interactions with the protoplanetary disc (i.e. either Type I or Type II disc-migration, Ward 1997a).

The transit containing a starspot anomaly observed in four optical passbands with GROND allowed the temperature of the starspot to be determined with $T_{spot} = 4777 \pm 80$ K. The extra data also allowed a comparison of the spot properties for two different spots from the same star. The co-latitude position of the two starspots are in agreement along with the angular dimensions. This could be an indication of an active zone on WASP-19 at a co-latitude between 60° and 65°. The GROND data also shows that dark starspots appear darker at UV wavelengths, which is expected for a black body model due to the dark starspot being cooler than the surrounding photosphere. Both WASP-19 and the Sun are G type dwarf stars. As such finding a starspot on WASP-19 that is consistent in both size and temperature to that of a Sunspot is encouraging in that the data, the analysis and modelling of the transits containing the starspot anomaly has been performed correctly.

4 The WASP-6 Planetary System

This Chapter describes the WASP-6 planetary system and the collection and analysis of four transit lightcurves. Section 4.1 presents an overview of WASP-6 beginning with the discovery of WASP-6 b to recent observations of the planet's optical transmission spectrum. Section 4.2 describes the data collection and reduction for four transits of WASP-6 using the Danish 1.54 m telescope in La Silla. In Section 4.3 the data analysis is presented along with the photometric results and measured physical properties. The photometric results of the starspots are also given together with the latitudinal rotation period of WASP-6 and the system's sky-projected spin orbit alignment (λ) value. Section 4.4 then ends the chapter with a brief discussion and conclusions.

4.1 Overview of the WASP-6 Planetary System

The WASP-6 b planet was discovered by Gillon et al. (2009a) using photometry from the WASP-South telescope (see Figure 4.1).

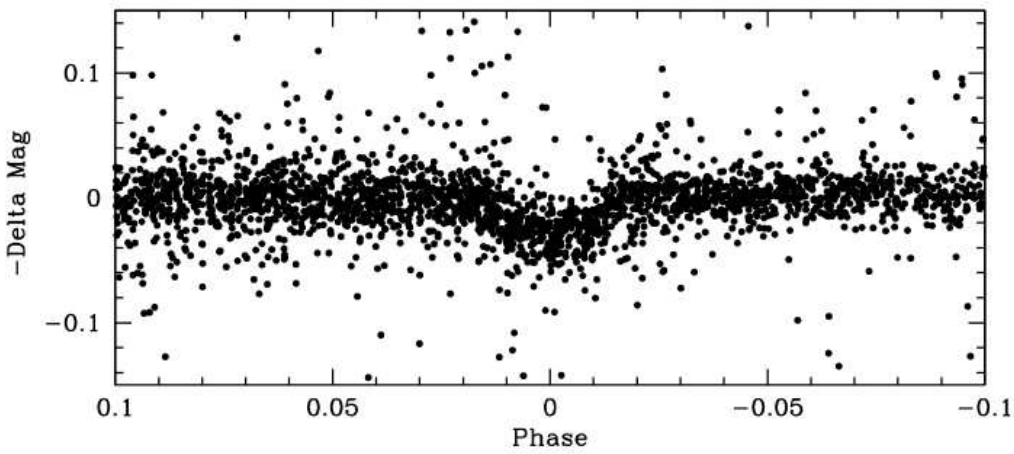

Figure 4.1: WASP-South discovery photometry of WASP-6 b (Gillon et al., 2009a). The data are phase folded using a period of $P = 3.361$ days.

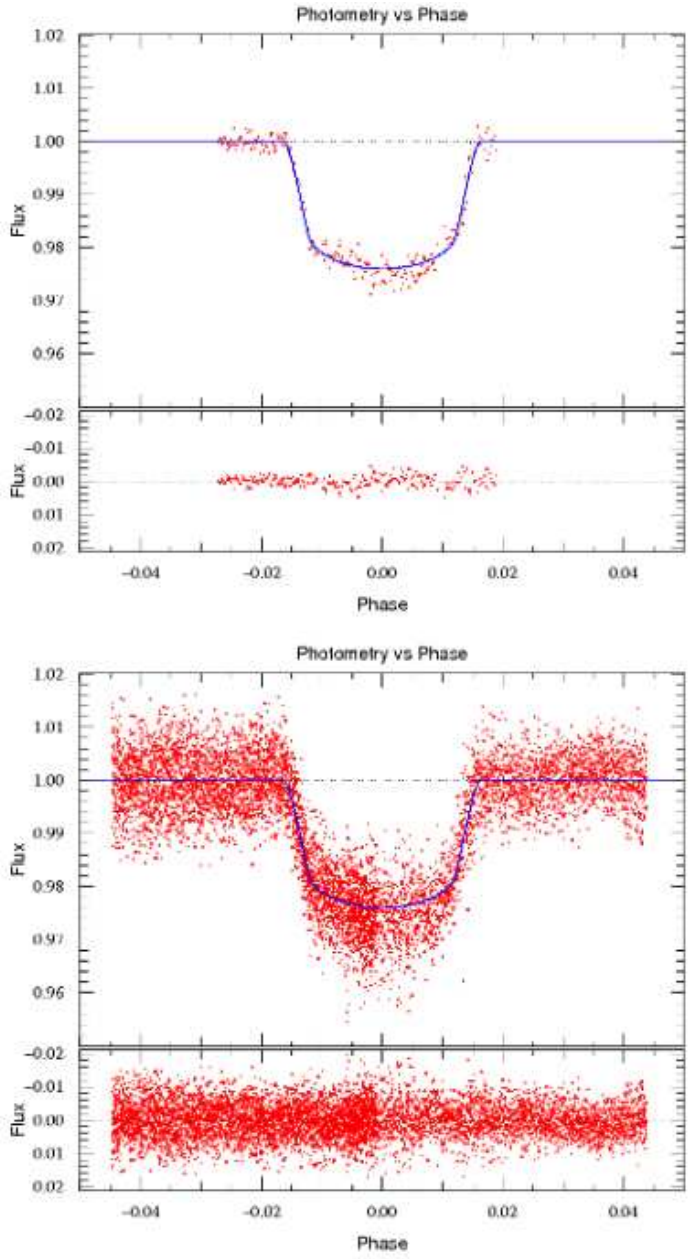

Figure 4.2: Transit photometry for WASP-6 using the FTS and the LT (Gillon et al., 2009a). The top panel shows the transit and best-fitting model coupled with the residuals from the FTS obtained in the i'-band. The bottom panel shows the transit and best-fitting model coupled with the residuals from the LT/RISE in the $V + R$ filter.

They determined an orbital period of $P = 3.361$ days for WASP-6 b. Followup photometric observations (see Figure 4.2) were then performed in the i'-band using the 2 m Faulkes Telescope South (FTS) and a second set of photometric observations performed in a broad band filter with a response approximately that of Cousins $V + R$ using RISE (Rapid Imaging Search for Exoplanets) (Steele et al., 2008) on the 2 m Liverpool Telescope (LT) in La Palma.

Followup RV observations were performed using the CORALIE spectrograph (Baranne et al., 1996; Queloz et al., 2000) on the 1.2 m Euler telescope. RV observations were also taken using the HARPS (High-Accuracy Radial velocity Planetary Searcher) spectrograph (Mayor et al., 2003) on the ESO 3.6 m telescope. Through the analysis of the data Gillon et al. (2009a) determined the stellar mass and radius to be $M_* = 0.88^{+0.05}_{-0.08}\,\mathrm{M}_\odot$ and $R_* = 0.870^{+0.025}_{-0.036}\,\mathrm{R}_\odot$, respectively. They found the planetary mass and radius to be $M_p = 0.503^{+0.019}_{-0.038}\,\mathrm{M_{Jup}}$ and $R_p = 1.224^{+0.051}_{-0.052}\,\mathrm{R_{Jup}}$.

Whilst Gillon et al. (2009a) did not look for variability in the WASP-South data due to starspots to determine a rotational period of WASP-6 they did determine a value for $v \sin I$ of $1.4 \pm 1.0\,\mathrm{km\,s^{-1}}$ from line width measurements in high resolution spectra with a macroturbulence (v_{mac}) value of $2\,\mathrm{km\,s^{-1}}$. They noted that if a value of $v_{mac} = 0\,\mathrm{km\,s^{-1}}$ is used then $v \sin I = 3.0 \pm 0.5\,\mathrm{km\,s^{-1}}$, while if v_{mac} became slightly larger than $2\,\mathrm{km\,s^{-1}}$ then $v \sin I$ would drop to zero. Macroturbulence represents the non-thermal gas velocities that occur in the region of where the spectral line is formed. But unlike microturbulence the cell size is larger than the unit optical depth (Howarth, 2004). Macroturbulence only causes the broadening of the spectral lines and not their strengths (Doyle et al., 2013).

From performing RV measurements of WASP-6 Gillon et al. (2009a) measured the Rossiter-McLaughlin (RM) effect (see Figure 4.3). They found that the system is in alignment with a sky-projected spin orbit alignment, $\lambda = 11^{\circ\,+14}_{\ -18}$.

The spectral analysis of 11 WASP host stars by Doyle et al. (2013) included WASP-6. Doyle et al. (2013) derived new values for the stellar mass and radius of $M_* = 0.87 \pm 0.06\,\mathrm{M}_\odot$ and $R_* = 0.77 \pm 0.07\,\mathrm{R}_\odot$, these new measurements of the stellar mass and radius are in agreement with that of Gillon et al. (2009a). Doyle et al. (2013)

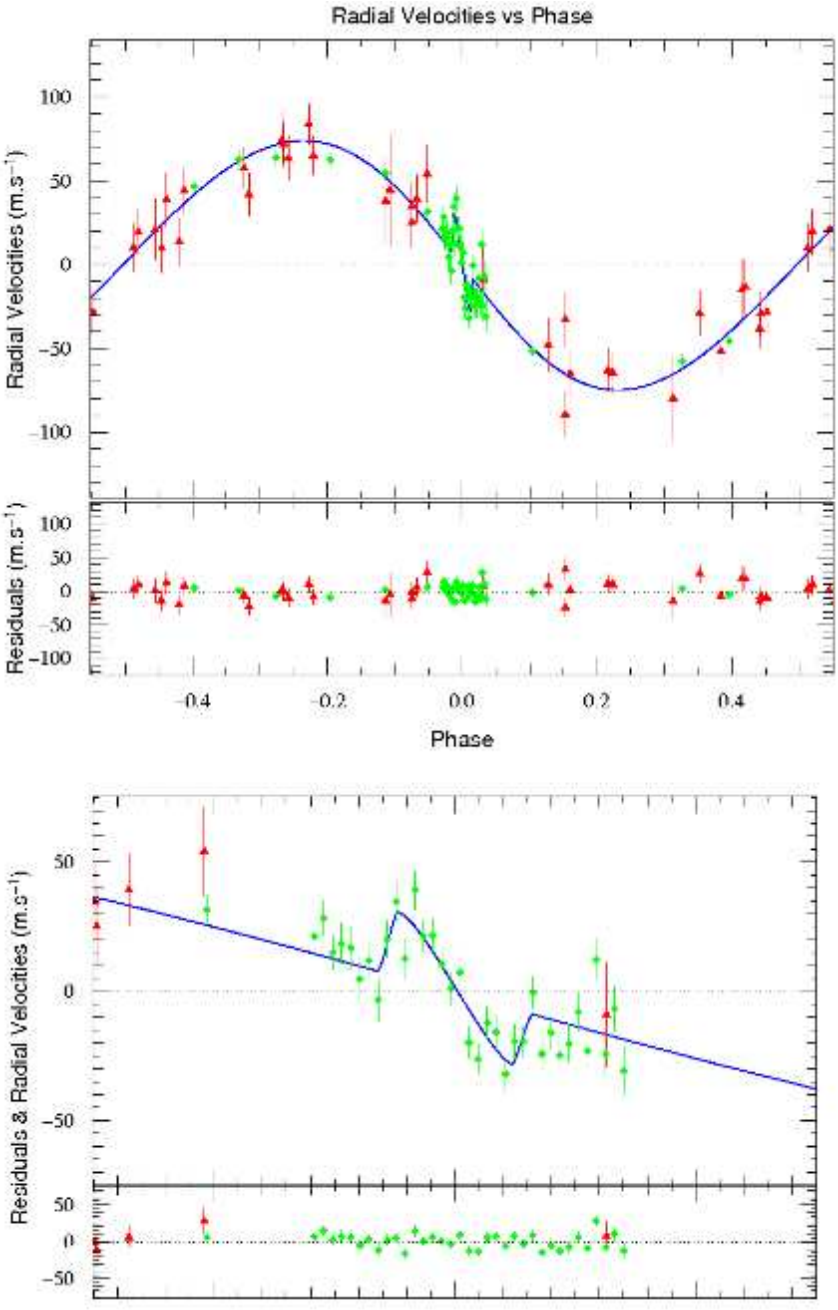

Figure 4.3: RV measurements of WASP-6 using CORALIE and HARPS (Gillon et al., 2009a). The green squares represent data from HARPS while the red triangles represent data from CORALIE. The top panel shows the RV measurements with the best-fitting model while the bottom panel is a close up during transit, which shows the RM effect.

determined a new value for the macroturbulence with $v_{mac} = 1.4 \pm 0.3\,\mathrm{km\,s^{-1}}$ and a new $v \sin I$ of $2.4 \pm 0.5\,\mathrm{km\,s^{-1}}$. They also measured an effective temperature of the photosphere of WASP-6, finding $T_{eff} = 5375 \pm 65\,\mathrm{K}$.

An optical transmission spectrum for WASP-6 b has also been constructed using multi-object differential spectrophotometry with the IMACS spectrograph on the Magellan Baade telescope (Jordán et al., 2013). The observations comprised 91 spectra in the spectral range of 480 to 860 nm. The analysis yielded a mostly featureless transmission spectrum with evidence of atmospheric hazes and condensates.

4.1.1 WASP-6 and Starspots

Four transits of WASP-6 were observed using the Danish 1.54 m telescope. The lightcurves were observed between 2009/06/26 and 2010/07/31, with two lightcurves observed on the 2009/08/02 and 2009/08/29 containing a starspot anomaly. Due to a 27 day gap between these two lightcurves it is not possible to conclusively determine if the spot anomaly is due to the same spot. However, if the two spot anomalies are due to the same starspot then the stellar rotation period and sky-projected spin orbit alignment can be calculated and compared to the values found by Gillon et al. (2009a) and Doyle et al. (2013). This provides an indirect check to see if the two spot anomalies are due to the same starspot. Another issue is whether the spot could last for a 27 day period. On the Sun a spot's lifetime T is proportional to its size A_0 following the Gnevyshev-Waldmeier relation (Gnevyshev, 1938; Waldmeier, 1955),

$$A_0 = WT \tag{4.1}$$

where A_0 is measured in MSH (Micro-Solar Hemispheres) and T is in days. Petrovay & van Driel-Gesztelyi (1997) state that $W = 10.89 \pm 0.18$. Henwood et al. (2010) showed that large Sunspots also followed the Gnevyshev-Waldmeier relationship. If the same relationship is extrapolated to starspots then, for a starspot to have a minimum lifetime of 30 days, using Equation 4.1 would give a minimum size for the starspot of 327 MSH

or an angular radius of just greater than 1°. Inspecting the amplitude of the starspot anomalies in the WASP-6 lightcurves it can be seen that the starspot(s) would be much greater than 1° and as such the starspot which caused the first anomaly would still be visible during the second transit if it is on the visible stellar hemisphere.

4.2 Observations and Data Reduction

Four transits of WASP-6 were observed on 2009/06/26, 2009/08/02, 2009/08/29 and 2010/07/31 by the MiNDSTEp (Microlensing Network for the Detection of Small Terrestrial Exoplanets) consortium using the Danish 1.54 m Telescope operated at ESO La Silla, Chile. The instrument used was the DFOSC imager, operated with a Bessell R filter. In this setup the CCD covers a field of view of $(13.7')^2$ with a pixel scale of $0.39''\,\mathrm{pixel}^{-1}$. The images were windowed down (see Table 4.1 for the individual window sizes for each data set) and were not binned, resulting in a dead time between consecutive images of between 22 and 35 s depending on each observing night. The exposure times ranged between 80–120 s depending on each observing night. The Moon brightness and distance to the target star is given in Table 4.1. The telescope was

Table 4.1: Log of the observations presented for WASP-6. N_{obs} is the number of observations.

Date	2009/06/26	2009/08/02	2009/08/29	2010/07/31
Start time (UT)	06:33	04:18	02:32	03:51
End time (UT)	10:43	10:31	07:47	10:20
N_{obs}	91	175	129	193
Exposure time (s)	120	90–120	120	80
Filter	Bessell R	Bessell R	Bessell R	Bessell R
Airmass	$1.32 \rightarrow 1.05$	$1.28 \rightarrow 1.44$	$1.28 \rightarrow 1.20$	$1.45 \rightarrow 1.34$
Fractional Moon illumination	0.271	0.934	0.750	0.686
Moon distance (°)	160.5	59.6	63.8	42.4
Window size (pixel)	1650×950	1600×800	1485×650	1700×1000
Aperture sizes (pixel)	45, 65, 70	20, 30, 40	25, 45, 90	20, 30, 40
Scatter (mmag)	1.178	1.138	0.597	0.662

defocused and the autoguiding was maintained through all observations. The amount of defocus applied caused the resulting PSFs to have a diameter of 86 pixels for the night of 2009/06/26, 32 pixels for the night of 2009/08/02, 44 pixels for the night of 2009/08/29 and 37 pixels for the night of 2010/07/31.

The data were reduced using the data reduction pipeline discussed in Section 2.5.1 and 3.2 and in an identical fashion to Southworth et al. (2009a,b,c, 2010). In short, aperture photometry using an IDL implementation of DAOPHOT (Stetson, 1987) was used and the aperture sizes were adjusted to obtain the best results (see Table 4.1). A first order polynomial was then fitted to the outside-transit data whilst simultaneously optimising the weights of the comparison stars. The resulting data have scatters ranging from 0.597 to 1.178 mmag per point versus a transit fit using PRISM. The timestamps from the fits files were converted to BJD/TDB (see Section 2.5.2).

4.3 Data Analysis

The spot-free data were modelled first using JKTEBOP and then PRISM and GEMC. This was done to check that PRISM and GEMC were obtaining the best-fitting solution. The two datasets containing a starspot anomaly were modelled using PRISM and GEMC. To do this a large parameter search space was selected to allow the global best fit solution to be found. As discussed in Section 2.8.3.4, the ability of GEMC to find the global minimum in a short amount of computing time meant that it was possible to search a large area of the parameter space to avoid the possibility of missing the best solution. The parameter search range used in analysing the WASP-6 datasets are given in Tables 4.2, 4.3, 4.4 and 4.5.

It was decided to model the two datasets containing a starspot anomaly independently due to the fact that it is not precisely known if the two anomalies were generated by the same starspot.

The four datasets of WASP-6 were modelled separately using PRISM, finding that the modelled parameters were within 1-σ of each other (Table 4.2, 4.3, 4.4 and 4.5). It

Table 4.2: Derived photometric parameters from the lightcurve taken on 2009/06/26, plus the interval within which the best fit was searched for using GEMC.

Parameter	Symbol	Search interval	2009/06/26
Radius ratio	r_p/r_s	0.05 to 0.30	0.1458 ± 0.0052
Sum of fractional radii	$r_s + r_p$	0.10 to 0.50	0.1096 ± 0.0056
Linear LD coefficient	u_1	0.0 to 1.0	0.386 ± 0.123
Quadratic LD coefficient	u_2	0.0 to 1.0	0.256 ± 0.035
Inclination (degrees)	i	70.0 to 90.0	87.64 ± 1.01
Transit epoch (BJD/TDB)	T_0	±0.5 in phase	2455009.83623 ± 0.00016

Table 4.3: Derived photometric parameters from the lightcurve taken on 2009/08/02, plus the interval within which the best fit was searched for using GEMC.

Parameter	Symbol	Search interval	2009/08/02
Radius ratio	r_p/r_s	0.05 to 0.30	0.1461 ± 0.0043
Sum of fractional radii	$r_s + r_p$	0.10 to 0.50	0.1091 ± 0.0039
Linear LD coefficient	u_1	0.0 to 1.0	0.333 ± 0.116
Quadratic LD coefficient	u_2	0.0 to 1.0	0.280 ± 0.034
Inclination (degrees)	i	70.0 to 90.0	87.68 ± 0.77
Transit epoch (BJD/TDB)	T_0	±0.5 in phase	2455046.80720 ± 0.00020
Longitude of spot (degrees)	θ	-90 to +90	-28.24 ± 0.56
Co-latitude of spot (degrees)	ϕ	0.0 to 90.0	79.66 ± 1.23
Spot angular radius (degrees)	$r_{\rm spot}$	0.0 to 30.0	13.53 ± 0.48
Spot contrast	$\rho_{\rm spot}$	0.0 to 1.0	0.679 ± 0.033

Table 4.4: Derived photometric parameters from the lightcurve taken on 2009/08/29, plus the interval within which the best fit was searched for using GEMC.

Parameter	Symbol	Search interval	2009/08/29
Radius ratio	r_p/r_s	0.05 to 0.30	0.1476 ± 0.0014
Sum of fractional radii	$r_s + r_p$	0.10 to 0.50	0.1113 ± 0.0022
Linear LD coefficient	u_1	0.0 to 1.0	0.380 ± 0.098
Quadratic LD coefficient	u_2	0.0 to 1.0	0.289 ± 0.028
Inclination (degrees)	i	70.0 to 90.0	87.89 ± 0.47
Transit epoch (BJD/TDB)	T_0	±0.5 in phase	2455073.69529 ± 0.00012
Longitude of spot (degrees)	θ	-90 to +90	22.59 ± 0.37
Co-latitude of spot (degrees)	ϕ	0.0 to 90.0	73.91 ± 0.93
Spot angular radius (degrees)	$r_{\rm spot}$	0.0 to 30.0	13.67 ± 0.34
Spot contrast	$\rho_{\rm spot}$	0.0 to 1.0	0.790 ± 0.015

was mentioned in Section 3.3 that starspots can affect the LD coefficients by up to 10% in the R band. This is not seen in the WASP-6 data. The scatter around the weighted

Table 4.5: Derived photometric parameters from the lightcurve taken on 2010/07/31, plus the interval within which the best fit was searched for using GEMC.

Parameter	Symbol	Search interval	2010/07/31
Radius ratio	r_p/r_s	0.05 to 0.30	0.1444 ± 0.0022
Sum of fractional radii	$r_s + r_p$	0.10 to 0.50	0.1114 ± 0.0027
Linear LD coefficient	u_1	0.0 to 1.0	0.420 ± 0.103
Quadratic LD coefficient	u_2	0.0 to 1.0	0.274 ± 0.031
Inclination (degrees)	i	70.0 to 90.0	87.60 ± 0.51
Transit epoch (BJD/TDB)	T_0	±0.5 in phase	2455409.79517 ± 0.00008

mean is $\chi^2_\nu = 0.316$ for the linear coefficient and 0.560 for the quadratic coefficient. The error bars on the LD coefficients are therefore too large to allow the effects of starspots to be detected due to the lower quality of the data compared to WASP-19 in Chapter 3.

4.3.1 Photometric Results

The final photometric parameters for the WASP-6 system are given in Table 4.6 and are weighted means plus 1-σ uncertainties of the results from the four individual fits. Figure 4.4 compares the lightcurves to the best-fitting models, including the residuals.

Table 4.6: Combined system and spot parameters for WASP-6. The system parameters are the weighted means from all four data sets. The spot angular size and contrast are the weighted mean from the two transits containing a starspot anomaly.

Parameter	Symbol	Value
Radius ratio	r_p/r_s	0.1466 ± 0.0011
Sum of fractional radii	$r_s + r_p$	0.1109 ± 0.0015
Linear LD coefficient	u_1	0.383 ± 0.054
Quadratic LD coefficient	u_2	0.276 ± 0.016
Inclination (degrees)	i	87.73 ± 0.30
Spot angular radius (degrees)	$r_{\rm spot}$	13.62 ± 0.28
Spot contrast	$\rho_{\rm spot}$	0.771 ± 0.014
Stellar rotation period (d)	$P_{\rm rot}$	23.56 ± 0.13
Projected spin orbit alignment (degrees)	λ	6.4 ± 2.3

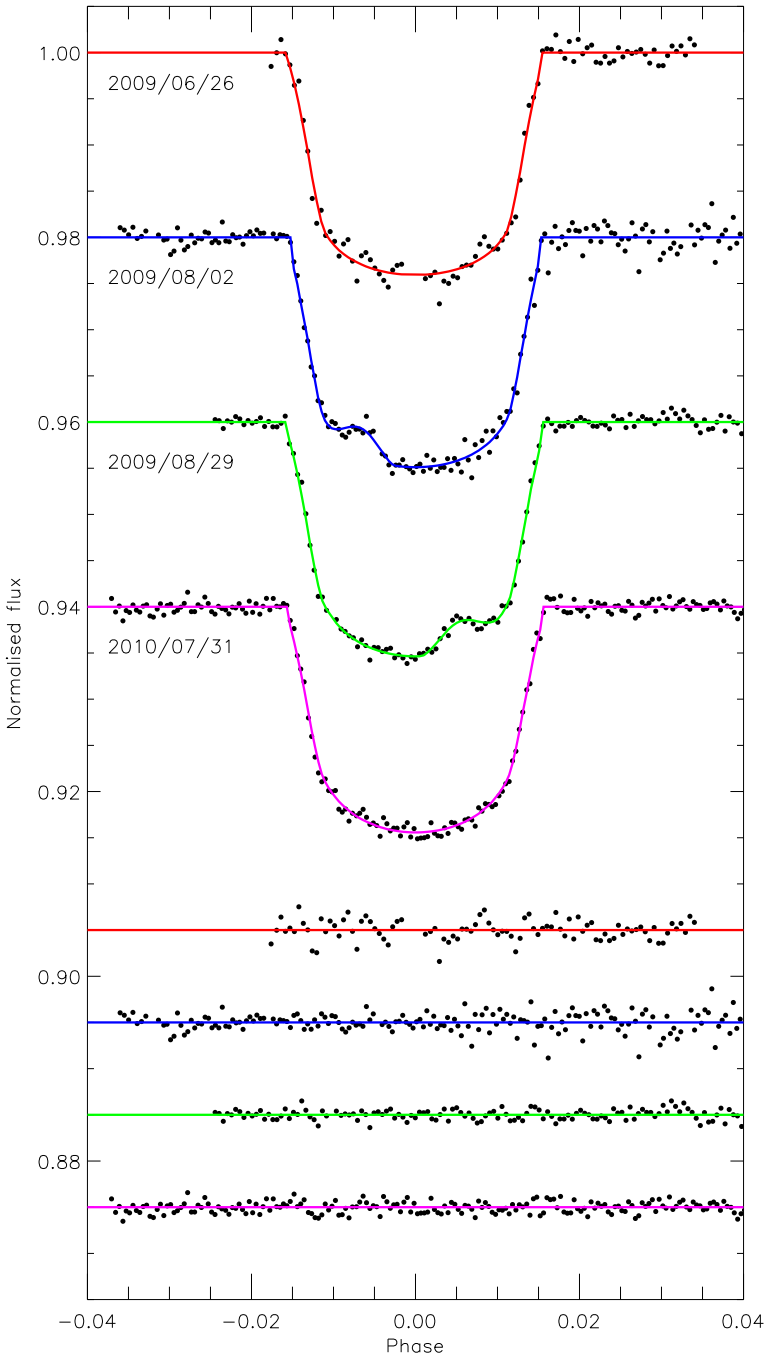

Figure 4.4: Transit lightcurves and the best-fitting models of WASP-6. The residuals are displayed at the base of the figure.

The results from modelling the spot anomalies on the nights of 2009/08/02 and 2009/08/29 suggest that they are due to the same spot rotating around the surface of the star, as the spot sizes are in good agreement. The difference in $\rho_{\rm spot}$ between the two nights can be explained by the evolution of the spot. Because the size of the spot anomaly is much greater than 1° (see Section 4.1.1), then the spot observed in the 2009/08/02 transit should still exist on the stellar surface. Figure 4.5 is a representation of the stellar disc, the spot and the transit chord for the two nights of observations.

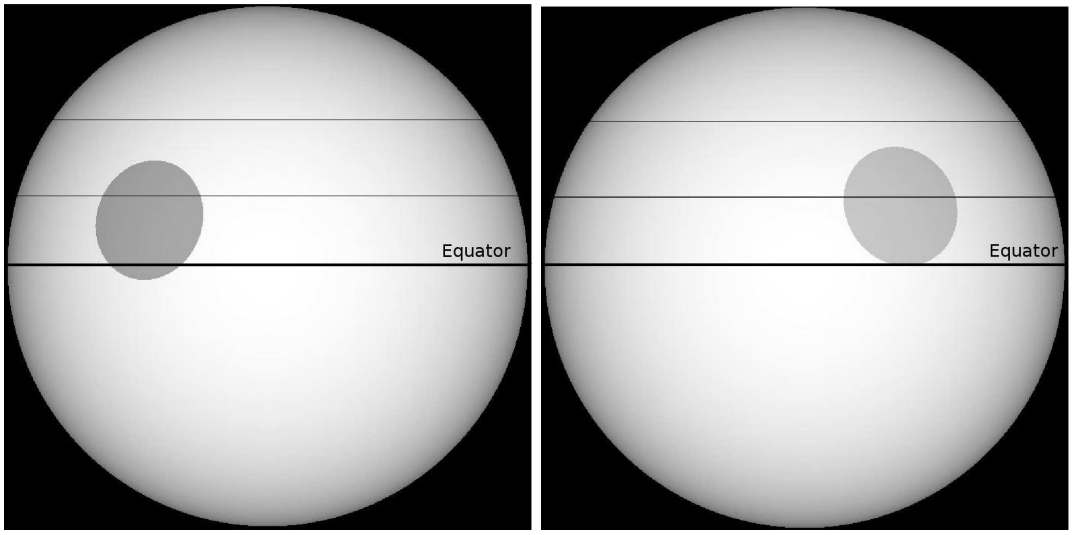

Figure 4.5: Representation of the stellar disc, starspot, transit chord and equator for the two datasets of WASP-6 containing spot anomalies. The axis of stellar rotation lies in the plane of the page and points upwards.

By assuming that the two spot anomalies are indeed caused by the same spot then by using the positions of the starspot at the time of the transits on the nights of 2009/08/02 and 2009/08/29, it is possible to calculate the rotational period of the star and the sky-projected spin orbit alignment of the system using simple geometry. To calculate the rotation period, different cases need to be examined. Due to the 27 day gap between the lightcurves the star could have rotated N full rotations plus $50.83° \pm 0.93°$. If $N = 0$ then this would imply that WASP-6 has a rotation period

of approximately 200 days and would imply that WASP-6 is older than the age of the universe. If $N = 1$ then the spot has travelled $410.83° \pm 0.93°$ in 26.8875 ± 0.0003 days, giving a rotational period of $P_{\rm rot} = 23.56 \pm 0.13$ d at a co-latitude of 77.5°. Combining this with the stellar radius (see Table 4.8), the latitudinal rotational velocity of the star was calculated to be $v_{(77.5°)} = 1.80 \pm 0.19\,{\rm km\,s^{-1}}$. This is in agreement with both Gillon et al. (2009a) and Doyle et al. (2013). If $N = 2$ then the spot has travelled $770.83° \pm 0.93°$ in 26.8875 ± 0.0003 days, giving a rotational period of $P_{\rm rot} = 12.56 \pm 0.13$ d at a co-latitude of 77.5°. (or $v_{(77.5°)} = 3.38 \pm 0.19\,{\rm km\,s^{-1}}$). This also agrees with both Gillon et al. (2009a) and Doyle et al. (2013). Because of this there is a degeneracy between the possible stellar rotation periods, which is discussed later in Section 4.4. In either case the positions of the spot finally yielded a sky-projected spin orbit alignment of $\lambda = 6.4° \pm 2.3°$ for WASP-6.

The available times of mid-transit for WASP-6 were collected from the literature (Gillon et al., 2009a; Dragomir et al., 2011; Sada et al., 2012). All timings were converted to the BJD/TDB timescale and used to obtain an improved orbital ephemeris:

$$T_0 = {\rm BJD/TDB}\ 2\,454\,596.43337(12) + 3.36099922(63) \times E$$

where E represents the cycle count with respect to the reference epoch and the bracketed quantities represent the uncertainty in the final digit of the preceding number. Figure 4.6 and Table 4.7 show the residuals of these times against the ephemeris. Ex-

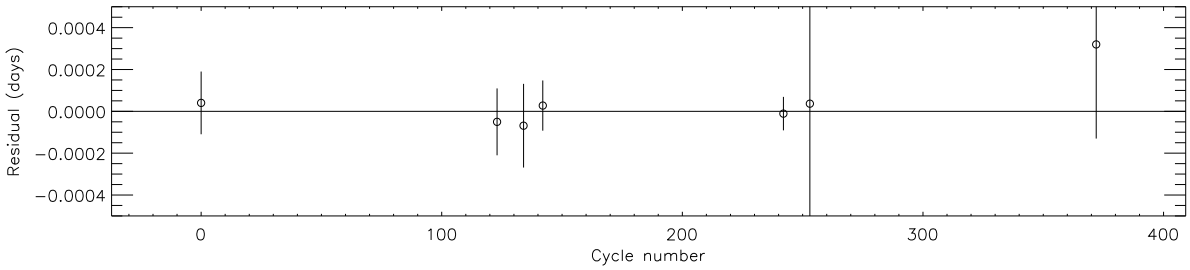

Figure 4.6: Residuals of the available times of mid-transit versus the orbital ephemeris found for WASP-6. The four timings from this work are the cluster of three points between the cycle numbers 120-150 and the point close to the 240 cycle count.

Table 4.7: Times of minimum light of WASP-6 and their residuals versus the ephemeris derived in this work.

Time of minimum (BJD/TDB − 2400000)	Cycle no.	Residual (BJD)	Reference
54596.43341 ± 0.00015	0.0	0.00004	1
55009.83622 ± 0.00016	123.0	-0.00005	2
55046.80720 ± 0.00020	134.0	-0.00007	2
55073.69529 ± 0.00012	142.0	0.00003	2
55409.79517 ± 0.00008	242.0	-0.00001	2
55446.76621 ± 0.00058	253.0	0.00004	3
55846.72540 ± 0.00045	372.0	0.00032	4

References: (1) Gillon et al. (2009a); (3) Dragomir et al. (2011); (4) Sada et al. (2012); (2) This work.

amining the results show no evidence for transit timing variations in the WASP-6 planetary system.

The time of mid-transit from Jordán et al. (2013) was not used in this analysis. The value $T_0 = 2455473.15364 \pm 0.00016$ is given in MHJD (Modified Heliocentric Julian Date) but no time system is given. If we assume that the time system being used is UTC and convert it to TDB the data point is a poor fit and is out by approximately 257 s (19-σ). If we assumed that the T_0 by Jordán et al. (2013) is already in the TDB time system then the data point is still a poor fit and is out by 191 s (14-σ). Until confirmation from the author on which time system was used it was decided to leave the Jordán et al. (2013) T_0 value out of the analysis.

4.3.2 Physical Properties of the WASP-6 System

It should be mentioned that at present PRISM only models a circular orbit (i.e. $e = 0$). While this allows PRISM to accurately model the majority of TEPs, in the case of WASP-6 the eccentricity will cause a small perturbation of the stellar radius. Using the equation to calculate the impact parameter b (see Equation 1.15) the effect of having

an eccentricity of $e = 0.054^{+0.018}_{-0.015}$ (Gillon et al., 2009a) and the argument of periastron $\omega = 97.4^{+6.9}_{-13.2}$ degrees (Gillon et al., 2009a) alters the values for the sum of the fractional radii to $r_s + r_p = 0.11672 \pm 0.00158$ and the inclination to $i = 87.841° \pm 0.313°$. k is not affected as it is determined directly from the transit lightcurve, therefore r_p is scaled by the same amount as r_s to allow k to remain unaffected.

The rest of the work in this subsection was performed by Dr John Taylor and is included here because it is an integral part of the analysis of WASP-6.

With the photometric properties of WASP-6 measured the physical characteristics could be determined. The analysis followed the method of Southworth (2009), which uses the parameters measured from the light curves and spectra, plus tabulated predictions of theoretical models. The values of $i = 87.841° \pm 0.313°$ and $r_s + r_p = 0.11672 \pm 0.00158$ were used in conjunction with r_p/r_s from Table 4.6 and coupled with the stellar properties of effective temperature $T_{\rm eff} = 5375 \pm 65\,{\rm K}$ (Doyle et al., 2013), velocity amplitude $K_{\rm s} = 74.3^{+1.7}_{-1.4}\,{\rm m\,s^{-1}}$ (Gillon et al., 2009a), eccentricity $e = 0.054^{+0.018}_{-0.015}$ (Gillon et al., 2009a) and metal abundance [Fe/H] $= -0.15 \pm 0.09$ (Doyle et al., 2013).

An initial value of the velocity amplitude of the planet, $K_{\rm p}$, was used to calculate the physical properties of the system using standard formulae and the physical constants listed by Southworth (2011). The mass and [Fe/H] of the star were then used to obtain the expected $T_{\rm eff}$ and radius, by interpolation within a set of tabulated predictions from stellar theoretical models. $K_{\rm p}$ was iteratively refined until the best agreement was found between the observed and expected $T_{\rm eff}$, and the measured $r_{\rm s}$ and expected $\frac{R_{\rm s}}{a}$. This was performed for ages ranging from the zero-age to the terminal-age main-sequence, in steps of 0.01 Gyr. The overall best fit was found, yielding estimates of the system parameters and the evolutionary age of the star.

This procedure was performed separately using five different sets of stellar theoretical models (see Southworth, 2010), and the spread of values for each output parameter was used to assign a systematic error. Statistical errors were propagated using a perturbation algorithm.

The final results of this process are in reasonable agreement with themselves and

Table 4.8: Physical properties of the WASP-6 system. Both statistical and systematic uncertainties are given. The first uncertainty is the statistical uncertainty and the second is the systematic uncertainty.

Parameter	Value
$M_{\rm A}$ ($\rm M_\odot$)	$0.833 \pm 0.038 \pm 0.021$
$R_{\rm A}$ ($\rm R_\odot$)	$0.905 \pm 0.019 \pm 0.008$
$\log g_{\rm A}$ (cgs)	$4.446 \pm 0.014 \pm 0.004$
$\rho_{\rm A}$ ($\rho_\odot$)	1.125 ± 0.046
$M_{\rm b}$ ($\rm M_{Jup}$)	$0.485 \pm 0.018 \pm 0.008$
$R_{\rm b}$ ($\rm R_{Jup}$)	$1.291 \pm 0.028 \pm 0.011$
$g_{\rm b}$ ($\rm m\,s^{-2}$)	7.21 ± 0.27
$\rho_{\rm b}$ ($\rho_{\rm Jup}$)	$0.211 \pm 0.011 \pm 0.002$
$T'_{\rm eq}$ (K)	1212 ± 16
Θ	$0.0372 \pm 0.0012 \pm 0.0003$
a (AU)	$0.04133 \pm 0.00064 \pm 0.00035$
Age (Gyr)	$12.3\,^{+5.3}_{-11.1}\,^{+2.3}_{-3.4}$

with published results for WASP-6. The stellar radius $R_{\rm A} = 0.905 \pm 0.019$ does disagree with the value determined by Doyle et al. (2013). This disagreement is most likely due to the fact that Doyle et al. (2013) used the Torres calibrations versus eclipsing binaries (Torres et al., 2010), which is a much simpler method to that used in this analysis. The final physical properties are given in Table 4.8 and incorporate separate statistical and systematic errorbars for those parameters which depend on the theoretical models. The final statistical errorbar for each parameter is the largest of the individual ones from the solutions using each of the five different stellar models. The systematic errorbar is the largest difference between the mean and the individual values of the parameter from the five solutions.

4.4 Discussion and Conclusions

Four transits of WASP-6 were modelled using both PRISM and GEMC. Two of the transits contained a starspot anomaly but are separated by 27 days, unlike the two

consecutive transits of WASP-19. Because of this it was not possible to precisely state that the spot anomalies are caused by the same starspot, but circumstantial evidence does seem to suggest that they are. PRISM indicates that the angular size of the starspot(s) in both lightcurves are the same, while the spot contrast does alter. This could be explained by the evolution of the starspot. As with WASP-19 (see Figure 3.9) from examining Figure 4.5 only a fraction of the starspot(s) are on the transit cord. Because the lightcurve can only tell us what is happening inside the transit cord then the more probable scenario is that the planet is passing over a band of smaller starspots, indicating an active region on WASP-6. In this active region, there would be a number of starspots each with sizes much less than 1° and therefore would have lifetimes smaller than 30 days (see Section 4.1.1). From this it would be expected to see changes in the overall contrast from the starspot region, but as a whole the region would remain a similar size and shape.

In the case of a single large starspot both r_{spot} (from Table 4.6) and R_* (from Table 4.8) can be combined to find the starspot radius in km, where $R_{spot} = 141012 \pm 9525$ km which equates to approximately 5.5% of the visible stellar surface. This value is similar to starspots found on other G-type stars (Strassmeier, 2009).

If the two starspot anomalies are assumed to be generated by the planet crossing the same starspot then it is possible to calculate the latitudinal rotation period of WASP-6. It was found that either $P_{\rm rot} = 23.56 \pm 0.13$ d or $P_{\rm rot} = 12.56 \pm 0.13$ d at a co-latitude of 77.5°. These calculation assumed that WASP-6 had made either one or two full rotations prior to the difference seen in the lightcurves. There is no rotation period measurement found in the literature but there are two measurements for $v \sin I$ from Gillon et al. (2009a) and Doyle et al. (2013). Both of these measurements agree with the v value found when combining $P_{\rm rot}$ and R_* at a co-latitude of 77.5° to give either $v_{(77.5°)} = 1.80 \pm 0.19\,{\rm km\,s^{-1}}$ or $v_{(77.5°)} = 3.38 \pm 0.19\,{\rm km\,s^{-1}}$. The problem that arises from checking measurements of v against $v \sin I$ is that due to the nature of $\sin I$ any value for v that is found to be greater than $v \sin I$ can be considered to agree. A second unknown is the amount of differential rotation that is experienced by WASP-6. In the absence of any differential rotation then the original value of $P_{\rm rot} = 23.56 \pm 0.13$ d

would lead to an equatorial rotational velocity of $v = 1.85 \pm 0.19\,\mathrm{km\,s^{-1}}$. This result agrees with the $v \sin I$ value from Gillon et al. (2009a) but does not agree with Doyle et al. (2013). Due to not knowing the extent of the differential rotation it is not possible to combine the measurements of v and $v \sin I$ to measure the angle between the stellar rotation axis and the plane of the sky I. The difference between v and $v \sin I$ is therefore formed from a mixture of the differential rotation and I.

Both WASP-6 and WASP-19 are of similar spectral types (G8 WASP-6 and G8V WASP-19). Considering that the size of the starspots detected on both WASP-6 and WASP-19 (see Tables 3.5 and 4.6) are of similar size then it is plausible that both stars are of similar magnetic activity. Combining this knowledge can lead to the proposal that both WASP-19 and WASP-6 should be of similar ages and therefore have similar rotation periods. The rotation period of WASP-19 was found to be $P_{\mathrm{rot}} = 11.76 \pm 0.09\,\mathrm{d}$ at a co-latitude of 65° and Hebb et al. (2010) gives P_{rot} of $10.5 \pm 0.2\,\mathrm{d}$ from rotational modulation of the star's brightness over several years. Both of these values are closest to $P_{\mathrm{rot}} = 12.56 \pm 0.13\,\mathrm{d}$ at a co-latitude of 77.5° for WASP-6. This implies that between the two transit that observed the starspot anomalies, WASP-6 had in fact rotated $N = 2$ full rotations plus $50.83° \pm 0.93°$. To definitely determine the exact rotation period of WASP-6, will require further consecutive transit observations containing starspot anomalies. But using WASP-19 as a potential twin can allow the rotation period of WASP-6 to be estimated at $P_{\mathrm{rot}} = 12.56 \pm 0.13\,\mathrm{d}$ at a co-latitude of 77.5°.

Despite the number of full rotations that WASP-6 potentially completed between the two lightcurves, if the starspot anomalies are due to the same spot then the sky-projected spin orbit alignment λ of the system can still be measured. The results show that $\lambda = 6.4° \pm 2.3°$ for WASP-6. This result agrees with, and is more precise than, the previous measurement of λ using the RM effect ($\lambda = 11° \,^{+14}_{-18}$; Gillon et al. 2009a). λ gives the lower boundary of the true spin-orbit angle, ψ. As stated in Section 1.4.1 and by Fabrycky & Winn (2009), finding a small value for λ can be interpreted in different ways. Either ψ lies close to λ and the system is aligned or ψ lies far from λ and the system is not aligned. Because the spot is close to the stellar equator then it could be assumed that the change in v at the equator due to the differential rotation would

be small. Coupled with the uncertainties measured in $v \sin I$ from both Gillon et al. (2009a) and Doyle et al. (2013) it is plausible that $\sin I \approx 1$ and therefore $\psi \approx 6^\circ$ (using Equation 1.38). Without any further evidence it is not possible to precisely determine the true obliquity of the system. It would therefore be desirable to observe consecutive transits of WASP-6 in an attempt to definitely identify multiple planetary crossings of the same starspot and to therefore precisely determine $P_{\rm rot}$, λ and potentially ψ of WASP-6.

If the starspot anomalies are due to the same starspot so that $\lambda = 6.4^\circ \pm 2.3^\circ$ then there is no direct evidence for a spin-orbit misalignment in the WASP-6 system. With potentially a low obliquity and a cool host star, WASP-6 seems to follow the idea put forward by Winn et al. (2010a) that planetary systems with cool stars will have a low obliquity. It also lends weight to the idea that WASP-6 b formed at a much greater distance from host star and suffered orbital decay through tidal interactions with the protoplanetary disc (i.e. either Type I or Type II disc-migration, Ward 1997a).

5 The WASP-50 Planetary System

This Chapter describes the WASP-50 planetary system and the collection and analysis of two transit lightcurves of WASP-50. The two lightcurves were collected using the defocused photometry technique applied to the ESO NTT, this approach resulted in the lowest known rms scatter achieved using a ground-based telescope. Section 5.1 begins with an overview of the WASP-50 planetary system including the discovery of WASP-50 b. Section 5.2 describes the data collection, reduction and confirmation of the low scatter. Section 5.3 presents both the photometric and physical results of fitting the transits using PRISM. Section 5.4 presents the discussion and conclusions for the Chapter. Sections 5.2 and 5.3 were published as first author in Monthly Notices of the Royal Astronomical Society (see Appendix A.1 for publication details).

5.1 Overview of the WASP-50 Planetary System

The discovery of the TEP system, WASP-50 was presented by Gillon et al. (2011b), who found it to comprise a TEP with a mass of $1.47 \pm 0.09\,M_{Jup}$ and radius of $1.15 \pm 0.05\,R_{Jup}$, orbiting a cool star with mass and radius $0.89 \pm 0.08\,M_{\odot}$ and $0.84 \pm 0.03\,R_{\odot}$. The discovery of WASP-50 used photometry from the WASP South telescope (see Figure 5.1). Gillon et al. (2011b) detected two similar periodic modulations of 16.09 ± 0.09 days and 16.65 ± 0.13 days with a FAP (False Alarm Probability) value of 0.05% and 0.1%, respectively, in two seasons of WASP-South data (see Figure 5.2), indicating stellar activity due to starspots rotating on and off the stellar disc. When taking into account that instrumental noise in the WASP data adds a systematic error of ± 0.5 days, Gillon et al. (2011b) calculated the stellar rotation period of WASP-50 as $P_{rot} = 16.3 \pm 0.5$ days.

Gillon et al. (2011b) performed photometric follow-up observations (see Figure 5.3) using TRAPPIST (TRAnsiting Planets and PlanetesImals Small Telescope; Gillon et al. 2011a) and the 1.2 m Euler telescope. They also performed RV follow-up

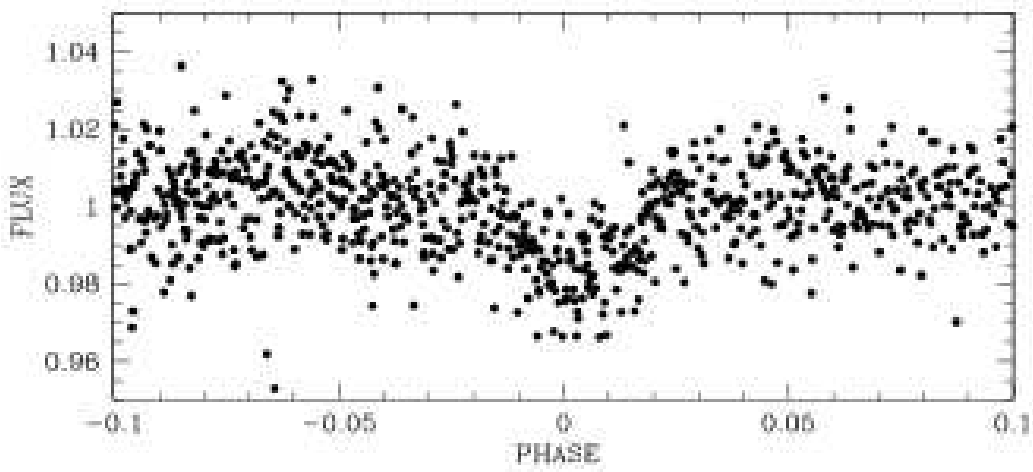

Figure 5.1: WASP-South discovery photometry of WASP-50 b (Gillon et al., 2011b). The data are phase folded using $T_0 = 54997.4996 \pm 0.0014$ and a period of $P = 1.955$ days.

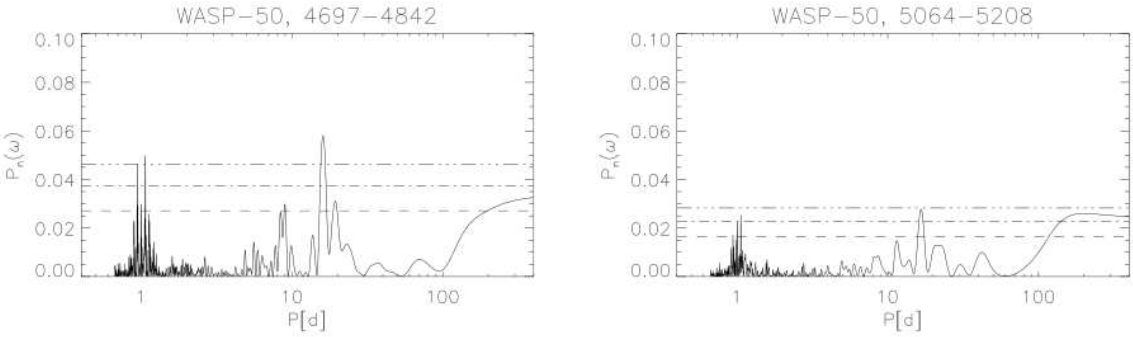

Figure 5.2: Periodograms for the WASP data from two seasons of WASP-50 (Gillon et al., 2011b). Each panel shows the date range (JD -245000). The horizontal lines represent the FAP levels 0.1, 0.01 and 0.001.

observations using the CORALIE spectrograph (Baranne et al., 1996; Queloz et al., 2000) on the 1.2 m Euler telescope.

They also determined the presence of Ca H+K emission in spectra of the host star. They deduced a chromospheric emission index of $\log R'_{HK} \sim -4.67$, which is similar

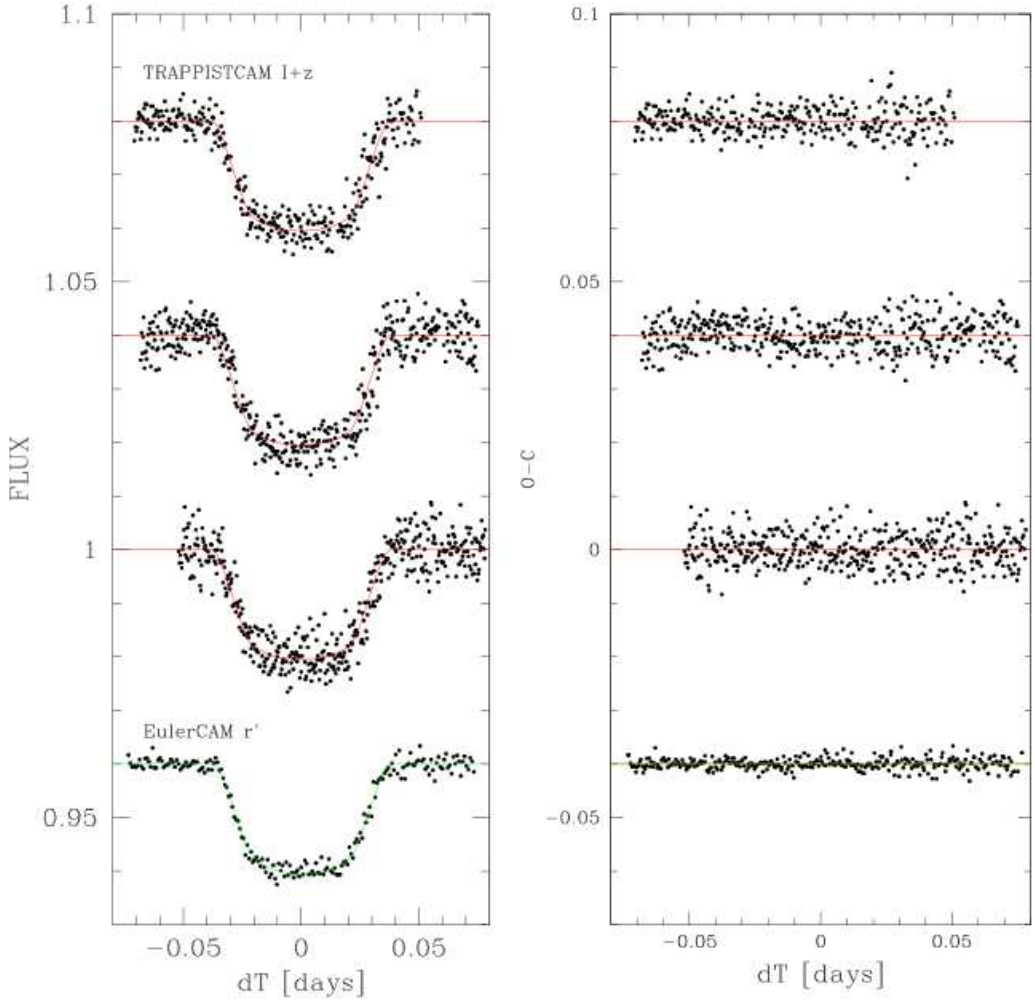

Figure 5.3: Transit lightcurves of WASP-50 from TRAPPIST and Euler (Gillon et al., 2011b). The left hand panel shows the transits and best-fitting models and the right hand panel shows the residuals. The bottom transit with the lowest scatter was obtained using the Euler telescope.

to that found for the magnetically active star WASP-41 A (Maxted et al., 2011b). They concluded that WASP-50 is magnetically active and that the periodic modulation detected in the WASP-South data is due to starspots.

The initial transit lightcurves and RV measurements of WASP-50 from Gillon

et al. (2011b) gave uncertainties in the planetary mass, radius, density and surface gravity of 6%, 4%, 9% and 6%, respectively. Coupled with the evidence of stellar activity from WASP-50, this makes the WASP-50 planetary system a prime candidate for further high-precision transit photometry to not just refine the system parameters but to also try and observe a starspot anomaly.

WASP-50 was observed with the aim of improving its measured physical properties, using the telescope-defocussing approach. Two complete transits of WASP-50 were observed using the NTT, achieving extremely low photometric scatters of 258 and 211 parts per million (ppm), respectively, versus a fitted model. The latter is the lowest scatter ever achieved in ground-based photometry per point for a point source.

Some of the highest photometric precisions previously accomplished for a TEP system are 479 ppm for CoRoT-1 using the 8.2 m VLT (Pont et al., 2010), 478 ppm for WASP-4 using the 6.5 m Magellan Baade telescope (Winn et al., 2009), 470 ppm for WASP-10 using the University of Hawaii 2.2 m telescope (Johnson et al., 2009), 387 ppm for WASP-2 using a 1.5 m telescope (Southworth et al., 2010), and 316 ppm for TrES-2 using the 10.4 m Gran Telescopio Canarias (Colón et al., 2010). The highest photometric precision from a ground-based telescope was previously 258 ppm in time-series observations of stars in the open cluster M67 (Gilliland et al., 1993).

An alternative metric which is well-suited for making direct comparisons is the signal-to-noise per unit time. The scatter was recalculated in ppm per minute of observing time for the datasets listed above. By this metric the 211 ppm dataset is almost exactly equal to the best one presented by Gilliland et al. (1993), and both of the light curves are better than any previously published ground-based photometric observations of a TEP system.

5.2 Observations and Data Reduction

Two transits of WASP-50 were observed on the nights of 2011/11/20 and 2011/11/24 using the NTT with the EFOSC2 instrument operated in imaging mode. In this setup

the CCD covers a field of view of $(4.1')^2$ with a pixel scale of $0.12''$ pixel^{-1}. The images were windowed down to 1100×1600 pixels and no binning was used, resulting in a dead time between consecutive images of 50 s. The observations were taken through a Gunn r filter (ESO filter #784). The Moon was below the horizon for half of the first transit and all of the second transit. The telescope was initially focused and the shape of its primary mirror was adjusted to obtain the best image possible. We then applied a defocus to the telescope and performed the full observing sequence without adjusting the telescope focus or mirror shape. The amount of defocus applied caused the resulting PSFs to have a diameter of 93 pixels for the night of 2011/11/20 and 102 pixels for the night of 2011/11/24.

Table 5.1: Log of the observations presented for WASP-50. $N_{\rm obs}$ is the number of observations.

Date	2011/11/20	2011/11/24
Start time (UT)	00:59	01:08
End time (UT)	06:02	06:27
$N_{\rm obs}$	127	124
Exposure time (s)	120–150	150
Filter	Gunn r	Gunn r
Airmass	$2.62 \rightarrow 1.48$	$2.10 \rightarrow 1.53$
Fractional Moon illumination	0.384	0.045
Moon distance (°)	91.2	137.4
Aperture sizes (pixel)	75, 105, 120	75, 100, 125
Scatter (ppm)	258	211

The pointing of the telescope was adjusted to allow a good comparison star to be observed simultaneously with WASP-50. The comparison star used was 2MASS J02544939−1051548, which is of a similar apparent magnitude and colour to WASP-50. The 2MASS $J - K_s$ colour indices of the two objects are 0.432 for WASP-50 and 0.357 for the comparison star (Skrutskie et al., 2006). We were able to keep the telescope autoguided through all observations. An observing log is given in Table 5.1.

Figure 5.4 shows the shape of the point spread function (PSF) of WASP-50 in an image taken at random from the observing sequence on the night of 2011/10/24.

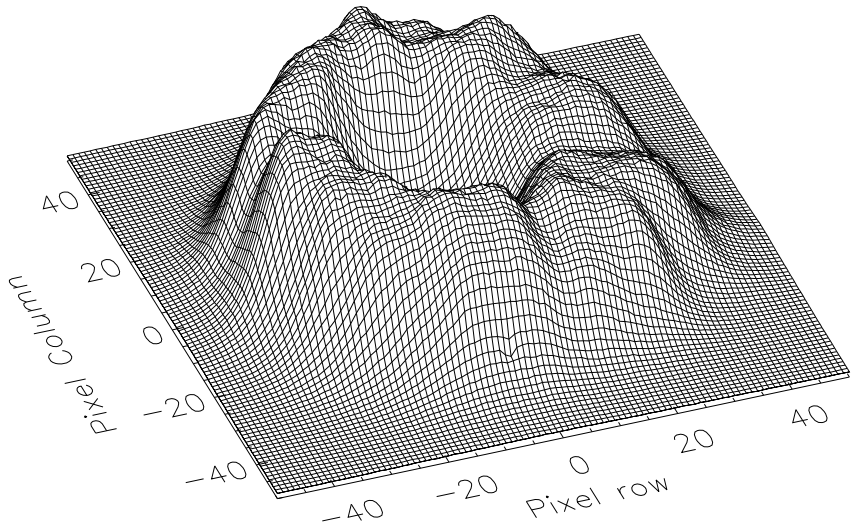

Figure 5.4: Surface plot of the PSF of WASP-50 in an image taken at random from the observing sequence on the night of 2011 October 24th. The x and y axes are in pixels. The lowest and highest counts are 684 and 24 726 ADUs, respectively, and the z axis is on a linear scale.

This provides an interesting comparison with similar observations of WASP-4 from a 1.5 m telescope of more traditional design (see Figure 2.3). The PSF for the current observations shows a much more rounded annulus of high counts, which allows a smaller amount of defocussing to be used to collect a given number of photons without saturating individual pixels.

The data were reduced in an identical fashion to Sections 2.5.1, 3.2, 4.2 and Southworth et al. (2009a). In short, aperture photometry was performed using an IDL implementation of DAOPHOT (Stetson, 1987), and the aperture sizes were adjusted to obtain the best results (see Table 5.1). A differential-magnitude light curve was calculated between the target and comparison star. A first-order polynomial was fitted to the outside-transit data and subtracted to remove a slow trend present in the differential magnitudes. The times of the start of the exposures were given in JD/UTC in the FITS file headers, and the times of the midpoints of the exposures were converted into BJD/TDB (see Section 2.5.2).

In order to confirm the low scatter of the resulting light curves a second independent data reduction was performed by Dr John Taylor. The STARLINK/AUTOPHOTOM package (Eaton et al., 1999) driven by a custom C-shell script (Southworth et al., 2004b), was used and yielded a light curve with an rms scatter of 414 ppm for the first night of data. This result agrees with our light curve from DAOPHOT, once the discretization of the datapoints (AUTOPHOTOM quotes instrumental magnitudes to only three decimal places) was taken into account.

5.3 Data Analysis

The WASP-50 data were fitted in a similar manner to Chapters 3 and 4. Limb darkening was implemented using the standard quadratic law (see Section 2.7 for more details). PRISM used six system parameters given in Table 5.2 to model the system.

GEMC was used to fit the model to the data (see Section 2.8.3). Because GEMC is a hybrid between the Markov Chain Monte Carlo approach and a genetic algorithm, the burn-in phase is relatively short, allowing us to use a large parameter search space. The boundaries of the search space for each parameter are given in Tables 5.2 and 5.3 and which also contains the individual results for the two light curves. Table 5.4 gives the final photometric parameters for the WASP-50 system, which are weighted means of the results from the two individual fits. All errorbars denote 1-σ uncertainties. Fig. 5.5

Table 5.2: Derived photometric parameters from the 2011/11/20 lightcurve, plus the interval within which the best fit was searched for using GEMC.

Parameter	Symbol	Search interval	2011/11/20
Radius ratio	r_p/r_s	0.05 to 0.30	0.13710 ± 0.00049
Sum of fractional radii	$r_s + r_p$	0.10 to 0.50	0.1552 ± 0.0018
Linear LD coefficient	u_1	0.0 to 1.0	0.386 ± 0.068
Quadratic LD coefficient	u_2	0.0 to 1.0	0.281 ± 0.099
Inclination (degrees)	i	70.0 to 90.0	84.43 ± 0.17
Transit epoch (BJD/UTC)	T_0	±0.5 in phase	2455855.78172 ± 0.000076

Table 5.3: Derived photometric parameters from the 2011/11/24 lightcurve, plus the interval within which the best fit was searched for using GEMC.

Parameter	Symbol	Search interval	2011/11/24
Radius ratio	r_p/r_s	0.05 to 0.30	0.13661 ± 0.00036
Sum of fractional radii	$r_s + r_p$	0.10 to 0.50	0.1553 ± 0.0016
Linear LD coefficient	u_1	0.0 to 1.0	0.385 ± 0.049
Quadratic LD coefficient	u_2	0.0 to 1.0	0.279 ± 0.043
Inclination (degrees)	i	70.0 to 90.0	84.45 ± 0.14
Transit epoch (BJD/UTC)	T_0	±0.5 in phase	2455859.691755 ± 0.000118

Table 5.4: Combined photometric parameters from both lightcurves.

Parameter	Symbol	Combined photometric parameters
Radius ratio	r_p/r_s	0.13678 ± 0.00029
Sum of fractional radii	$r_s + r_p$	0.1552 ± 0.0012
Linear LD coefficient	u_1	0.386 ± 0.040
Quadratic LD coefficient	u_2	0.280 ± 0.040
Inclination (degrees)	i	84.44 ± 0.11

and 5.6 compares the light curves to the best-fitting models, including the residuals. The two datasets were modelled individually, and the agreement between the best-fit parameters is exceptionally good. The best-fit limb-darkening coefficients are also in good agreement with the theoretically predicted values for WASP-50 of $u_1 = 0.407$ and $u_2 = 0.281$ (Claret, 2004a).

The data were taken with 120 s and 150 s exposures, so the relatively long exposure times were checked to see if they affected the derived parameters. For this the data were modelled using the JKTEBOP code (Southworth et al., 2004a), finding results in good agreement with those from PRISM. JKTEBOP was then used to numerically integrate the model over the duration of each exposure whilst finding the best fit (Southworth, 2011). The final parameters for each lightcurve were altered by only 0.1 to 0.25-σ, allowing the conclusion that smearing of the transit shape due to long exposure times did not have a significant effect on the results.

To check for correlated 'red' noise the Monte Carlo and residual-permutation

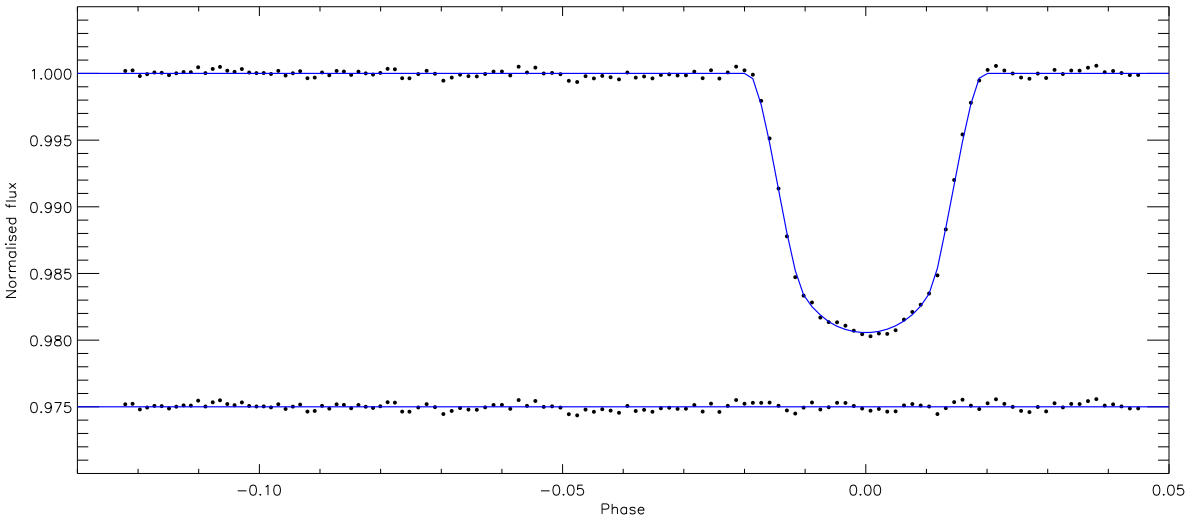

Figure 5.5: Transit light curve and the best-fitting model for WASP-50 on 2011/11/20. The residuals are displayed at the base of the figure.

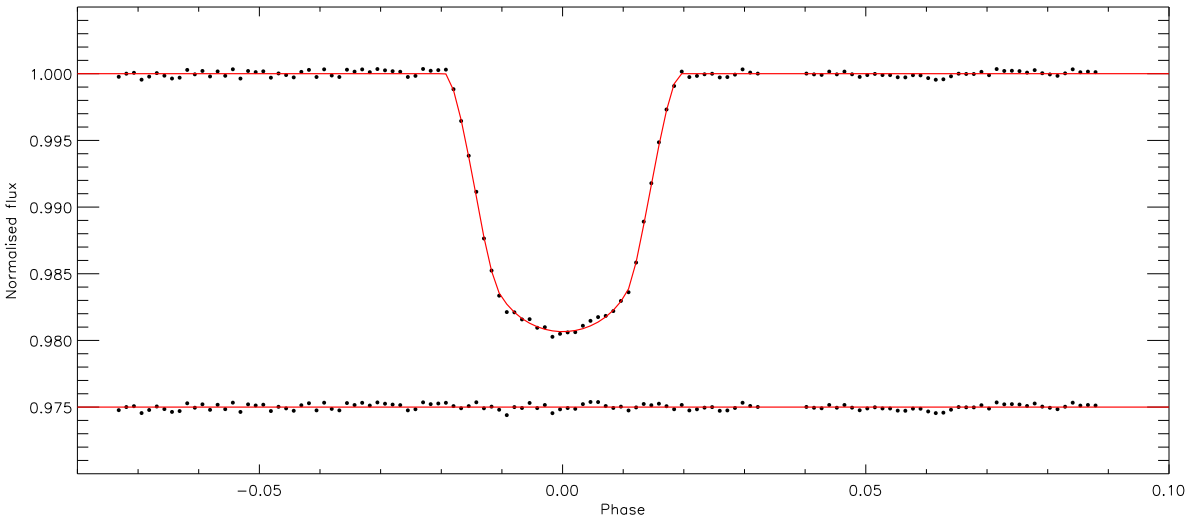

Figure 5.6: Transit light curve and the best-fitting model for WASP-50 on 2011/11/24. The residuals are displayed at the base of the figure. The gap in the data between phases 0.03 and 0.04 was caused by a technical difficulty with the shutter on EFOSC2. This was corrected by a shutdown and restart of the instrument. The telescope pointing was unaffected.

algorithms in JKTEBOP (Southworth, 2008) were used to assess the uncertainties in the fitted parameters. A difference between the two methods of only 0.1% was found, which showed that correlated noise was not present at a significant level in the data.

JKTEBOP was also used to check whether the removal of the slow drift in brightness with a first-order polynomial had any effect on the results. It was found that including the polynomial coefficients as fitted parameters caused changes in the other parameters of roughly 0.001-σ. Therefore the detrending process has had no deleterious effect on the results.

The available times of mid-transit for WASP-50 were collected from the literature (Gillon et al., 2011b; Sada et al., 2012). All timings were converted to the BJD/TDB timescale and used to obtain an improved orbital ephemeris:

$$T_0 = \mathrm{BJD/TDB}\ 2\,455\,558.61237(20) + 1.9550938(13) \times E$$

where E represents the cycle count with respect to the reference epoch and the bracketed quantities represent the uncertainty in the final digit of the preceding number. Figure 5.7 and Table 5.5 show the residuals of these times against the ephemeris. Examining the results show no evidence for transit timing variations in the WASP-50 planetary system.

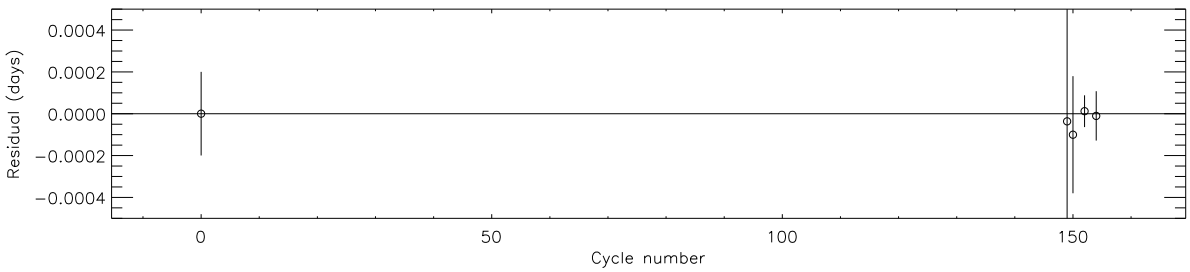

Figure 5.7: Residuals of the available times of mid-transit versus the orbital ephemeris found in this work. The two timings from this work are the last two points after cycle number 150.

Table 5.5: Times of minimum light of WASP-50 and their residuals versus the ephemeris derived in this work.

Time of minimum (BJD/TDB − 2400000)	Cycle no.	Residual (BJD)	Reference
55558.61237 ± 0.00020	0.0	0.00000	1
55849.92131 ± 0.00060	149.0	-0.00004	2
55851.87634 ± 0.00028	150.0	-0.00010	2
55855.78664 ± 0.00008	152.0	0.00001	3
55859.69680 ± 0.00012	154.0	-0.00001	3

References: (1) Gillon et al. (2011b); (2) Sada et al. (2012); (3) This work.

5.3.1 Physical Properties of the WASP-50 System

The work in this subsection was performed by Dr John Taylor and is included here because it is an integral part of the analysis of WASP-50.

With the photometric properties of WASP-50 measured the physical characteristics could be determined. The same approach as in Section 3.3.2 was used, which uses the parameters measured from the light curves and spectra, plus tabulated predictions of several theoretical models. The values of i, r_p/r_s and $r_s + r_p$ were used from Table 5.4, and the stellar properties of effective temperature $T_{\rm eff} = 5400 \pm 100\,{\rm K}$, metal abundance $[{\rm Fe/H}] = -0.12 \pm 0.08$ and velocity amplitude $K_{\rm s} = 256.6 \pm 4.4\,{\rm m\,s^{-1}}$ were taken from Gillon et al. (2011b).

An initial value of the velocity amplitude of the planet, $K_{\rm p}$, was used to calculate the physical properties of the system using standard formulae and the physical constants listed by Southworth (2011). The mass and [Fe/H] of the star were then used as interpolates within tabulated predictions from stellar theoretical models, in order to find the expected $T_{\rm eff}$ and radius. $K_{\rm p}$ was then iteratively refined to find the best agreement between the observed and predicted $T_{\rm eff}$, and the light-curve-derived $r_{\rm s}$ and predicted $\frac{R_{\rm s}}{a}$. This was performed for ages ranging from zero-age to the terminal-age main-sequence, in steps of 0.01 Gyr. The overall best fit was identified, yielding esti-

mates of the physical properties of the system and the evolutionary age of the star. This procedure was performed separately using five different sets of stellar theoretical models (see Southworth, 2010) and the spread of values for each output parameter was used to determine a systematic error. Statistical errors were propagated by perturbing each input parameter in turn to quantify the effect on each output parameter.

Table 5.6: Physical properties of the WASP-50 system. The equilibrium temperature, $T'_{\rm eq}$, is for an assumed zero albedo and full heat redistribution. Θ is the Safronov (1972) number. Both statistical and systematic uncertainties are given. The first uncertainty is the statistical uncertainty and the second is the systematic uncertainty.

Parameter	This work	Gillon et al. (2011b)
$M_{\rm A}$ ($\mathrm{M}_{\odot}$)	$0.861 \pm 0.052 \pm 0.023$	$0.892^{+0.080}_{-0.074}$
$R_{\rm A}$ ($\mathrm{R}_{\odot}$)	$0.855 \pm 0.018 \pm 0.007$	0.843 ± 0.031
$\log g_{\rm A}$ (cgs)	$4.509 \pm 0.012 \pm 0.004$	4.537 ± 0.022
$\rho_{\rm A}$ ($\rho_{\odot}$)	1.376 ± 0.032	$1.48^{+0.10}_{-0.09}$
$M_{\rm b}$ ($\mathrm{M}_{\rm Jup}$)	$1.437 \pm 0.063 \pm 0.025$	$1.468^{+0.091}_{-0.086}$
$R_{\rm b}$ ($\mathrm{R}_{\rm Jup}$)	$1.138 \pm 0.024 \pm 0.010$	1.153 ± 0.048
$g_{\rm b}$ ($\mathrm{m\,s^{-2}}$)	27.50 ± 0.64	27.5 ± 1.6
$\rho_{\rm b}$ ($\rho_{\rm Jup}$)	$0.911 \pm 0.032 \pm 0.008$	$0.958^{+0.095}_{-0.082}$
$T'_{\rm eq}$ (K)	1410 ± 26	1393 ± 30
Θ	$0.0853 \pm 0.0024 \pm 0.0007$	
a (AU)	$0.02913 \pm 0.00059 \pm 0.00025$	0.02945 ± 0.00085
Age (Gyr)	$8.1\,^{+6.7\,+1.5}_{-4.4\,-1.3}$	

The final results of this process have good internal agreement (between the five sets of theoretical models) and are also consistent with those found by Gillon et al. (2011b). The final physical properties are given in Table 5.6 and include separate statistical and systematic errorbars for those parameters with a dependence on the theoretical models. The final statistical errorbar for each parameter is the largest of the individual ones from the solutions using each of the five different stellar models. The systematic errorbar is the largest difference between the mean and the individual values of the parameter from the five solutions.

5.4 Discussion and Conclusions

While the two transits of WASP-50 showed no evidence of starspot anomalies, they achieved a ground breaking precision for ground-based transit photometry. When viewing the Euler transit from Gillon et al. (2011b) with the second transit of WASP-50 (see Figure 5.8) the difference in the rms scatter is evident. It should be noted that the two telescopes are of different sizes, with the NTT being 3.58 m and the Euler telescope being 1.2 m. Therefore the NTT is able to collect approximately nine times more photons than the Euler.

In the pursuit of obtaining accurate properties for transiting extrasolar planetary systems, photometric precisions of 258 and 211 ppm were achieved in observations of WASP-50, which are a record for ground-based photometry of a point source. The approach was to heavily defocus the 3.6 m NTT and to use exposure times of 120–150 s. The observations also benefited from the presence of a good comparison star, at a distance of 2.25 arcmin from WASP-50 and with similar colours and r-band apparent magnitude. The sky brightness was also low, as the Moon was below the horizon for most of the observations.

The reduction of the data used two independent pipelines, finding agreement between them. The lightcurves were modelled using two different models (PRISM and JKTEBOP), again finding good agreement. From these results and published spectroscopic measurements it was possible to deduced the physical properties of the WASP-50 system to a high-precision. The properties of the planet WASP-50 b are now known to within 5% (mass), 2% (radius), 4% (density) and 2% (surface gravity). This compares to 6%, 4%, 9% and 6%, respectively, in the discovery paper (Gillon et al., 2011b). It was also possible to obtain a refined orbital ephemeris. Further improvements in precision could be made in the shorter term by obtaining additional radial velocity measurements, and in the longer term by using sets of stellar models that show a better interagreement on properties of the host star WASP-50.

In the study of WASP-19 (Chapter 3) a modest discrepancy was found between the limb-darkening coefficients measured from the three datasets taken with the same

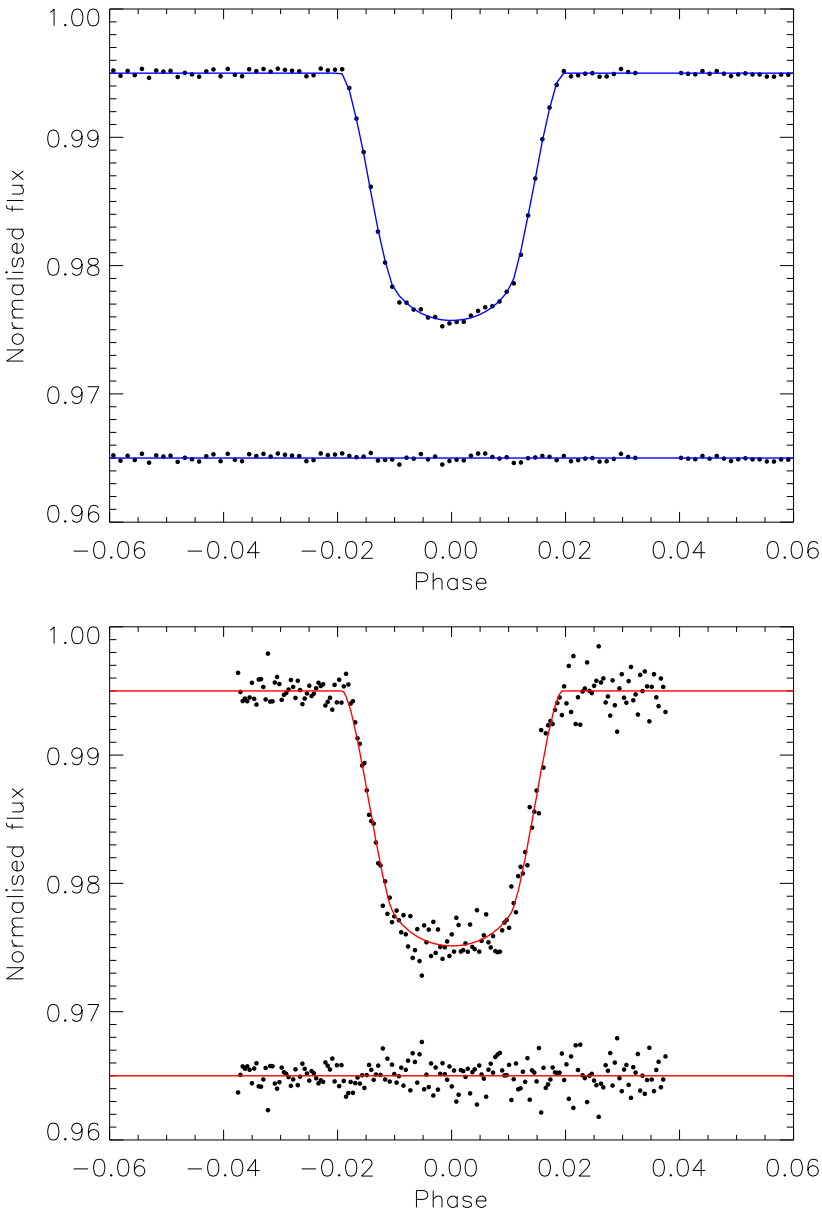

Figure 5.8: Comparison between the best transits from the NTT and Gillon et al. (2011b). The top panel shows a transit and best-fitting model for the NTT observation of WASP-50 taken on 2011/10/24. The bottom panel shows a transit and best-fitting model for WASP-50 using the Euler telescope from Gillon et al. (2011b).

telescope. This was attributed to the fact that WASP-19 A is an active star with significant starspot activity, which alters the limb-darkening behaviour of the star (Ballerini et al., 2012). Whilst WASP-50 does show modest chromospheric activity, as judged from emission in the Ca II H and K lines (Gillon et al., 2011b), starspot anomalies have not been observed in any of the six transit light curves of this system. The limb-darkening coefficients found from the two WASP-50 datasets are in excellent agreement (0.02-σ), supporting the suggestion that starspots affect stellar limb-darkening.

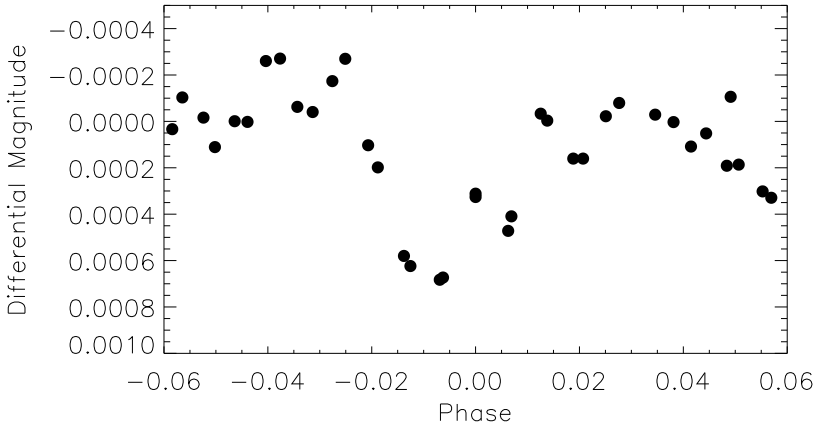

Figure 5.9: Simulated light curve of a $2\,R_\oplus$ planet orbiting WASP-50.

Observations at this high-precision were then checked to see if they could be used to characterise transiting super-Earths. A synthetic transit of a $2\,R_\oplus$ planet was placed in front of WASP-50 by injecting the transit into the residuals of the best fits from both nights, and then binning the data together. This simulated light curve (Fig. 5.9) shows a clear transit signature, suggesting that ground-based defocused photometry of transiting super-Earths is a viable possibility.

6 Summary and Final Discussion

This Chapter draws upon the discussions and conclusions from the application of PRISM and GEMC to the analysis of TEPs. Section 6.1 provides a brief summary of the research contained in this thesis and gives the main conclusions of the research. Section 6.2 describes the key implications that PRISM and GEMC have had on the exoplanet community together with the results from WASP-19 and WASP-50. It then goes on to discuss future modifications that will be made to both PRISM and GEMC and future observational strategies which can make use of these new tools. Section 6.3 then ends the Chapter with a final wrap-up.

6.1 Summary of Research and Main Conclusions

The research performed for this thesis required the creation of a model (PRISM) to precisely determine the photometric properties of a TEP's lightcurve containing a starspot anomaly. Because of the method employed in modelling starspots on a stellar disc, the required computing time of a single function iteration was approximately one second. When combined with an MCMC algorithm to both optimise the model and to perform a Bayesian statistical analysis the total computing time increased to 10^6 seconds or 11.6 days. To reduce the computing time a new form of optimisation algorithm was created (GEMC). GEMC is a hybrid between MCMC and a genetic algorithm (GA) and is based on DE-MC put forward by Ter Braak (2006). While running tests on GEMC, it out-performed both an MCMC and a GA in ascertaining the best fit to transit photometry and the associated parameter uncertainties by only taking 14 hours per data set for WASP-19.

After the creation of PRISM and GEMC the next step was to analyse transit photometry of TEPs containing starspot anomalies. This was done for three transits of WASP-19 and four transits of WASP-6. Two transits of WASP-50 that did not contain a starspot anomaly were also analysed.

Two consecutive transits of WASP-19 separated by approximately 19 hours contained a starspot anomaly and as such it was possible to determine that the two starspot anomalies were caused by the same starspot. From this it was possible to precisely determine the latitudinal rotation period of WASP-19 to be $P_{\rm rot} = 11.76 \pm 0.09\,{\rm d}$ at a co-latitude of 65°. This equated to a surface velocity of $v_{(65^\circ)} = 3.88 \pm 0.15\,{\rm km\,s^{-1}}$. With the position of the starspot known at two different but distinct times it was possible to calculate the sky-projected spin orbit alignment of $\lambda = 1.0^\circ \pm 1.2^\circ$. Combined with the fact that there is no evidence to suggest that the true system obliquity ψ was large, then it followed that WASP-19 b experienced disc-migration through interactions with the protoplanetary disc to position the planet close to its host star.

Two transits of WASP-6 contained a starspot anomaly, but unlike WASP-19 the two transits were separated by 27 days. Therefore it is not possible to definitively state whether or not the starspot anomalies were caused by the same starspot. When modelled by PRISM the starspot from both data sets were the same angular size. Coupled with the fact that for a starspot to survive for 30 days it must have an angular size greater than 1° (see Section 4.1.1) then it is feasible that the anomalies are due to the same starspot. Using the circumstantial evidence both $P_{\rm rot}$ and λ could be calculated for WASP-6 by making the assumptions that the two starspot anomalies were generated by the same starspot and that WASP-6 is similar in magnetic activity, age and therefore rotation as WASP-19. It was found that $P_{\rm rot} = 12.56 \pm 0.13\,{\rm d}$ at a co-latitude of 77.5° but it is also conceivable that $P_{\rm rot} = 23.56 \pm 0.13\,{\rm d}$, due to the surface velocity v of both rotation periods agreeing with previous measurements of $v \sin I$ (see Gillon et al. 2009a; Doyle et al. 2013). In either case it was found that $\lambda = 6.4^\circ \pm 2.3^\circ$, indicating potential axial alignment for the WASP-6 planetary system. This helps deduce that WASP-6 b formed beyond the snowline and through disc-migration came to orbit close to the host star, providing that the two starspot anomalies are created by the planet crossing the same starspot twice.

The original observing strategy for WASP-50 was to obtain two consecutive lightcurves containing starspot anomalies. It can be seen from Chapter 5 that no starspot anomalies were detected. However, in the process the highest precision for

ground-based photometry of a TEP was achieved. The rms (root mean squared) scatter for each data set when compared to the best-fitting model generated from PRISM and GEMC are 211 and 258 ppm (parts per million). This compares to 316 ppm for TrES-2 using the 10.4 m Gran Telescopio Canarias (Colón et al., 2010). The analysis of the WASP-50 lightcurves yielded new refined parameters for the host star's mass $0.861 \pm 0.057\,M_{\odot}$, radius $0.855 \pm 0.019\,R_{\odot}$ and the planet's mass $1.437 \pm 0.068\,M_{Jup}$, radius $1.138 \pm 0.026\,R_{Jup}$ and density $0.911 \pm 0.033\,\rho_{Jup}$. The results from the WASP-50 lightcurves reduced the uncertainties in the system parameters from 6% (mass), 4% (radius), 9% (density) and 6% (surface gravity) to 5%, 2%, 4% and 2% respectively.

6.1.1 Main Conclusions

The development of GEMC has allowed for a major reduction in the amount of computing time required to find the global solution (compared to an MCMC and a GA) in a large and rugged parameter space. This can be seen by comparing panel f in Figure 2.15 and Figure 2.20. PIKAIA took around 2000 function iterations to find the global solution peak (Figure 2.15) while GEMC only took 200 function iterations to find the global maximum peak (Figure 2.20), a 10-fold improvement. At present GEMC only takes 4000 function iterations to find the global solution for a transit lightcurve[1]. GEMC still requires a further 10^6 (10 chains of a 10^5 length) to perform a detailed Bayesian analysis for the photometric uncertainties. This is due to GEMC still performing a MCMC analysis after the best-fitting solution is found.

In Section 1.5 it was shown that starspots affect the whole transit lightcurve and therefore a new model was required to precisely determine the transit properties. In the case of WASP-19 (Chapter 3) three transit lightcurves had been observed but two of the lightcurves contained a starspot anomaly and as such when using conventional models the photometric parameters from the three lightcurves did not agree within

[1] Using 200 chains for 20 generations for the WASP-6 data.

their 1-σ uncertainties. This meant that only one of the lightcurves was able to be used in the analysis of the WASP-19 system (see Hellier et al. 2011).

The research performed for both WASP-19 and WASP-6 show that using PRISM to model transit lightcurves containing starspot anomalies, allows a precise determination of the system parameters. This shows that even if used as a stand alone method both PRISM and GEMC allow transit lightcurves contaminated by a starspot anomaly to be used in the determination of the photometric parameters of TEPs. Without the ability to analyse the two transits containing a starspot anomaly for WASP-19 then the final photometric parameter uncertainties would have increased.[2]

In the event when two closely spaced transits both contain a starspot anomaly (such as WASP-19) it is possible to determine the latitudinal rotational velocity and, when combined with the physical stellar radius, the latitudinal surface velocity can be found. It is also possible to measure λ and potentially the true stellar obliquity ψ. In the case of WASP-19, λ was calculated by determining the angle between a vector connecting the centre of the starspot at the two different positions and the horizontal. In the event that ψ is large then the stellar rotation axis would be pointing either towards or away from the observer and therefore the path traced out by the starspot would represent a curved motion across the curved stellar surface. If it was possible for a fourth transit of WASP-19 to have been observed between the two transits containing the starspot anomaly then the precise value of ψ could have been calculated. This is because if the centre of the starspot fell on the vector connecting the centre of the two starspots then the stellar rotation axis would lie in the plane of the sky and ψ would be equal to λ. On the other-hand if the centre of the starspot did not fall on the vector then the travel path of the starspot would have been curved and the stellar rotation axis would have been pointing either towards or away from the observer and ψ would be greater than λ.

By determining λ and ψ of the planetary system it is possible to begin to under-

[2]For the inclination of WASP-19 the uncertainty would increase from $\pm 0.23^\circ$ to $\pm 0.44^\circ$, almost a 100% increase.

stand the primary process in the dynamical evolution of the system. In Section 1.4.2 it was mentioned that the Rossiter-McLaughlin (RM) effect can be used to ascertain a value for λ. One limitation of this method though is from an excess radial velocity jitter (stellar activity aka. starspots). Therefore, the use of the RM effect either requires magnetically quiet stars or the transit cord of the planet to bypass any active latitudes on the stellar disc. The opposite is true when using starspot anomalies in lightcurves to determine λ. Due to this the two different methods compliment each other in probing the dominant process in the dynamical evolution of TEPs. It should be noted that in both the cases of WASP-19 and WASP-6 the measured uncertainty in λ is much smaller than measured using the RM effect. This implies that the starspot method to measure λ is superior to the RM effect in terms of reduced uncertainty in measuring λ. However, as was shown in observing WASP-50, the starspot method does not always work in terms of obtaining transit lightcurves affected by a starspot anomaly. The RM effect does have a high success rate in measuring a value of λ but rarely achieves a similar precision.

Winn et al. (2010a) suggest that cool host stars will harbour planets with low orbital obliquities due to having a thicker convective zone compared to hotter stars (i.e. $T_{eff} > 6250\,\mathrm{K}$). They propose that the planetary orbit realigns with the photosphere of cooler stars due to tidal dissipation with the stars convective zone. Winn et al. (2010a) based their conclusions on the analysis of 19 planetary systems (see Figure 6.1).

At present there are 68 TEPs with published λ values[3]. The λ values for WASP-6 and WASP-19 were updated to the values found in this work and a new plot of λ against T_{eff} was created (see Figure 6.2). To remove any ambiguity in the plot due to negative values of λ the magnitudes, $|\lambda|$ were calculated and plotted. As can be seen, a large proportion of cool stars ($T_{eff} < 6250\,\mathrm{K}$) harbour aligned systems, while the majority of misaligned systems have hot host stars. This trend supports the re-wording of Winn et al. (2010a) from hot stars with hot-Jupiters will have high obliquities to

[3]All measured λ and T_{eff} values of the known TEPs were obtained from the 30/01/2014 version of the TEPCat catalogue (Southworth, 2011).
(`http://www.astro.keele.ac.uk/~jkt/tepcat/`)

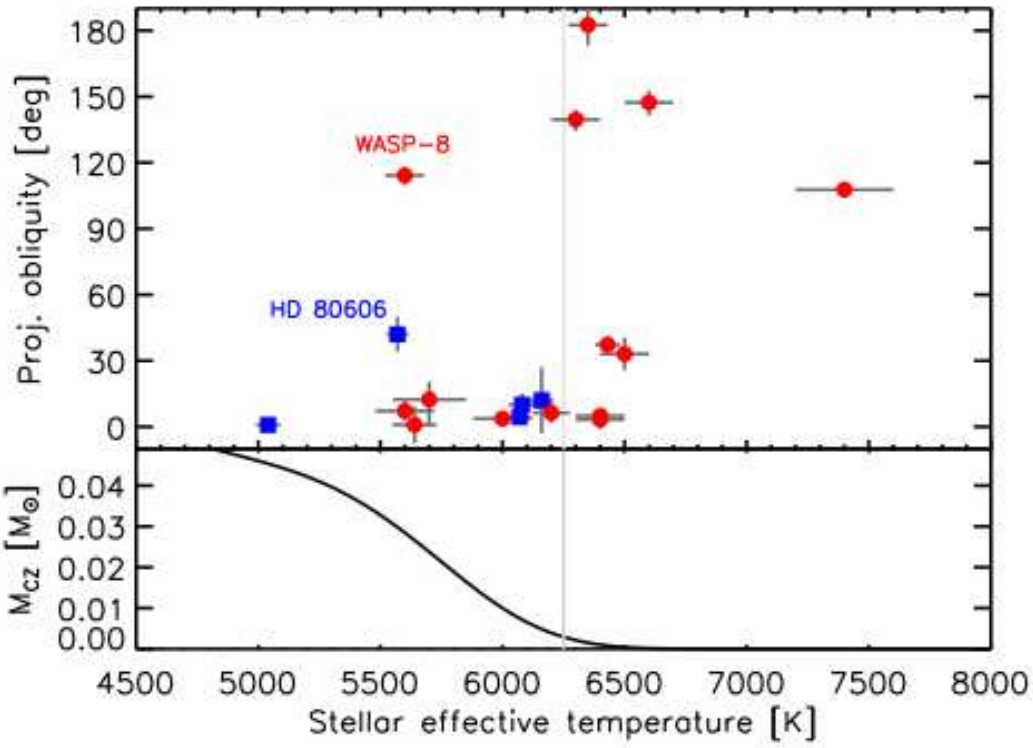

Figure 6.1: Cool stars have low obliquities (Winn et al., 2010a). The top panel shows λ plotted against T_{eff} of the host star for 19 planetary systems. The blue squares indicate planets found from RV surveys while the red circles represent planets found from transit surveys. The $T_{eff} = 6250\,\mathrm{K}$ line represents the transition between aligned and non aligned systems, with the two exceptions named. The bottom panel shows the mass of the convective zone as a function of T_{eff} (Pinsonneault et al., 2001).

cool stars with hot-Jupiters will have low obliquities. This trend can also be explained by the time required for the system to align. Hot stars will have thinner convective zones and will therefore take longer to align the photosphere with the planetary orbit. Because of this, by examining λ of hot stars a greater proportion will have misaligned systems compared to cool stars where the alignment process is much shorter and so will have a higher proportion of aligned systems. Cool stars also live longer so the ones that are observed are on average older. They have therefore had more time for tidal effects to work (Triaud, 2011b).

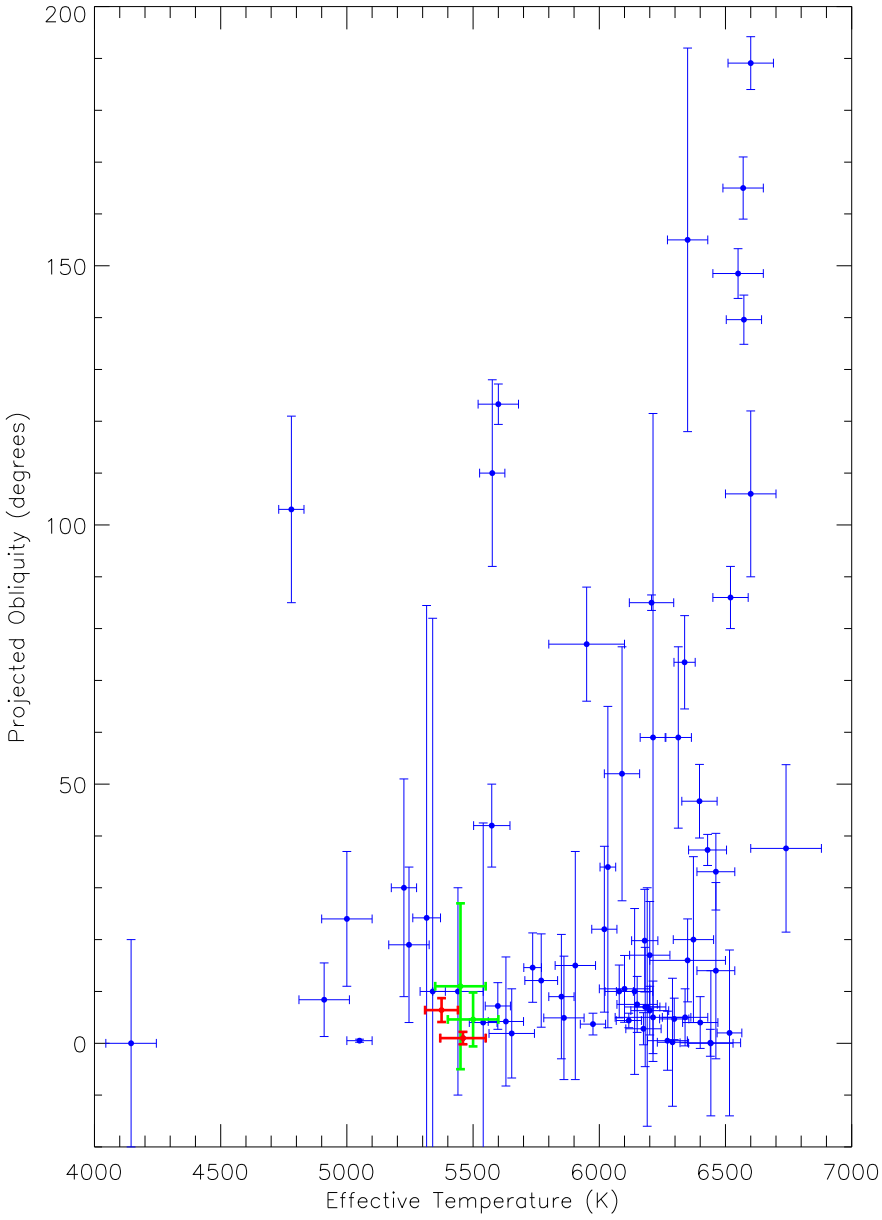

Figure 6.2: $|\lambda|$ against T_{eff} for 68 TEPs from TEPCat including WASP-19 and WASP-6. The green and red data points are WASP-6 (left) and WASP-19 (right). The green data points represent values from the literature (e.g. WASP-6: Gillon et al. 2009a and WASP-19: Hellier et al. 2011) and the red data points represent the values found from this work. The trend in the data suggests that cool host stars harbour aligned systems.

6.2 Implications and Further Work

From the development of PRISM it is now possible for researchers to accurately model both the transit and the starspot parameters from transit photometry of a TEP. The development of GEMC has shown how it is possible to combine MCMC with a genetic algorithm to allow a fast and efficient exploration of a large and complex parameter space, while maintaining the ability to perform a Bayesian statistical analysis. Making these two new codes publicly available allows researchers to use starspot 'contaminated' lightcurves in their analysis to determine the physical properties of a TEP. It also allows them to use transit photometry to measure λ and to investigate the dominant process in the dynamical evolution of TEPs.

Since PRISM and GEMC have been made publicly available[4], they have been used by the HAT-South research group to model transits containing a starspot anomaly for the planetary system HATS-2 (Mohler-Fischer et al., 2013). Two transits of HATS-2 were observed in four optical passbands using GROND, obtaining eight transit light curves. The optical passbands used are the same as those used for WASP-19 in Section 3.4. In the first transit a dark starspot anomaly was detected coupled with a faint bright starspot, while the second transit contained both a starspot and a clear bright starspot anomaly in the g'-band (see Figure 6.3).

The bright starspot in the g'-band transit observed on 2012/06/01 can also be seen in the other bands with decreasing amplitude, but due to PRISM only being able to model a single starspot the g'-band lightcurve from the 2012/06/01 was left out of the analysis. The other three lightcurves from 2012/06/01 were just modelled for a single dark starspot.

Because the two transits were separated by 94 days Mohler-Fischer et al. (2013) could not precisely determine that the dark starspot anomaly seen was generated from the same starspot. However, they calculated that $P_{\rm rot} = 31 \pm 1\,{\rm d}$ and $\lambda = 8^\circ \pm 8^\circ$ for HATS-2 under the assumption that the two dark starspot anomalies are due to the

[4] `http://www.astro.keele.ac.uk/~jtr/downloads.html`

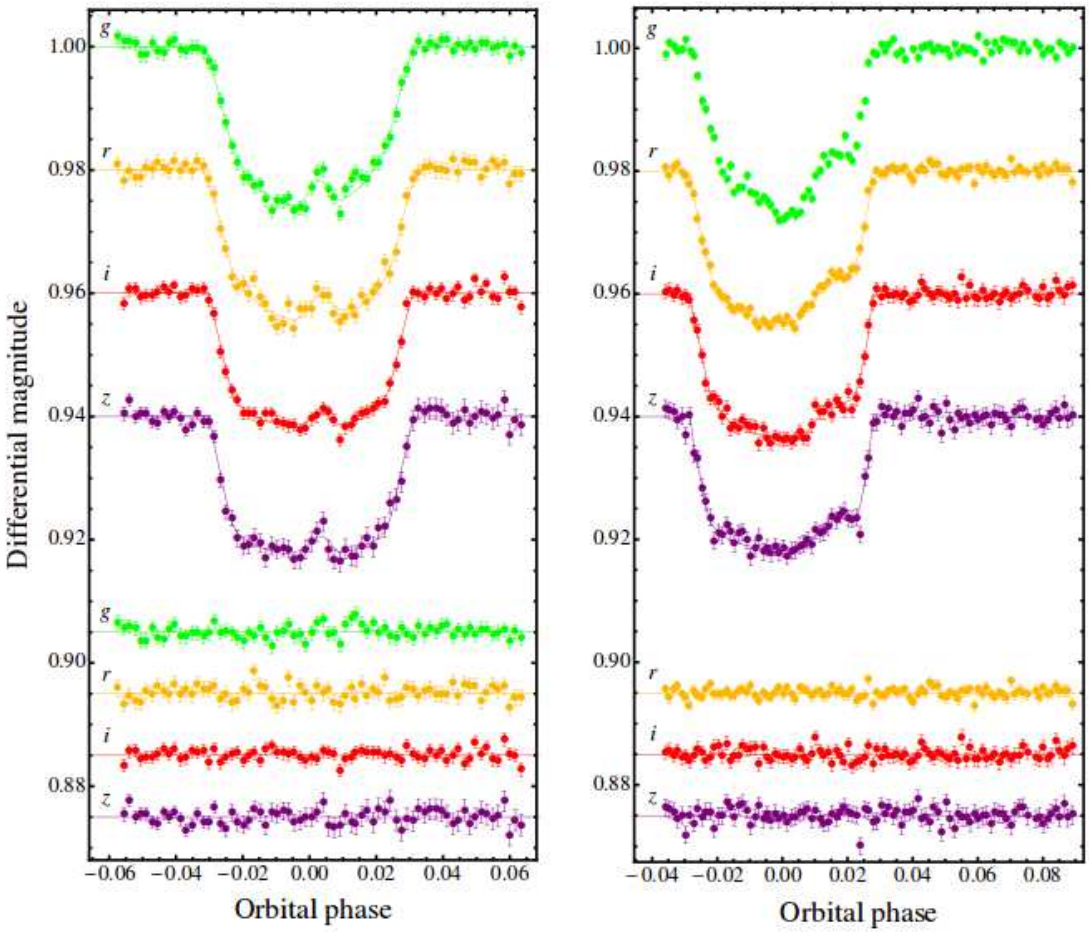

Figure 6.3: Two simultaneous optical transits of HATS-2 together with the best-fitting models using PRISM and GEMC (Mohler-Fischer et al., 2013). The left panel shows the transit from 2012/02/28 and shows a dark starspot. The right panel shows the transit from 2012/06/01 and shows a dark starspot in all four bands and a bright starspot in the g'-band.

same starspot. Due to observing the dark starspot in four optical bands they were then able to determine the temperature of the dark starspot and found both the temperature and size of the starspot to be in agreement with other G-K dwarf stars. Mohler-Fischer et al. (2013) was then able to use the final system photometric parameters from the PRISM and GEMC fits in the final analysis.

The research conducted by Mohler-Fischer et al. (2013) has shown how both PRISM and GEMC are starting to be used in the scientific community and are an invaluable tool in the analysis of transit lightcurves of TEPs containing a starspot anomaly. The research conducted by Mohler-Fischer et al. (2013) has also highlighted areas in which both PRISM and GEMC could be improved to increase the usefulness of the codes to the scientific community.

6.2.1 Future Improvements to PRISM and GEMC

At present PRISM models a planetary transit using a circular orbit. While this allows efficient modelling of the vast majority of TEPs it does leave some inconsistencies when modelling TEPs with slightly eccentric orbits. This was encountered when modelling the four transit lightcurves of WASP-6 where $e = 0.054^{+0.018}_{-0.015}$. To solve this, PRISM can be modified to use e and ω in calculating the position of the planet. Both e and ω will be set as fixed parameters in the same way that the orbital period is. PRISM will not be set to fit for e or ω because it is not possible to ascertain these values from photometry only (due to only observing a small fraction of the orbit) unless an occultation is observed (Kipping et al., 2012).

At present PRISM models the position of a starspot using longitude and co-latitude coordinates. This allows a starspot to be positioned anywhere on the stellar disc but the latitudinal position of the starspot is confined to lie within the transit cord. To improve efficiency and convergence, the latitudinal position of the starspot could be parametrised to a value $-1 \leq t \geq 1$, where $t = 0$ equates the centre of the starspot to the impact parameter b, $t = 1$ represents the edge of the starspot touching the upper edge of the transit cord ($b + r_p + r_{spot}$) and $t = -1$ would represent the opposite ($b - r_p - r_{spot}$). With this new parametrisation the inclination of the planetary orbit i can be perturbed and the latitudinal position of the starspot will automatically shift to the corresponding position on the stellar disc and so maintain the amplitude of the starspot anomaly.

GEMC is currently hard coded to fit for a single starspot. This was done due to

designing an input file, edited by the user. From this the user can select the desired parameter search space for each of the spot's parameters. Removing this feature and allowing GEMC to select the parameter search space for each of the spot's parameters would allow the input file to simply ask how many dark and bright spots are to be fitted for. This will allow GEMC to fit for multiple starspot anomalies in a single transit.

Before the MCMC component of GEMC begins the user designates in which generation the 'burn in' should end. Depending on the number of chains being used and the size of the parameter space this can be after 20 generations. By introducing the Gelman-Rubin statistic (Gelman & Rubin, 1992) GEMC could self check the variance within the chains and the population. Once the Gelman-Rubin statistic reaches a user defined threshold (e.g. less than 1.1) GEMC could display the best fit and allow the user an option to resume with finding the parameter uncertainties or to stop to allow the user to alter the parameter search space or the number of chains being used.

To find the uncertainties in the parameters GEMC uses an MCMC algorithm. Due to PRISM using 10 different parameters, trying to find the correct step size for each parameter for individual data sets can take time and requires multiple runs. Replacing the MCMC component with DE-MC would remove the need to do this. This is because the step size for each parameter is dependent on the variance in the population clustered around the solution. Replacing MCMC with DE-MC will also remove the need to run GEMC with a large number of chains to find the optimal solution and to then re-run GEMC with a small number of chains to allow for longer chain length to accurately probe the posterior distribution. Using DE-MC it is possible to use over 100 chains for only 1500 generations (Welsh et al., 2012) or approximately 10^5 function iterations. This is a 10-fold decrease in the amount of function iterations required compared to the MCMC section of GEMC.

To improve the efficiency in modelling and fitting multiband photometry, PRISM will be modified to fit multiple transits simultaneously which will increase PRISM's usability to the scientific community. The idea will allow users to set which parameters are shared between the individual lightcurves (e.g. inclination) and set which parameters are independent for each lightcurve (e.g. transit depth).

It was seen in Chapter 3 that the LD coefficients of transit lightcurves affected by a starspot anomaly do not usually agree with theoretical values. Ballerini et al. (2012) states that the LD coefficients are affected by starspots due to the LD coefficients being wavelength dependent. Because a starspot will have a different temperature compared to the surrounding photosphere then the LD coefficients of the region of the photosphere affected by the starspot will be different to those of the stellar disc (Ballerini et al., 2012). To help solve this problem PRISM will be modified to model two sets of LD coefficients. The first set represents the LD of the stellar disc while the second set will represent the LD of the starspot itself. This should allow the LD coefficients of the stellar disc to agree with tabulated theoretical values.

To decrease the amount of time required to find the optimal solution PRISM will be re-written in FORTRAN. This will have two major effects. The first will make PRISM more valuable to the scientific community, as users will no longer require an expensive IDL licence. The second will yield an expected improvement of a factor of five in speed (e.g. Eastman et al., 2013). It was mentioned in Section 2.6.1 that the fastest method to model planetary transits was to use an analytical approach. The final improvement to PRISM would be to write a new analytical version, A-PRISM (Analytical Planetary Retrospective Integrated Starspot Model). This final foreseeable improvement will require the greatest investment of time, but the rewards of having a model that can perform tens of function evaluations a second will allow multiple lightcurves to be fitted simultaneously by greatly reducing the overall computation time for each lightcurve to a matter of hours.

6.2.2 Future Observational Strategies

The primary future observational strategy is to probe the dynamical evolution of TEPs. By performing high-precision defocused photometry of TEPs coupled with using PRISM and GEMC it is possible to accurately model transit photometry containing a starspot anomaly. If two closely spaced transits contain a starspot anomaly it should be possible to precisely determine if the anomaly is generated from the same starspot. From this

method it is then possible to obtain P_{rot} and λ of the system. By increasing the number of known TEPs with measurements of λ it will be possible to explore the exact dynamical evolution process involved in creating these systems. An offshoot from this observational strategy would be in obtaining high-precision photometry which would lead to measuring the physical properties of TEPs to an extremely high-precision (e.g. Chapter 5). By achieving high-precision measurements of a planet's radius it is then possible to determine the mass of the planetary core using theoretical models (e.g. Fortney et al., 2007).

For highly irradiated planets, the atmosphere at optical wavelengths is a vital part of the energy budget of the planet, as it is where the bulk of the stellar flux is deposited (Sing et al., 2011). By using either GROND on the ESO-MPG 2.2 m or BUSCA on the 2.2 m telescope at Calar Alto, Spain to perform simultaneous multiband defocused photometry of TEPs, it is possible to measure variations in the planetary radius at different wavelengths. Such variations can arise from Rayleigh scattering and from molecular opacities, so are tracers of the atmospheric conditions and chemical composition (Southworth et al., 2012a; Mancini et al., 2013a,b,c). By using a wide wavelength range (GROND simultaneously covers the optical to NIR and BUSCA covers the optical) a broadband transmission spectrum can be constructed (e.g. Nikolov et al., 2013). Whilst the Hubble Space Telescope (HST) is the instrument of choice for such work, its extremely high cost coupled with large and unavoidable systematic effects means it has been used for only a very few objects. Figure 6.4 shows an example of multiband defocused photometry of HAT-P-32 taken using BUSCA. The rms scatter in the UV band is only 920 ppm, a record for a ground-based optical UV band lightcurve. The lightcurves were observed on 2011/08/24.

It is possible to perform multiband photometry to study the effect of starspots on the transit shape as a function of wavelength. The presence of starspots hampers accurate measurements of the planetary radius. By using PRISM this is not an issue. Modelling a starspot at multiple wavelengths allows the temperature of the spot to be found and breaks the degeneracy between the contrast and size of a starspot in single-band photometry. This has already been done for a starspot in a single transit

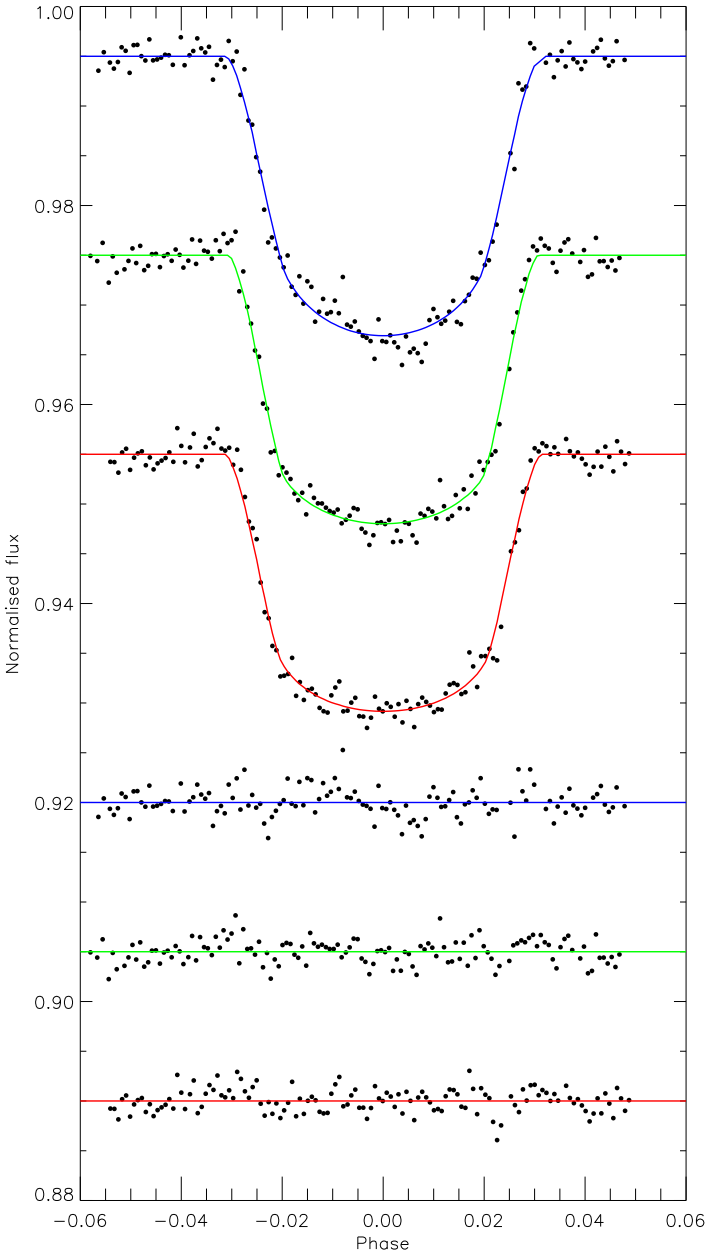

Figure 6.4: Three simultaneous optical transits of HAT-P-32 observed using BUSCA on 2011/08/24. The best fits are shown where blue represents the Strömgren u-band, green represents Strömgren b-band and red represents the Strömgren y-band. The rms scatters from top to bottom are 920, 850 and 890 ppm.

of WASP-19 observed by GROND and modelled using PRISM (see Section 3.4.2) and two transits of HATS-2 (Mohler-Fischer et al., 2013), resulting in a measurement of the spot's temperature. Using GROND and BUSCA to observe planetary transits therefore allows the temperature and size of starspots to be determined, probe the dynamical evolution of the system, construct a broadband transmission spectrum of the planet, and to determine the precise physical properties of the planet and its host star.

The transit-spot method gives a precise measurement of the stellar rotation period which combined with the gyrochronology relationship (e.g. Barnes, 2007) gives the age of the host star. The age can then be compared to results from stellar evolution models. This was done for WASP-19 by Hebb et al. (2010) using $P_{rot} = 10.5 \pm 0.2$ days from rotational modulation resulting in an age of 500–600 Myr for a G8V star like WASP-19. This was not consistent with an older age inferred from stellar evolution models. They proposed that as WASP-19 b has been spiralling in towards the host star during the planets lifetime and that the planet has increased the spin rate for the host star.

By combining observations of the calcium H and K lines (which are indicators of stellar magnetic activity) by using VLT/UVES with the starspot method it would be possible to compare the starspot properties with both the stellar rotation period and the calcium H and K lines. From this the relationship between the calcium H and K lines and the physical properties of starspots can be investigated.

The speed of the improved version of A-PRISM will allow transit lightcurves of TEPs containing starspot anomalies in the *Kepler* public science data to be used to probe the dominant process in the dynamical evolution of these systems (e.g. Sanchis-Ojeda & Winn, 2011; Sanchis-Ojeda et al., 2012, 2013), hence increasing the number of possible TEPs for which a λ measurement is available.

6.3 Final Wrap-up

The work completed for this thesis has developed a new set of tools to allow researchers to model starspot anomalies in planetary transits. Once developed the new tools were

then used in the modelling of eight transits for three TEPs. This work will have the affect of allowing transit lightcurves contaminated with a starspot anomaly to be used in precisely determining the transit parameters of the system. When multiple transits contaminated with a starspot anomaly are used PRISM will allow researchers to determine the co-latitudinal rotation period of the host star and will also allow them to determine λ. Because of this PRISM and GEMC can be used to help researchers begin in determining the dominant process in the dynamical evolution of the planetary system.

A Peer-Reviewed Publications

A.1 First Author Publications

Tregloan-Reed J., Southworth J., 2014 IAU Symposium, vol. 293, p. 116
Observation and Modelling of Transits and Starspots in the WASP-19 Planetary System

Tregloan-Reed J., Southworth J., 2013 MNRAS, 431, 966.
An extremely high photometric precision in ground-based observations of two transits in the WASP-50 planetary system

Tregloan-Reed J., Southworth J., Tappert C., 2013 MNRAS, 428, 3671.
Transits and Starspots in the WASP-19 Planetary System

A.2 Co-Author Publications

Southworth J., et al., (including Tregloan-Reed J.,) 2014, MNRAS, 444, 776
High-precision photometry by telescope defocussing - VI. WASP-24, WASP-25 and WASP-26

Mancini L., et al., (including Tregloan-Reed J.,) 2014, MNRAS, 443, 2391
Physical properties, starspot activity, orbital obliquity, and transmission spectrum of the Qatar-2 planetary system from multi-colour photometry

Tsapras Y., et al., (including Tregloan-Reed J.,) 2014, ApJ, 782, 48.
A Super-Jupiter Orbiting a Late-type Star: A Refined Analysis of Microlensing Event OGLE-2012-BLG-0406

Mancini L., et al., (including Tregloan-Reed J.,) 2013 MNRAS, 436, 2.
Physical properties, transmission and emission spectra of the WASP-19 planetary system from multi-colour photometry

Southworth J., et al., (including Tregloan-Reed J.,) 2013 MNRAS, 434, 1300.
High-precision photometry by telescope defocusing. V. WASP-15 and WASP-16

Arellano Ferro A., et al., (including Tregloan-Reed J.,) 2013 MNRAS, 434, 1220.
A detailed census of variable stars in the globular cluster NGC 6333 (M9) from CCD differential photometry

Kains N., et al., (including Tregloan-Reed J.,) 2013, A&A, 555, A36.
Estimating the parameters of globular cluster M 30 (NGC 7099) from time-series photometry

Mahtani D. P., et al., (including Tregloan-Reed J.,) 2013 MNRAS, 432, 693.
Warm Spitzer occultation photometry of WASP-26b at 3.6 and 4.5 μm

Choi J. -Y., et al., (including Tregloan-Reed J.,) 2013 ApJ, 768, 129.
Microlensing Discovery of a Population of Very Tight, Very Low-mass Binary Brown Dwarfs

Skottfelt J., et al., (including Tregloan-Reed J.,) 2013, A&A, 553 A111.
EMCCD photometry reveals two new variable stars in the crowded central region of the globular cluster NGC 6981

Mancini L., et al., (including Tregloan-Reed J.,) 2013 MNRAS, 430, 2932.
Physical properties of the WASP-44 planetary system from simultaneous multi- colour photometry

Kains N., et al., (including Tregloan-Reed J.,) 2013, A&A, 552, A70.
A giant planet beyond the snow line in microlensing event OGLE-2011-BLG-0251

Mancini L., et al., (including Tregloan-Reed J.,) 2013, A&A, 551, A11.
A lower radius and mass for the transiting extrasolar planet HAT-P-8 b

Hebrard G., et al., (including Tregloan-Reed J.,) 2013, A&A, 549, A134.
WASP-52 b, WASP-58 b, WASP-59 b, and WASP-60 b: Four new transiting close-in giant planets

Harpsoe K. B. W., et al., (including Tregloan-Reed J.,) 2013, A&A, 549, A10.
The transiting system GJ-1214: high-precision defocused transit observations and a search for evidence of transit timing variation

Shin I. -G., et al., (including Tregloan-Reed J.,) 2012, ApJ, 760, 116.
Microlensing Binaries with Candidate Brown Dwarf Companions

Southworth J., et al., (including Tregloan-Reed J.,) 2012, MNRAS, 426, 1338.
High-precision photometry by telescope defocusing - IV. Confirmation of the huge radius of WASP-17 b

Choi J. -Y., et al., (including Tregloan-Reed J.,) 2012, ApJ, 756, 48.
A New *Type of Ambiguity in the Planet and Binary Interpretations of Central Perturbations of High-magnification Gravitational Microlensing Events*

Shin I. -G., et al., (including Tregloan-Reed J.,) 2012, ApJ, 755, 91.
Characterizing Low-mass Binaries from Observation of Long-timescale Caustic- crossing Gravitational Microlensing Events

Southworth J., et al., (including Tregloan-Reed J.,) 2012, MNRAS, 426, 1338.
Physical properties and radius variations in the HAT-P-5 planetary system from simultaneous four-colour photometry

Bibliography

Abe, L., et al., 2013, A&A, 553, A49

Agol, E., Steffen, J., Sari, R., Clarkson, W., 2005, MNRAS, 359, 567

Albrecht, S., et al., 2011, ApJ, 738, 50

Albrecht, S., et al., 2012, ApJ, 757, 18

Aldenius, M., Tanner, J. D., Johansson, S., Lundberg, H., Ryan, S. G., 2007, A&A, 461, 767

Anderson, D. R., et al., 2010a, A&A, 513, L3

Anderson, D. R., et al., 2010b, ApJ, 709, 159

Anderson, D. R., et al., 2011, A&A, 534, A16

Anderson, D. R., et al., 2012, MNRAS, 422, 1988

Anderson, D. R., et al., 2013, MNRAS, 430, 3422

Arras, P., Socrates, A., 2010, ApJ, 714, 1

Baglin, A., et al., 2006, in 36th COSPAR Scientific Assembly, vol. 36 of *COSPAR Meeting*, p. 3749

Bakos, G., Noyes, R. W., Kovács, G., Stanek, K. Z., Sasselov, D. D., Domsa, I., 2004, PASP, 116, 266

Bakos, G. Á., et al., 2009, ApJ, 707, 446

Bakos, G. Á., et al., 2010, ApJ, 710, 1724

Bakos, G. Á., et al., 2012, AJ, 144, 19

Baliunas, S. L., et al., 1995, ApJ, 438, 269

Ballard, S., et al., 2011, ApJ, 743, 200

Ballerini, P., Micela, G., Lanza, A. F., Pagano, I., 2012, A&A, 539, A140

Baranne, A., et al., 1996, A&AS, 119, 373

Barban, C., Goupil, M. J., Van't Veer-Menneret, C., Garrido, R., Kupka, F., Heiter, U., 2003, A&A, 405, 1095

Barnes, S. A., 2007, ApJ, 669, 1167

Barros, S. C. C., Boué, G., Gibson, N. P., Pollacco, D. L., Santerne, A., Keenan, F. P., Skillen, I., Street, R. A., 2013, MNRAS, 430, 3032

Barros, S. C. C., et al., 2014, A&A, 561, L1

Batygin, K., Stevenson, D. J., 2010, ApJL, 714, L238

Bean, J. L., Désert, J.-M., Seifahrt, A., Madhusudhan, N., Chilingarian, I., Homeier, D., Szentgyorgyi, A., 2013, ApJ, 771, 108

Beaulieu, J.-P., et al., 2006, Nature, 439, 437

Bennett, D. P., Rhie, S. H., 1996, ApJ, 472, 660

Berdyugina, S. V., 2005, Living Reviews in Solar Physics, 2, 8

Bodenheimer, P., Laughlin, G., Lin, D. N. C., 2003, ApJ, 592, 555

Boisse, I., Bonfils, X., Santos, N. C., 2012, A&A, 545, A109

Boisse, I., et al., 2013, A&A, 558, A86

Bond, I. A., et al., 2001, MNRAS, 327, 868

Bond, I. A., et al., 2004, ApJL, 606, L155

Borucki, W. J., et al., 2010, Science, 327, 977

Borucki, W. J., et al., 2012, ApJ, 745, 120

Borucki, W. J., et al., 2013, Science, 340, 587

Boss, A. P., 1997, Science, 276, 1836

Boston, P. J., Ivanov, M. V., McKay, C. P., 1992, Icarus, 95, 300

Boyle, W. S., Smith, G. E., 1970, Bell System Technical Journal, 49, 587

Bruntt, H., Southworth, J., Torres, G., Penny, A. J., Clausen, J. V., Buzasi, D. L., 2006, A&A, 456, 651

Burrows, A., Hubeny, I., Budaj, J., Hubbard, W. B., 2007, 661, 502

Burrows, A., Rauscher, E., Spiegel, D. S., Menou, K., 2010, ApJ, 719, 341

Burton, J. R., Watson, C. A., Littlefair, S. P., Dhillon, V. S., Gibson, N. P., Marsh, T. R., Pollacco, D., 2012, ApJS, 201, 36

Butler, R. P., Marcy, G. W., Williams, E., McCarthy, C., Dosanjh, P., Vogt, S. S., 1996, PASP, 108, 500

Butler, R. P., Marcy, G. W., Fischer, D. A., Brown, T. M., Contos, A. R., Korzennik, S. G., Nisenson, P., Noyes, R. W., 1999, ApJ, 526, 916

Carter, J. A., Winn, J. N., Holman, M. J., Fabrycky, D., Berta, Z. K., Burke, C. J., Nutzman, P., 2011, ApJ, 730, 82

Castelli, F., Kurucz, R. L., 2003, in Piskunov, N., Weiss, W. W., Gray, D. F., eds., Modelling of Stellar Atmospheres, vol. 210 of *IAU Symposium*, p. 20P

Charbonneau, D., Brown, T. M., Latham, D. W., Mayor, M., 2000, ApJ, 529, L45

Charbonneau, D., et al., 2005, ApJ, 626, 523

Charbonneau, D., et al., 2009, Nature, 462, 891

Charbonneau, P., 1995, AJ, 101, 309

Chatterjee, S., Ford, E. B., Matsumura, S., Rasio, F. A., 2008, ApJ, 686, 580

Chauvin, G., Lagrange, A.-M., Dumas, C., Zuckerman, B., Mouillet, D., Song, I., Beuzit, J.-L., Lowrance, P., 2004, A&A, 425, L29

Claret, A., 2000, A&A, 363, 1081

Claret, A., 2003, A&A, 401, 657

Claret, A., 2004a, A&A, 428, 1001

Claret, A., 2004b, A&A, 424, 919

Claret, A., 2005, A&A, 440, 647

Claret, A., 2006, A&A, 453, 769

Claret, A., 2007, A&A, 467, 1389

Claret, A., Bloemen, S., 2011, A&A, 529, A75

Claret, A., Hauschildt, P. H., 2003, A&A, 412, 241

Collier Cameron, A., et al., 2007a, MNRAS, 380, 1230

Collier Cameron, A., et al., 2007b, MNRAS, 375, 951

Colón, K. D., Ford, E. B., Lee, B., Mahadevan, S., Blake, C. H., 2010, MNRAS, 408, 1494

Dartnell, L. R., Desorgher, L., Ward, J. M., Coates, A. J., 2007, Geophysical Research Letters, 34, 2207

Deeg, H. J., Garrido, R., Claret, A., 2001, New Astronomy, 6, 51

Demarque, P., Woo, J.-H., Kim, Y.-C., Yi, S. K., 2004, ApJS, 155, 667

Deming, D., Seager, S., Richardson, L. J., Harrington, J., 2005, Nature, 434, 740

Désert, J.-M., et al., 2011, ApJS, 197, 14

Diaz-Cordoves, J., Gimenez, A., 1992, A&A, 259, 227

Diaz-Cordoves, J., Claret, A., Gimenez, A., 1995, A&AS, 110, 329

Doyle, A. P., et al., 2013, MNRAS, 428, 3164

Doyle, L. R., et al., 2011, Science, 333, 1602

Dragomir, D., et al., 2011, ApJ, 142, 115

Dravins, D., Lindegren, L., Mezey, E., Young, A. T., 1998, PASP, 110, 610

Eastman, J., Siverd, R., Gaudi, B. S., 2010, PASP, 122, 935

Eastman, J., Gaudi, B. S., Agol, E., 2013, PASP, 125, 83

Eaton, N., Draper, P. W., Allen, A., 1999, Starlink User Note 45.9

Etzel, P. B., 1981, in Carling, E. B., Kopal, Z., eds., Photometric and Spectroscopic Binary Systems, NATO ASI Ser. C., 69, Kluwer, Dordrecht, p. 111

Fabrycky, D., Tremaine, S., 2007, ApJ, 669, 1298

Fabrycky, D. C., Winn, J. N., 2009, ApJ, 696, 1230

Fabrycky, D. C., et al., 2012, ApJ, 750, 114

Faedi, F., et al., 2013, A&A, 551, A73

Fortney, J. J., Marley, M. S., Barnes, J. W., 2007, ApJ, 659, 1661

Fortney, J. J., Lodders, K., Marley, M. S., Freedman, R. S., 2008, ApJ, 678, 1419

Fortney, J. J., Shabram, M., Showman, A. P., Lian, Y., Freedman, R. S., Marley, M. S., Lewis, N. K., 2010, ApJ, 709, 1396

Gaudi, B. S., Winn, J. N., 2007, ApJ, 655, 550

Gelman, A., Rubin, R., 1992, Statistical Science, 7, 457

Gibson, N. P., et al., 2010, MNRAS, 404, L114

Gilliland, R. L., et al., 1993, ApJ, 106, 2441

Gillon, M., Jehin, E., Magain, P., Chantry, V., Hutsemékers, D., Manfroid, J., Queloz, D., Udry, S., 2011a, in European Physical Journal Web of Conferences, vol. 11 of *European Physical Journal Web of Conferences*, p. 6002

Gillon, M., et al., 2009a, A&A, 501, 785

Gillon, M., et al., 2009b, A&A, 496, 259

Gillon, M., et al., 2011b, A&A, 533, A88

Giménez, A., 2006, A&A, 450, 1231

Girardi, L., Bressan, A., Bertelli, G., Chiosi, C., 2000, A&AS, 141, 371

Gizon, L., Solanki, S. K., 2003, ApJ, 589, 1009

Gnevyshev, M. N., 1938, Izvestiya Glavnoj Astronomicheskoj Observatorii v Pulkove, 16, 36

Goldreich, P., Tremaine, S., 1980, ApJ, 241, 425

Gould, A., Loeb, A., 1992, ApJ, 396, 104

Gray, D., 2008, The Observation and Analysis of Stellar Photospheres, 3rd Ed., Cambridge University Press

Greiner, J., et al., 2008, PASP, 120, 405

Güedel, M., Guinan, E. F., Skinner, S. L., 1997, ApJ, 483, 947

Gustafsson, B., Bell, R. A., Eriksson, K., Nordlund, A., 1975, A&A, 42, 407

Gustafsson, B., Edvardsson, B., Eriksson, K., Jørgensen, U. G., Nordlund, Å., Plez, B., 2008, A&A, 486, 951

Hartman, J. D., et al., 2012, AJ, 144, 139

Hastings, W. K., 1970, Biometrika, 57, 97

Hatzes, A. P., 1999, in Hearnshaw, J. B., Scarfe, C. D., eds., IAU Colloq. 170: Precise Stellar Radial Velocities, vol. 185 of *Astronomical Society of the Pacific Conference Series*, p. 259

Hebb, L., et al., 2010, ApJ, 708, 224

Hellier, C., Anderson, D. R., Collier-Cameron, A., Miller, G. R. M., Queloz, D., Smalley, B., Southworth, J., Triaud, A. H. M. J., 2011, ApJ, 730, L31

Hellier, C., et al., 2012, MNRAS, 426, 739

Henry, G. W., Marcy, G. W., Butler, R. P., Vogt, S. S., 2000, ApJ, 529, L41

Henwood, R., Chapman, S. C., Willis, D. M., 2010, Solar Physics, 262, 299

Hilditch, R. W., 2001, An Introduction to Close Binary Stars, Cambridge University Press.

Hirano, T., Narita, N., Shporer, A., Sato, B., Aoki, W., Tamura, M., 2011, PASJ, 63, 531

Holman, M. J., Murray, N. W., 2005, Science, 307, 1288

Holman, M. J., et al., 2010, Science, 330, 51

Holt, J. R., 1893, Astronomy and Astro-Physics, XII, 646

Howard, A. W., et al., 2012, ApJ, 749, 134

Howarth, I. D., 2004, in Maeder, A., Eenens, P., eds., Stellar Rotation, vol. 215 of *IAU Symposium*, p. 33

Howarth, I. D., 2011, MNRAS, 418, 1165

Howe, A. R., Burrows, A. S., 2012, ApJ, 756, 176

Huitson, C. M., et al., 2013, MNRAS, 434, 3252

Ibgui, L., Burrows, A., 2009, 700, 1921

Jackson, B., Barnes, R., Greenberg, R., 2009, ApJ, 698, 1357

Johnson, J. A., Winn, J. N., Cabrera, N. E., Carter, J. A., 2009, ApJL, 692, L100

Jordán, A., et al., 2013, ApJ, 778, 184

Kasting, J. F., Whitmire, D. P., Reynolds, R. T., 1993, Icarus, 101, 108

Kipping, D. M., Dunn, W. R., Jasinski, J. M., Manthri, V. P., 2012, MNRAS, 421, 1166

Kivelson, M. G., Khurana, K. K., Russell, C. T., Volwerk, M., Walker, R. J., Zimmer, C., 2000, Science, 289, 1340

Klinglesmith, D. A., Sobieski, S., 1970, AJ, 75, 175

Konacki, M., Torres, G., Jha, S., Sasselov, D. D., 2003, Nature, 421, 507

Kopparapu, R. K., et al., 2013, ApJ, 765, 131

Kozai, Y., 1962, AJ, 67, 591

Krejčová, T., Budaj, J., Krushevska, V., 2010, Contributions of the Astronomical Observatory Skalnate Pleso, 40, 77

Kurucz, R. L., 1979, ApJS, 40, 1

Lammer, H., Selsis, F., Ribas, I., Guinan, E. F., Bauer, S. J., Weiss, W. W., 2003, ApJL, 598, L121

Lendl, M., Gillon, M., Queloz, D., Alonso, R., Fumel, A., Jehin, E., Naef, D., 2013, A&A, 552, A2

Levenberg, K., 1944, The Quarterly of Applied Mathematics 2, 168

Lidov, M. L., 1962, Planetary and Space Science, 9, 719

Lissauer, J. J., et al., 2011, Nature, 470, 53

Lynden-Bell, D., Pringle, J. E., 1974, MNRAS, 168, 603

Maciejewski, G., Raetz, S., Nettelmann, N., Seeliger, M., Adam, C., Nowak, G., Neuhäuser, R., 2011, A&A, 535, A7

Mahtani, D. P., et al., 2013, MNRAS, 432, 693

Mamajek, E. E., Hillenbrand, L. A., 2008, ApJ, 687, 1264

Mancini, L., et al., 2013a, A&A, 551, A11

Mancini, L., et al., 2013b, MNRAS, 430, 2932

Mancini, L., et al., 2013c, MNRAS, 436, 2

Mandel, K., Agol, E., 2002, ApJL, 580, L171

Mao, S., Paczynski, B., 1991, ApJL, 374, L37

Marois, C., Macintosh, B., Barman, T., Zuckerman, B., Song, I., Patience, J., Lafrenière, D., Doyon, R., 2008, Science, 322, 1348

Marquardt, D., 1963, Journal of the Society for Industrial and Applied Mathematics, 11, 431

Matsumura, S., Peale, S. J., Rasio, F. A., 2010, ApJ, 725, 1995

Maxted, P. F. L., Koen, C., Smalley, B., 2011a, MNRAS, 418, 1039

Maxted, P. F. L., et al., 2011b, PASP, 123, 547

Mayor, M., Queloz, D., 1995, Nature, 378, 355

Mayor, M., et al., 2003, The Messenger, 114, 20

Mazeh, T., Zucker, S., Pont, F., 2005, MNRAS, 356, 955

McLaughlin, D. B., 1924, ApJ, 60, 22

Metcalfe, T. S., Charbonneau, P., 2003, Journal of Computational Physics, 185, 176

Metropolis, N., Rosenbluth, A. W., Rosenbluth, M. N., Teller, A. H., Teller, E., 1953, J. Comp. Phys., 21, 1087

Miller, B. L., Goldberg, D. E., 1995, Complex Systems, 9, 193

Miller, N., Fortney, J. J., Jackson, B., 2009, 702, 1413

Miralda-Escudé, J., 2002, ApJ, 564, 1019

Mohler-Fischer, M., et al., 2013, A&A, 558, A55

Moulds, V. E., Watson, C. A., Bonfils, X., Littlefair, S. P., Simpson, E. K., 2013, MNRAS, 430, 1709

Mucciarelli, A., Pancino, E., Lovisi, L., Ferraro, F. R., Lapenna, E., 2013, ApJ, 766, 78

Mumma, M. J., DiSanti, M. A., Dello Russo, N., Magee-Sauer, K., Gibb, E., Novak, R., 2003, Advances in Space Research, 31, 2563

Nelson, B., Davis, W. D., 1972, ApJ, 174, 617

Nesvorný, D., Kipping, D., Terrell, D., Hartman, J., Bakos, G. Á., Buchhave, L. A., 2013, ApJ, 777, 3

Nikolov, N., Chen, G., Fortney, J. J., Mancini, L., Southworth, J., van Boekel, R., Henning, T., 2013, A&A, 553, A26

Noyes, R. W., Hartmann, L. W., Baliunas, S. L., Duncan, D. K., Vaughan, A. H., 1984, ApJ, 279, 763

Nutzman, P. A., Fabrycky, D. C., Fortney, J. J., 2011, ApJL, 740, L10

Orosz, J. A., et al., 2012, Science, 337, 1511

Oshagh, M., Boisse, I., Boué, G., Montalto, M., Santos, N. C., Bonfils, X., Haghighipour, N., 2013, A&A, 549, A35

Papaloizou, J. C. B., Larwood, J. D., 2000, MNRAS, 315, 823

Pepper, J., et al., 2013, ApJ, 773, 64

Petrovay, K., van Driel-Gesztelyi, L., 1997, Solar Physics, 176, 249

Pinsonneault, M. H., DePoy, D. L., Coffee, M., 2001, ApJL, 556, L59

Pollacco, D., et al., 2008, MNRAS, 385, 1576

Pollacco, D. L., et al., 2006, PASP, 118, 1407

Pollack, J. B., Hubickyj, O., Bodenheimer, P., Lissauer, J. J., Podolak, M., Greenzweig, Y., 1996, Icarus, 124, 62

Pont, F., et al., 2007, A&A, 476, 1347

Pont, F., et al., 2010, MNRAS, 402, L1

Popper, D. M., Etzel, P. B., 1981, AJ, 86, 102

Press, W. H., Teukolsky, S. A., Vetterling, W. T., Flannery, B. P., 1993, Numerical recipes in Fortran: the art of scientific computing, Cambridge University Press

Price, K., Storn, R., 1997, Dr Dobb's Journal, 264, 18

Queloz, D., et al., 2000, A&A, 354, 99

Rabus, M., et al., 2009, A&A, 494, 391

Rajpaul, V., 2012a, MNRAS, 427, 1755

Rajpaul, V., 2012b, in 56th Annual Conference of the South African Institute of Physics (SAIP), vol. 56 of *Proceedings of SAIP*, p. 519

Rasio, F. A., Ford, E. B., 1996, Science, 274, 954

Ribas, I., Jordi, C., Torra, J., 1999, MNRAS, 309, 199

Ross, M. N., Schubert, G., 1987, Nature, 325, 133

Rossiter, R. A., 1924, ApJ, 60, 15

Sada, P. V., et al., 2012, PASP, 124, pp. 212

Safronov, V. S., 1972, Evolution of the Protoplanetary Cloud and Formation of the Earth and Planets (Jerusalem: Israel Program for Scientific Translation)

Sanchis-Ojeda, R., Winn, J. N., 2011, ApJ, 743, 61

Sanchis-Ojeda, R., Winn, J. N., Holman, M. J., Carter, J. A., Osip, D. J., Fuentes, C. I., 2011, ApJ, 733, 127

Sanchis-Ojeda, R., et al., 2012, Nature, 487, 449

Sanchis-Ojeda, R., et al., 2013, ApJ, 775, 54

Schlaufman, K. C., 2010, ApJ, 719, 602

Schlesinger, F., 1910, Publications of the Allegheny Observatory of the University of Pittsburgh, 1, 123

Schlesinger, F., 1916, Publications of the Allegheny Observatory of the University of Pittsburgh, 3, 23

Schneider, J., Dedieu, C., Le Sidaner, P., Savalle, R., Zolotukhin, I., 2011, A&A, 532, A79

Schwamb, M. E., et al., 2013, ApJ, 768, 127

Showman, A. P., Guillot, T., 2002, A&A, 385, 166

Silva, A. V. R., 2003, ApJ, 585, L147

Silva-Valio, A., 2008, ApJ, 683, L179

Sing, D. K., 2010, A&A, 510, A21

Sing, D. K., et al., 2011, MNRAS, 416, 1443

Skrutskie, M. F., et al., 2006, AJ, 131, 1163

Skumanich, A., 1972, ApJ, 171, 565

Snellen, I. A. G., de Kok, R. J., le Poole, R., Brogi, M., Birkby, J., 2013, ApJ, 764, 182

Southworth, J., 2008, MNRAS, 386, 1644

Southworth, J., 2009, MNRAS, 394, 272

Southworth, J., 2010, MNRAS, 408, 1689

Southworth, J., 2011, MNRAS, 417, 2166

Southworth, J., Maxted, P. F. L., Smalley, B., 2004a, MNRAS, 351, 1277

Southworth, J., Maxted, P. F. L., Smalley, B., 2004b, MNRAS, 349, 547

Southworth, J., Bruntt, H., Buzasi, D. L., 2007a, A&A, 467, 1215

Southworth, J., Wheatley, P. J., Sams, G., 2007b, MNRAS, 379, L11

Southworth, J., Mancini, L., Maxted, P. F. L., Bruni, I., Tregloan-Reed, J., Barbieri, M., Ruocco, N., Wheatley, P. J., 2012a, MNRAS, 422, 3099

Southworth, J., et al., 2009a, MNRAS, 396, 1023

Southworth, J., et al., 2009b, MNRAS, 399, 287

Southworth, J., et al., 2009c, ApJ, 707, 167

Southworth, J., et al., 2010, MNRAS, 408, 1680

Southworth, J., et al., 2012b, MNRAS, 426, 1338

Spearman, C., 1904, The American Journal of Psychology, 15, pp. 72

Spiegel, D. S., Burrows, A., Milsom, J. A., 2011, ApJ, 727, 57

Steele, I. A., Bates, S. D., Gibson, N., Keenan, F., Meaburn, J., Mottram, C. J., Pollacco, D., Todd, I., 2008, in Society of Photo-Optical Instrumentation Engineers (SPIE) Conference Series, vol. 7014 of *Society of Photo-Optical Instrumentation Engineers (SPIE) Conference Series*

Stempels, H. C., Collier Cameron, A., Hebb, L., Smalley, B., Frandsen, S., 2007, MNRAS, 379, 773

Stetson, P. B., 1987, PASP, 99, 191

Steves, B. A., Hendry, M., Cameron, A. C., 2011, Extra-Solar Planets: The Detection, Formation, Evolution and Dynamics of Planetary Systems, CRC Press

Storn, R., Price, K., 1997, Journal of Global Optimisation, 11, 341

Strassmeier, K. G., 2009, A&A Rev, 17, 251

Taylor, J. R., 1997, Introduction to Error Analysis, 2nd Ed. (cloth) p 268, University Science Books

Ter Braak, C. J. F., 2006, Statistics and Computing, 16, 239

Torres, G., Andersen, J., Giménez, A., 2010, A&A Rev, 18, 67

Triaud, A. H. M. J., 2011a, A&A, 534, L6

Triaud, A. H. M. J., 2011b, A&A, 534, L6

Tyler, R. H., 2008, Nature, 456, 770

Udalski, A., 2003, Acta Astronomica, 53, 291

Udalski, A., Zebrun, K., Szymanski, M., Kubiak, M., Soszynski, I., Szewczyk, O., Wyrzykowski, L., Pietrzynski, G., 2002, Acta Astronomica, 52, 115

Valenti, J. A., Piskunov, N., 1996, A&AS, 118, 595

Van't Veer, F., 1960, L'assombrissement centre-bord des etoiles.

Waldmeier, M., 1955, Ergebnisse und Probleme der Sonnenforschung.

Ward, W. R., 1997a, Icarus, 126, 261

Ward, W. R., 1997b, ApJL, 482, L211

Wells, D. C., Greisen, E. W., Harten, R. H., 1981, A&AS, 44, 363

Welsh, W. F., et al., 2012, Nature, 481, 475

Winn, J. N., 2011, Exoplanet Transits and Occultations, University of Arizona Press, p. 55

Winn, J. N., Holman, M. J., Fuentes, C. I., 2007a, AJ, 133, 11

Winn, J. N., Holman, M. J., Carter, J. A., Torres, G., Osip, D. J., Beatty, T., 2009, AJ, 137, 3826

Winn, J. N., Fabrycky, D., Albrecht, S., Johnson, J. A., 2010a, ApJ, 718, L145

Winn, J. N., et al., 2007b, ApJ, 133, 1828

Winn, J. N., et al., 2010b, ApJ, 723, L223

Wolszczan, A., Frail, D. A., 1992, Nature, 355, 145

Wu, Y., Murray, N., 2003, ApJ, 589, 605

Xie, J.-W., 2013a, ApJS, 208, 22

Xie, J.-W., 2013b, ArXiv: 1309.2329

Yao, L., Sethares, W., 1994, Signal Processing, IEEE Transactions on, 42, 927

Youdin, A. N., Mitchell, J. L., 2010, ApJ, 721, 1113